

https://dspace.org/

Phase equilibrium diagram of Co-Fe-Pd

Ukabhai, Kiyaasha Dyal

2019

https://hdl.handle.net/10539/28372

Dyal Ukabhai, Kiyaasha (2019) Phase equilibrium diagram of Co-Fe-Pd, University of the Witwatersrand, Johannesburg, <http://hdl.handle.net/10539/28372>

Downloaded from a DSpace repository. https://dspace.org/



Phase equilibrium diagram of Co-Fe-Pd

Kiyaasha Dyal Ukabhai

A dissertation submitted to the Faculty of Engineering and the Built Environment, University of the Witwatersrand, in fulfilment of the requirements for the degree of Masters of Science in Metallurgical Engineering

Johannesburg, May 2019

DECLARATION

I hereby declare that, unless otherwise acknowledged, this dissertation is my own unaided work and has not been submitted previously at this, or any other institution of learning for any degree or examination.

_____ _____

Signature Date

Abstract

There is potential to use Co-Fe-Pd rare earth-doped alloys for magnets. The system offers possible alternatives for the heavy and expensive rare-earth magnets. The phase diagram of Co-Fe-Pd was derived nearly sixty years ago and is inconsistent. Therefore, the system needs to be studied again to provide an accurate and updated phase diagram to facilitate the development of the potential magnetic alloys.

Samples of different compositions of Co-Fe-Pd were made in a button arc furnace, under an argon atmosphere on a water-cooled copper hearth. They were sectioned and part was kept in the as-cast state and the other part annealed. The samples were analysed in a scanning electron microscope with energy dispersive X-ray spectroscopy to observe the microstructures and to determine the overall and phase compositions. Samples were also analysed in an X-ray diffractometer to confirm the phases. The same analysis procedure was followed for the as-cast and the annealed samples.

Coring occurred in many samples, which was expected due to the wide solid solutions in the system. The microstructures were not similar to any of the previous work. There was better agreement of the as-cast samples with the assessed 25°C isothermal section of Raghavan [1992Rag], than with the experimental one of Kuprina and Grigorev [1961Kup]. The deduced liquidus slope agreed with both of the liquidus surfaces published.

Some of the phases were too fine to be analysed in the as-cast samples. It was expected that annealing the samples would have coarsened the grains, but the phases were still to fine to analyse. The 1000°C alloys were not homogenous and apart from three alloys which had two phases, the others comprised only one phase. The FePd and $FePd_3$ regions of the Fe-Pd binary diagram did not extend perceptibly into the ternary system. The 1000°C isothermal section was comprised mainly of the A1 (γFe, αCo, Pd) phase.

The samples were also annealed at 650°C. The ordered α' peaks were difficult to identify by XRD, and FePd and $FePd_3$ were difficult to distinguish from A1 (γFe, αCo, Pd). There was a A1 (γFe, αCo, Pd) miscibility gap in the system, around Co_{71}:Fe_{16}:Pd_{13} – Co_{31}:Fe_{22}:Pd_{47}. The hardness of the alloys increased with increased Fe and decreased Pd contents. The three conditions followed the same trends for hardnesses.

Dedication

This dissertation is dedicated to

my Mother and Father for their support and encouragement and,

without whom none of my success would have been possible.

Acknowledgements

I would like to give my sincere thanks to the following people and organisations for their help to complete this project:

- My supervisor, Prof L.A. Cornish, for her support, motivation and constant guidance.
- The DST and NRF for supporting the DST-NRF Centre of Excellence in Strong Materials (CoE-SM), which gave financial support.
- The School of Chemical and Metallurgical Engineering at the University of the Witwatersrand, for providing facilities and equipment.
- Mintek, for providing the raw materials for the samples, making the samples and Alain Mwamba for organizing everything.
- Brayner Ndivhuwo Nelwalani for his assistance with SEM analysis of samples.
- Lastly, my wholehearted thanks to my siblings, family and friends, for the motivation and assistance.

Outputs from this research

- K. Dyal Ukabhai and L.A. Cornish, Study of as-cast Co-Fe-Pd samples, AMI Precious Metals 2017, The Precious Metals Development Network (PMDN) Conference, (Book of) Abstracts of papers presented at the conference, pp. 63-64, Polokwane, South Africa, 17th-19th October 2017.

- K. Dyal Ukabhai and L.A. Cornish, Initial study of as-cast Co-Fe-Pd samples, Proceedings of Microscopy Society of Southern Africa (MSSA), Vol. 47, p. 27, Bela-Bela, South Africa, 4th- 7th December 2017.

- L.A. Cornish, K. Dyal Ukabhai and A. Fabuyide, Co-Fe-Pd Ternary Phase Diagram Evaluation, Ternary Evaluations, MSI Eureka, MSI, Materials Science International, Stuttgart, 2018, available at: http://www.msi-eureka.com/full-html/10.41430.1.0/Co-Fe-Pd_Ternary.

- K. Dyal Ukabhai, I.A. Mwamba and L.A. Cornish, Phase analyses of the Co-Fe-Pd ternary alloys, CoSAAMI-2018, IOP Conf. Series: Materials Science and Engineering, 430, 012023, Vanderbijlpark, South Africa, 23rd-26th October 2018.

Contents

Abstract iii

Dedication iv

Acknowledgements v

Outputs from this research vi

List of Tables xi

List of Figures xiv

Chapter 1: Introduction 1

1.1. Background 1

1.2. Research objectives 2

Chapter 2: Literature review 3

2.1. Ordering 3

2.2. Magnetism 6

2.3. Constituent binary systems of the Co-Fe-Pd system 7

2.3.1. Co-Fe 7

2.3.2. Co-Pd 8

2.3.3. Fe-Pd 9

2.4. Work done on Co-Fe-Pd phase diagram 11

2.5. Properties of Co-Fe-Pd alloys 16

Chapter 3: Research methodology 18

3.1. Compositions 18

3.2. Manufacturing samples 19

3.3. Metallographic preparation 20

3.4. Analysis of samples 21

3.4.1. Scanning electron microscopy (SEM) 21

3.4.2. X-ray diffraction (XRD) 21

Chapter 4: Results - SEM and XRD 22
4.1. As-cast samples 22
4.1.1. Alloy 1: Nominal Co_{30}:Fe_{60}:Pd_{10} (at.%) 22
4.1.2. Alloy 2: Nominal Co_{6}:Fe_{44}:Pd_{50} (at.%) 25
4.1.3. Alloy 3: Nominal Co_{20}:Fe_{50}:Pd_{30} (at.%) 28
4.1.4. Alloy 4: Nominal Co_{10}:Fe_{15}:Pd_{75} (at.%) 31
4.1.5. Alloy 5: Nominal Co_{30}:Fe_{30}:Pd_{40} (at.%) 34
4.1.6. Alloy 6: Nominal Co_{50}:Fe_{20}: Pd_{30} (at.%) 37
4.1.7. Alloy 7: Nominal Co_{10}:Fe_{30}:Pd_{60} (at.%) 40
4.1.8. Alloy 8: Nominal Co_{25}:Fe_{20}:Pd_{55} (at.%) 43
4.1.9. Alloy 9: Nominal Co_{10}:Fe_{50}:Pd_{40} (at.%) 46
4.1.10. Alloy 10: Nominal Co_{40}:Fe_{30}:Pd_{30} (at.%) 49
4.1.11. Alloy 11: Nominal Co_{20}:Fe_{60}:Pd_{20} (at.%) 52
4.1.12. Alloy 12: Nominal Co_{60}:Fe_{20}:Pd_{20} (at.%) 55
4.2. Samples annealed at 1000°C 58
4.2.1. Alloy 1: Nominal Co_{30}:Fe_{60}:Pd_{10} (at.%) 58
4.2.2. Alloy 2: Nominal Co_{6}:Fe_{44}:Pd_{50} (at.%) 61
4.2.3. Alloy 3: Nominal Co_{20}:Fe_{50}:Pd_{30} (at.%) 64
4.2.4. Alloy 4: Nominal Co_{10}:Fe_{15}:Pd_{75} (at.%) 67
4.2.5. Alloy 5: Nominal Fe_{30}:Co_{30}:Pd_{40} (at.%) 70
4.2.6. Alloy 6: Nominal Co_{50}:Fe_{20}:Pd_{30} (at.%) 73
4.2.7. Alloy 7: Nominal Co_{10}:Fe_{30}:Pd_{60} (at.%) 76
4.2.8. Alloy 8: Nominal Co_{25}:Fe_{20}:Pd_{55} (at.%) 79
4.2.9. Alloy 9: Nominal Co_{10}:Fe_{50}:Pd_{40} (at.%) 82
4.2.10. Alloy 10: Nominal Co_{40}:Fe_{30}:Pd_{30} (at.%) 85
4.2.11. Alloy 11: Nominal Co_{20}:Fe_{60}:Pd_{20} (at.%) 88

4.2.12. Alloy 12: Nominal Co_{60}:Fe_{20}:Pd_{20} (at.%) 91
4.3. Samples annealed at 650°C 94
4.3.1. Alloy 1: Nominal Co_{30}:Fe_{60}:Pd_{10} (at.%) 94
4.3.2. Alloy 2: Nominal Co_{6}:Fe_{44}:Pd_{50} (at.%) 97
4.3.3. Alloy 3: Nominal Co_{20}:Fe_{50}:Pd_{30} (at.%) 100
4.3.4. Alloy 4: Nominal Co_{10}:Fe_{15}:Pd_{75} (at.%) 103
4.3.5. Alloy 5: Nominal Co_{30}:Fe_{30}:Pd_{40} (at.%) 106
4.3.6. Alloy 6: Nominal Co_{50}:Fe_{20}:Pd_{30} (at.%) 109
4.3.7. Alloy 7: Nominal Co_{10}:Fe_{30}:Pd_{60} (at.%) 112
4.3.8. Alloy 8: Nominal Co_{25}:Fe_{20}:Pd_{55} (at.%) 115
4.3.9. Alloy 9: Nominal Co_{10}:Fe_{50}:Pd_{40} (at.%) 118
4.3.10. Alloy 10: Nominal Co_{40}:Fe_{30}:Pd_{30} (at.%) 121
4.3.11. Alloy 11: Nominal Co_{20}:Fe_{60}:Pd_{20} (at.%) 124
4.3.12. Alloy 12: Nominal Co_{60}:Fe_{20}:Pd_{20} (at.%) 127
Chapter 5: - Microhardness results 130
Chapter 6: Discussion 133
6.1. Interpretation of the data 133
6.2. As-cast alloys 134
6.3. Alloys annealed at 1000°C 137
6.4. Alloys annealed at 650°C 140
6.5. Microhardness results 144
Chapter 7: Conclusions 148
7.1. As-cast alloys 148
7.2. Alloys annealed at 1000°C 148
7.3 Alloys annealed at 650°C 149
7.4. Microhardness 149

Chapter 8: Recommendations for Future work 150

References 151

Appendix A: Peaks used to match phases on XRD patterns 158

Appendix B: Work published 159

List of Tables

Table 3. 1. Summary of composition of the alloys..... 19

Table 4.1. EDX phase analyses for nominal Co_{30}:Fe_{60}:Pd_{10} (at.%), Alloy 1, as-cast condition..... 23

Table 4.2. EDX phase analyses for nominal Co_{6}:Fe_{44}:Pd_{50} (at.%), Alloy 2, as-cast condition..... 25

Table 4.3. EDX phase analyses for nominal Co_{20}:Fe_{50}:Pd_{30} (at.%), Alloy 3, as-cast condition..... 28

Table 4.4. EDX phase analyses for nominal Co_{10}:Fe_{15}:Pd_{75} (at.%), Alloy 4, as-cast condition..... 31

Table 4.5. EDX phase analyses for nominal Co_{30}:Fe_{30}:Pd_{40} (at.%), Alloy 5, as-cast condition..... 34

Table 4.6. EDX phase analyses for nominal Co_{50}:Fe_{20}:Pd_{30} (at.%), Alloy 6, as-cast condition..... 37

Table 4.7. EDX phase analyses for nominal Co_{10}:Fe_{30}:Pd_{60} (at.%), Alloy 7, as-cast condition..... 40

Table 4.8. EDX phase analyses for nominal Co_{10}:Fe_{25}:Pd_{55} (at.%), Alloy 8, as-cast condition..... 43

Table 4.9. EDX phase analyses for nominal Co_{10}:Fe_{30}:Pd_{40} (at.%), Alloy 9, as-cast condition..... 46

Table 4.10. EDX phase analyses for nominal Co_{40}:Fe_{30}:Pd_{30} (at.%), Alloy 10, as-cast condition..... 49

Table 4.11. EDX phase analyses for nominal Co_{20}:Fe_{60}:Pd_{20} (at.%), Alloy 11, as-cast condition..... 52

Table 4.12. EDX phase analyses for nominal Co_{60}:Fe_{20}:Pd_{20} (at.%), Alloy 12, as-cast condition..... 55

Table 4.13. EDX phase analyses for nominal Co_{30}:Fe_{60}:Pd_{10} (at.%), Alloy 1, annealed at 1000°C condition. 58

Table 4.14. EDX phase analyses for nominal Co_{6}:Fe_{44}:Pd_{50} (at.%), Alloy 2, annealed at 1000°C condition. 61

Table 4.15. EDX phase analyses for nominal Co_{20}:Fe_{50}:Pd_{30} (at.%), Alloy 3, annealed at 1000°C condition. 64

Table 4.16. EDX phase analyses for nominal Co_{10}:Fe_{15}:Pd_{75} (at.%), Alloy 4, annealed at 1000°C condition. 67

Table 4.17. EDX phase analyses for nominal Co_{30}:Fe_{30}:Pd_{40} (at.%), Alloy 5, annealed at 1000°C condition. 70

Table 4.18. EDX phase analyses for nominal Co_{50}:Fe_{20}:Pd_{30} (at.%), Alloy 6, annealed at 1000°C condition. 73

Table 4.19. EDX phase analyses for nominal Co_{10}:Fe_{30}:Pd_{60} (at.%), Alloy 7, annealed at 1000°C condition. 76

Table 4.20. EDX phase analyses for nominal Co_{10}:Fe_{25}:Pd_{55} (at.%), Alloy 8, annealed at 1000°C condition. 79

Table 4.21. EDX phase analyses for nominal Co_{10}:Fe_{30}:Pd_{40} (at.%), Alloy 9, annealed at 1000°C condition. 82
Table 4.22. EDX phase analyses for nominal Co_{40}:Fe_{30}:Pd_{30} (at.%), Alloy 10, annealed at 1000°C annealed condition. 85
Table 4.23. EDX phase analyses for nominal Co_{20}:Fe_{60}:Pd_{20} (at.%), Alloy 11, annealed at 1000°C condition. 88
Table 4.24. EDX phase analyses for nominal Co_{60}:Fe_{20}:Pd_{20} (at.%), Alloy 12, annealed at 1000°C condition. 91
Table 4.25. EDX phase analyses for nominal Co_{30}:Fe_{60}:Pd_{10} (at.%), Alloy 1, annealed at 650°C condition. 94
Table 4.26. EDX phase analyses for nominal Co_{6}: Fe_{44}:Pd_{50} (at.%), Alloy 2, annealed at 650°C condition. 97
Table 4.27. EDX phase analyses for nominal Co_{20}:Fe_{50}:Pd_{30} (at.%), Alloy 3, annealed at 650°C condition. 100
Table 4.28. EDX phase analyses for nominal Co_{10}:Fe_{15}:Pd_{75} (at.%), Alloy 4, annealed at 650°C condition. 103
Table 4.29. EDX phase analyses for nominal Co_{30}:Fe_{30}:Pd_{40} (at.%), Alloy 5, annealed at 650°C condition. 106
Table 4.30. EDX phase analyses for nominal Co_{50}:Fe_{20}:Pd_{30} (at.%), Alloy 6, annealed at 650°C condition. 109
Table 4.31. EDX phase analyses for nominal Co_{10}:Fe_{30}:Pd_{60} (at.%), Alloy 7, annealed at 650°C condition. 112
Table 4.32. EDX phase analyses for nominal Co_{10}:Fe_{25}:Pd_{55} (at.%), Alloy 8, annealed at 650°C condition. 115
Table 4.33. EDX phase analyses for nominal Co_{10}:Fe_{30}:Pd_{40} (at.%), Alloy 9, annealed at 650°C condition. 118
Table 4.34. EDX phase analyses for nominal Co_{40}:Fe_{30}:Pd_{30} (at.%), Alloy 10, annealed at 650°C condition. 121
Table 4.35. EDX phase analyses for nominal Co_{20}:Fe_{60}:Pd_{20} (at.%), Alloy 11, annealed at 650°C condition. 124
Table 4.36. EDX phase analyses for nominal Co_{60}:Fe_{20}:Pd_{20} (at.%), Alloy 12, annealed at 650°C condition. 127

Table 5.1. Vickers microhardness values and errors for all alloys. 130

Table 6.1. Unidentified peaks for the as-cast alloys. 137

List of Figures

Figure 2.1. a) Fe-Pd binary diagram with disordered and ordered FePd phase structure [2018Lau] and b) schematic representation of ordered $FePd_3$ ordered alloy [2012Kva]. 4
Figure 2.2. Schematic representation of the ordered and disordered α' phase [2018Pei]. 4
Figure 2.3. Binary diagram for Co-Fe system [2002Ohn]. 7
Figure 2. 4. Previously accepted Co-Fe phase diagram [1984Nis]. 8
Figure 2.5. Binary diagram for Pd-Co system [1990Mas]. 9
Figure 2.6. Binary diagram for Fe-Pd system [1990Mas]. 10
Figure 2.7. Isothermal section at ~25°C of Co-Fe-Pd system [1961Kup]. 12
Figure 2.8. Co-Fe binary system previously accepted [1988Ray]. 13
Figure 2.9. Co-Fe-Pd Isothermal section at ~25°C (at.%) [1992Rag] 14
Figure 2.10. Liquidus surfaces of Co-Fe-Pd: a) Kuprina and Grigorev [1958Kup], and b) Raghavan [1992Rag]. 15

Figure 3. 1. Co-Fe-Pd isothermal section at ~25°C in (at.%) [1992Rag] with plotted compositions of interest. 18

Figure 4.1. SEM-BSE images of as-cast Co_{30}:Fe_{60}:Pd_{10} (at.%), Alloy 1 showing: a) dendrites (darker), and b) showing decomposition at higher magnification. 22
Figure 4.2. EDX analyses of nominal Co_{30}:Fe_{60}:Pd_{10} (at.%), Alloy 1 as-cast condition. (■ Overall composition; ● phases) 23
Figure 4.3. XRD patterns for nominal Co_{30}:Fe_{60}:Pd_{10} (at.%), Alloy 1 as-cast condition: a) raw, and b) labelled. 24
Figure 4.4. SEM images of as-cast Co_6:Fe_{44}:Pd_{50} (at.%), Alloy 2 showing: a) SE grains, and b) BSE higher magnification. 25
Figure 4.5. EDX analyses of nominal Co_6:Fe_{44}:Pd_{50} (at.%), Alloy 2 as-cast condition. (■ Overall composition; ● phases) 26
Figure 4.6. XRD patterns for nominal Co_6:Fe_{44}:Pd_{50} (at.%), Alloy 2 as-cast condition: a) raw, and b) labelled. 27
Figure 4.7. a) SEM-SE, and b) SEM-BSE images of as-cast Co_{20}:Fe_{50}:Pd_{30} (at.%), Alloy 3 showing grains and different contrasts. 28

Figure 4.8. EDX analyses of nominal Co_{20}:Fe_{50}:Pd_{30} (at.%), Alloy 3 as-cast condition. (■ Overall composition; ● phases)..... 29
Figure 4.9. XRD patterns for nominal Co_{20}:Fe_{50}:Pd_{30} (at.%), Alloy 3 as-cast condition: a) raw, and b) labelled. 30
Figure 4.10. SEM-BSE images of as-cast Co_{10}:Fe_{15}:Pd_{75} (at.%), Alloy 4 showing: a) dendrites (lighter), and interdendritic areas (dark) and b) higher magnification..... 31
Figure 4.11. EDX analyses of nominal Co_{10}:Fe_{15}:Pd_{75} (at.%), Alloy 4 as-cast condition. (■ Overall composition; ● phases)..... 32
Figure 4.12. XRD patterns for nominal Co_{10}:Fe_{15}:Pd_{75} (at.%), Alloy 4 as-cast condition: a) raw, and b) labelled. 33
Figure 4.13. SEM-SE image of as-cast Co_{30}:Fe_{30}:Pd_{40} (at.%), Alloy 5 showing a single phase with pores... 34
Figure 4.14. EDX analyses of nominal Co_{30}:Fe_{30}:Pd_{40} (at.%), Alloy 5 as-cast condition. (■ Overall composition; ● phases)..... 35
Figure 4.15. XRD patterns for nominal Co_{30}:Fe_{30}:Pd_{40} (at.%), Alloy 5 as-cast condition: a) raw, and b) labelled. 36
Figure 4.16. SEM-BSE images of as-cast Co_{50}:Fe_{20}:Pd_{30} (at.%), Alloy 6 showing a) coring and dark grain boundaries at low magnification and b) high magnification. 37
Figure 4.17. EDX analyses of nominal Co_{50}:Fe_{20}:Pd_{30} (at.%), Alloy 6 as-cast condition. (■ Overall composition; ● phases)..... 38
Figure 4.18. XRD patterns for nominal Co_{50}:Fe_{20}:Pd_{30} (at.%), Alloy 6 as-cast condition: a) raw, and b) labelled. 39
Figure 4.19. SEM-BSE images of as-cast Co_{10}:Fe_{30}:Pd_{60} (at.%), Alloy 7 showing: a) the formation of needles surrounded by a lighter phase, and b) a local area of inhomogeneity. 40
Figure 4.20. EDX analyses of nominal Co_{10}:Fe_{30}:Pd_{60} (at.%), Alloy 7 as-cast condition. (■ Overall composition; ● phases)..... 41
Figure 4.21. XRD patterns for nominal Co_{10}:Fe_{30}:Pd_{60} (at.%), Alloy 7 as-cast condition: a) raw, and b) labelled. 42
Figure 4.22. SEM-BSE images of as-cast Co_{25}:Fe_{20}:Pd_{55} (at.%), Alloy 8 showing: a) scratches surrounded by darker phase, and b) etched out particles surrounded by a light phase. 43
Figure 4.23. EDX analyses of nominal Co_{25}:Fe_{20}:Pd_{55} (at.%), Alloy 8 as-cast condition. (■ Overall composition; ● phases)..... 44

Figure 4.24. XRD patterns for nominal Co_{25}:Fe_{20}:Pd_{55} (at.%), Alloy 8 as-cast condition: a) raw, and b) labelled. 45
Figure 4.25. SEM-BSE images of as-cast Co_{10}:Fe_{50}:Pd_{40} (at.%), Alloy 9 showing: a) the formation of a light phase surrounded by a dark phase, and b) a differently etched area with particles surrounded by a matrix. 46
Figure 4.26. EDX analyses of nominal Co_{10}:Fe_{50}:Pd_{40} (at.%), Alloy 9 as-cast condition. (■ Overall composition; ● phases)..... 47
Figure 4.27. XRD patterns for nominal Co_{10}:Fe_{50}:Pd_{40} (at.%), Alloy 9 as-cast condition: a) raw, and b) labelled. 48
Figure 4.28. SEM-BSE images of as-cast Co_{40}:Fe_{30}:Pd_{30} (at.%), Alloy 10 showing: a) coring, and b) etched patch with particles surrounded by a matrix. 49
Figure 4.29. EDX analyses of nominal Co_{40}:Fe_{30}:Pd_{30} (at.%), Alloy 10 as-cast condition. (■ Overall composition; ● phases)..... 50
Figure 4.30. XRD patterns for nominal Co_{40}:Fe_{30}:Pd_{30} (at.%), Alloy 10 as-cast condition: a) raw, and b) labelled. 51
Figure 4.31. SEM-BSE images of as-cast Co_{20}:Fe_{60}:Pd_{20} (at.%), Alloy 11 showing the formation of dendrites surrounded by a matrix a) low magnification and b) higher magnification. 52
Figure 4.32. EDX analyses of nominal Co_{20}:Fe_{60}:Pd_{20} (at.%), Alloy 11 as-cast condition. (■ Overall composition; ● phases)..... 53
Figure 4.33. XRD patterns for nominal Co_{20}:Fe_{60}:Pd_{20} (at.%), Alloy 11 as-cast condition: a) raw, and b) labelled. 54
Figure 4.34. SEM-BSE images of as-cast Co_{60}:Fe_{20}:Pd_{20} (at.%), Alloy 12 showing dendrites surrounded by a lighter grey phase and porosity. 55
Figure 4.35. EDX analyses of nominal Co_{60}:Fe_{20}:Pd_{20} (at.%), Alloy 12 as-cast condition. (■ Overall composition; ● phases)..... 56
Figure 4.36. XRD patterns for nominal Co_{60}:Fe_{20}:Pd_{20} (at.%), Alloy 12 as-cast condition: a) raw, and b) labelled. 57
Figure 4.37. SEM-BSE images of Co_{30}:Fe_{60}:Pd_{10} (at.%), Alloy 1 annealed at 1000°C for 1000 h showing: a) the lamellar microstructure and b) at higher magnification. 58
Figure 4.38. EDX analyses of nominal Co_{30}:Fe_{60}:Pd_{10} (at.%), Alloy 1 1000°C annealed condition. (■ Overall composition; ● phases)..... 59

Figure 4.39. XRD patterns for nominal Co_{30}:Fe_{60}:Pd_{10} (at.%), Alloy 1 1000°C annealed condition: a) raw, and b) labelled. 60
Figure 4.40. SEM-BSE images of Co_6:Fe_{44}:Pd_{50} (at.%), Alloy 2 annealed at 1000°C for 1000 h showing: a) differently etched areas, and b) a better etched area at higher magnification. 61
Figure 4.41. EDX analyses of nominal Co_6:Fe_{44}:Pd_{50} (at.%), Alloy 2 1000°C annealed condition. (■ Overall composition; ● phases) 62
Figure 4.42. XRD patterns for nominal Co_6:Fe_{44}:Pd_{50} (at.%), Alloy 2 1000°C annealed condition: a) raw, and b) labelled. 63
Figure 4.43. SEM-BSE images of Co_{20}:Fe_{50}:Pd_{30} (at.%), Alloy 3 annealed at 1000°C for 1000 h showing: a) an etched area, and b) two-phase area at higher magnification. 64
Figure 4.44. EDX analyses of nominal Co_{20}:Fe_{50}:Pd_{30} (at.%), Alloy 3 1000°C annealed condition. (■ Overall composition; ● phases) 65
Figure 4.45. XRD patterns for nominal Co_{20}:Fe_{50}:Pd_{30} (at.%), Alloy 3 1000°C annealed condition: a) raw, and b) labelled. 66
Figure 4.46. SEM-BSE images of Co_{10}:Fe_{15}:Pd_{75} (at.%), Alloy 4 annealed at 1000°C for 1000 h showing: a) grains of different contrast, and b) grain boundaries, $FePd_3$ precipitates and a region of different composition. 67
Figure 4.47. EDX analyses of nominal Co_{10}:Fe_{15}:Pd_{75} (at.%), Alloy 4 1000°C annealed condition. (■ Overall composition; ● phases) 68
Figure 4.48. XRD patterns for nominal Co_{10}:Fe_{15}:Pd_{75} (at.%), Alloy 4 1000°C annealed condition: a) raw, and b) labelled. 69
Figure 4.49. SEM-BSE images of Co_{30}:Fe_{30}:Pd_{40} (at.%), Alloy 5 annealed at 1000°C for 1000 h showing: a) light and dark areas, and b) a magnified patch that was etched 70
Figure 4.50. EDX analyses of nominal Co_{30}:Fe_{30}:Pd_{40} (at.%), Alloy 5 1000°C annealed condition. (■ Overall composition; ● phases) 71
Figure 4.51. XRD patterns for nominal Co_{30}:Fe_{30}:Pd_{40} (at.%), Alloy 5 1000°C annealed condition: a) raw, and b) labelled. 72
Figure 4.52. SEM-BSE images of Co_{50}:Fe_{20}:Pd_{30} (at.%), Alloy 6 annealed at 1000°C for 1000 h showing: a) at low magnification the overall area, and b) a better etched area. 73
Figure 4.53. EDX analyses of nominal Co_{50}:Fe_{20}:Pd_{30} (at.%), Alloy 6 1000°C annealed condition. (■ Overall composition; ● phases) 74

Figure 4.54. XRD patterns for nominal Co_{50}:Fe_{20}:Pd_{30} (at.%), Alloy 6 1000°C annealed condition: a) raw 10 minutes, b) labelled, and c) raw 20 minutes..... 75
Figure 4.55. SEM-BSE images of Co_{10}:Fe_{30}:Pd_{60} (at.%), Alloy 7 annealed at 1000°C for 1000 h showing: a) etched-out patches, and b) patch at higher magnification. 76
Figure 4.56. EDX analyses of nominal Co_{10}:Fe_{30}:Pd_{60} (at.%), Alloy 7 1000°C annealed condition. (■ Overall composition; ● phases)..... 77
Figure 4.57. XRD patterns for nominal Co_{10}:Fe_{30}:Pd_{60} (at.%), Alloy 7 1000°C annealed condition: a) raw, and b) labelled. 78
Figure 4. 58. SEM images of Co_{25}:Fe_{20}:Pd_{55} (at.%), Alloy 8 annealed at 1000°C for 1000 h showing: a) BSE image at low magnification and b) SE image of a region at higher magnification. 79
Figure 4.59. EDX analyses of nominal Co_{25}:Fe_{20}:Pd_{55} (at.%), Alloy 8 1000°C annealed condition. (■ Overall composition; ● phases)..... 80
Figure 4.60. XRD patterns for nominal Co_{25}:Fe_{20}:Pd_{55} (at.%), Alloy 8 1000°C annealed condition: a) raw, and b) labelled. 81
Figure 4.61. SEM-BSE image of Co_{10}:Fe_{50}:Pd_{40} (at.%), Alloy 9 annealed at 1000°C for 1000 h showing differently etched lighter grey particles. 82
Figure 4.62. EDX analyses of nominal Co_{10}:Fe_{50}:Pd_{40} (at.%), Alloy 9 1000°C annealed condition. (■ Overall composition; ● phases)..... 83
Figure 4.63. XRD patterns for nominal Co_{10}:Fe_{50}:Pd_{40} (at.%), Alloy 9 1000°C annealed condition: a) raw, and b) labelled. 84
Figure 4.64. SEM-BSE image of Co_{40}:Fe_{30}:Pd_{30} (at.%), Alloy 10 annealed at 1000°C for 1000 h showing contrasting grains. 85
Figure 4.65. EDX analyses of nominal Co_{40}:Fe_{30}:Pd_{30} (at.%), Alloy 10 1000°C annealed condition. (■ Overall composition; ● phases)..... 86
Figure 4.66. XRD patterns for nominal Co_{40}:Fe_{30}:Pd_{30} (at.%), Alloy 10 1000°C annealed condition: a) raw, and b) labelled. 87
Figure 4.67. SEM-BSE images of Co_{20}:Fe_{60}:Pd_{20} (at.%), Alloy 11 annealed at 1000°C for 1000 h showing: a) contrasting regions with grain boundaries) and b) fine precipitates. 88
Figure 4.68. EDX analyses of nominal Co_{20}:Fe_{60}:Pd_{20} (at.%), Alloy 11 1000°C annealed condition. (■ Overall composition; ● phases)..... 89
Figure 4.69. XRD patterns for nominal Co_{20}:Fe_{60}:Pd_{20} (at.%), Alloy 11 1000°C annealed condition: a) raw, and b) labelled. 90

Figure 4.70. SEM-BSE image of Co_{60}:Fe_{20}:Pd_{20} (at.%), Alloy 12 annealed at 1000°C for 1000 h showing light and dark grains.....91
Figure 4.71. EDX analyses of nominal Co_{60}:Fe_{20}:Pd_{20} (at.%), Alloy 12 1000°C annealed condition. (■ Overall composition; ● phases).....92
Figure 4.72. XRD patterns for nominal Co_{60}:Fe_{20}:Pd_{20} (at.%), Alloy 12 1000°C annealed condition: a) raw, and b) labelled. 93
Figure 4.73. SEM-BSE images of Co_{30}:Fe_{60}:Pd_{10} (at.%), Alloy 1 annealed at 650°C for 1000 h showing: a) apparent dendrites, and b) higher magnification light and dark fine phases. 94
Figure 4.74. EDX analyses of nominal Co_{30}:Fe_{60}:Pd_{10} (at.%), Alloy 1 650°C annealed condition. (■ Overall composition; ● phases).....95
Figure 4.75. XRD patterns for nominal Co_{30}:Fe_{60}:Pd_{10} (at.%), Alloy 1 650°C annealed condition: a) raw, and b) labelled. 96
Figure 4.76. SEM-SE image of Co_{6}:Fe_{44}:Pd_{50} (at.%), Alloy 2 annealed at 650°C for 1000 h showing light and dark grains.....97
Figure 4.77. EDX analyses of nominal Co_{6}:Fe_{44}:Pd_{50} (at.%), Alloy 2 650°C annealed condition. (■ Overall composition; ● phases).....98
Figure 4.78. XRD patterns for nominal Co_{6}:Fe_{44}:Pd_{50} (at.%), Alloy 2 650°C annealed condition: a) raw, and b) labelled. 99
Figure 4.79. SEM-BSE images of Co_{20}:Fe_{50}:Pd_{30} (at.%), Alloy 3 annealed at 650°C for 1000 h showing: a) the overall etched area, and b) higher magnification.....100
Figure 4.80. EDX analyses of nominal Co_{20}:Fe_{50}:Pd_{30} (at.%), Alloy 3 650°C annealed condition. (■ Overall composition; ● phases).....101
Figure 4.81. XRD patterns for nominal Co_{20}:Fe_{50}:Pd_{30} (at.%), Alloy 3 650°C annealed condition: a) raw, and b) labelled. 102
Figure 4.82. SEM-SE and SEM-BSE images of Co_{10}:Fe_{15}:Pd_{75} (at.%), Alloy 4 annealed at 650°C for 1000 h: a) showing contrasting areas, and b) showing contrasting areas and grain boundaries. 103
Figure 4.83. EDX analyses of nominal Co_{10}:Fe_{15}:Pd_{75} (at.%), Alloy 4 650°C annealed condition. (■ Overall composition; ● phases).....104
Figure 4.84. XRD patterns for nominal Co_{10}:Fe_{15}:Pd_{75} (at.%), Alloy 4 650°C annealed condition: a) raw, and b) labelled. 105
Figure 4.85. SEM-BSE images of Co_{30}:Fe_{30}:Pd_{40} (at.%), Alloy 5 annealed at 650°C for 1000 h showing: a) representative area of the alloy, and b) magnified image. 106

Figure 4.86. EDX analyses of nominal Co_{30}:Fe_{30}:Pd_{40} (at.%), Alloy 5 650°C annealed condition. (■ Overall composition; ● phases)..... 107
Figure 4.87. XRD patterns for nominal Co_{30}:Fe_{30}:Pd_{40} (at.%), Alloy 5 650°C annealed condition: a) raw, and b) labelled. 108
Figure 4.88. SEM images of Co_{50}:Fe_{20}:Pd_{30} (at.%), Alloy 6 annealed at 650°C for 1000 h showing: a) BSE overall of the alloy and b) SE microstructure at higher magnification. 109
Figure 4.89. EDX analyses of nominal Co_{50}:Fe_{20}:Pd_{30} (at.%), Alloy 6 650°C annealed condition. (■ Overall composition; ● phases)..... 110
Figure 4.90. XRD patterns for nominal Co_{50}:Fe_{20}:Pd_{30} (at.%), Alloy 6 650°C annealed condition: a) raw, and b) labelled. 111
Figure 4.91. SEM-BSE image of Co_{10}:Fe_{30}:Pd_{60} (at.%), Alloy 7 annealed at 650°C for 1000 h showing different grains..... 112
Figure 4.92. EDX analyses of nominal Co_{10}:Fe_{30}:Pd_{60} (at.%), Alloy 7 650°C annealed condition. (■ Overall composition; ● phases)..... 113
Figure 4.93. XRD patterns for nominal Co_{10}:Fe_{30}:Pd_{60} (at.%), Alloy 7 650°C annealed condition: a) raw, and b) labelled. 114
Figure 4.94. SEM-BSE image of Co_{25}:Fe_{20}:Pd_{55} (at.%), Alloy 8 annealed at 650°C for 1000 h showing coring. 115
Figure 4.95. EDX analyses of nominal Co_{25}:Fe_{20}:Pd_{55} (at.%), Alloy 8 650°C annealed condition. (■ Overall composition; ● phases)..... 116
Figure 4.96. XRD patterns for nominal Co_{25}:Fe_{20}:Pd_{55} (at.%), Alloy 8 650°C annealed condition: a) raw, and b) labelled. 117
Figure 4.97. SEM-BSE images of Co_{10}:Fe_{50}:Pd_{40} (at.%), Alloy 9 annealed at 650°C for 1000 h showing: a) fine microstructure and b) fine and coarse two-phase regions..... 118
Figure 4.98. EDX analyses of nominal Co_{10}:Fe_{50}:Pd_{40} (at.%), Alloy 9 650°C annealed condition. (■ Overall composition; ● phases)..... 119
Figure 4.99. XRD patterns for nominal Co_{10}:Fe_{50}:Pd_{40} (at.%), Alloy 9 650°C annealed condition: a) raw, and b) labelled. 120
Figure 4.100. SEM-BSE images of Co_{40}:Fe_{30}:Pd_{30} (at.%), Alloy 10 annealed at 650°C for 1000 h showing: a) an overall, and b) formation of fine phase, light and dark phases. 121
Figure 4.101. EDX analyses of nominal Co_{40}:Fe_{30}:Pd_{30} (at.%), Alloy 10 650°C annealed condition. (■ Overall composition; ● phases)..... 122

Figure 4.102. XRD patterns for nominal Co_{40}:Fe_{30}:Pd_{30} (at.%), Alloy 10 650°C annealed condition: a) raw, and b) labelled. 123
Figure 4.103. SEM images of Co_{20}:Fe_{60}:Pd_{20} (at.%), Alloy 11 annealed at 650°C for 1000 h showing: a) BSE apparent dendrites and b) SE higher magnification fine phase. 124
Figure 4.104. EDX analyses of nominal Co_{20}:Fe_{60}:Pd_{20} (at.%), Alloy 11 650°C annealed condition. (■ Overall composition; ● phases)..... 125
Figure 4.105. XRD patterns for nominal Co_{20}:Fe_{60}:Pd_{20} (at.%), Alloy 11 650°C annealed condition: a) raw, and b) labelled. 126
Figure 4.106. SEM-BSE images of Co_{60}:Fe_{20}:Pd_{20} (at.%), Alloy 12 annealed at 650°C for 1000 h showing: a) dendrites, and b) higher magnification decomposition of dendrites. 127
Figure 4.107. EDX analyses of nominal Co_{60}:Fe_{20}:Pd_{20} (at.%), Alloy 12 650°C annealed condition. (■ Overall composition; ● phases)..... 128
Figure 4.108. XRD patterns for nominal Co_{60}:Fe_{20}:Pd_{20} (at.%), Alloy 12 650°C annealed condition: a) raw, and b) labelled. 129

Figure 5.1. Ternary plot with microhardness values and errors for as-cast alloys. (■ Overall composition) 131
Figure 5.2. Ternary plot with microhardness values and errors for alloys annealed at 1000°C. (■ Overall composition) 131
Figure 5.3.Ternary plot with hardness values and errors for alloys annealed at 650°C. (■ Overall composition) 132

Figure 6.1 Solidification projection for the as-cast Co-Fe-Pd system. (■ Overall composition; ● phases) 137
Figure 6.2. Results of the alloys annealed at 1000°C for the Co-Fe-Pd system (at.%). (■ Overall composition; ● phases)..... 139
Figure 6.3. Isothermal section at 1000°C for the Co-Fe-Pd system (at.%). (■ Overall composition; ● phases) 140
Figure 6.4. Results for the alloys annealed at 650°C for the Co-Fe-Pd system (at.%). (■ Overall composition; ● phases)..... 141

Figure 6.5. Isothermal section at 650°C annealed for the Co-Fe-Pd system (at.%). (■ Overall composition; ● phases)..... 142
Figure 6.6. Solidification projection with hardnesses for as-cast Co-Fe-Pd alloys. (■ Overall composition) 145
Figure 6.7. Isothermal section at 1000°C for the Co-Fe-Pd system with hardnesses. (■ Overall composition) 145
Figure 6.8. Isothermal section at 650°C for the Co-Fe-Pd system with hardnesses. (■ Overall composition) 146
Figure 6.9. Comparison of hardnesses for all of the alloys in the different conditions..... 147

Chapter 1: Introduction

1.1. Background

Magnetic materials are essential in many industries, and there is a need to replace expensive rare earth metals with cheaper and more readily available metals. Historically, patents held by American and Japanese companies have been a barrier to entry to the magnet market, but China's establishment of research institutes in the 1950s and 1960s and the expiry of the American and Japanese patents in the 1980s, enabled China to enter and dominate the magnet market. Currently, China has a monopoly on the magnet value chain, producing 90% of the world's permanent magnets, and China also has most of the world's rare earth resources.

One of the new magnetic materials being investigated is the Co-Fe-Pd alloy, which has potential applications in biotechnology, electronics and green technologies (hybrid vehicles and direct drive wind turbines). Magnetic thin films and nanostructures that are magnetized perpendicular to their surface are essential to many developing technologies, including spintronics devices [2006Man] and patterned media [1999Tod, 2013Din], especially because of the need to maintain thermal stability as device dimensions became increasingly nanoscale. Multilayers or superlattice structures consisting of alternating ferromagnetic and non-magnetic layers are highly suitable for these applications, due to their tunable perpendicular magnetic anisotropy (PMA) and saturation magnetization [2005Ter, 2010Rip].

By combining the soft magnetic properties of iron and the hard magnetic properties of cobalt and palladium, an optimal magnetic material could be developed. Fe-Co alloys have a B2 structure which makes them extremely brittle at room temperature [2016Mat]. The workability of these alloys can be improved by substitution of nickel or palladium, and substitution of palladium led to higher tensile strength and elongation at room temperature [2016Mat].

Apart from the mechanical properties [2016Mat] of the Co-Fe-Pd alloy and research on the magnetic shape memory properties [2001Koe, 1981Osh, 2012Kau], little work has been done on the ternary phase diagram [1958Kup, 1959Kup, 1961Kup, 1961Gri, 1992Rag]. The Co-Fe-Pd phase diagram was derived nearly sixty years ago and is inconsistent, even within papers of the same authors [1958Kup, 1959Kup,

1961Kup, 1961Gri]. In order to understand the alloy better, the ternary phase diagram needs to be updated to more reliably show the different phases. Knowing the phases and microstructure will help to understand what could be optimal composition for a magnetic material. This work was a partner project of Mrs H.C. Mantyi's PhD project at Mintek, "Development of a nano-crystalline Fe-Co-Pd alloy" [2017Man1, 2017Man2].

1.2. Research objectives

- To analyse Co-Fe-Pd alloy microstructures at different compositions and temperatures.
- To draw the solidification projection and isothermal sections for 650°C and 1000°C.

Chapter 2: Literature review

In this study, very little information regarding the ternary phase diagram was found, although there was ample information with regard to studies that used the alloy for its other properties.

2.1. Ordering

Ordering involves a change from a statistically nearly random distribution of atoms in the atom sites into a more regular arrangement, whereby designated sites are occupied predominantly by one kind of atom [1980Bar]. In a disordered AB solution, atoms A and B would occupy any atom site, whereas in an ordered solution, A and B atoms occupy designated atomic sites, creating a specific lattice [1980Bar]. The segregation of atoms to specific atomic sites can take place with little or no deformation of the lattice, creating an ordered solid solution out of a random solid solution [1980Bar]. The structures of ordered alloys usually produce diffraction patterns which have additional peaks, associated with new and larger planar spacings, sometimes smaller as with FePd, which are not present in patterns of disordered alloys [1980Bar].

There is long-range and short-range order; long-range order is described by the formation of superlattices and usually takes place at lower temperatures [1980Bar]. Short range order is when structures are neither perfectly ordered, nor perfectly random [1980Bar]. There are many types of superlattices, e.g. $L1_2$, $L1_0$, and B2. Ordering can be determined by studying its influence on certain mechanical, physical and thermal properties [1980Bar], as well as by X-ray diffraction. Figure 2.1 a) [2018Lau] and b) [2012Kva] shows the types of ordering that takes place at lower temperatures from the higher temperature A1 fcc solid solution for FePd which has the $L1_2$ structure, and $FePd_3$ which has $L1_0$ structure.

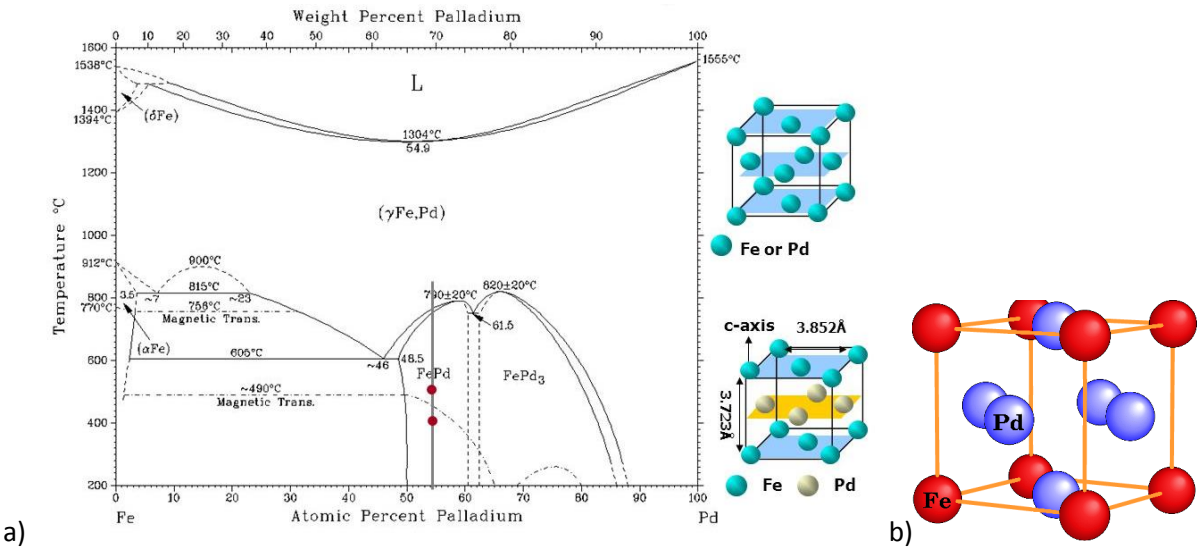


Figure 2.1. a) Fe-Pd binary diagram with disordered and ordered FePd phase structure [2018Lau] and b) schematic representation of ordered $FePd_3$ ordered alloy [2012Kva].

Figure 2.2 [2018Pei] shows the ordering of α', (αFe) transforms by second-order reaction to ordered α' [1982Kub]. A review by Raynor [1988Ray] found three ordered phases in the Co-Fe binary diagram, although a later review by [2008Oka] had only one ordered phase, which is accepted now.

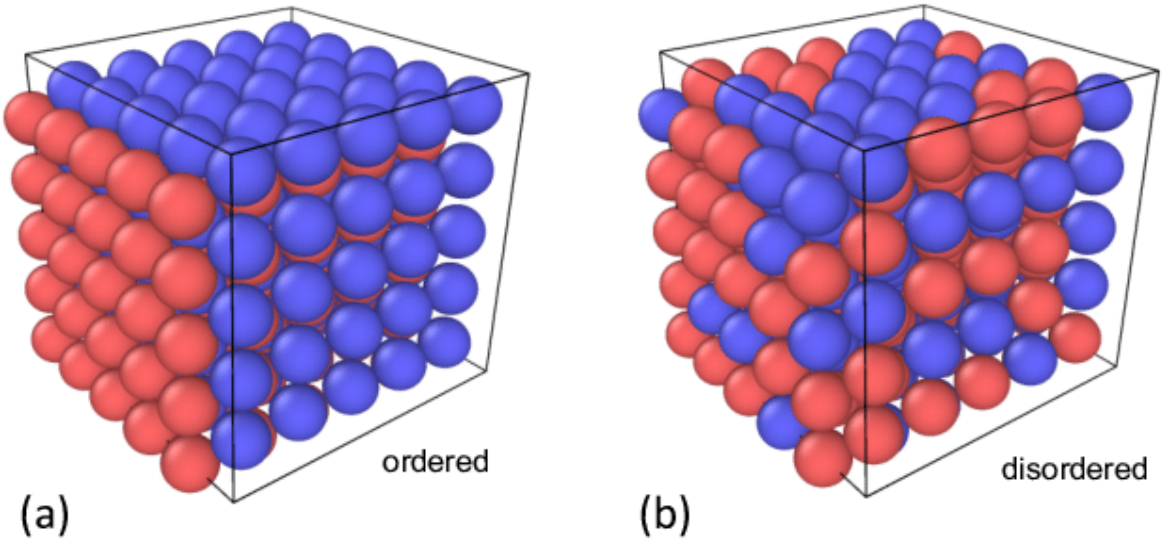


Figure 2.2. Schematic representation of the ordered and disordered α' phase [2018Pei].

A good example of a system which shows different types of ordering is the Au-Cu binary; there are several superlattices which exist at low temperatures near compositions: Cu_3Au ($L1_2$), CuAu ($L1_0$) and $CuAu_3$ ($L1_2$), all of fcc-type [1980Bar]. These superlattices form fcc, fct and orthomhombic structures [1980Bar]. Another type of superlattice is the B2 beta-brass type [1972Cha], in which has two interpenetrating simple cubic sublattices [1980Bar].

In ordering, the solution can have short range order (SRO) or long range order (LRO). The SRO is when there is an equivalent number of atom sites A-B in a substitutional solid solution. The probability that any given site in the lattice will contain an atom A will be equal to the fraction of A atoms in the solution X_A (similarly for X_B). The degree of ordering can be quantified by defining a SRO parameter S (Equation 2.1) [2009Por].

$$S = \frac{P_{AB} - P_{AB}(random)}{P_{AB}(\max) - P_{AB}\,(random)} \quad \text{..... Equation 2.1}$$

where P_{AB}(max) and P_{AB}(random) refer to the maximum number of bonds for solution [2009Por].

The LRO is when atom sites are no longer equivalent, but can be labelled as A-sites and B-sites. This happens in solutions with compositions that are close to a simple ratio A-B atoms. Such a solution can be considered to be a different (ordered) phase separate from the random or nearly random solution [2009Dav]. The degree of order for LRO can be quantified by defining a LRO parameter L (Equation 2.2)[2009Por].

$$L = \frac{r_A - x_A}{1 - x_A} \text{ or } L = \frac{r_B - x_B}{1 - x_B} \quad \text{.....Equation 2.2}$$

where x_A is the mole fraction of A in the alloy and r_A is the probability that an A sublattice site is occupied by the "right" kind of atom [2009Por].

Also used to describe ordering is first order and second order reactions. In first order reactions at the equilibrium transformation temperature, the first derivatives of the Gibbs free energy are discontinuous, characterized by discontinuous change in S, an example of this is Cu_3Au. There is also a discontinuous change in enthalpy corresponding to the evolution of a latent heat of transformation. For second order

reactions at the equilibrium transformation temperature, the second derivatives of the Gibbs free energy are discontinuous, however the first derivatives are continuous, and enthalpy is continuous, an example is β → β' (CuZn) [2009Por].

Gilles et al. [2011Gil] showed that furnace cooled specimens were mostly ordered with constant ordering parameters (S), whereas water quenched specimens of Co-Fe-Pd showed no ordering below 400°C, but ordering increased above, and then decreased at T_c (the critical (ordering) temperature, maximum 730°C). Air-cooled samples had intermediate behaviour [2011Gil]. The degree of ordering affects magnetic properties such as Curie temperature, domain interfaces and the mean magnetic moment [1996Kim, 2003Nos].

2.2. Magnetism

Magnetism is a force that attracts or repels objects which are magnetic [2019Nat]. The atom is said to be magnetic if it carries a permanent magnetic moment [2005Gig]. There are a few types of magnetism; some of the better known are paramagnetism, diamagnetism and ferromagnetism [1963Got]. Paramagnetism and diamagnetism have very weak magnetic moments that do not produce any additional fields compared to ferromagnetism, which has a great effect on the magnetic fields [1963Got]. In materials, magnetic behavior is characterized by four interrelated vector quantities; the flux density or magnetic induction, the magnetic field, magnetization and polarization [1951Boz, 1972Cul, 1962Kne]. Some other fundamental properties are the Curie temperature, energy product and magnetic anisotropy [1951Boz, 1972Cul, 1962Kne].

The FePd ferromagnetic metallic compound has attracted considerable research interest as hard magnetic materials (ultra-high density magnetic recording media [2003Tak, 2006Nag]) and permanent magnets for dental applications [2005Gop, 1973Yos]. Other attractive features are their large uniaxial magnetic anisotropy energy [1973Iva, 1964Kus] and high resistance to corrosion [2007Yab].

Permanent magnets play a key role in various technologies like energy conversion, data storage and sensors and actuators [2010Chb]. Long range ordered intermetallic compounds based on Fe, Co and noble metals like Pt or Pd exhibit high uniaxial magnetocrystalline anisotropy, with potential large energy products, and good mechanical [1998Wha] and corrosion properties [1999Wel]. They can be used for

both thin film device applications (high density magnetic recording media) [2006Iss] and permanent magnets [2004Des]. In spite of their high costs, these materials are attractive for some specific applications, like medical implants or extreme conditions where high strength and excellent corrosion resistance are required [2010Chb].

2.3. Constituent binary systems of the Co-Fe-Pd system

2.3.1. Co-Fe

The phases described for the Co-Fe-Pd system are in the Pettifor order [1986Pet]: FeCoPd. The Co-Fe phase diagram published by Okamoto [2008Oka] is shown in Figure 2.3, and is based on the assessment of Massalski [1990Mas] and later lower temperature work of Ohnuma [2002Ohn]. The solid phases present have the following structures: bcc (δFe and αFe), fcc (αCo, γFe) and bct (α'). Across the Co-Fe system, the liquidus and solidus temperatures were very close.

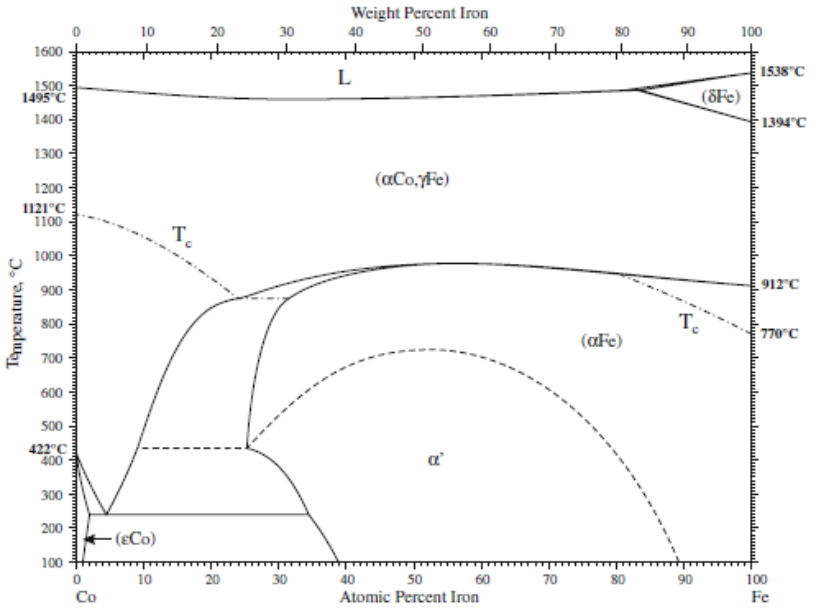


Figure 2.3. Binary diagram for Co-Fe system [2002Ohn].

The peculiar shape of the α/γ phase boundary in Figure 2.3 is mainly due to the magnetic contribution [2002Ohn]. There are two regions where the magnetic transformation takes place (T_c for the fcc Co solid solution and T_c for the bcc Fe solution), and the temperature at which this happens between is 770-1121°C [1984Nis]. When Raghavan [1992Rag] redrew the ternary system, he used a previously accepted Co-Fe

binary (Figure 2.8) [1988Ray], which had three different α phases which are not accepted now (although they are fairly similar to those accepted now), which gave another reason to update the ternary system.

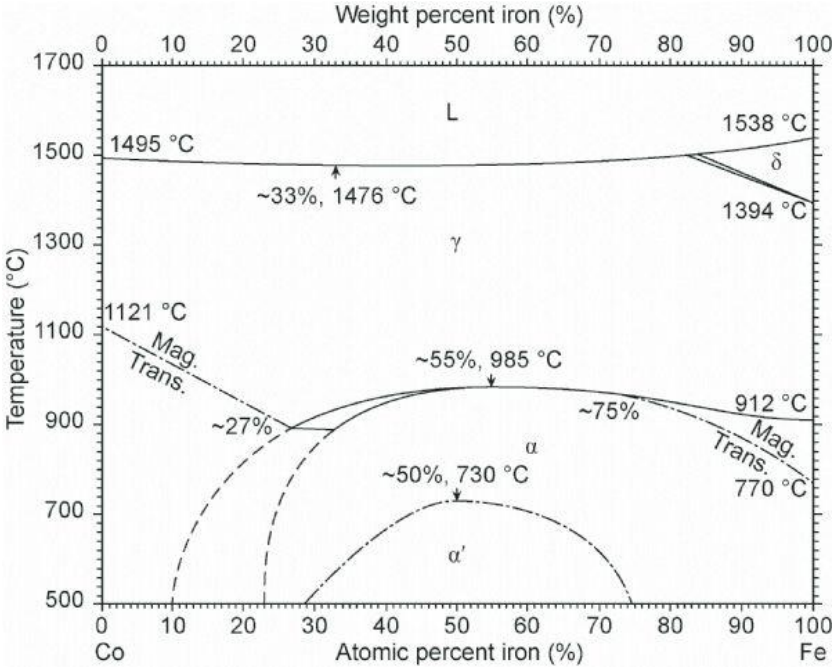


Figure 2. 4. Previously accepted Co-Fe phase diagram [1984Nis].

2.3.2. Co-Pd

The Co-Pd phase diagram published by Massalski [1990Mas] is shown in Figure 2.5.

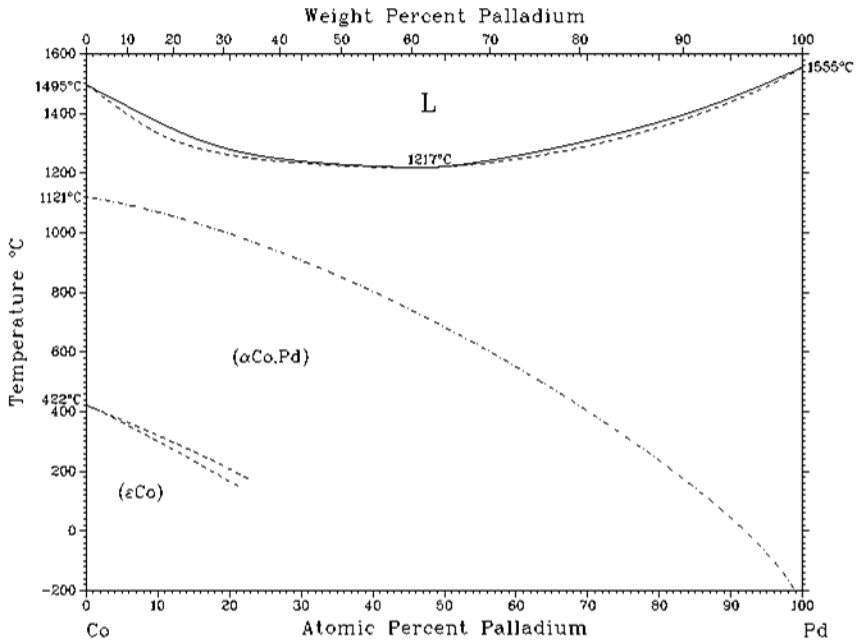


Figure 2.5. Binary diagram for Pd-Co system [1990Mas].

There are three equilibrium phases present: (αCo,Pd), (εCo) and (αCo,Pd) + (εCo). The magnetic transformation temperature changes continuously from 1121°C to -266°C. Within the fcc phase, the system has $L1_o$ and $L1_2$ ordered phases which are metastable [1991Ish]. Ferromagnetism exists in the solution up to 99.9 at.% Pd [1961Boz]. Ghosh et al. [1999Gho] used thermodynamics to calculate the Co-Pd phase diagram; they found good agreement between the calculated Co-Pd phase diagram and the experimental data [1971Vat].

2.3.3. Fe-Pd

The Fe-Pd phase diagram published by Massalski [1990Mas] is shown on Figure 2.6. The red rectangle was of interest to see whether the $FePd_3$ section extends further into the ternary system, and it was expected that this would occur at higher temperatures.

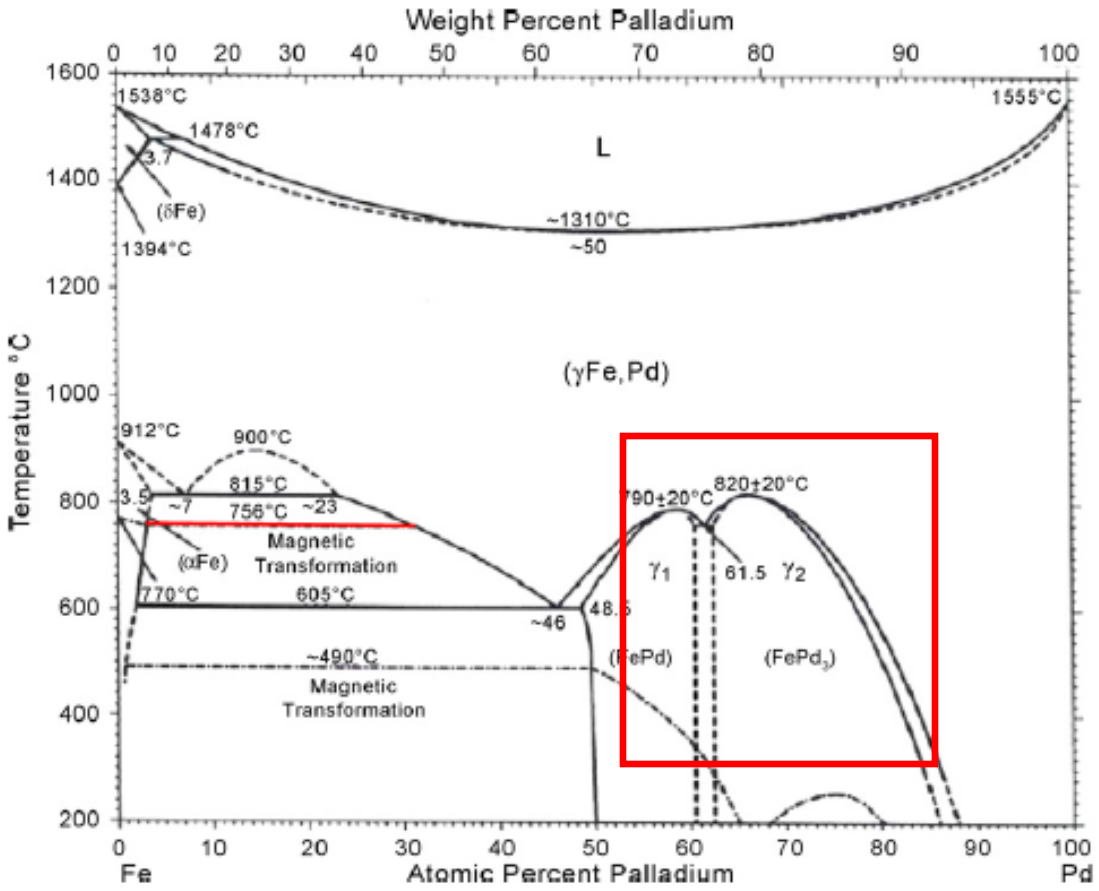


Figure 2.6. Binary diagram for Fe-Pd system [1990Mas].

In Figure 2.6, there are two superstructures, FePd and $FePd_3$ which, form congruently. These phases are also ordered structures with $L1_0$ and $L1_2$ structures [1992Rag]. There are two magnetic transformations at 756°C and 490°C. Buschow [1983Bus] reported another ordered phase, fct ($L2_0$) for annealed $Fe_{45}Pd_{55}$. Fe-Pd alloys can be shape memory alloys, with the optimum composition around Fe-30 at.% Pd. Decreasing Pd content reduces the martensite transformation temperature from about 22°C, although at 29.4 at.% Pd, the non-elastic bct marternsite is formed instead of fct, and the shape memory effect is lost [1981Osh].

Additionally, there are two metastable martensite phases in binary Fe-Pd, based on γ' fct martensite, face-centred tetragonal (which is thermo-elastic, suggesting that it is a good shape memory alloy) [2002Kat] around 29.7 at.% Pd, and based on bct, body-centred tetragonal (non-thermo-elastic) [1981Osh] at 29.4 at.% Pd. The stability range of the fct-based martensite is increased by Co additions (Co being an austenite stabilizer) [2003Tsu], and Co increases the transformation temperature, although Vokoun et al. [2005Vok] found the opposite effect. The (γFe, Pd) fcc to γ' fct transformation is weakly first-order. The appearance

of the α' (bct martensite) phase directly depends on the tetragonality of the γ' (fct martensite phase) which irreversibly transforms to α' (bct martensite) was reduced by the presence of Co [2010San]. Using first principles studies, Kauffmann-Weiss [2012Kau] demonstrated the fcc ↔ fct ↔ bct ↔ bcc relationships between the transformations.

Ghosh et al. [2011Gho] calculated the invariant equilibria in the Fe-Pd system, and found overall agreement between the calculated phase boundaries and the experimental data [1971Vat], but a major disagreement was found in the γ(Fe,Pd)/γ(Fe,Pd)+FePd and γ(Fe,Pd)/γ(Fe,Pd)+$FePd_3$ phase boundaries. However, that disagreement was primarily due to highly off-stoichiometric compositions for congruent ordering of the FePd and $FePd_3$ phases. The order-disorder transition in the Fe-Pd system affects the mechanical properties: ductile when disordered, and more brittle when ordered. Magnetism affects the structural stability, as well as the ordering [2011Gil].

2.4. Work done on Co-Fe-Pd phase diagram

The published phase diagram work is from four papers by a group in Russia [1958Kup, 1959Kup, 1961Kup, 1961Gri] and these papers are contradictory, even sometimes within the same paper. Figure 2.7 [1961Kup] shows an isothermal section of the system with the binaries, but the phase boundaries on the edge of the system do not agree with the Co-Fe binary shown there.

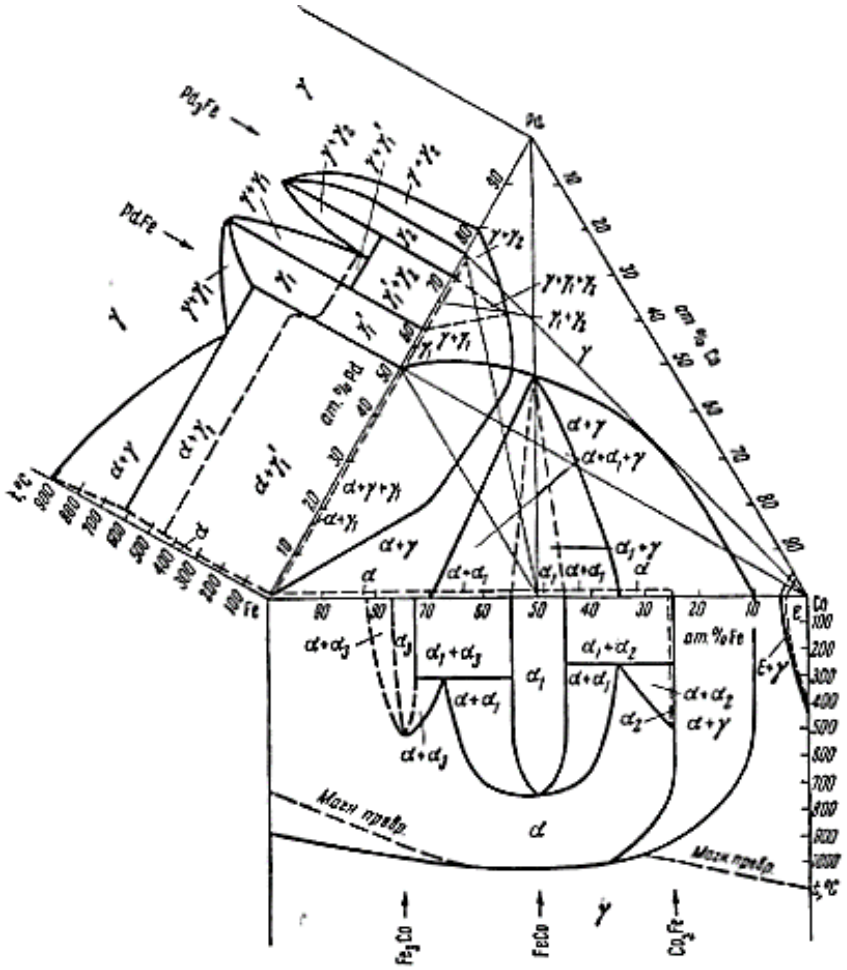


Figure 2.7. Isothermal section at ~25 ℃ of Co-Fe-Pd system [1961Kup].

Ragavhan [1992Rag] attempted to assess the system, and also used the Co-Pd phase diagram of Ishida [1991Ish] and Nishizawa [1995Nis], rather than that currently accepted [1990Mas]. The Co-Fe binary used then had three different α phases, Figure 2.8 [1988Ray], which are now not accepted, and Raghavan [1992Rag] redrew the sections, using the accepted binary systems then, including [1991Ish], and admitted that the diagram was only approximate, because considerable modifications were necessary due to the large changes in the accepted binary phase diagrams. He was unable to satisfactorily interpret the system, due to the contradictory data. His isothermal section at ~25°C is given in Figure 2.9 [1992Rag], and is much simpler than that of Grigorev and Kuprina [1961Gri]. However, the isothermal section was drawn at a temperature for which [1961Gri] had very few data, especially compared to their much larger amounts of higher temperature data [1958Kup, 1959Kup, 1961Kup, 1961Gri].

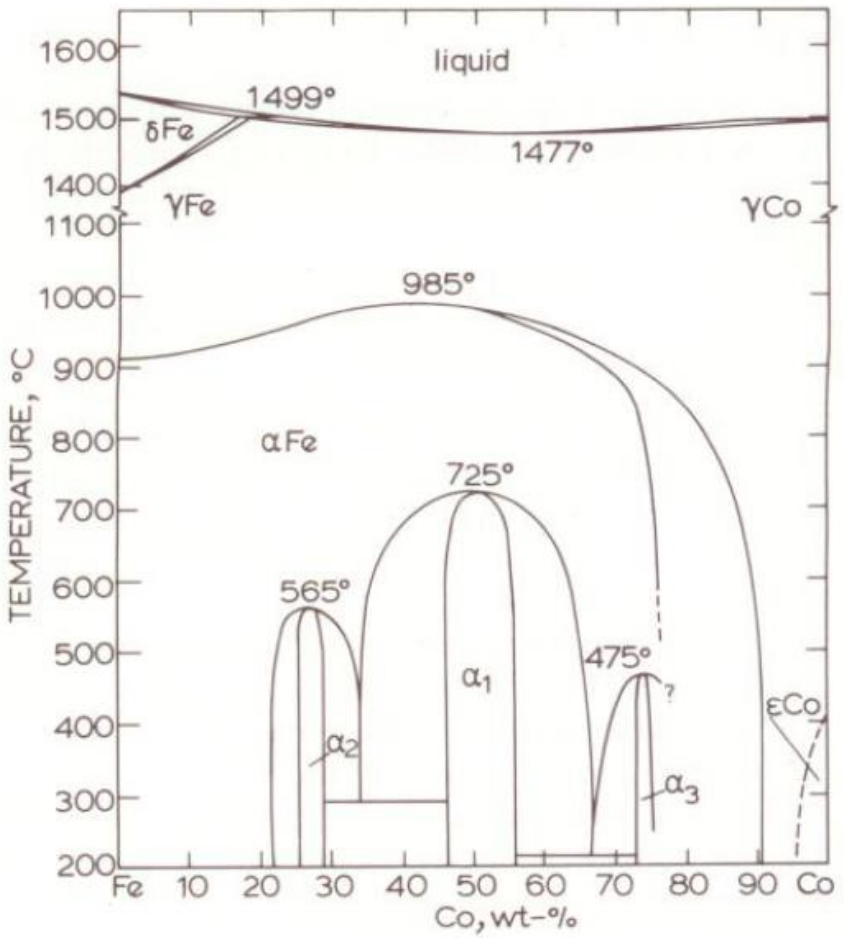


Figure 2.8. Co-Fe binary system previously accepted [1988Ray].

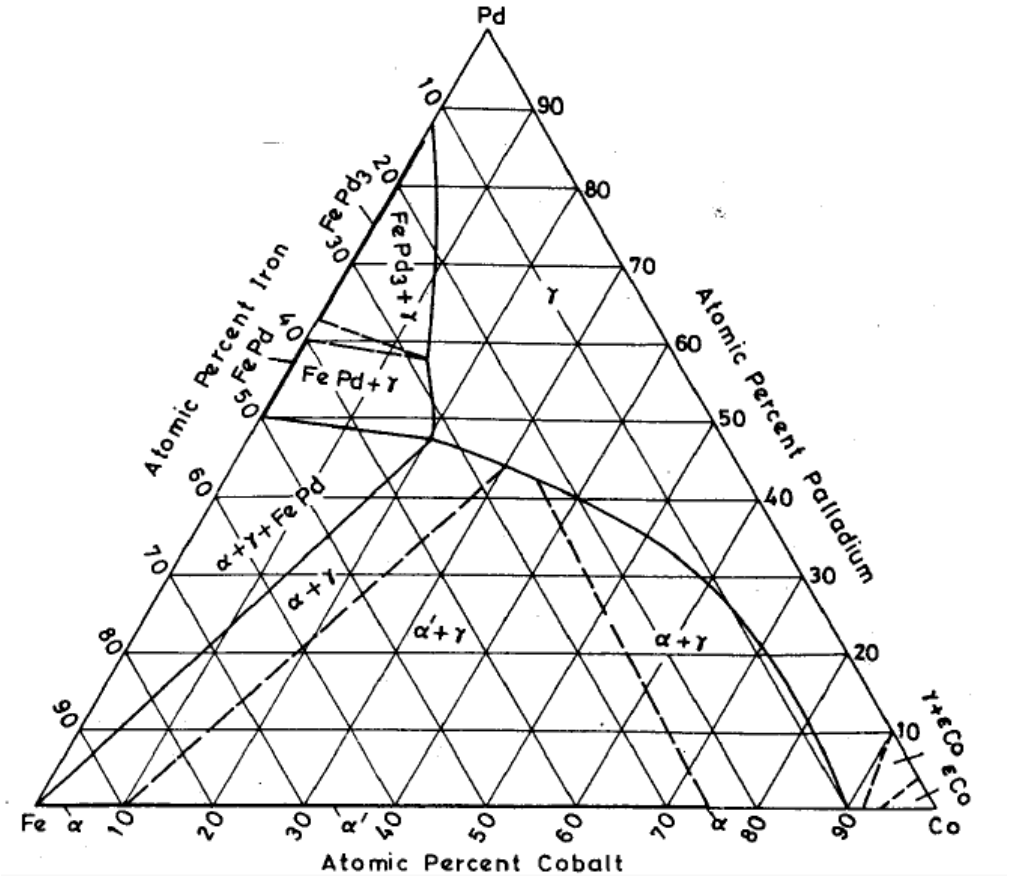
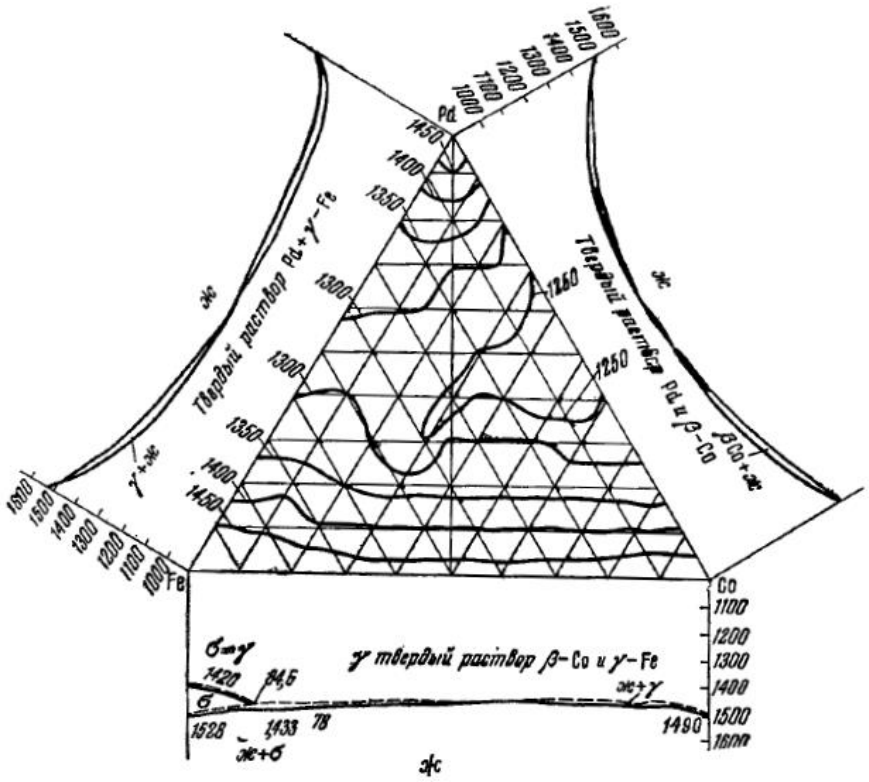
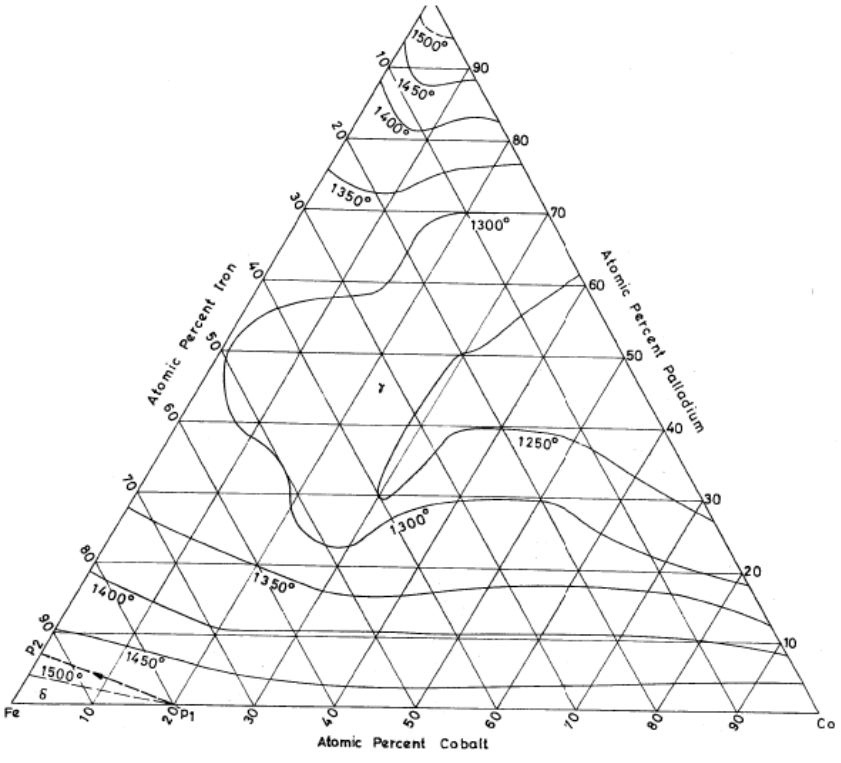


Figure 2.9. Co-Fe-Pd Isothermal section at ~25°C (at.%) [1992Rag].

The liquidus surface was drawn by Kuprina and Grigorev [1958Kup], and Raghavan [1992Rag] redrew it to be consistent with the binary phase diagram of Ishida and Nishizawa [1991Ish], and these are shown in Figure 2.10. The liquidus of Kuprina and Grigorev [1958Kup] has a more irregular surface, and Raghavan [1992Rag] made it smoother. The more irregular surface of the liquidus of Kuprina and Grigorev [1958Kup] was caused by incorrect labelling on some of the graphs within their paper [2018Cor]. Since the α → α' transition in Fe-Co-based alloys is a second-order reaction, there are no α + α' two-phase regions drawn. Thus, no isothermal section is yet accepted, because there are too few actual data at the temperature, and that which was initially drawn by Grigorev and Kuprina [1961Gri] was drawn to fit binary systems which are now not accepted [1958Kup, 1959Kup].



a)



b)

Figure 2.10. Liquidus surfaces of Co-Fe-Pd: a) Kuprina and Grigorev [1958Kup], and b) Raghavan [1992Rag].

2.5. Properties of Co-Fe-Pd alloys

A study by Matsuda et al. [2016Mat] focused on the mechanical properties of $Co_{50}:Fe_{50-x}:Pd_x$ alloys substituted by up to 10 at.% Pd, which consisted mainly of α′ phase with a B2 structure. They [2016Mat] added Pd to compositions based on $Fe_{50}:Co_{50}$, and the tensile tests showed that $Fe_{40}:Co_{50}:Pd_{10}$ alloys were more ductile than $Fe_{50}:Co_{40}:Pd_{10}$ and $Fe_{50}:Co_{50}$. The binary alloy was α′ (B2) and both ternary alloys were α′ + A1 (γFe,αCo,Pd) (fcc). With more compositions (up to 15 at.% Pd substituting for Fe), they [2016Mat] identified $Fe_{40}:Co_{50}:Pd_{10}$ alloy as the most ductile, attributing this to the α′ matrix, some A1 (γFe,αCo,Pd) with small amounts of $L1_0$ and $L1_2$ precipitates at the grain boundaries. The size and number of Co-Pd precipitates increased with increased Pd content, and the grain size was refined by Pd substitution.

Working on the magnetic properties of nanowires, Vega et al. [2012Veg] found that highly ordered (Fe, Co)–Pd (27-63 % Pd) nanowire arrays of ~70 nm diameter and between 0.6–1.6 m in length could be successfully fabricated. Kauffman-Weiss et al. [2012Kau] worked on a magnetic shape memory system, and identified the possibility to tune structure and magnetic properties of Fe–Pd–X films by epitaxial interfaces as a promising route to adjust properties for the use in microsystems.

Shape memory alloys can be actuators which convert thermal energy to mechanical energy and have about three times higher output energy density than other actuator materials, such as magnetostrictive materials and piezo ceramics [2001Koe]. However, their disadvantage is that they have a slower response, because they rely on heat conduction. This is alleviated in magnetic shape memory alloys (MSMAs) (also called ferromagnetic shape memory alloys (FSMAs), hence they work well. This is because of a martensitic transformation with a magnetic transition, giving large displacements with rapid responses, because the effect is driven by the magnetic field-induced martensitic transformation, which gives large magnetic field induced strain (MFIS), or by field-induced rearrangements of the martensitic twins, “twinning magnetostriction” [2001Koe, 2018Cor]. FePd alloys can be shape memory alloys, with the optimum around Fe-30 at.% Pd, and decreasing Pd content reduces the martensite transformation temperature from about 22°C, although at 29.4 at.% Pd, the non-elastic bct martensite formed instead of fct, and the shape memory effect was lost [1981Osh]

Another important property is the magnetostriction of the fct martensite in Fe-Pd [1998Fur, 1998Jam], giving better mechanical properties and a higher Curie temperature than the usual Ni-Mn-Ga alloys. The disadvantageous stability of the fct phase of Fe-Pd was extended by Co additions Oshima et al. [1982Osh],

and Tsuchiya [2003Tsu] found that the magnetisation was higher with added Co. Also, the magnetisation curves were similar for both A1 (γFe,αCo,Pd) (fcc) and γ' (fct) phases, unlike for Ni-Mn-Ga alloys. Co decreases the reversible and irreversible martensitic transformation effects, thus proving the relation to *e*/*a*. Using this concept, Vokoun et al. [2005Vok] found that Co additions lowered the A_f and hence M_s temperatures, and suppressed the formation of the bcc martensite, and also improved the shape memory recovery properties. Sanchez-Alarcos et al. [2008San] confirmed that Co additions lower both the reversible fcc-fct, and the irreversible fct-bct transformation temperatures.

The change in the transformation temperatures of the irreversible transformation was nearly twice that of the reversible one, thus enlarging the temperature range for the magnetic field-induced strain. The amount of fct martensite which transformed to the irreversible bct phase was also reduced by the Co addition, from ~53% in the $Fe_{70}Pd_{30}$ alloy to ~33% in the Fe_{67}:Co_3:Pd_{30} ternary alloy, making the ternary alloys good candidates for low temperature magnetic field-induced strain applications.

Zhang et al. [2015Zha] investigated multilayers and their properties, and found that the Fe_{10}:Co_{90} layer thickness was the primary factor determining the magnetic domain size and the perpendicular magnetization: both decreased as the thickness increased. In most of these alloy studies [2012Kau, 2012Veg, 2015Zha], adding Pd to FeCo alloys improved the properties.

Chapter 3: Research methodology

3.1. Compositions

The composition of the samples were determined by choosing two- or three-phase regions from the 25°C isothermal section of Raghavan [1992Rag], as well as compositions of interest for magnetic properties [2017Man1].

The compositions of interest for magnetic properties were:

- $Fe_{70}Co_{3-X}Pd_X$ - for its ferromagnetic shape memory properties
- $Fe_{44}Co_{56-}Pd_X$ - for the L_{10} hard magnetic phase

  $Fe_{30}Co_{70-X}Pd_X$ - for the magnetic softening properties [1990Mas].

Although the first samples were chosen based on the regions of interest of Mantyi [2017Man1], as well as regions chosen from [1992Rag], the rest of the samples were manufactured based on queries that the first samples gave. The compositions of the 12 samples are shown in Figure 3.1.

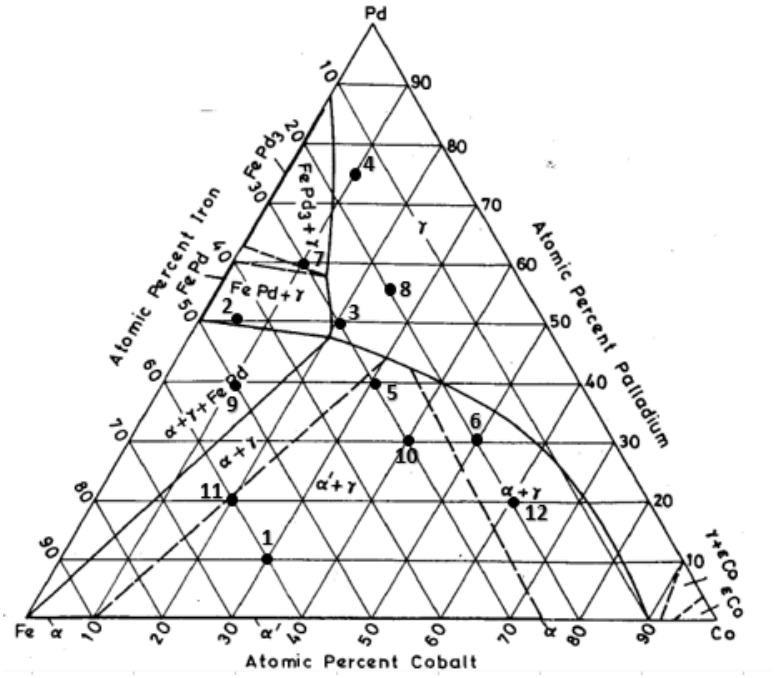


Figure 3. 1. Co-Fe-Pd isothermal section at ~25°C in (at.%) [1992Rag] with plotted compositions of interest.

3.2. Manufacturing samples

The atomic percent of the compositions were converted to weight percent using Equation 3.1 [1990ASM].

$$\text{wt \% Ni} = \frac{\text{at.\% Ni} \times \text{at.wt of Ni}}{(\text{at.\% Ni} \times \text{at.wt of Ni}) + (\text{at.\% V} \times \text{at.wt of V}) + (\text{at.\% C} \times \text{at.wt of C})} \quad \text{.....Equation 3.1}$$

The compositions are given in Table 3.1.

Table 3.1. Summary of composition of the alloys.

Alloys	Co (at.%)	Fe (at.%)	Pd (at.%)	Co (wt%)	Fe (wt%)	Pd (wt %)	Co (g)	Fe (g)	Pd (g)
1	30	60	10	29	54	17	2.86	5.42	1.72
2	6	44	50	4	30	65	0.43	3.02	6.54
3	20	50	30	16	39	45	1.65	3.9	4.46
4	10	15	75	6	9	85	0.63	0.89	8.48
5	30	30	40	23	22	55	2.3	2.18	5.53
6	50	20	30	41	15	44	3.04	1.15	3.29
7	10	30	60	7	19	74	0.68	1.94	7.38
8	25	20	55	17	13	69	1.74	1.32	6.93
9	10	50	40	8	37	56	0.77	3.66	5.57
10	40	30	30	33	23	44	3.26	2.32	4.42
11	20	60	20	18	50	32	1.77	5.03	3.2
12	60	20	20	52	16	31	5.21	1.65	3.14
						TOTAL	24.35	32.47	60.66

The samples were each 10 grams and were made in groups of six. The samples were prepared using pure (99.9%) elemental powders of Fe, Co and Pd. The powders were weighed, mixed and compacted and then melted in a button arc-furnace (BAF) at Mintek, according to their standard preparation method PMD-SOP-O37, in an argon atmosphere on a water-cooled copper hearth with a titanium oxygen-getter which was melted before melting each sample.

3.3. Metallographic preparation

The samples were cut using a Struers automatic cutting machine with an Accutom cutting wheel, then mounted using a mounting press, ground and polished using a Saphire 520 automatic machine. Half of the sample was vacuum sealed with an acetylene torch under argon gas in a quartz tube to ensure no oxidation would take place, the pressure when sealing was ~80 kPa vacuum. They were then annealed in a tube furnace exposed to air at 650°C and 1000°C for 1000 hours (41 days), and the other half was studied in the as-cast condition. The annealed samples were removed from the furnace and quenched in room temperature water.

The annealed and as-cast samples were mounted in polyfast for metallographic examination at 180°C for approximately 6 minutes, 3 minutes heating and then water cooled for 3 minutes under constant 250 bar pressure. The samples were then ground using MD Piano220 with water and MD Piano1200 with water. They were polished using MD Mol with DiaPro Mol 3 micron solution and MD Chem with oxide polishing (OP-S). During the grinding and polishing stages, DP-Lubricant blue was used with the solutions.

Due to the wide range of compositions of the samples (from 10-75 at.% Pd), different etching techniques had to be tried, and the best results for each sample was used. The first etch used was with a steel wire cathode and a solution of water and hydrochloric acid [1996Win]. The second etch was immersion in a solution of distilled water (50 ml), hydrochloric acid (SG 1.19, 100 ml) and nitric acid (SG 1.4, 10ml) [1996Win]. The third technique was to etch electrically in a solution of distilled water and hydrochloric acid using a graphite cathode [1996Win]. The electric etching voltage range was between 3 V and 10 V. The fourth technique was immersion etching in Aqua Regia, which is a solution made up of 3:1 volume hydrochloric acid to nitric acid [2007Van]. Once the samples were etched, they were checked on the optical microscope for visible microstructure.

Hardness tests were conducted using a Vickers microhardness tester with an applied load of 1 kgf and a loading time of 15s. Five indentations were made to obtain an average hardness.

3.4. Analysis of samples

3.4.1. Scanning electron microscopy (SEM)

The microstructures of the samples were examined using a Sigma Zeiss scanning electron microscope in backscattered (BSE) and secondary electron (SE) modes. The phases of the samples were analysed by energy dispersive X-ray spectroscopy (EDS) in the SEM. Phase analyses by EDX were only done on areas that were larger than 2 microns to obtain an accurate result. An operating voltage of 20 kV, and a working distance of 7.5-10.5 mm was used. The 20 kV voltage was necessary to excite the Pd X-rays for EDX.

3.4.2. X-ray diffraction (XRD)

The phases found using EDS were confirmed using a conventional Bruker D2 phaser with a copper tube. This was done on the polished samples that had been removed from the polyfast resin. They were secured in the sample holder using plasticene and leveled using a thick glass slide. The Diffrac Plus EVA program was used to compare the experimental crystal structures with the ICDD (International Centre for Diffraction Data) PDF2 (Powder Diffraction File) 2018 release database.

Since the A1 (γFe,αCo,Pd) solid solution phase had such a wide extent, and there were no available ternary XRD data files, those from the constituent binaries had to be used. This meant that often peaks were identified as being A1 (γFe,αCo,Pd) from phases of two different binaries, even though it was a single (sometimes cored) phase.

Chapter 4: Results - SEM and XRD

4.1. As-cast samples

For the Co-Pd binary on the ternary diagram, the location of the (εCo) + (αCo,Pd) two-phase region was a rough estimation of the composition, and was extrapolated from Figure 2.5. There was no certain way to tell how far the two-phase region would extend.

4.1.1. Alloy 1: Nominal Co_{30}:Fe_{60}:Pd_{10} (at.%)

For Alloy 1, Nominal Co_{30}:Fe_{60}:Pd_{10} (at.%), the dendrites formed in Figure 4.1 a) were probably due to coring, from the fast cooling from arc-melting, given the lack of a definite interface between the dendritic and interdendritic regions, and they also had similar compositions. At higher magnification (Figure 4.1 b)), their decomposition to two fine phases was observed, but these two phases were too fine to analyse individually. It was surmised that the fine phases were the (αFe) (bcc) ferrite within A1 (γFe,αCo,Pd) (fcc). Due to the low Pd content, the etchant used was not as aggressive as the other etchants, and this etching was done using a steel wire cathode in a solution of water and hydrochloric acid.

The primary phase formed by the following reaction:

$$L \rightarrow A1\ (\gamma Fe,\alpha Co,Pd)\ (cored).$$

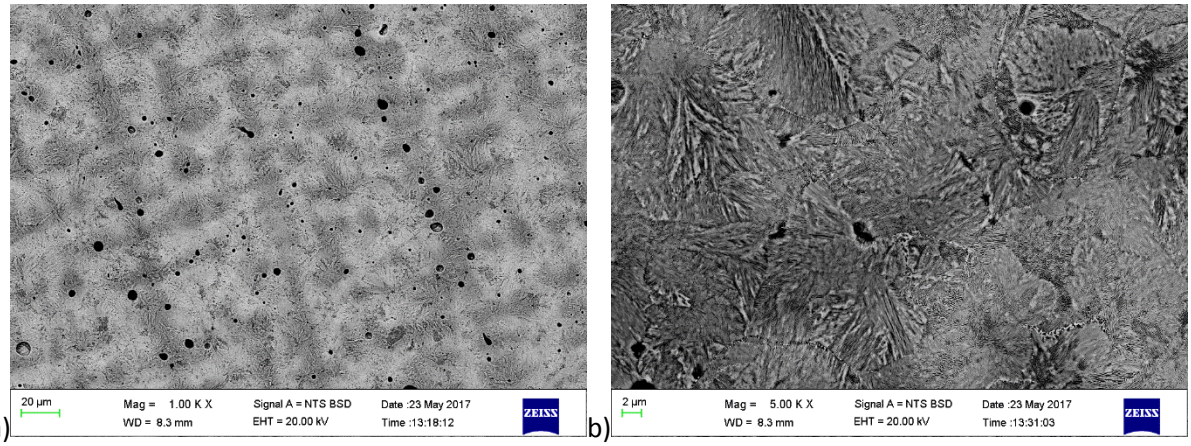


Figure 4.1. SEM-BSE images of as-cast Co_{30}:Fe_{60}:Pd_{10} (at.%), Alloy 1 showing: a) dendrites (darker), and b) showing decomposition at higher magnification.

Table 4.1 gives the analysis for each phase and the overall composition. The data from Table 4.1 were plotted in Figure 4.2, the overall composition was outside the two phases found, which could be due to alteration of compositions in some areas during etching, or the sample being inhomogeneous. The XRD results are shown in Figure 4.3, which confirm that one of the phases was A1 (γFe,αCo,Pd). One other phase was also detected, α; this phase was most likely not discernable by EDX, due to the microstructure being fine.

Table 4.1. EDX phase analyses for nominal Co_{30}:Fe_{60}:Pd_{10} (at.%), Alloy 1, as-cast condition.

Phase description	Co	Fe	Pd	Phase
Overall	29.1 ± 0.1	59.6 ± 0.1	11.3 ± 0.0	-
Dendrite (Inner Dark)	28.5 ± 0.3	59.1 ± 0.1	12.4 ± 0.3	Cored (γFe,αCo,Pd)
Light	25.8 ± 0.1	55.5 ± 0.1	18.7 ± 0.1	Cored (γFe,αCo,Pd)

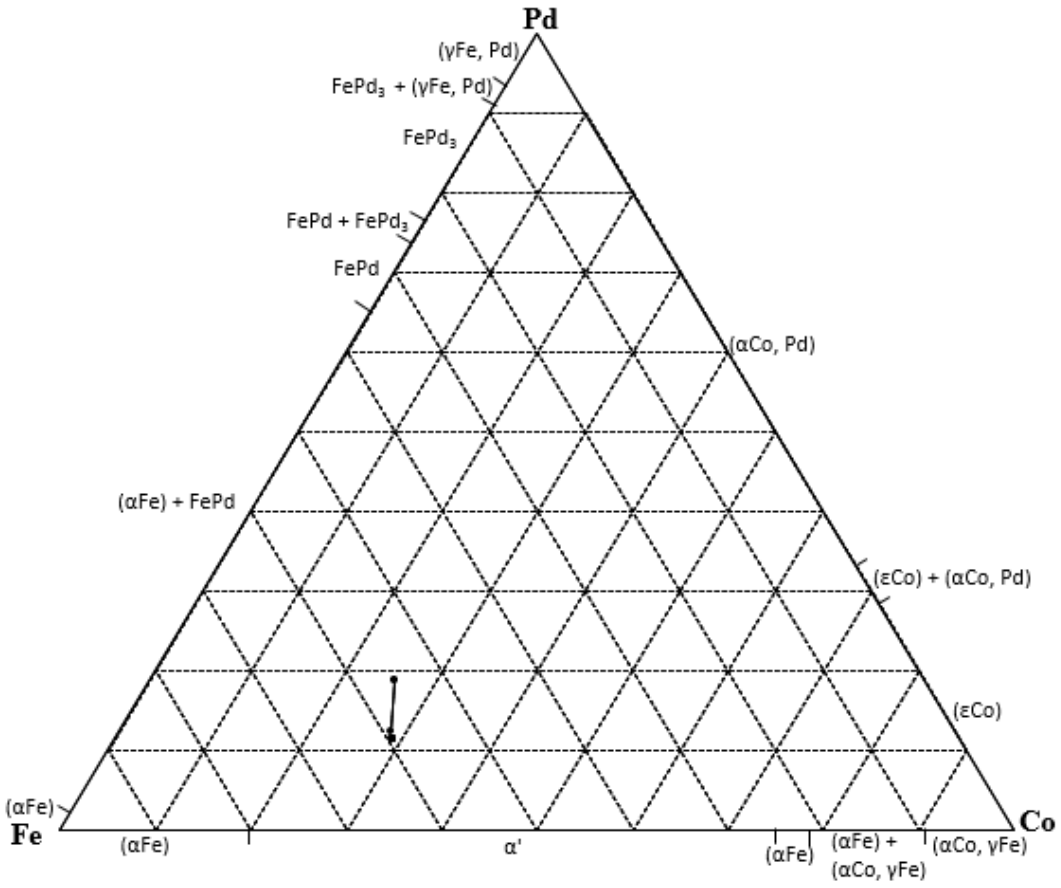


Figure 4.2. EDX analyses of nominal Co_{30}:Fe_{60}:Pd_{10} (at.%), Alloy 1 as-cast condition. (■ Overall composition; ● phases)

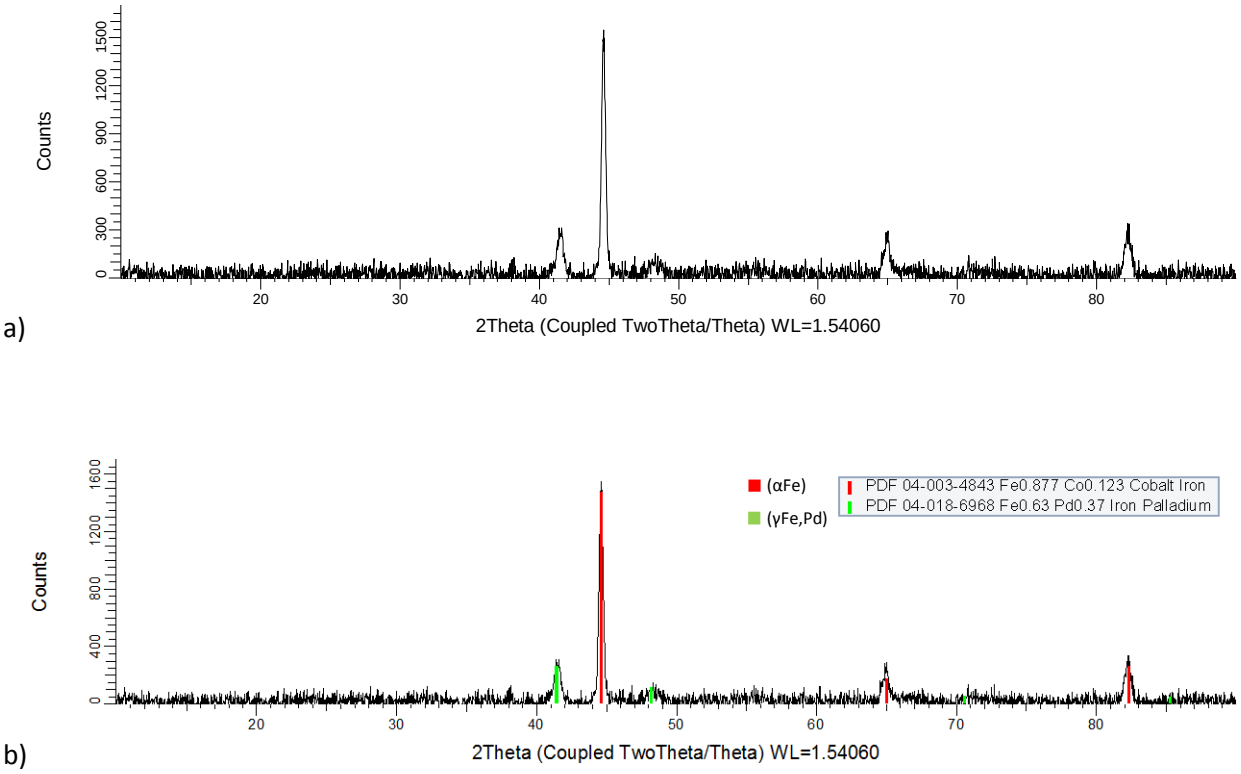


Figure 4.3. XRD patterns for nominal $Co_{30}:Fe_{60}:Pd_{10}$ (at.%), Alloy 1 as-cast condition: a) raw, and b) labelled.

4.1.2. Alloy 2: Nominal Co_6:Fe_{44}:Pd_{50} (at.%)

Figure 4.4 shows that Alloy 2, Nominal Co_6:Fe_{44}:Pd_{50} (at.%), was a solid solution. This was confirmed by the EDX results plotted in Figure 4.5, where the data points are on top of each other, and the XRD results (Figure 4.6), which identified the phase as γ, a solid solution of A1 (γFe,αCo,Pd). Figure 4.6 shows very few peaks, because there was only the fcc A1 (γFe,αCo,Pd) phase present.

The phase formed by the following reaction:

$$L \rightarrow A1\ (\gamma Fe,\alpha Co,Pd)\ (cored).$$

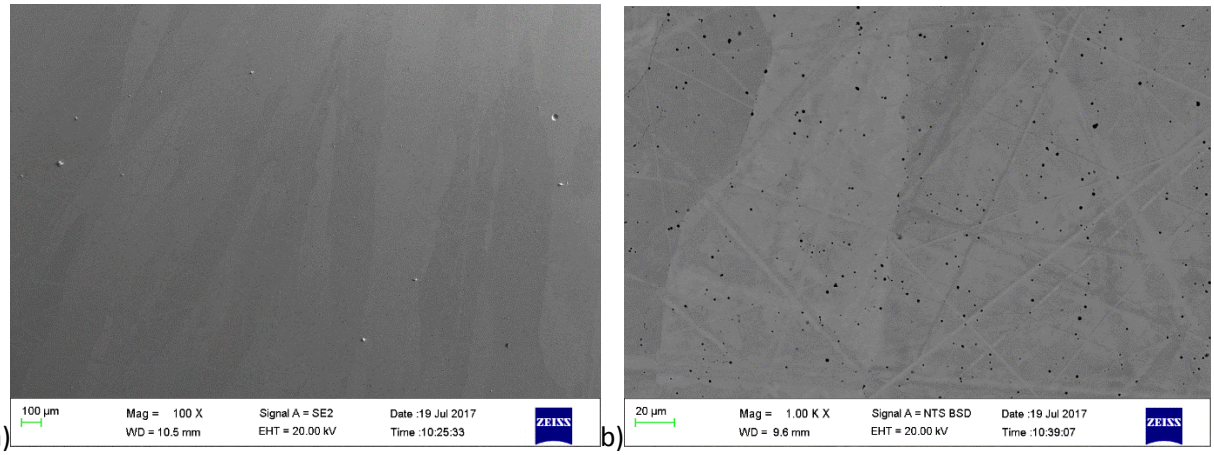


Figure 4.4. SEM images of as-cast Co_6:Fe_{44}:Pd_{50} (at.%), Alloy 2 showing: a) SE grains, and b) BSE higher magnification.

Table 4.2 gives a summary of the EDX results and the phases present. There was very little difference between the analyses, and they were within the experimental errors.

Table 4.2. EDX phase analyses for nominal Co_6:Fe_{44}:Pd_{50} (at.%), Alloy 2, as-cast condition.

Phase description	Co	Fe	Pd	Phase
Overall	5.9 ± 0.1	41.2 ± 0.1	52.9 ± 0.1	-
Dark	5.8 ± 0.3	41.0 ± 0.3	53.2 ± 0.2	Cored A1 (γFe,αCo,Pd)
Light	5.9 ± 0.4	41.0 ± 0.3	53.1 ± 0.3	Cored A1 (γFe,αCo,Pd)

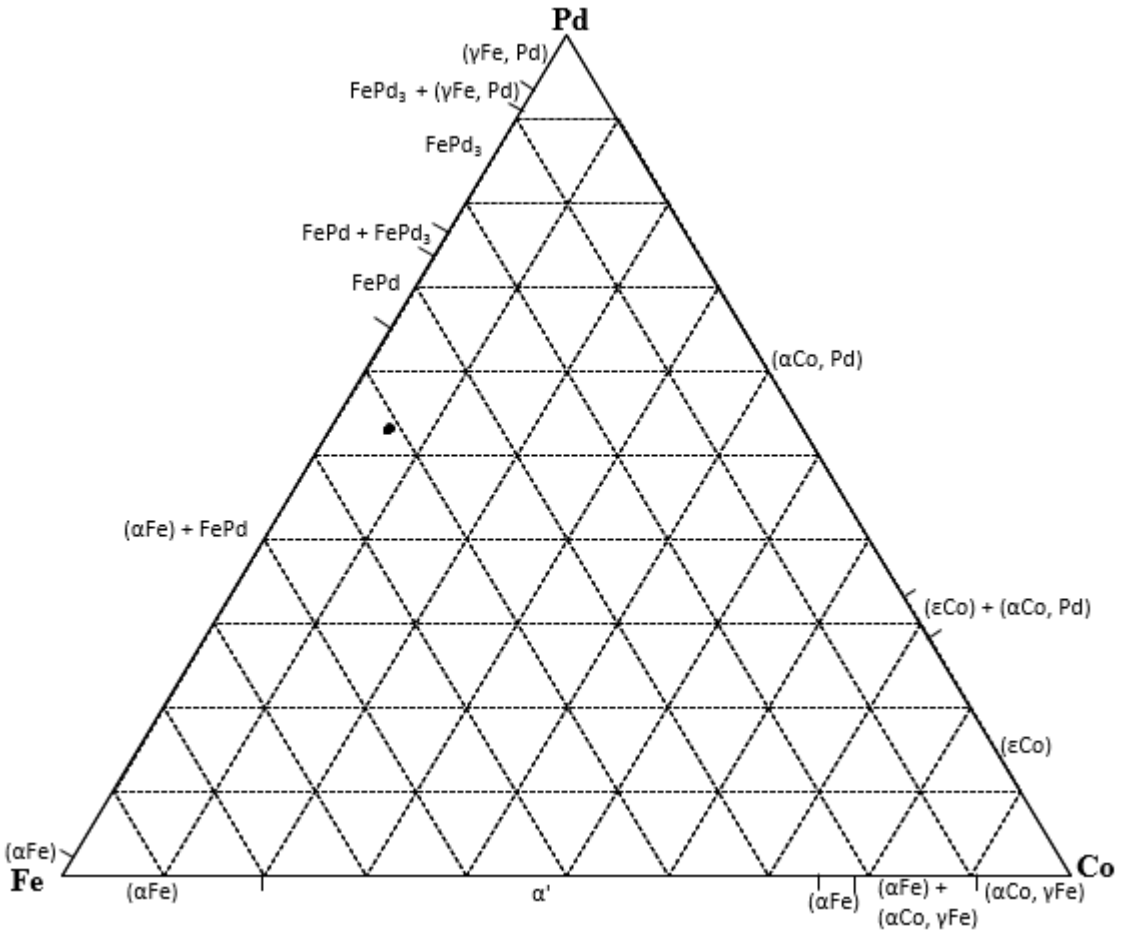


Figure 4.5. EDX analyses of nominal $Co_6:Fe_{44}:Pd_{50}$ (at.%), Alloy 2 as-cast condition. (■ Overall composition; ● phases)

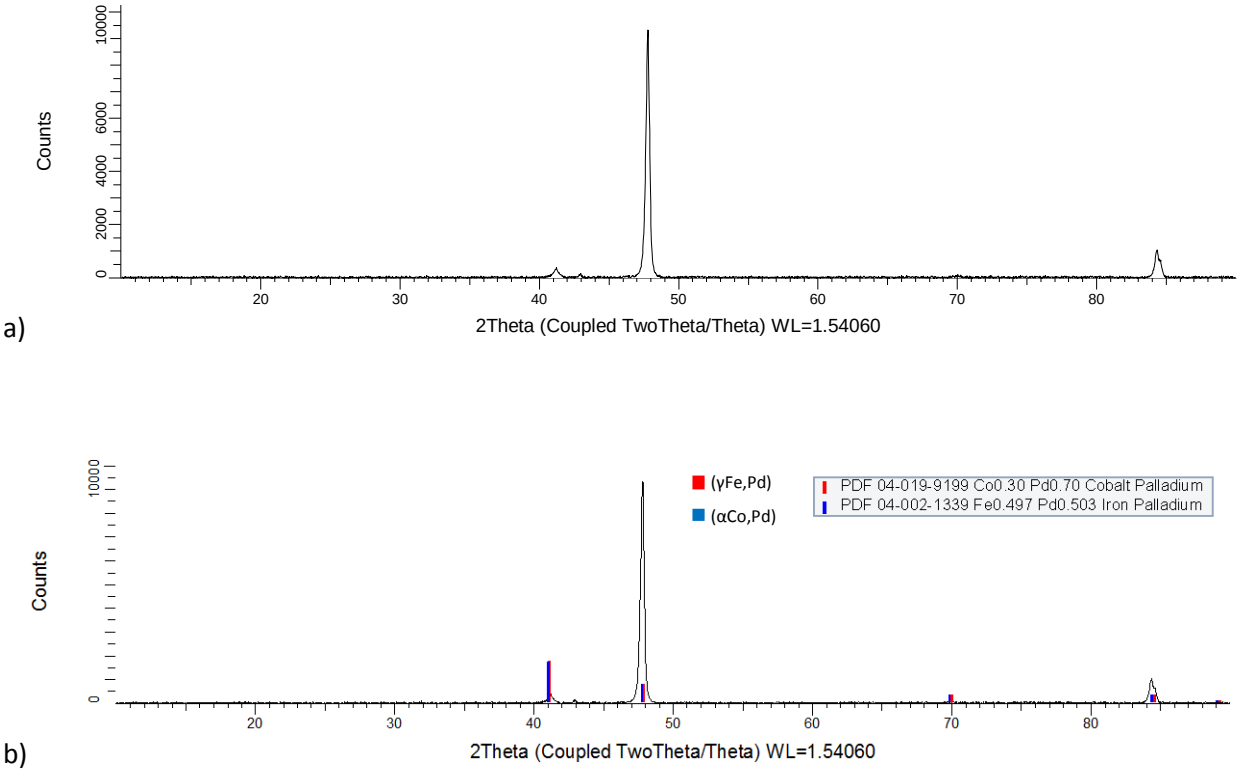


Figure 4.6. XRD patterns for nominal Co_6:Fe_{44}:Pd_{50} (at.%), Alloy 2 as-cast condition: a) raw, and b) labelled.

4.1.3. Alloy 3: Nominal Co_{20}:Fe_{50}:Pd_{30} (at.%)

Figure 4.7 (Alloy 3, Nominal Co_{20}:Fe_{50}:Pd_{30} (at.%)) shows a solid solution with coring, given the similar compositions in Table 4.3. Figure 4.8 shows the values obtained for the EDX lie outside of the errors. From XRD, the phase detected was A1 (γFe,αCo,Pd) (Figure 4.9), and the shifts were in different directions, suggesting the fcc structure was not quite cubic, possibly tending to fct. The largest peak in the XRD pattern was due to preferred orientation.

The phase formed by the following reaction:

$$L \rightarrow A1\ (\gamma Fe,\alpha Co,Pd)\ (cored).$$

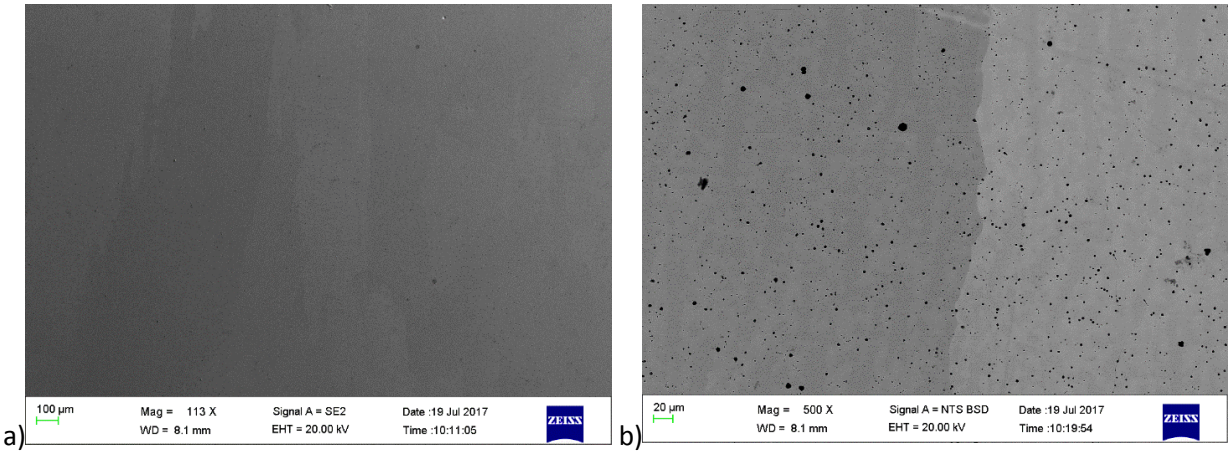


Figure 4.7. a) SEM-SE, and b) SEM-BSE images of as-cast Co_{20}:Fe_{50}:Pd_{30} (at.%), Alloy 3 showing grains and different contrasts.

Table 4.3. EDX phase analyses for nominal Co_{20}:Fe_{50}:Pd_{30} (at.%), Alloy 3, as-cast condition.

Phase description	Co	Fe	Pd	Phase
Overall	18.8 ± 0.2	48.4 ± 0.2	32.8 ± 0.1	-
Dark	18.8 ± 0.1	49.1 ± 0.4	32.1 ± 0.4	Cored A1(γFe,αCo,Pd)
Light	18.9 ± 0.2	48.4 ± 0.4	32.7 ± 0.2	Cored A1(γFe,αCo,Pd)

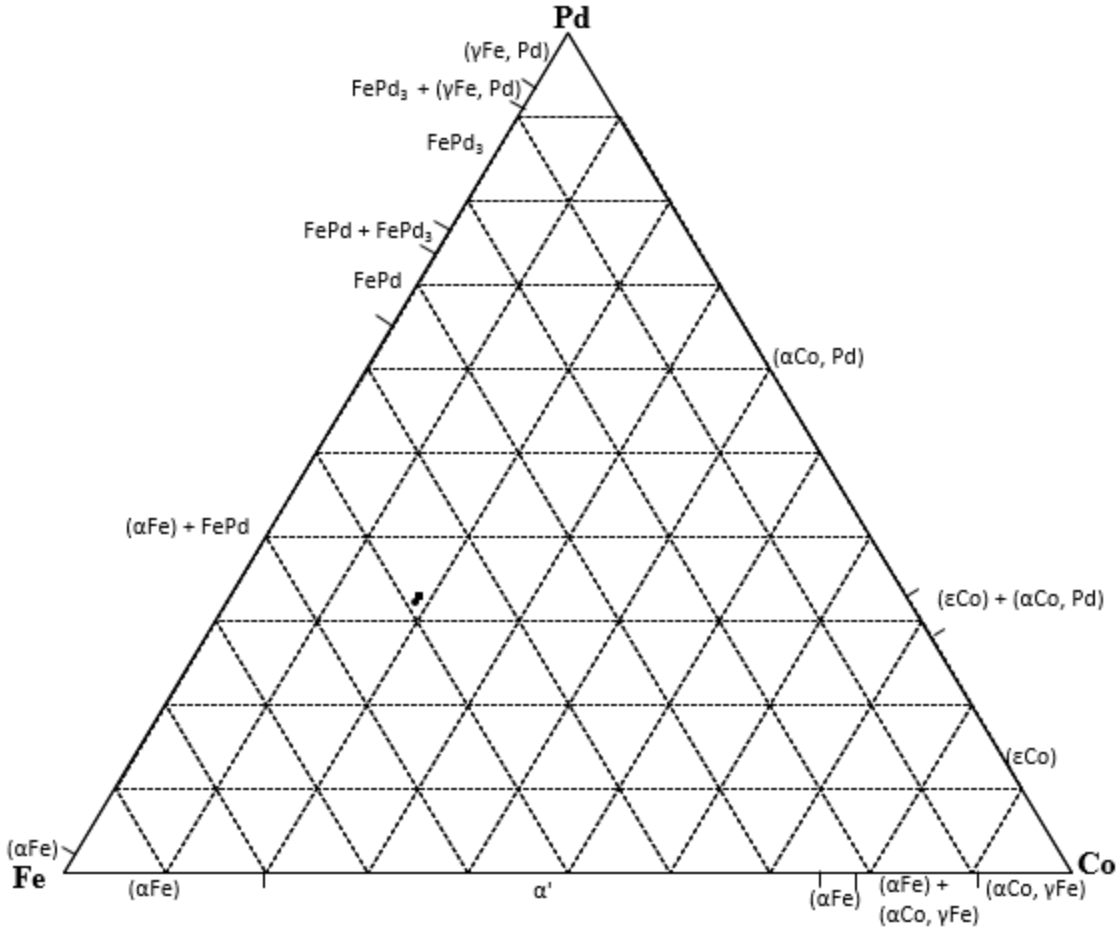


Figure 4.8. EDX analyses of nominal Co_{20}:Fe_{50}:Pd_{30} (at.%), Alloy 3 as-cast condition. (■ Overall composition; ● phases)

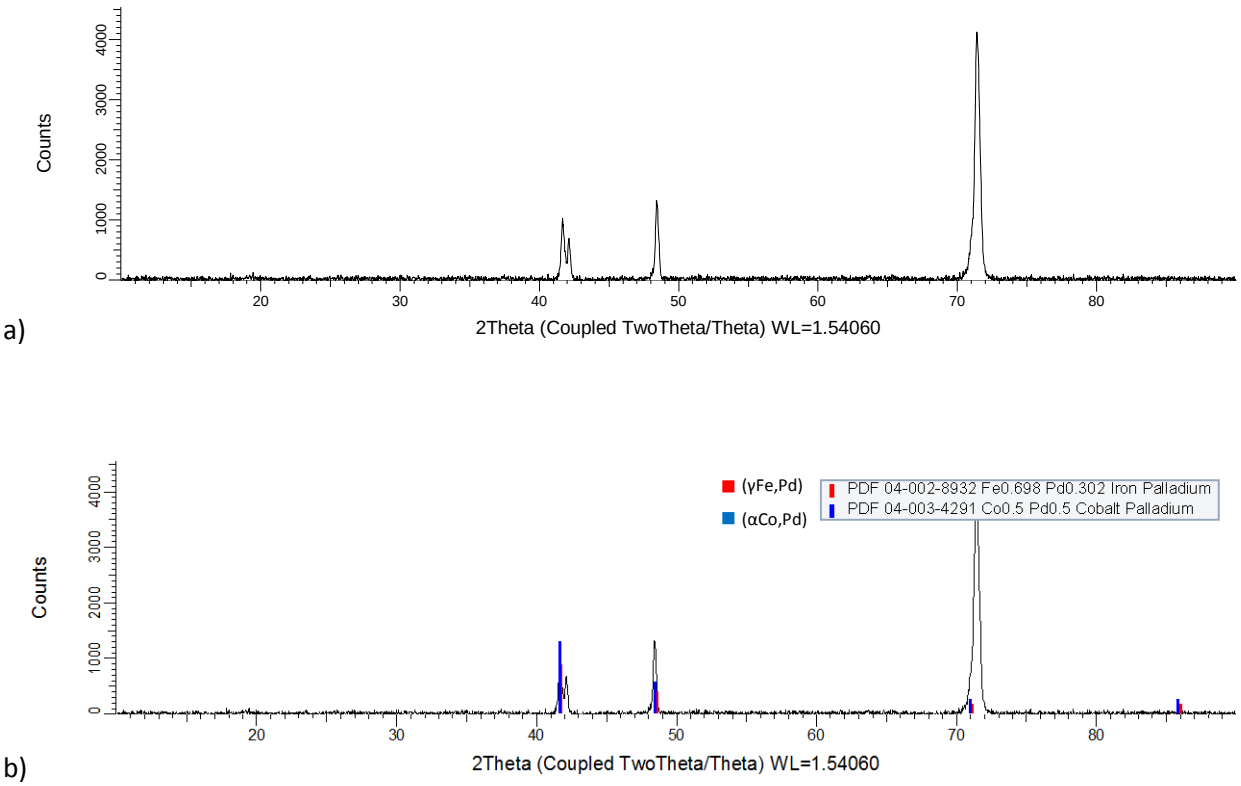


Figure 4.9. XRD patterns for nominal Co_{20}:Fe_{50}:Pd_{30} (at.%), Alloy 3 as-cast condition: a) raw, and b) labelled.

4.1.4. Alloy 4: Nominal Co_{10}:Fe_{15}:Pd_{75} (at.%)

Alloy 4, Nominal Co_{10}:Fe_{15}:Pd_{75} (at.%), needed the most aggressive etchant because of the high Pd content of the alloy. The microstructure in Figure 4.10 a) shows dendrites, which were due to coring of a single phase because of the similar compositions between the dendritic and interdendritic areas, and the lack of a distinct interface. This agreed with the similar compositions shown in Table 4.4 and Figure 4.11, although they were outside of the measured errors. At higher magnification, Figure 4.10 b), there was another phase, which was too fine to analyse. The peaks in Figure 4.12 overlapped, showing the crystal structures had some similar interplanar spacings. The XRD pattern (Figure 4.12) indicated $FePd_3$ and A1 (γFe,αCo,Pd) were present.

The phases formed by the following reactions:

$$L \rightarrow A1\ (\gamma Fe,\alpha Co,Pd)$$

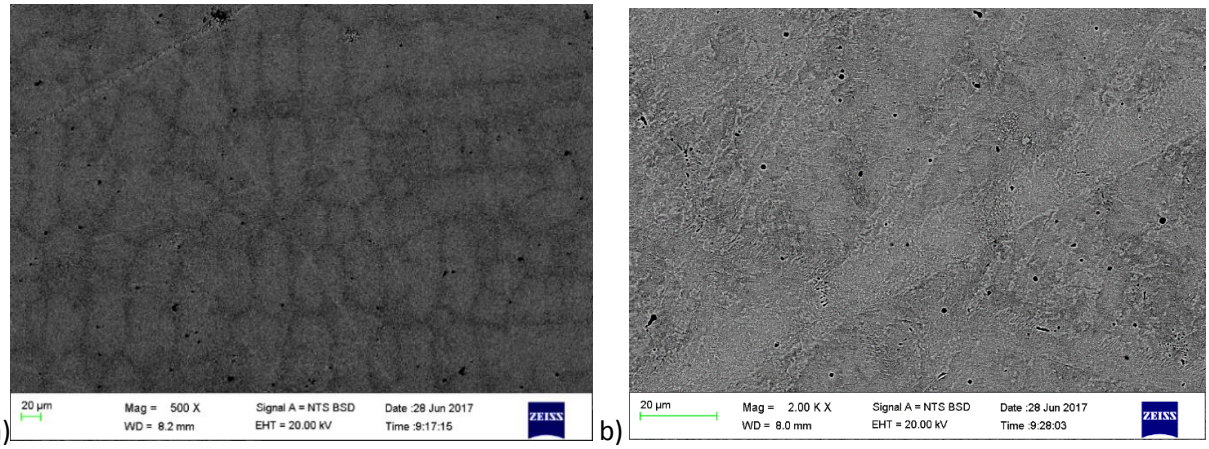


Figure 4.10. SEM-BSE images of as-cast Co_{10}:Fe_{15}:Pd_{75} (at.%), Alloy 4 showing: a) dendrites (lighter), and interdendritic areas (dark) and b) higher magnification.

Table 4.4. EDX phase analyses for nominal Co_{10}:Fe_{15}:Pd_{75} (at.%), Alloy 4, as-cast condition.

Phase description	Co	Fe	Pd	Phase
Overall	9.0 ± 0.1	13.7 ± 0.1	77.3 ± 0.1	-
Dark	11.1 ± 1.3	14.5 ± 0.1	74.4 ± 1.2	~$FePd_3$
Light	8.2 ± 0.4	13.4 ± 0.4	78.4 ± 0.5	(γFe,αCo,Pd)

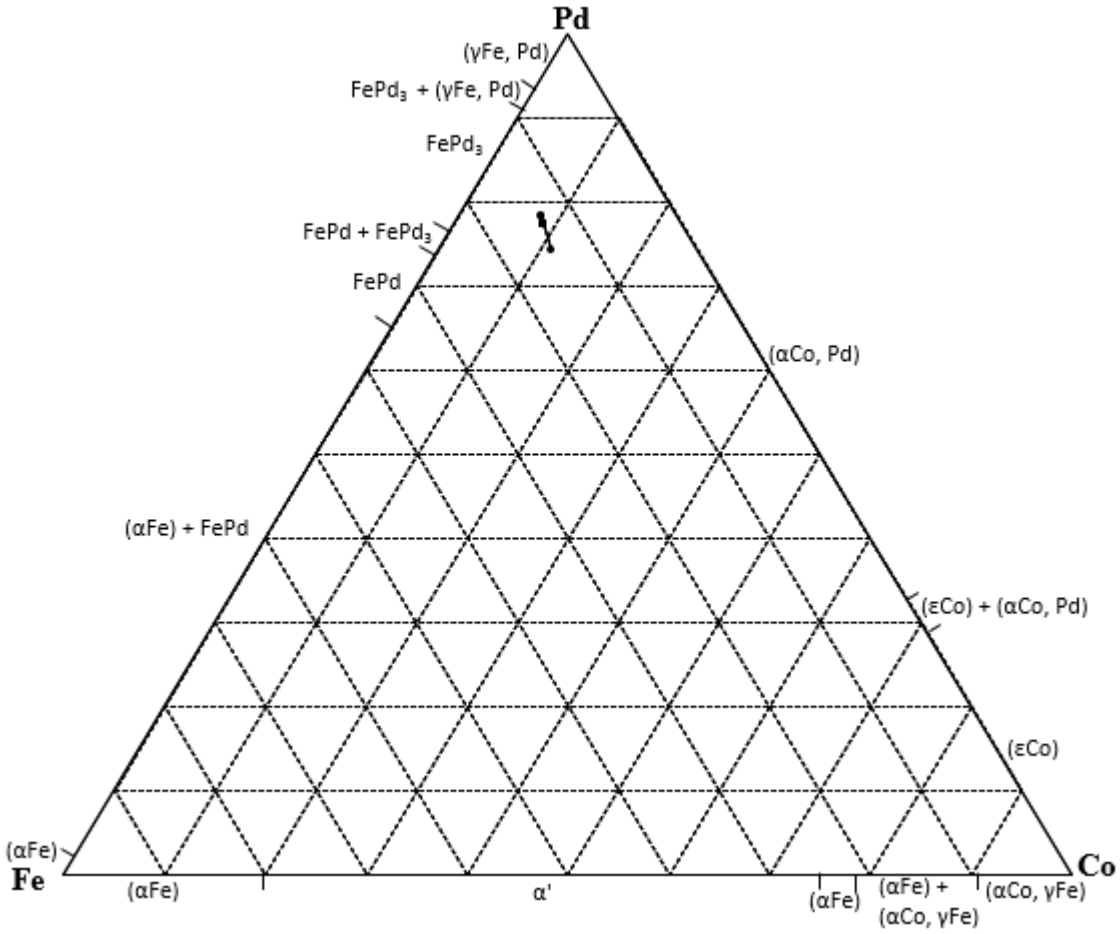


Figure 4.11. EDX analyses of nominal $Co_{10}:Fe_{15}:Pd_{75}$ (at.%), Alloy 4 as-cast condition. (■ Overall composition; ● phases)

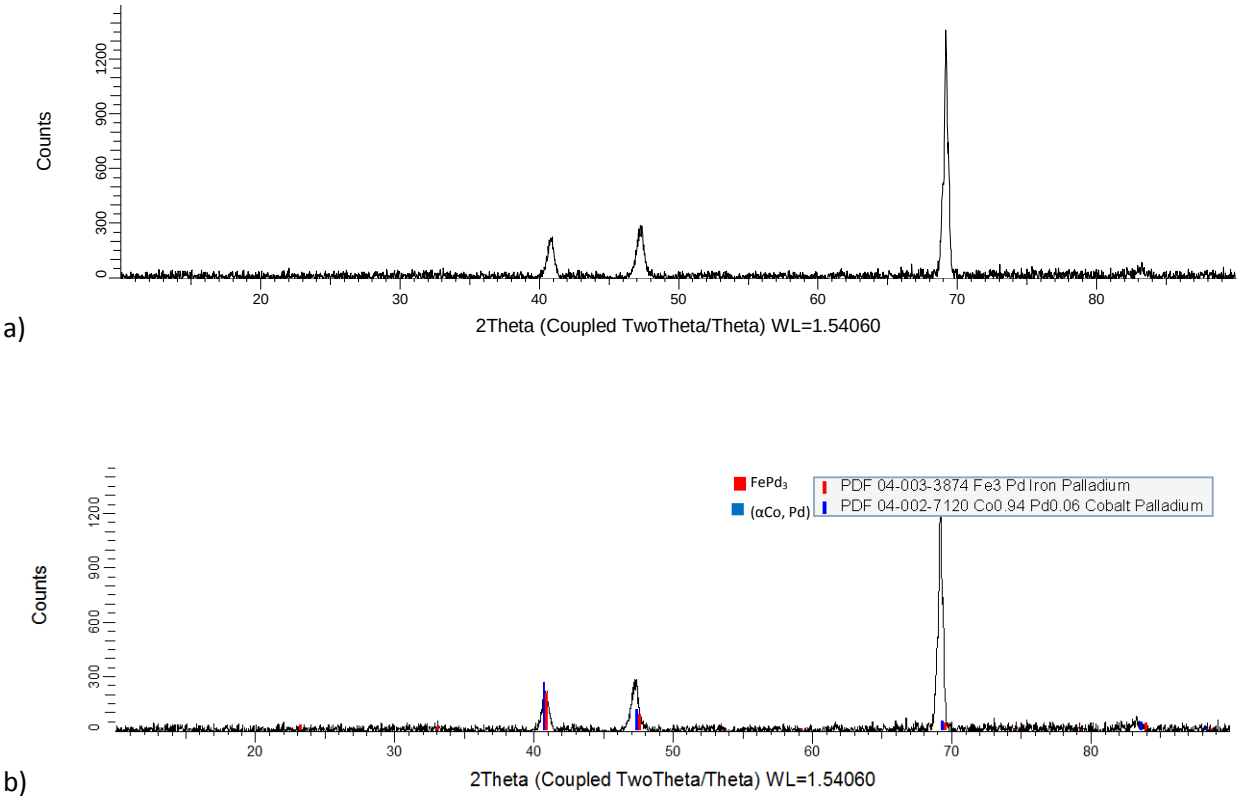


Figure 4.12. XRD patterns for nominal Co_{10}:Fe_{15}:Pd_{75} (at.%), Alloy 4 as-cast condition: a) raw, and b) labelled.

4.1.5. Alloy 5: Nominal Co_{30}:Fe_{30}:Pd_{40} (at.%)

The microstructure of Alloy 5, Nominal Co_{30}:Fe_{30}:Pd_{40} (at.%), Figure 4.13, shows shows a single phase, with pores filled with debris from grinding. The compositions for the contrasting regions were similar, shown in Table 4.5 and Figure 4.13. The XRD pattern in Figure 4.15 shows one major phase which matched two different compositions of A1 (γFe,αCo,Pd), with wide peaks, indicating a cored phase, and all the peaks shifted in the same direction, showing the phase was cubic.

The phase formed by the following reaction:

$$L \rightarrow A1\ (\gamma Fe,\alpha Co,Pd).$$

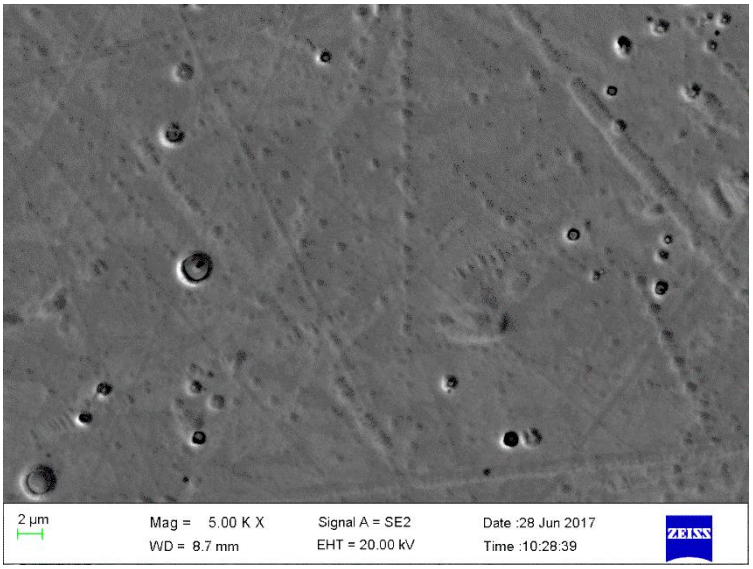


Figure 4.13. SEM-SE image of as-cast Co_{30}:Fe_{30}:Pd_{40} (at.%), Alloy 5 showing a single phase with pores.

Table 4.5. EDX phase analyses for nominal Co_{30}:Fe_{30}:Pd_{40} (at.%), Alloy 5, as-cast condition.

Phase description	Co	Fe	Pd	Phase
Overall	28.1 ± 0.2	28.8 ± 0.2	43.1 ± 0.1	-
Dark	28.3 ± 0.2	28.7 ± 0.1	43.0 ± 0.1	Cored A1 (γFe,αCo,Pd)
Light	27.7 ± 0.1	29.2 ± 0.1	43.1 ± 0.1	Cored A1 (γFe,αCo,Pd)

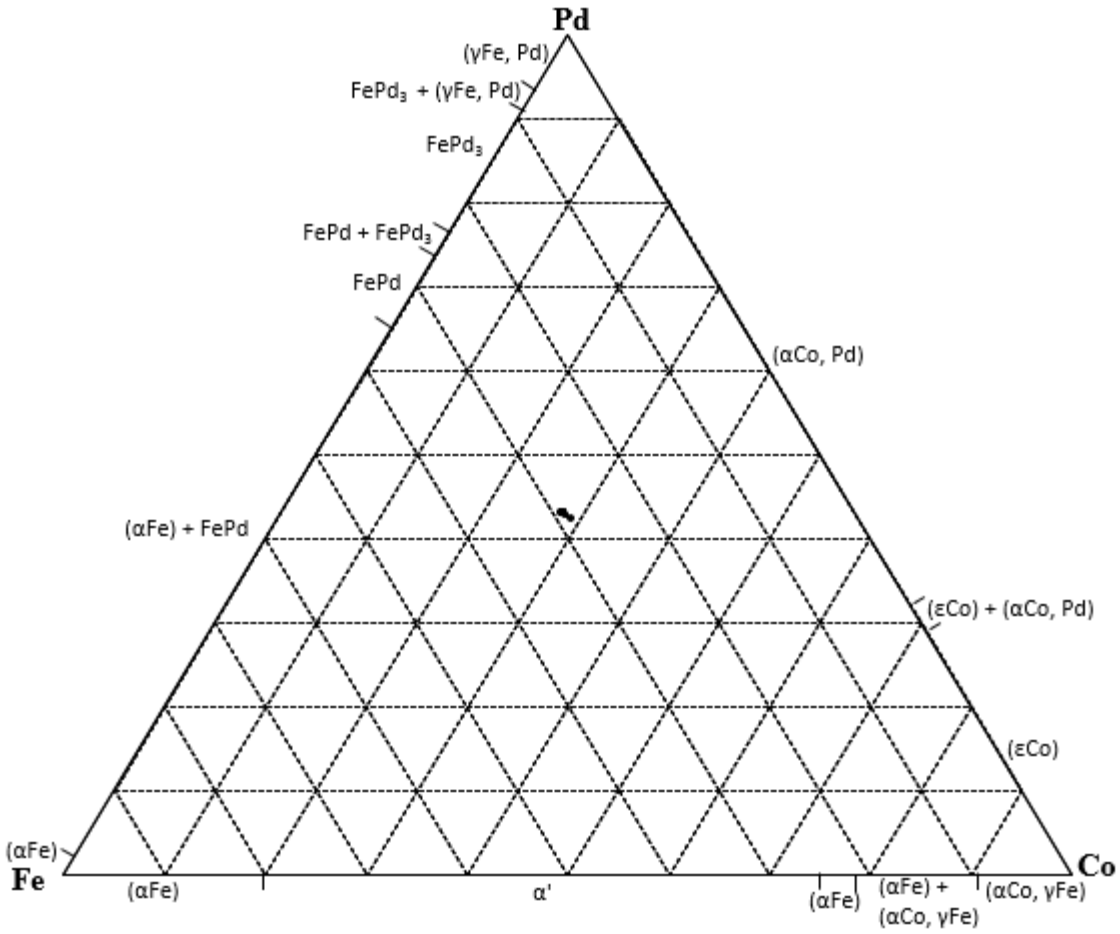


Figure 4.14. EDX analyses of nominal $Co_{30}:Fe_{30}:Pd_{40}$ (at.%), Alloy 5 as-cast condition. (■ Overall composition; ● phases)

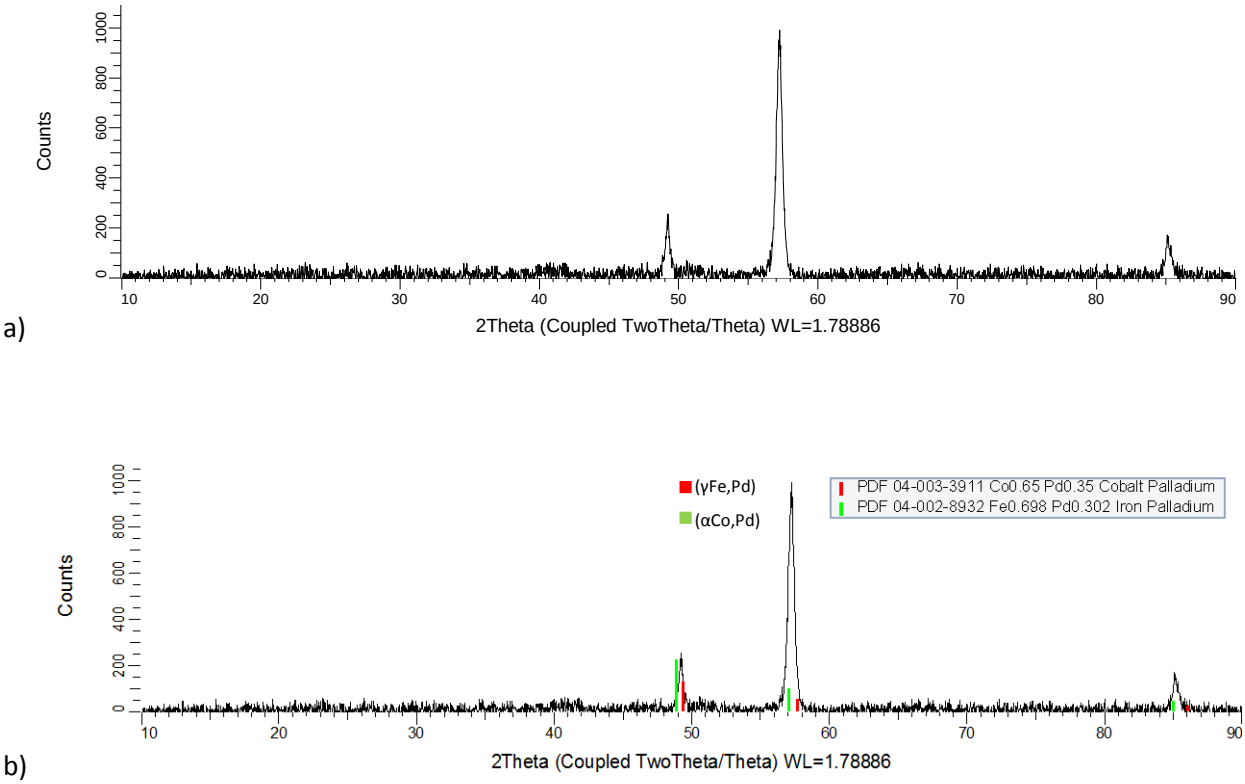


Figure 4.15. XRD patterns for nominal Co_{30}:Fe_{30}:Pd_{40} (at.%), Alloy 5 as-cast condition: a) raw, and b) labelled.

4.1.6. Alloy 6: Nominal Co_{50}:Fe_{20}: Pd_{30} (at.%)

For Alloy 6, Nominal Co_{50}:Fe_{20}:Pd_{30} (at.%), Figure 4.16 b, shows a two-phase microstructure with the grain boundaries being etched. The compositions of the two differently contrasted regions were very similar (Table 4.6 and Figure 4.17) with no distinct interface, showing coring, and the darker phase was richer in Co. There was also some porosity, which is likely to have formed on sample manufacture. The XRD pattern of the sample had very few peaks and there were some peak shifts from the reference pattern for (αCo,Pd) in Figure 4.18.

The phase formed by the following reaction:

$$L \rightarrow A1\ (\gamma Fe,\alpha Co,Pd)\ (cored).$$

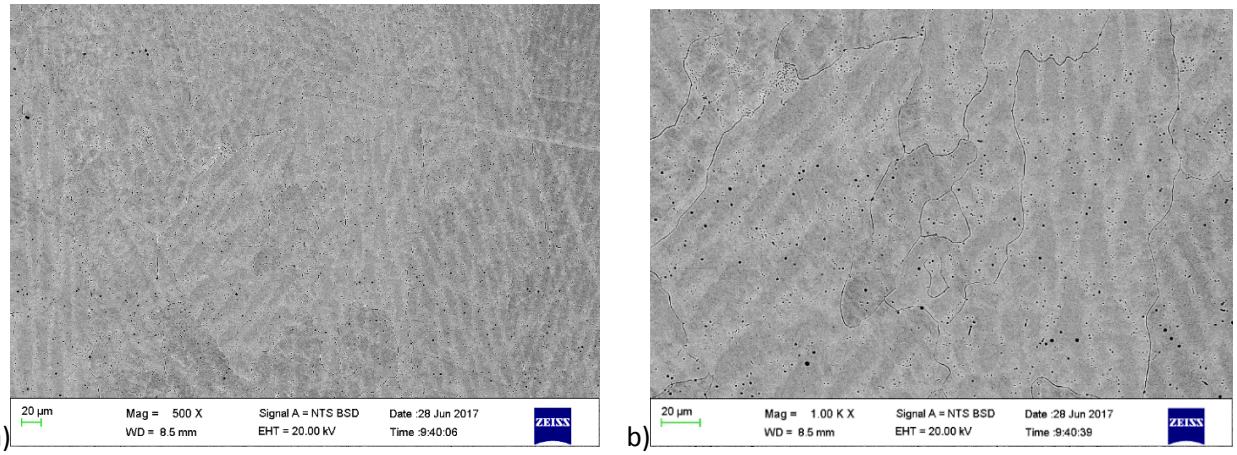


Figure 4.16. SEM-BSE images of as-cast Co_{50}:Fe_{20}:Pd_{30} (at.%), Alloy 6 showing a) coring and dark grain boundaries at low magnification and b) high magnification.

Table 4.6. EDX phase analyses for nominal Co_{50}:Fe_{20}:Pd_{30} (at.%), Alloy 6, as-cast condition.

Phase description	Co	Fe	Pd	Phase
Overall	48.0 ± 0.1	19.7 ± 0.1	32.3 ± 0.1	-
Dark	49.3 ± 0.5	19.2 ± 0.1	31.5 ± 0.5	Cored (γFe,αCo,Pd)
Light	46.3 ± 0.1	18.7 ± 0.1	35.0 ± 0.1	Cored (γFe,αCo,Pd)

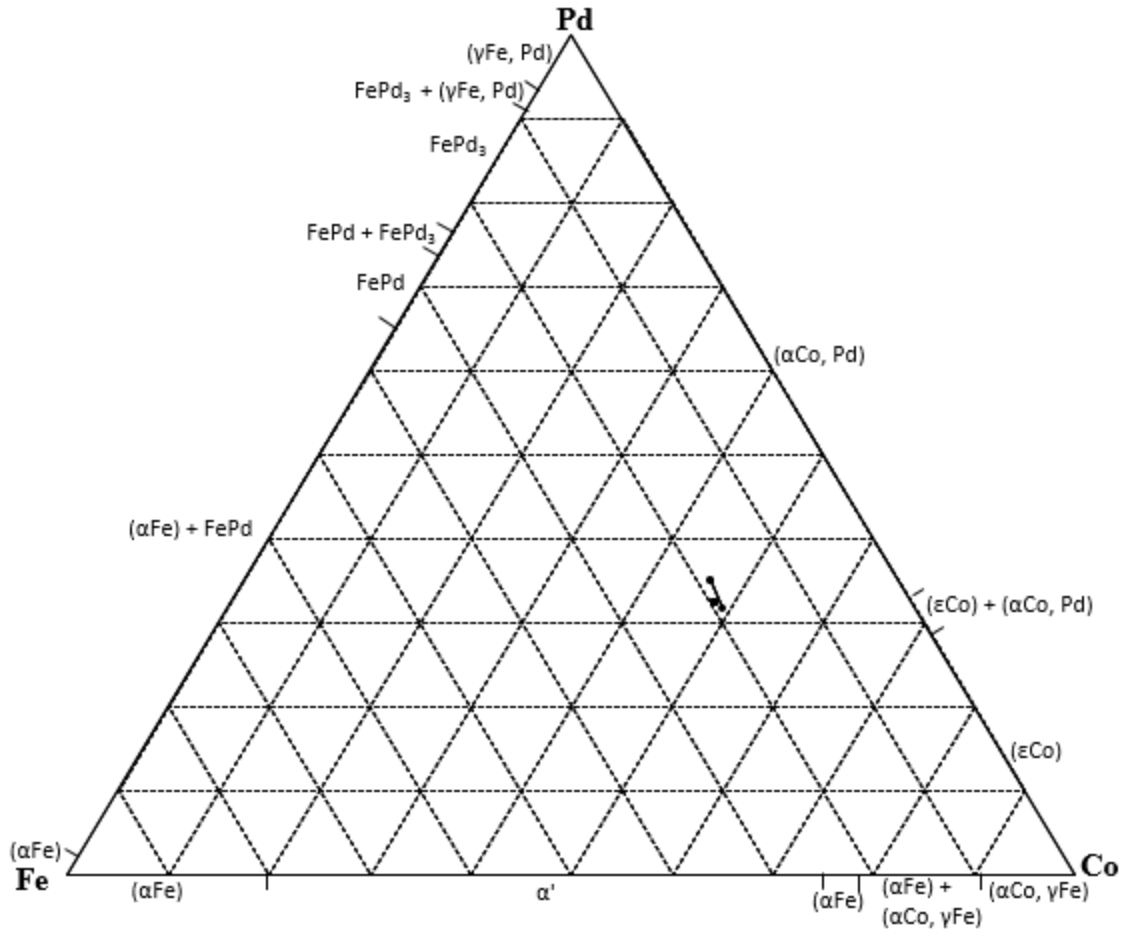


Figure 4.17. EDX analyses of nominal Co_{50}:Fe_{20}:Pd_{30} (at.%), Alloy 6 as-cast condition. (■ Overall composition; ● phases)

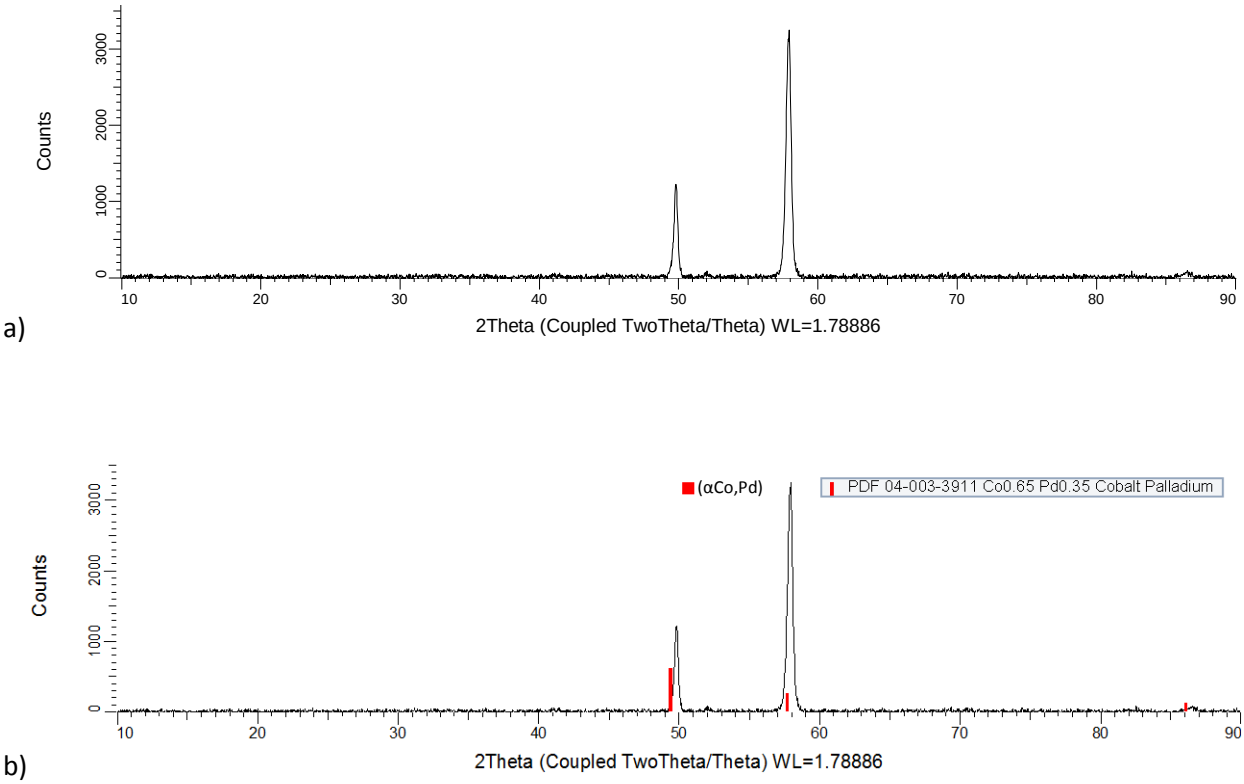


Figure 4.18. XRD patterns for nominal Co_{50}:Fe_{20}:Pd_{30} (at.%), Alloy 6 as-cast condition: a) raw, and b) labelled.

4.1.7. Alloy 7: Nominal Co_{10}:Fe_{30}:Pd_{60} (at.%)

Figure 4.19 a) (Alloy 7, Nominal Co_{10}:Fe_{30}:Pd_{60} (at.%)) shows needles surrounded by a lighter phase. Figure 4.19 b) shows a different region within the matrix. The compositions of the different contrasts in the microstructure were very similar (Table 4.7 and Figure 4.20), and within the errors, except for the region which had a different appearance, which had slightly more Co. Figure 4.21 shows that the phases present were A1 (γFe,αCo,Pd) and ~$FePd_3$ (where ~ denotes that the phase was not stoichiometric, or having at least some Co).

The phases formed by the following reactions:

$$L \rightarrow A1\ (\gamma Fe,\alpha Co,Pd)$$

$$A1\ (\gamma Fe,\alpha Co,Pd) \rightarrow A1\ (\gamma Fe,\alpha Co,Pd) + {\sim}FePd_3\ \text{(precipitation of } {\sim}FePd_3\text{)}.$$

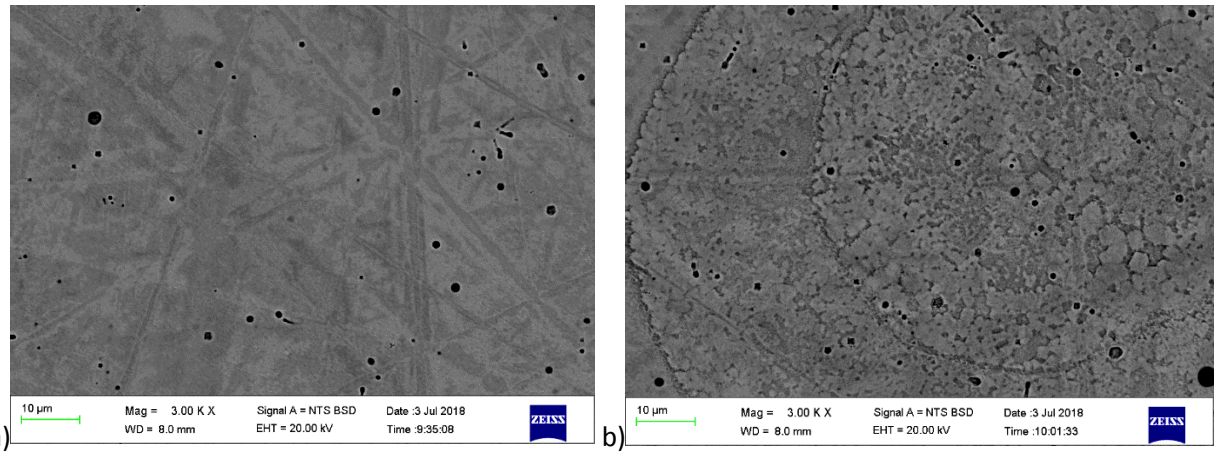


Figure 4.19. SEM-BSE images of as-cast Co_{10}:Fe_{30}:Pd_{60} (at.%), Alloy 7 showing: a) the formation of needles surrounded by a lighter phase, and b) a local area of inhomogeneity.

Table 4.7. EDX phase analyses for nominal Co_{10}:Fe_{30}:Pd_{60} (at.%), Alloy 7, as-cast condition.

Phase description	Co	Fe	Pd	Phase
Overall	8.9 ± 0.1	28.4 ± 0.1	62.7 ± 0.1	-
Dark	8.9 ± 0.3	28.4 ± 0.3	62.7 ± 0.3	(γFe,αCo,Pd)
Light	8.8 ± 0.3	28.5 ± 0.1	62.7 ± 0.4	(γFe,αCo,Pd)
Area of inhomogeneity	9.2 ± 0.4	28.4 ± 0.2	62.3 ± 0.4	(γFe,αCo,Pd) + ~$FePd_3$

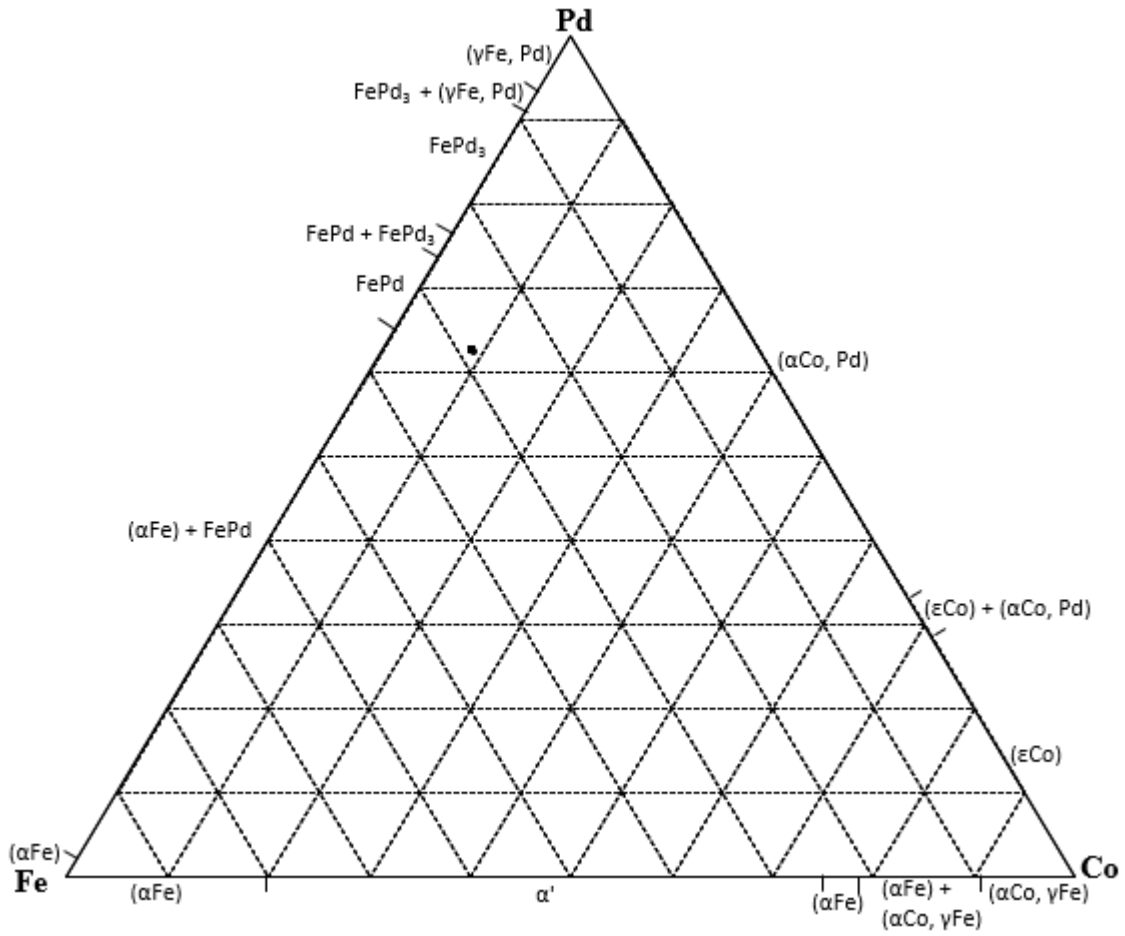


Figure 4.20. EDX analyses of nominal Co_{10}:Fe_{30}:Pd_{60} (at.%), Alloy 7 as-cast condition. (■ Overall composition; ● phases)

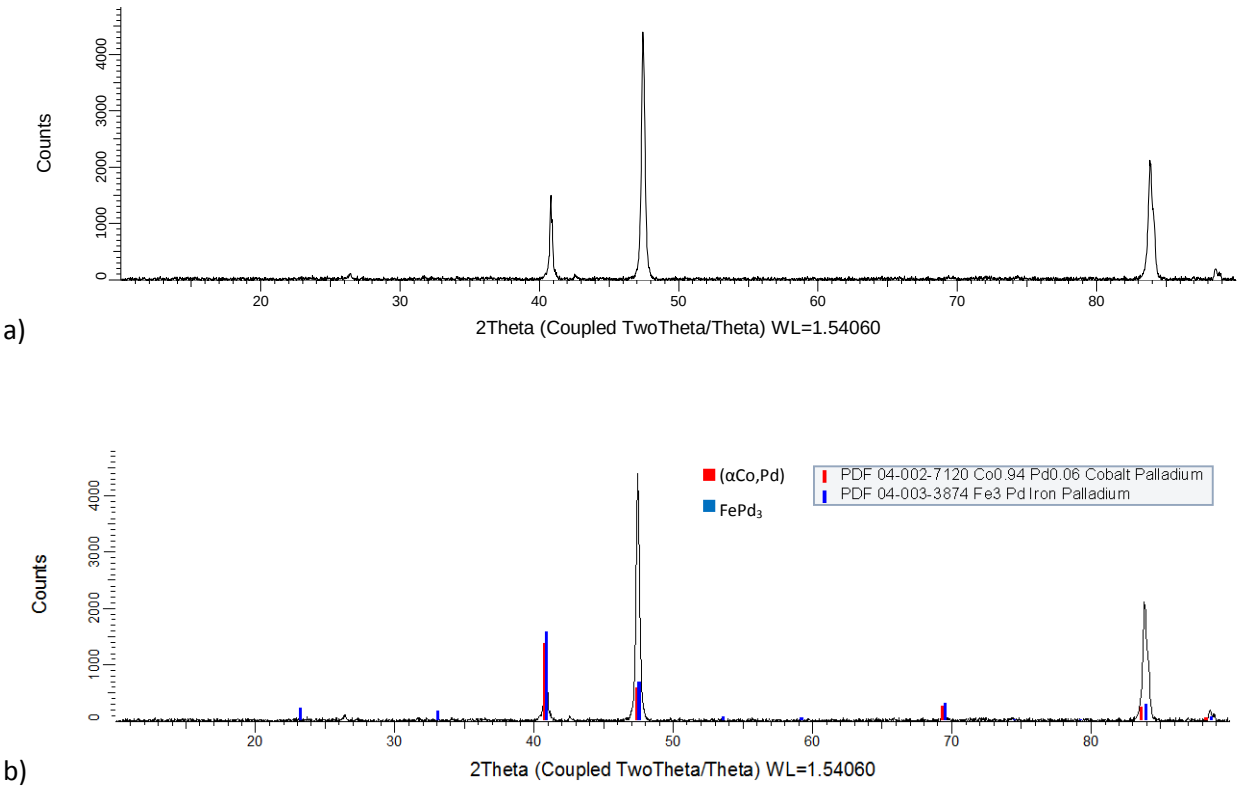


Figure 4.21. XRD patterns for nominal Co_{10}:Fe_{30}:Pd_{60} (at.%), Alloy 7 as-cast condition: a) raw, and b) labelled.

4.1.8. Alloy 8: Nominal Co_{25}:Fe_{20}:Pd_{55} (at.%)

For Alloy 8, Nominal Co_{25}:Fe_{20}:Pd_{55} (at.%), particles were observed in a matrix. At lower magnification, Figure 4.22 a), scratches were observed, showing that the matrix was soft. The phases were all very similar in composition (Figure 4.23 and Table 4.8), and the precipitates were too small to analyse accurately, but were richer in Pd, suggesting they were ~$FePd_3$. The phases were surmised to be A1 (γFe,αCo,Pd) and ~$FePd_3$. The second largest peak on the XRD pattern was likely to be due to preferred orientation.

The phases formed by the following reactions:

$$L \rightarrow A1\ (\gamma Fe,\alpha Co,Pd)$$

$$A1\ (\gamma Fe,\alpha Co,Pd) \rightarrow A1\ (\gamma Fe,\alpha Co,Pd) + {\sim}FePd_3.$$

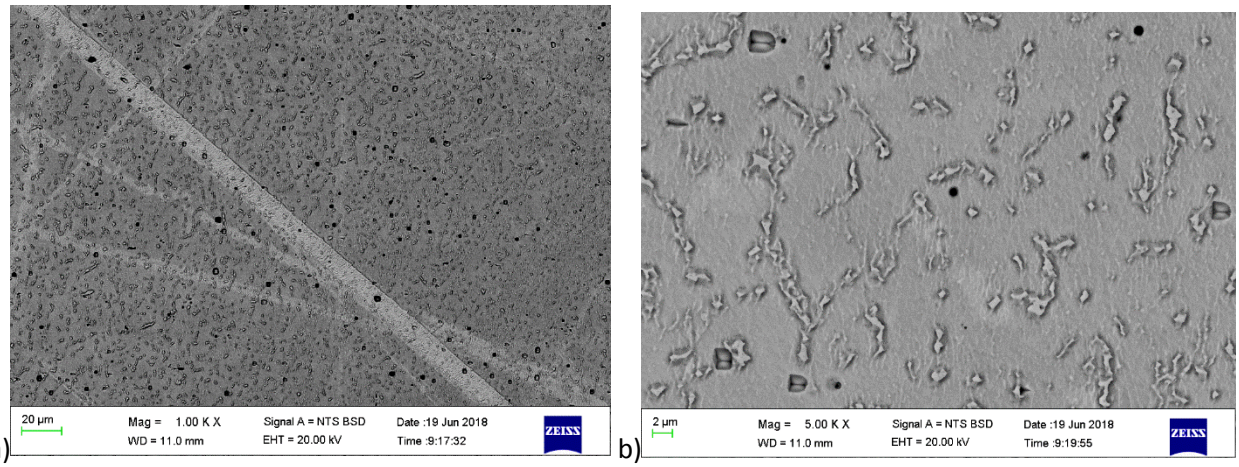


Figure 4.22. SEM-BSE images of as-cast Co_{25}:Fe_{20}:Pd_{55} (at.%), Alloy 8 showing: a) scratches surrounded by darker phase, and b) etched out particles surrounded by a light phase.

Table 4.8. EDX phase analyses for nominal Co_{10}:Fe_{25}:Pd_{55} (at.%), Alloy 8, as-cast condition.

Phase description	Co	Fe	Pd	Phase
Overall	22.7 ± 0.1	18.9 ± 0.2	58.4 ± 0.1	-
Light	21.9 ± 0.4	18.8 ± 0.1	59.3 ± 0.5	A1 (γFe,αCo,Pd)
Particles	21.3 ± 0.5	18.8 ± 0.1	59.9 ± 0.5	~$FePd_3$

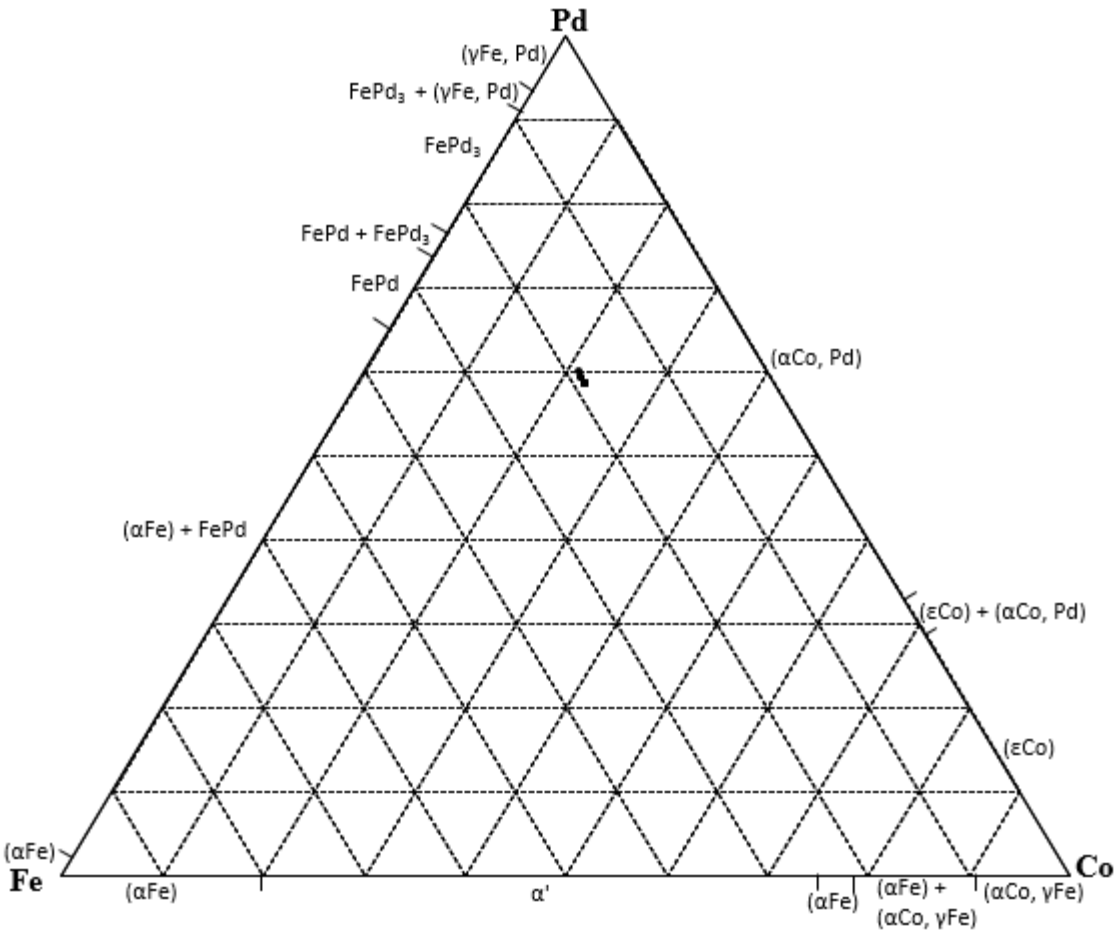


Figure 4.23. EDX analyses of nominal $Co_{25}:Fe_{20}:Pd_{55}$ (at.%), Alloy 8 as-cast condition. (■ Overall composition; ● phases)

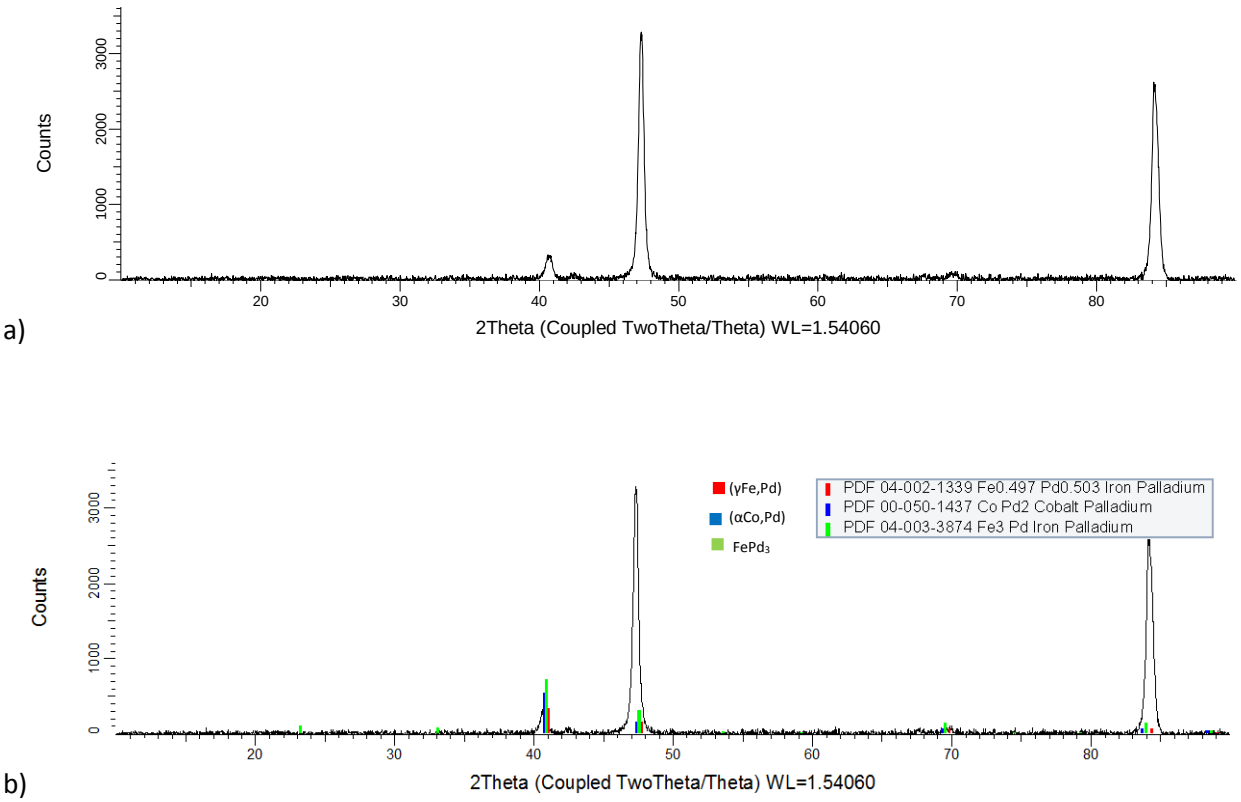


Figure 4.24. XRD patterns for nominal Co_{25}:Fe_{20}:Pd_{55} (at.%), Alloy 8 as-cast condition: a) raw, and b) labelled.

4.1.9. Alloy 9: Nominal Co_{10}:Fe_{50}:Pd_{40} (at.%)

The microstructure of Alloy 9, Nominal Co_{10}:Fe_{50}:Pd_{40} (at.%), at low magnification (Figure 4.25 a)) shows light and dark contrasts, which had very similar compositions (Figure 4.26) and no distinct interface (with the compositions being within the errors, Table 4.9), suggesting coring. The matrix in the differently appearing area shown at a higher magnification (Figure 4.25 b)) had a slightly higher amount of Fe. From the XRD pattern (Figure 4.27), only the A1 (γFe,Pd) phase was detected, showing the sample was the A1 (γFe,αCo,Pd) solid solution, and the largest peak was due to preferred orientation. There was also an unidentified peak at ~75° (2 Theta).

The phase formed by the following reaction:

$$L \rightarrow A1\ (\gamma Fe,\alpha Co,Pd).$$

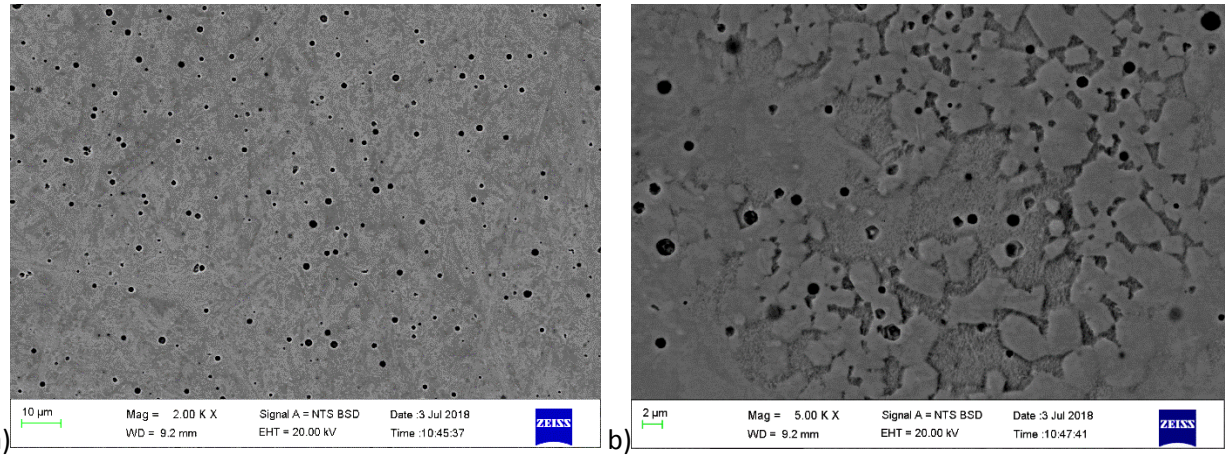


Figure 4.25. SEM-BSE images of as-cast Co_{10}:Fe_{50}:Pd_{40} (at.%), Alloy 9 showing: a) the formation of a light phase surrounded by a dark phase, and b) a differently etched area with particles surrounded by a matrix.

Table 4.9. EDX phase analyses for nominal Co_{10}:Fe_{30}:Pd_{40} (at.%), Alloy 9, as-cast condition.

Phase description	Co	Fe	Pd	Phase
Overall	9.0 ± 0.1	48.1 ± 0.1	42.9 ± 0.1	-
Dark	8.9 ± 0.2	47.8 ± 0.3	43.3 ± 0.3	A1 (γFe,αCo,Pd)
Light	8.9 ± 0.2	47.9 ± 0.2	43.2 ± 0.2	A1 (γFe,αCo,Pd)
Precipitates	8.9 ± 0.2	47.9 ± 0.3	43.2 ± 0.3	A1 (γFe,αCo,Pd)
Matrix	8.8 ± 0.2	48.1 ± 0.6	43.1 ± 0.4	A1 (γFe,αCo,Pd)

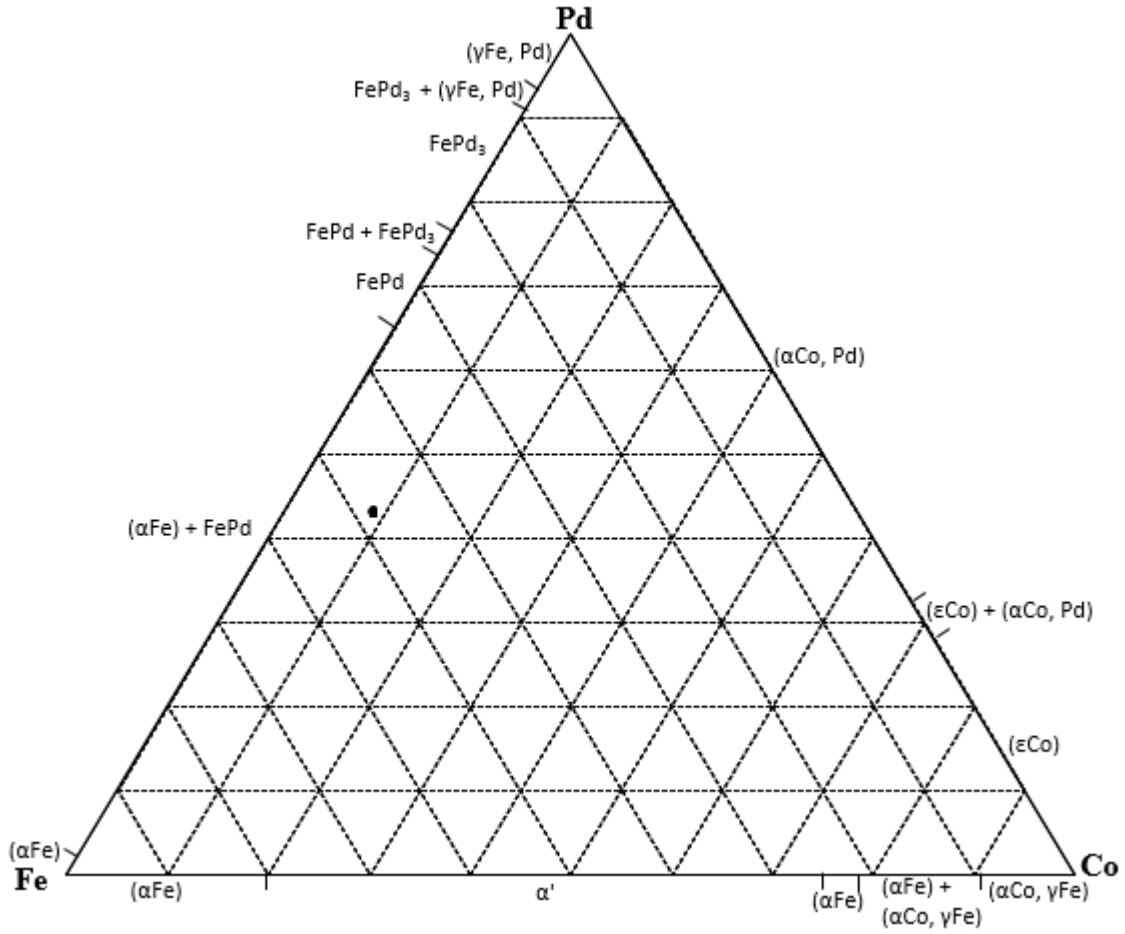


Figure 4.26. EDX analyses of nominal Co_{10}:Fe_{50}:Pd_{40} (at.%), Alloy 9 as-cast condition. (■ Overall composition; ● phases)

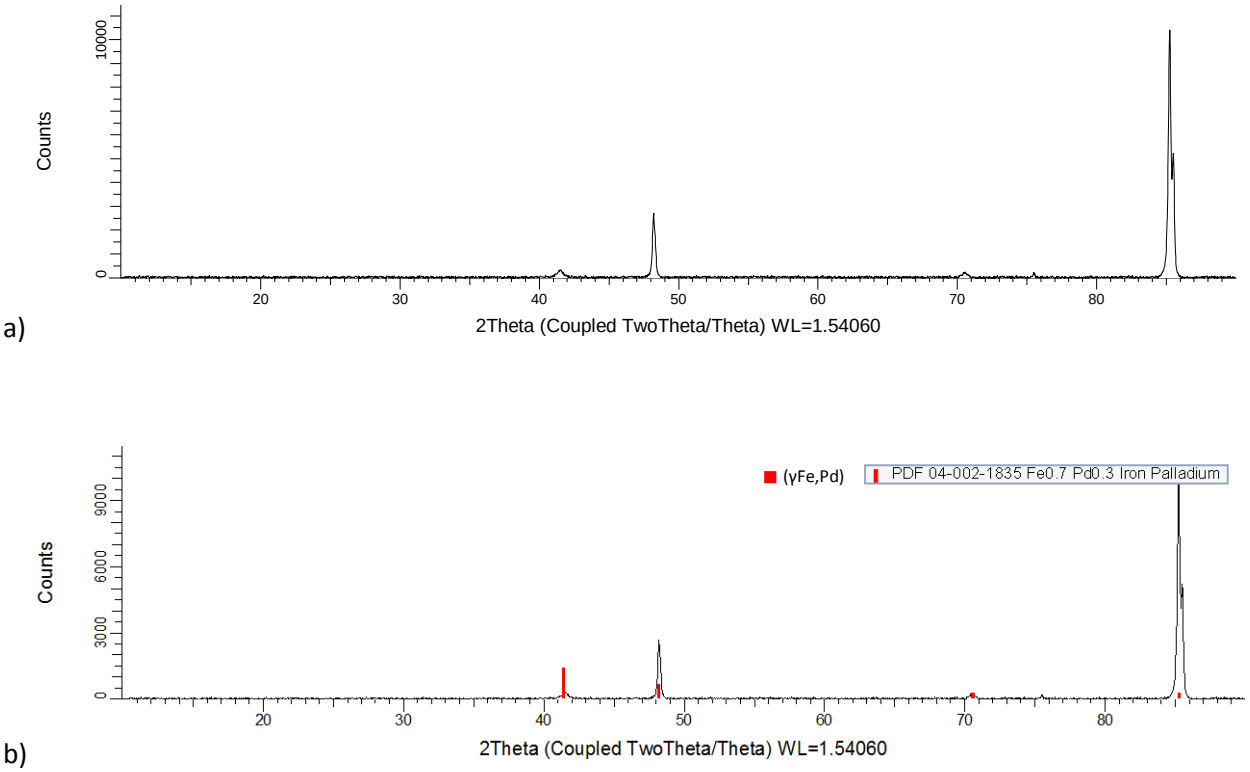


Figure 4.27. XRD patterns for nominal Co_{10}:Fe_{50}:Pd_{40} (at.%), Alloy 9 as-cast condition: a) raw, and b) labelled.

4.1.10. Alloy 10: Nominal Co_{40}:Fe_{30}:Pd_{30} (at.%)

Alloy 10, Nominal Co_{40}:Fe_{30}:Pd_{30} (at.%), had contrasting cored regions, Figure 4.28 a), with the lighter regions having more Fe and Pd than the darker regions, as expected from the BSE image (higher atomic number elements having lighter contrast in BSE imaging). The surrounding area in Figure 4.28 b) had less Co than the fine particles, Table 4.10 and Figure 4.29. The XRD pattern (Figure 4.30) only showed one major peak, with a shift from the reference pattern [2018Dif]. From XRD, it was surmised that the sample was the A1 (γFe,αCo,Pd) solid solution and there was also one small peak at ~38° (2 Theta) which could not be identified.

The phase formed by the following reaction:

$$L \rightarrow A1\ (\gamma Fe,\alpha Co,Pd).$$

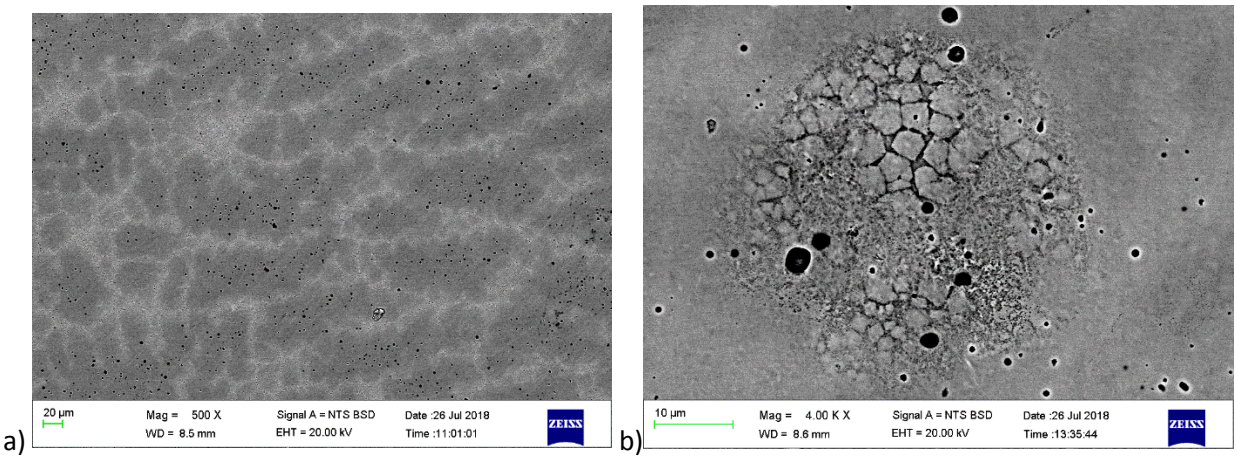


Figure 4.28. SEM-BSE images of as-cast Co_{40}:Fe_{30}:Pd_{30} (at.%), Alloy 10 showing: a) coring, and b) etched patch with particles surrounded by a matrix.

Table 4.10. EDX phase analyses for nominal Co_{40}:Fe_{30}:Pd_{30} (at.%), Alloy 10, as-cast condition.

Phase description	Co	Fe	Pd	Phase
Overall	37.5 ± 0.1	29.0 ± 0.1	33.5 ± 0.1	-
Dark	38.5 ± 0.1	29.5 ± 0.3	32.0 ± 0.3	A1 (γFe,αCo, Pd)
Light	35.6 ± 0.5	27.7 ± 1.0	36.7 ± 0.7	A1 (γFe,αCo, Pd)
Globules	37.1 ± 0.8	28.6 ± 0.7	34.3 ± 0.9	A1 (γFe,αCo, Pd)
Matrix	28.4 ± 0.2	29.1 ± 0.4	32.5 ± 0.3	A1 (γFe,αCo, Pd)

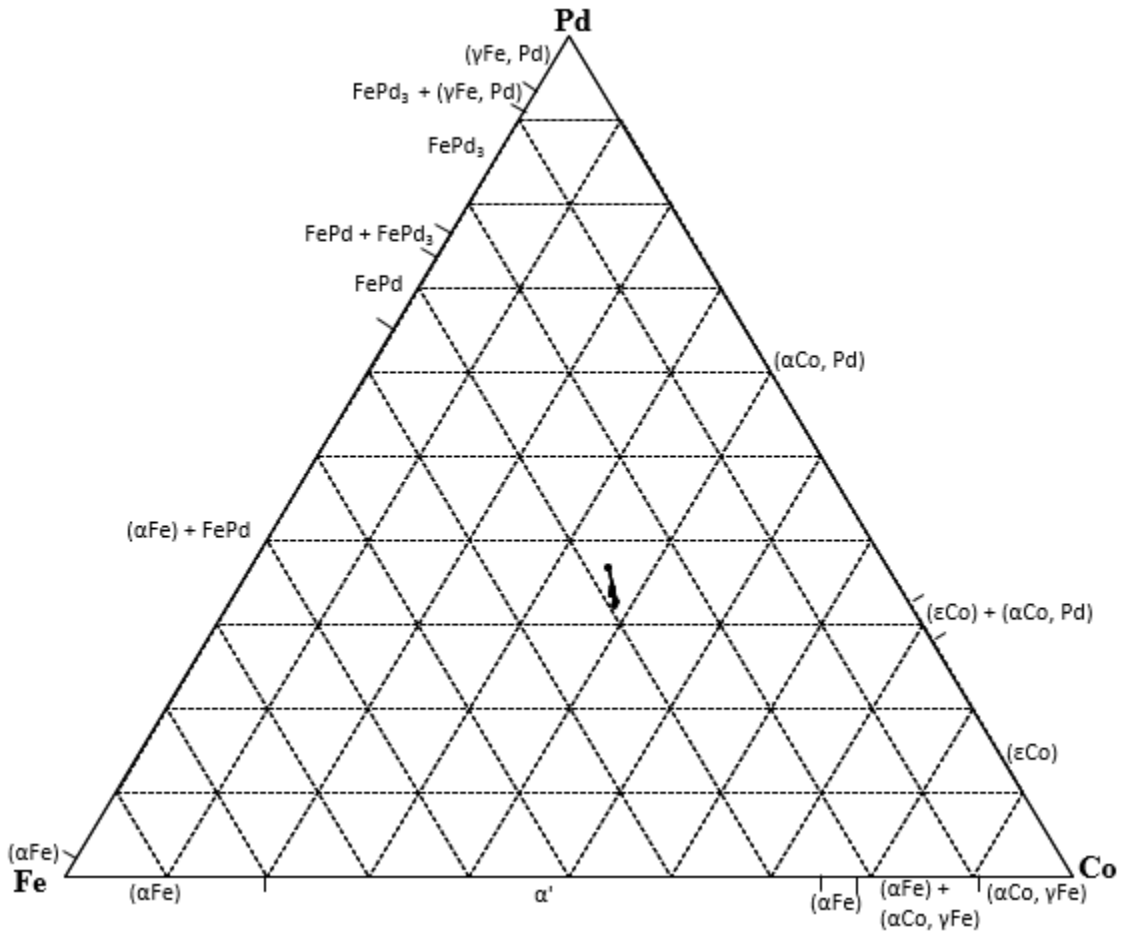


Figure 4.29. EDX analyses of nominal Co_{40}:Fe_{30}:Pd_{30} (at.%), Alloy 10 as-cast condition. (■ Overall composition; ● phases)

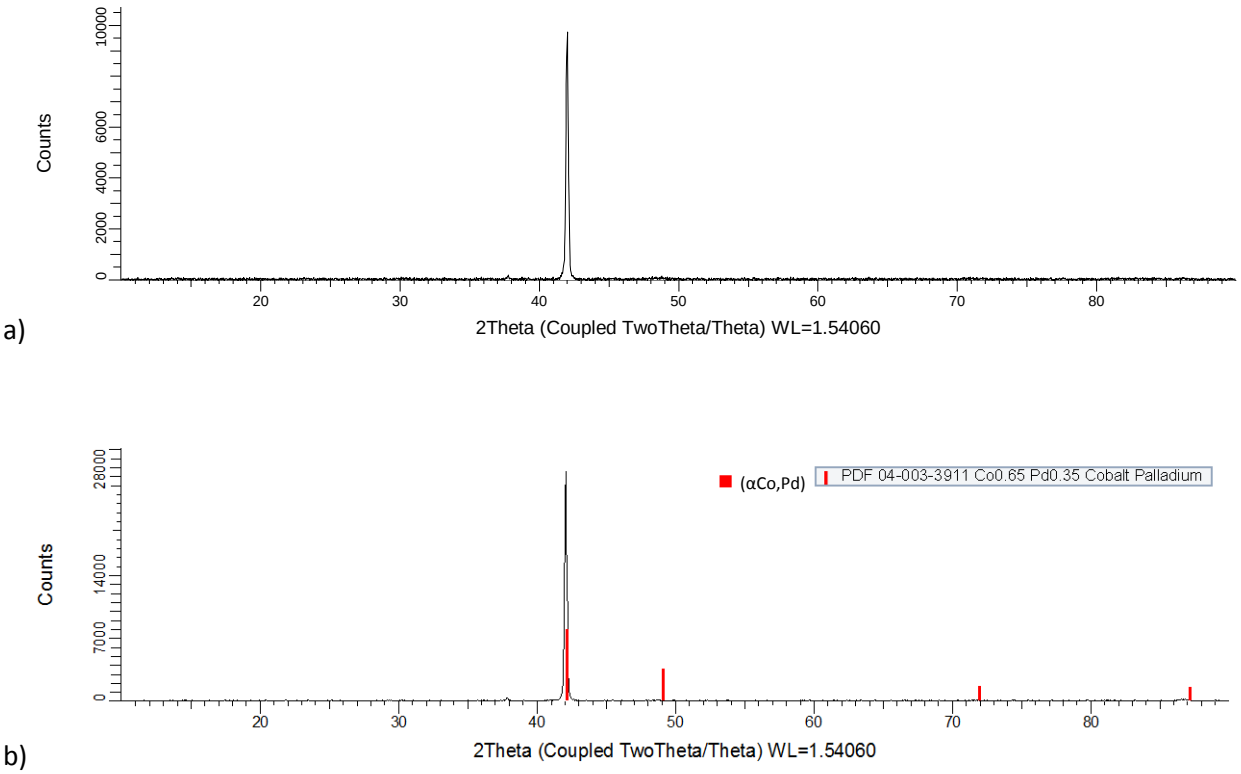


Figure 4.30. XRD patterns for nominal Co_{40}:Fe_{30}:Pd_{30} (at.%), Alloy 10 as-cast condition: a) raw, and b) labelled.

4.1.11. Alloy 11: Nominal Co_{20}:Fe_{60}:Pd_{20} (at.%)

Figure 4.31 (Alloy 11: Nominal Co_{20}:Fe_{60}:Pd_{20} (at.%)) shows dendrites surrounded by a matrix. The dendrites appear to have a phase etched out of them, leaving irregular Widmanstätten precipitates. The matrix had less Fe and more Pd than the dendrites, Table 4.11 and Figure 4.32. The XRD pattern (Figure 4.33) was very poor, being very noisy with low peak counts, and having one unresolvable peak at ~80° (2 Theta).

The main phase formed by the following reaction:

$$L \rightarrow A1\ (\gamma Fe,\alpha Co,Pd).$$

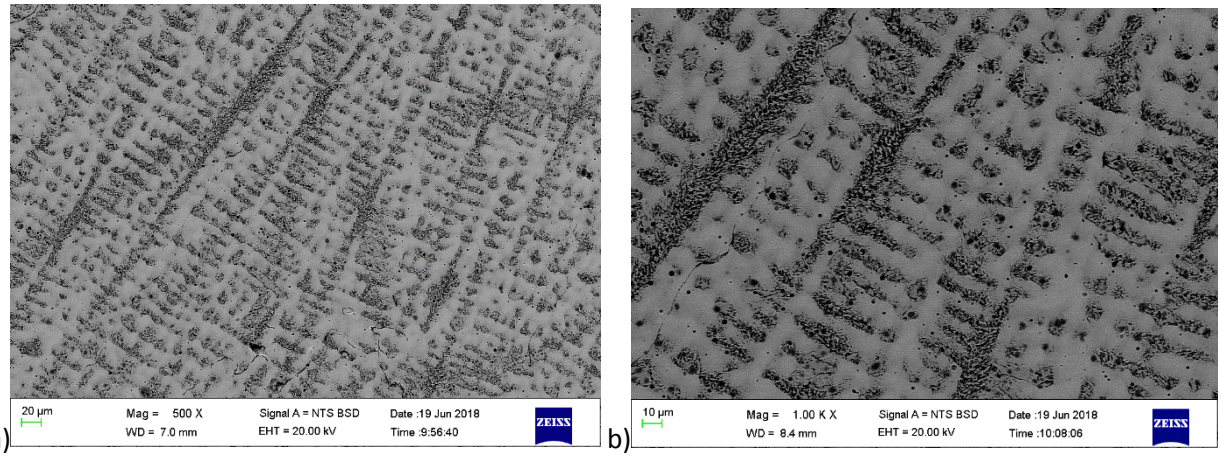


Figure 4.31. SEM-BSE images of as-cast Co_{20}:Fe_{60}:Pd_{20} (at.%), Alloy 11 showing the formation of dendrites surrounded by a matrix a) low magnification and b) higher magnification.

Table 4.11. EDX phase analyses for nominal Co_{20}:Fe_{60}:Pd_{20} (at.%), Alloy 11, as-cast condition.

Phase description	Co	Fe	Pd	Phase
Overall	19.0 ± 0.1	58.6 ± 0.1	22.4 ± 0.1	-
Dendrite (inner dark)	19.3 ± 0.2	58.4 ± 0.5	22.3 ± 0.7	A1 (γFe,αCo, Pd)
Matrix (light)	18.6 ± 0.2	56.6 ± 0.8	24.8 ± 1.0	A1 (γFe,αCo, Pd)

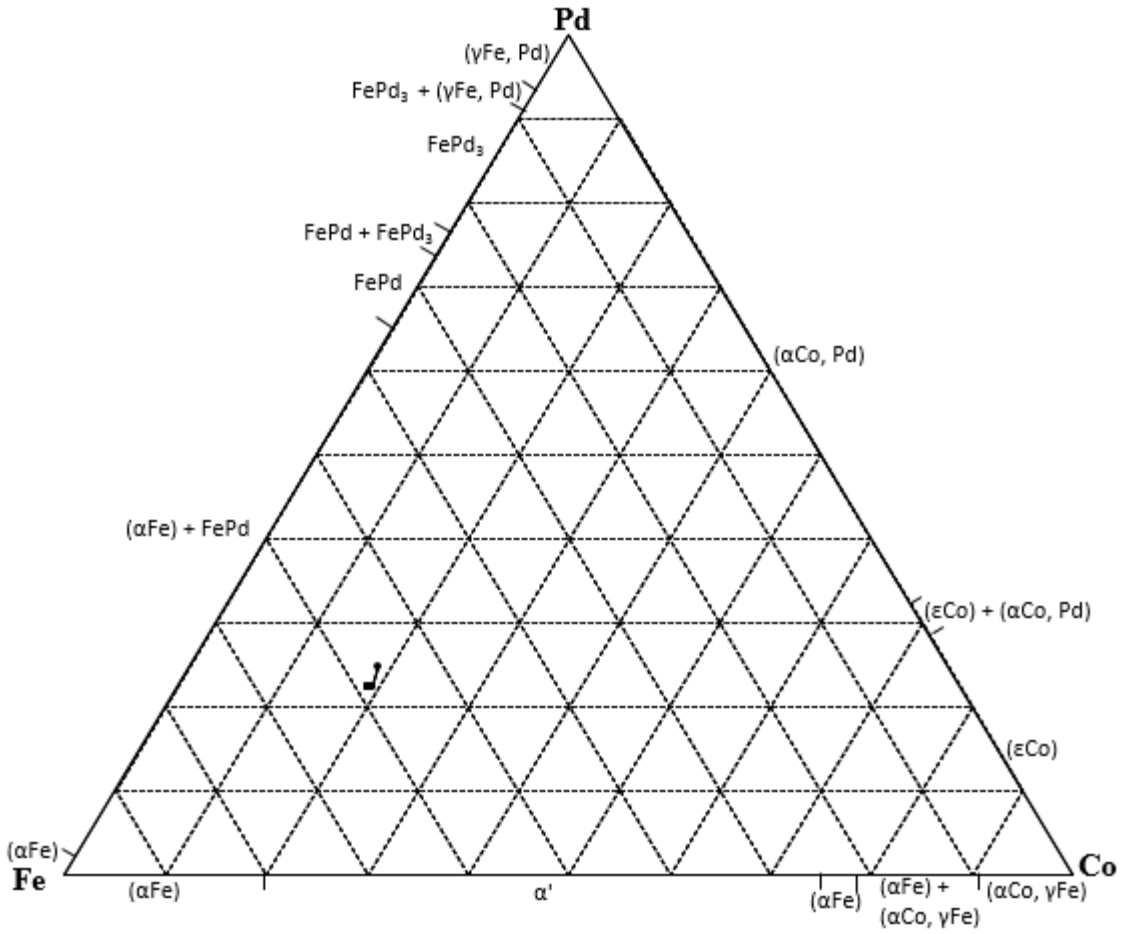


Figure 4.32. EDX analyses of nominal Co_{20}:Fe_{60}:Pd_{20} (at.%), Alloy 11 as-cast condition. (■ Overall composition; ● phases)

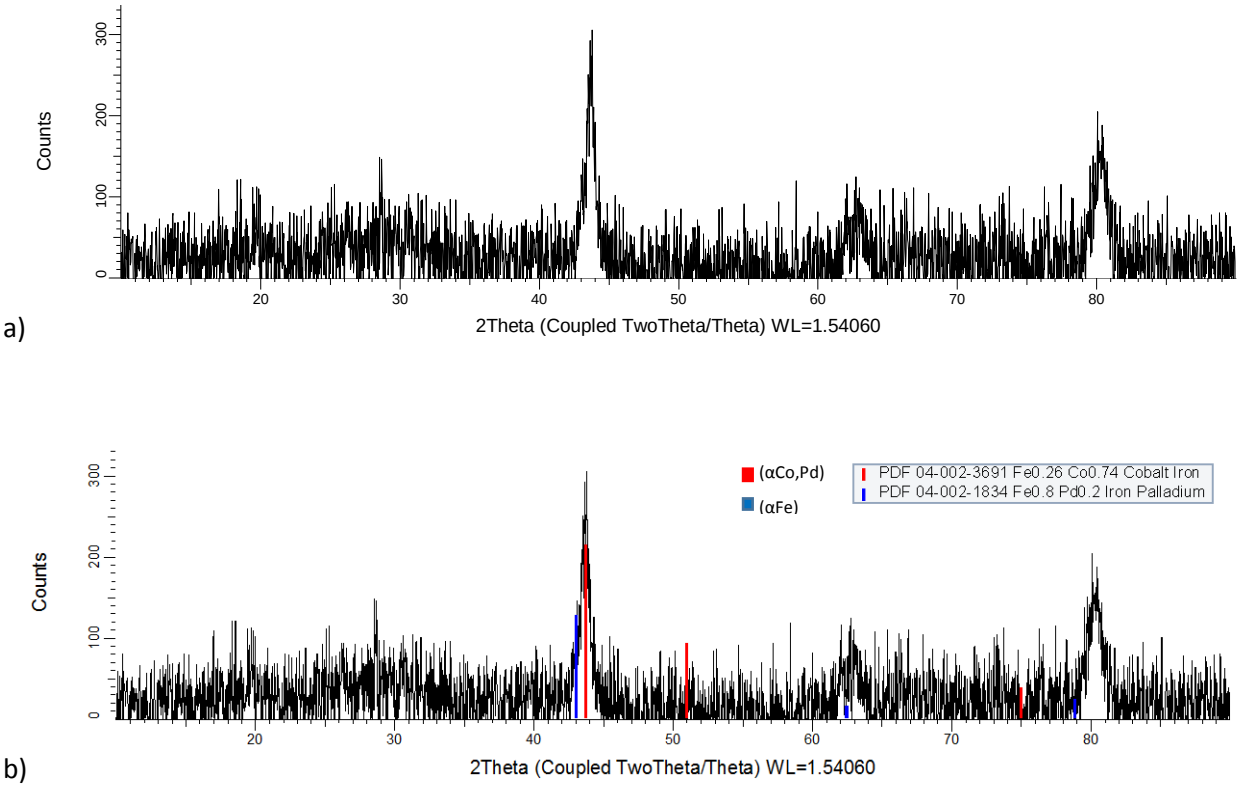


Figure 4.33. XRD patterns for nominal Co_{20}:Fe_{60}:Pd_{20} (at.%), Alloy 11 as-cast condition: a) raw, and b) labelled.

4.1.12. Alloy 12: Nominal Co_{60}:Fe_{20}:Pd_{20} (at.%)

For Alloy 12, Nominal Co_{60}:Fe_{20}:Pd_{20} (at.%), the dendrites are shown in Figure 4.34, and they were surrounded by a lighter phase and pores. The composition of the dendrites had more Co and less Pd than the light matrix phase, Figure 4.35 and Table 4.12. The XRD pattern, Figure 4.36 had an unidentified peak at ~73° (2 Theta), which could have been a shifted A1 peak.

The phases formed by the following reactions:

$$L \rightarrow A1\ (\gamma Fe,\alpha Co,Pd)$$

$$A1\ (\gamma Fe,\alpha Co,Pd) \rightarrow A1\ (\gamma Fe,\alpha Co,Pd) + (\alpha Fe)$$

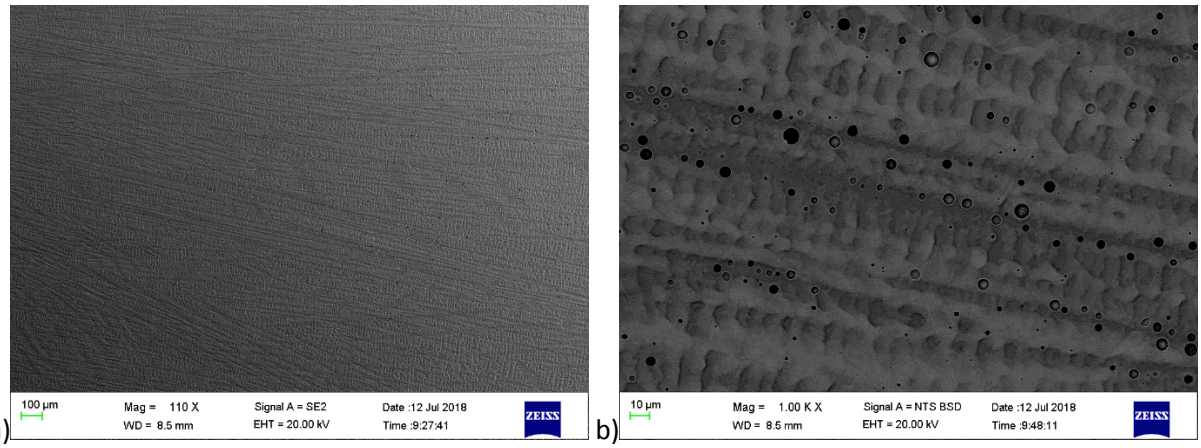


Figure 4.34. SEM-BSE images of as-cast Co_{60}:Fe_{20}:Pd_{20} (at.%), Alloy 12 showing dendrites surrounded by a lighter grey phase and porosity.

Table 4.12. EDX phase analyses for nominal Co_{60}:Fe_{20}:Pd_{20} (at.%), Alloy 12, as-cast condition.

Phase description	Co	Fe	Pd	Phase
Overall	58.2 ± 0.2	19.4 ± 0.2	22.4 ± 0.1	-
Light	52.7 ± 0.5	18.5 ± 0.1	28.8 ± 0.5	A1 (γFe,αCo,Pd)
Inner dendrite	63.3 ± 0.3	19.1 ± 0.1	17.6 ± 0.3	A1 (γFe,αCo,Pd) + (αFe)

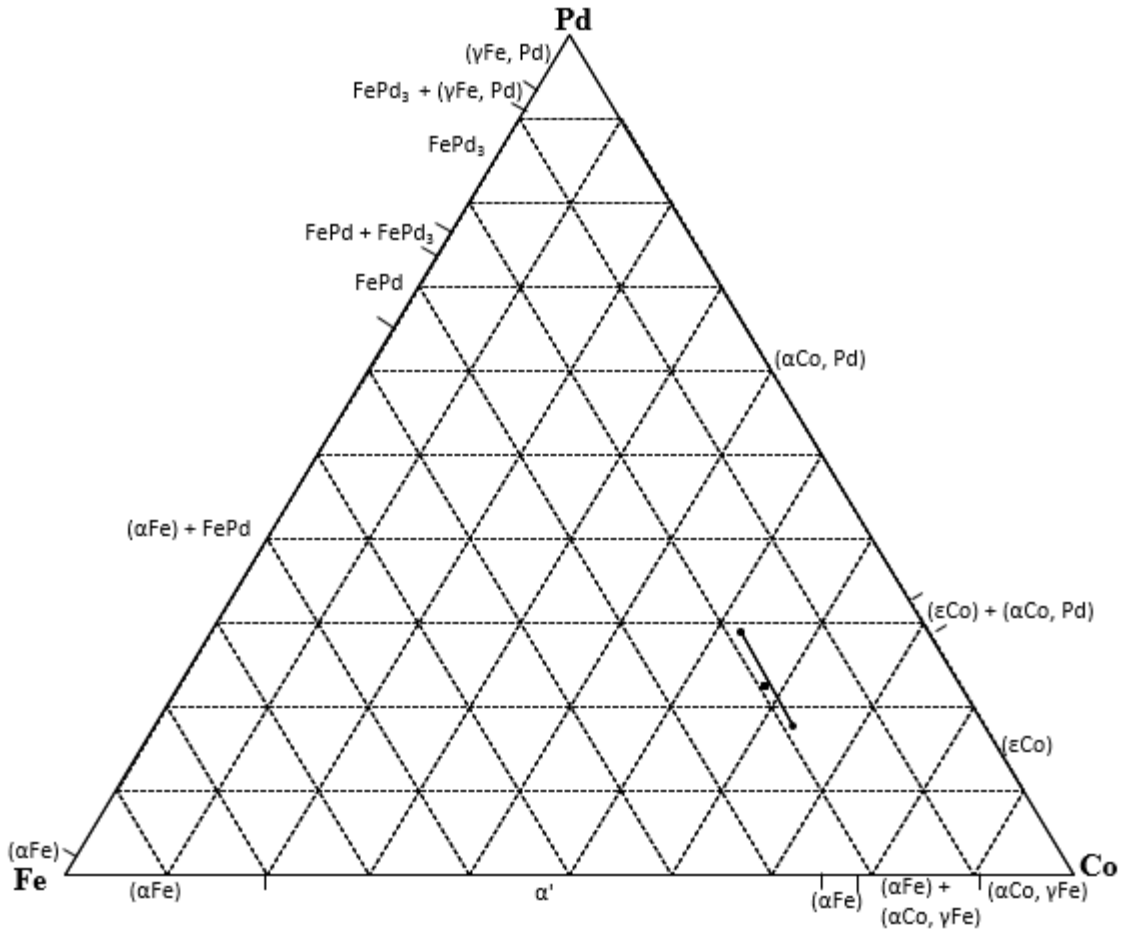


Figure 4.35. EDX analyses of nominal Co_{60}:Fe_{20}:Pd_{20} (at.%), Alloy 12 as-cast condition. (■ Overall composition; ● phases)

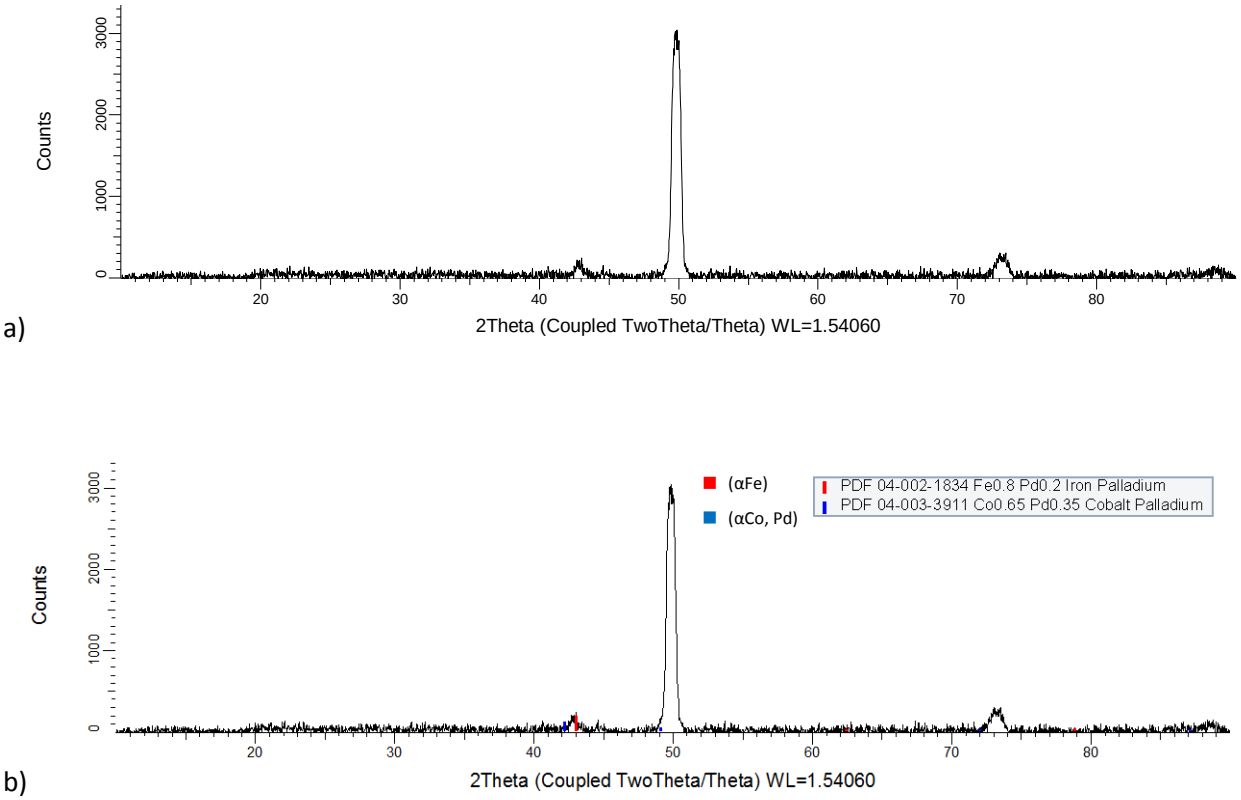


Figure 4.36. XRD patterns for nominal Co_{60}:Fe_{20}:Pd_{20} (at.%), Alloy 12 as-cast condition: a) raw, and b) labelled.

4.2. Samples annealed at 1000°C

4.2.1. Alloy 1: Nominal Co_{30}:Fe_{60}:Pd_{10} (at.%)

Figure 4.37 (Alloy 1, Nominal Co_{30}:Fe_{60}:Pd_{10} (at.%)) shows different colonies with lamellar microstructures. The spacing between the lamellae varied in different areas of the sample, although the compositions of the different areas were very similar (Table 4.13 and Figure 4.38), showing it was an orientation effect. Figure 4.39 shows the XRD results, the two phases present were (αFe) (bcc) and (γFe, Pd) (fcc), actually A1 (γFe,αCo,Pd). The 1000°C annealed phases identified by XRD results were the same as the as-cast results for this alloy.

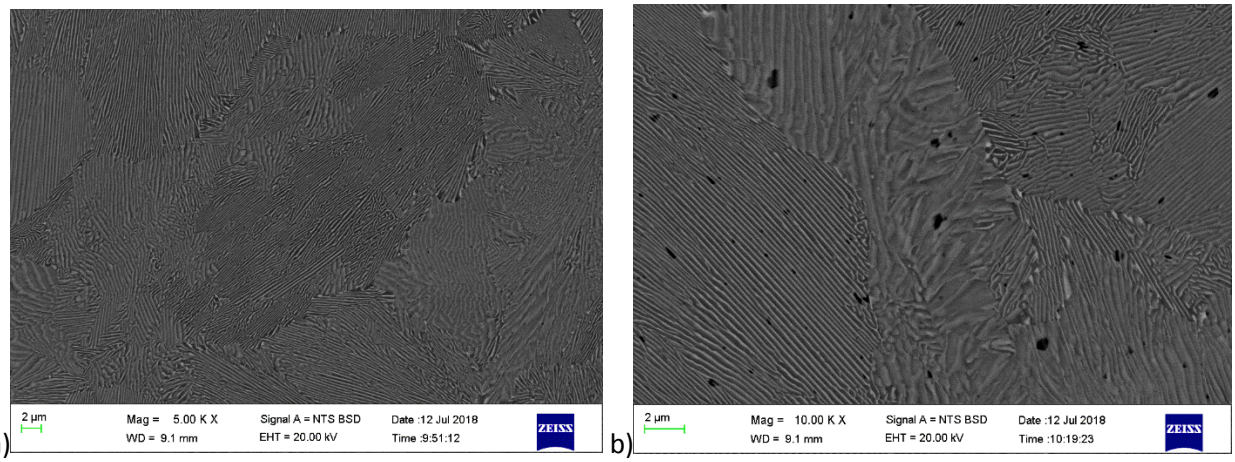


Figure 4.37. SEM-BSE images of Co_{30}:Fe_{60}:Pd_{10} (at.%), Alloy 1 annealed at 1000°C for 1000 h showing: a) the lamellar microstructure and b) at higher magnification.

Table 4.13. EDX phase analyses for nominal Co_{30}:Fe_{60}:Pd_{10} (at.%), Alloy 1, annealed at 1000°C condition.

Phase description	Co	Fe	Pd	Phase
Overall	29.1 ± 0.2	59.6 ± 0.2	11.3 ± 0.1	-
Coarse lamellae	28.9 ± 0.2	59.2 ± 0.1	11.9 ± 0.1	(αFe) + A1 (γFe,αCo,Pd)
Fine lamellae	28.9 ± 0.1	59.2 ± 0.2	11.9 ± 0.2	(αFe) + A1 (γFe,αCo,Pd)

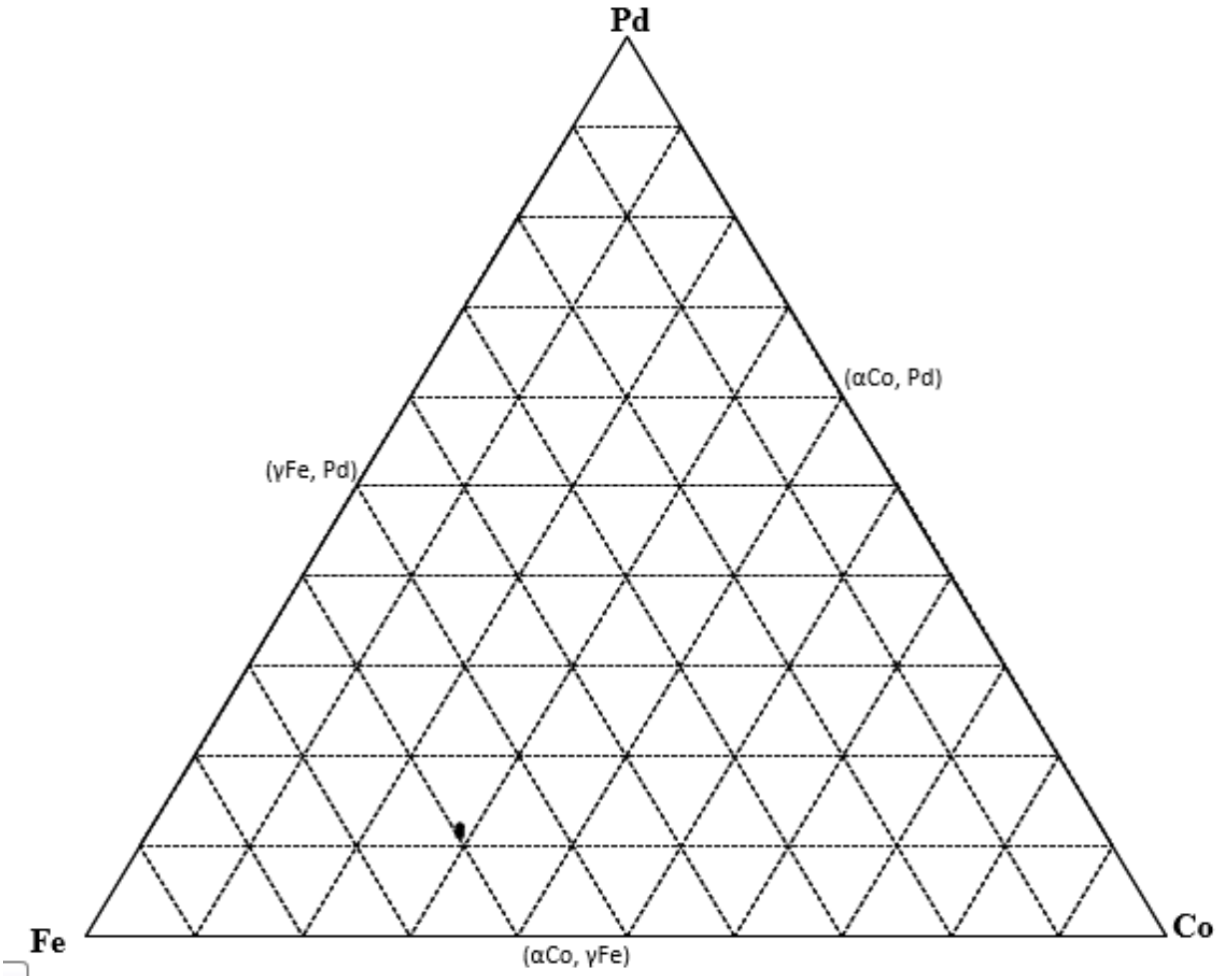


Figure 4.38. EDX analyses of nominal Co_{30}:Fe_{60}:Pd_{10} (at.%), Alloy 1 1000°C annealed condition. (■ Overall composition; ● phases).

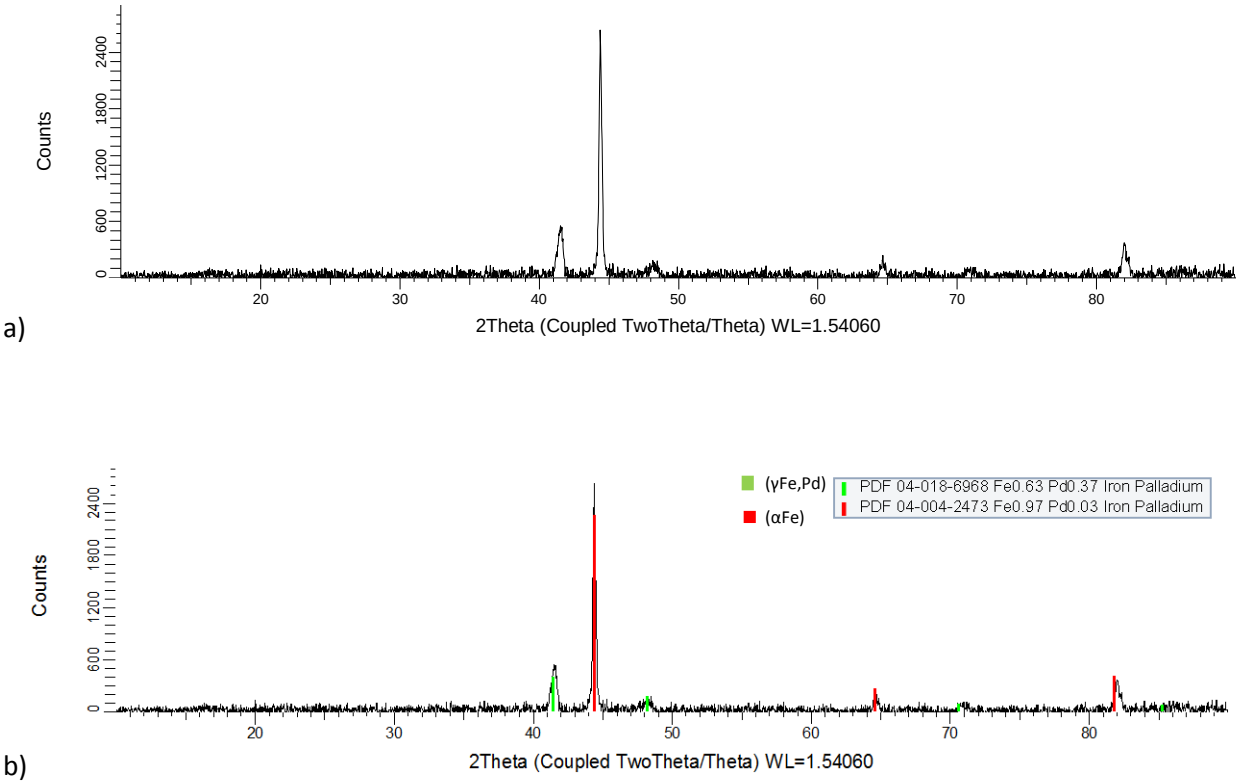


Figure 4.39. XRD patterns for nominal Co_{30}:Fe_{60}:Pd_{10} (at.%), Alloy 1 1000°C annealed condition: a) raw, and b) labelled.

4.2.2. Alloy 2: Nominal Co_6:Fe_{44}:Pd_{50} (at.%)

For Alloy 2, Nominal Co_6:Fe_{44}:Pd_{50} (at.%) had regions which etched differently, within the solid solution, Figure 4.40. Figure 4.41 and Table 4.14 shows the similarity of compositions of those different areas. The XRD results (Figure 4.42) showed that the solid solution was A1 (γFe,αCo,Pd), with large shifts, especially at higher angles, and the highest peak was much higher due to preferred orientation which had not been annealed out from the as-cast condition.

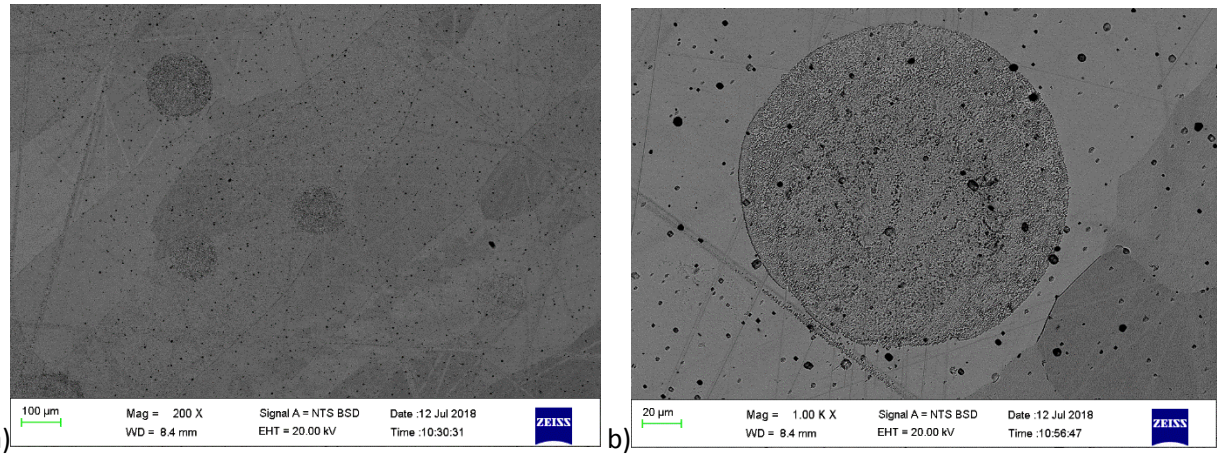


Figure 4.40. SEM-BSE images of Co_6:Fe_{44}:Pd_{50} (at.%), Alloy 2 annealed at 1000°C for 1000 h showing: a) differently etched areas, and b) a better etched area at higher magnification.

Table 4.14. EDX phase analyses for nominal Co_6:Fe_{44}:Pd_{50} (at.%), Alloy 2, annealed at 1000°C condition.

Phase description	Co	Fe	Pd	Phase
Overall	5.9 ± 0.1	41.0 ± 0.2	53.1 ± 0.2	-
Dark	5.9 ± 0.1	41.6 ± 0.1	52.5 ± 0.1	Cored A1 (γFe,αCo,Pd)
Light	6.0 ± 0.1	41.6 ± 0.1	52.4 ± 0.2	Cored A1 (γFe,αCo,Pd)

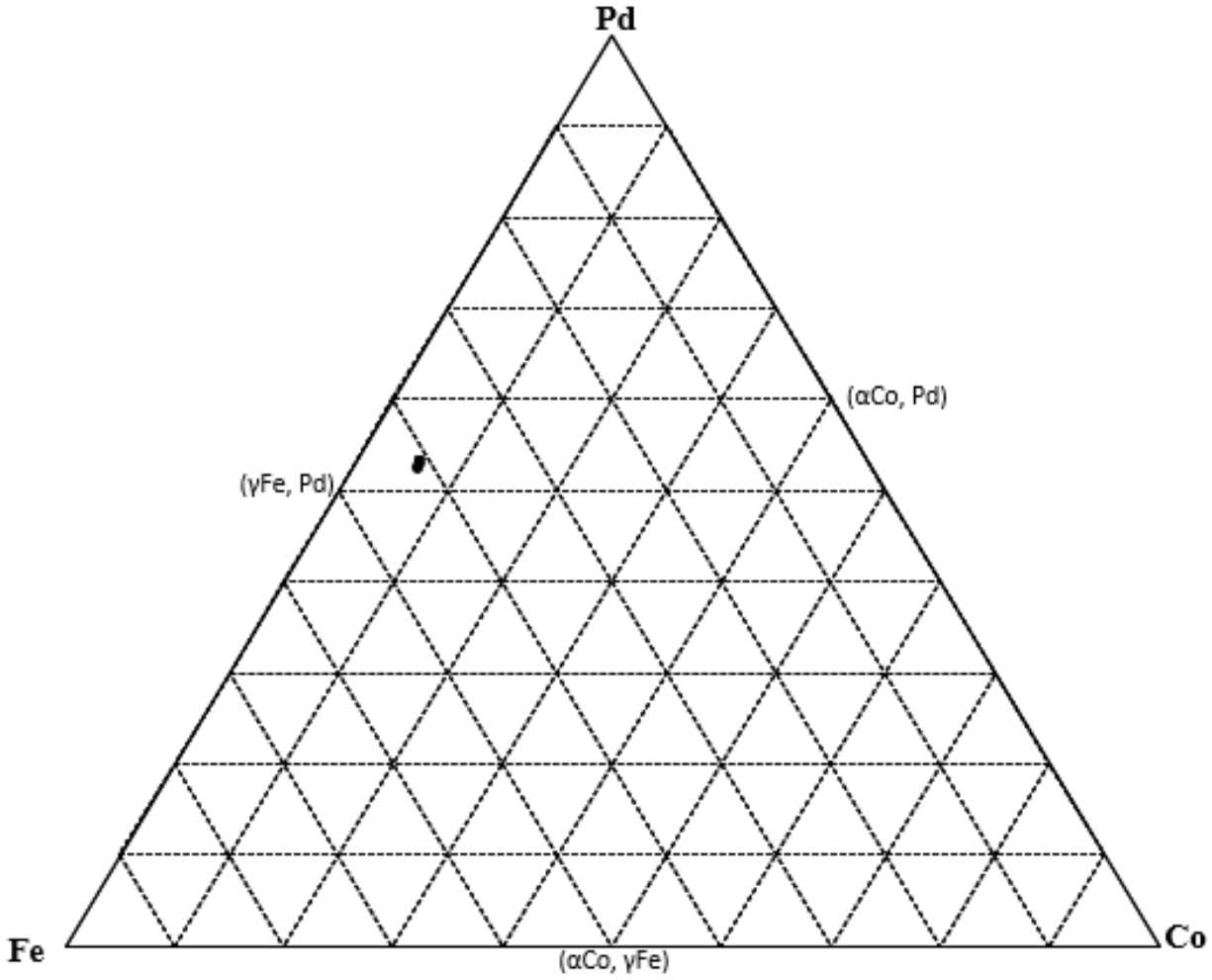


Figure 4.41. EDX analyses of nominal Co_6:Fe_{44}:Pd_{50} (at.%), Alloy 2 1000°C annealed condition. (■ Overall composition; ● phases)

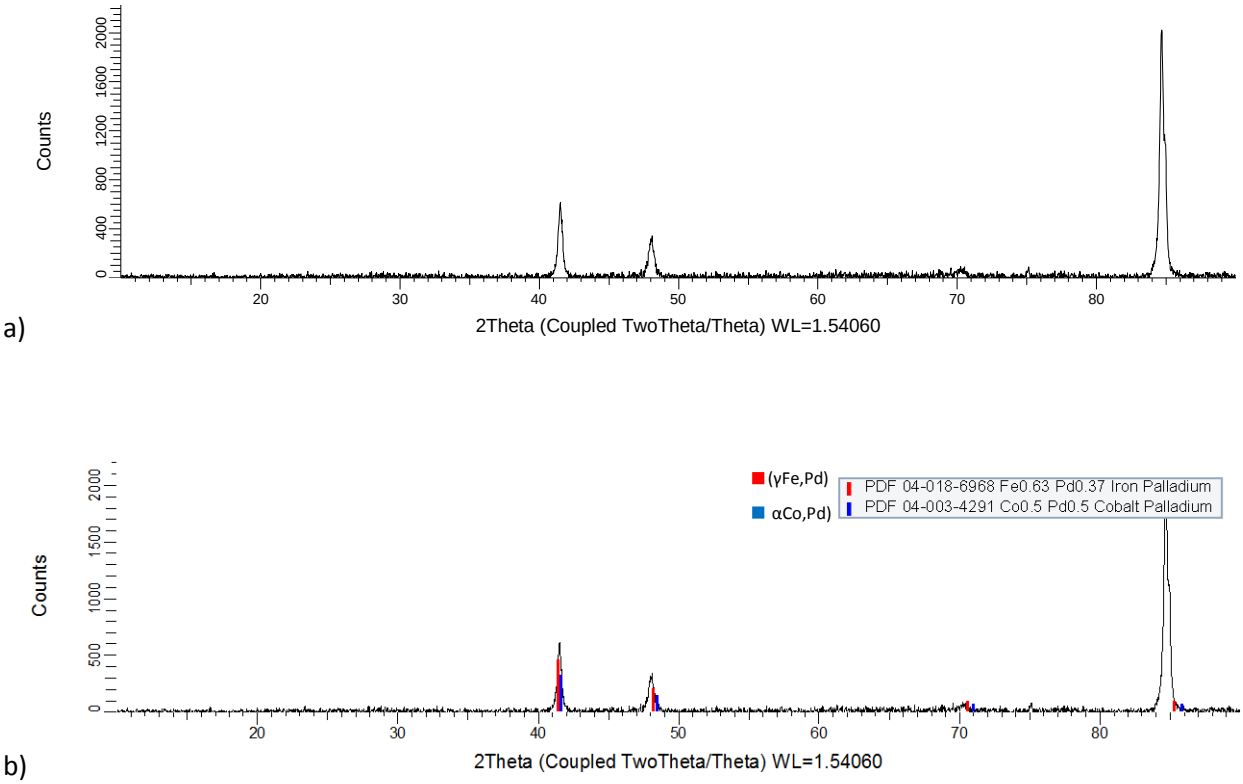


Figure 4.42. XRD patterns for nominal Co_6:Fe_{44}:Pd_{50} (at.%), Alloy 2 1000°C annealed condition: a) raw, and b) labelled.

4.2.3. Alloy 3: Nominal Co_{20}:Fe_{50}:Pd_{30} (at.%)

Alloy 3, Nominal Co_{20}:Fe_{50}:Pd_{30} (at.%) shown in Figure 4.43 had fine two-phase areas surrounded by the A1 (γFe,αCo,Pd) solid solution. Table 4.15 and Figure 4.44 shows that the two-phase area had more Pd and less Co than the surrounding A1 solid solution. The XRD results, Figure 4.45, showed that there was A1 (γFe,αCo,Pd) present, although the two-phase region was only a small proportion (less than 4 volume percent) of the sample and would not have been identified by XRD.

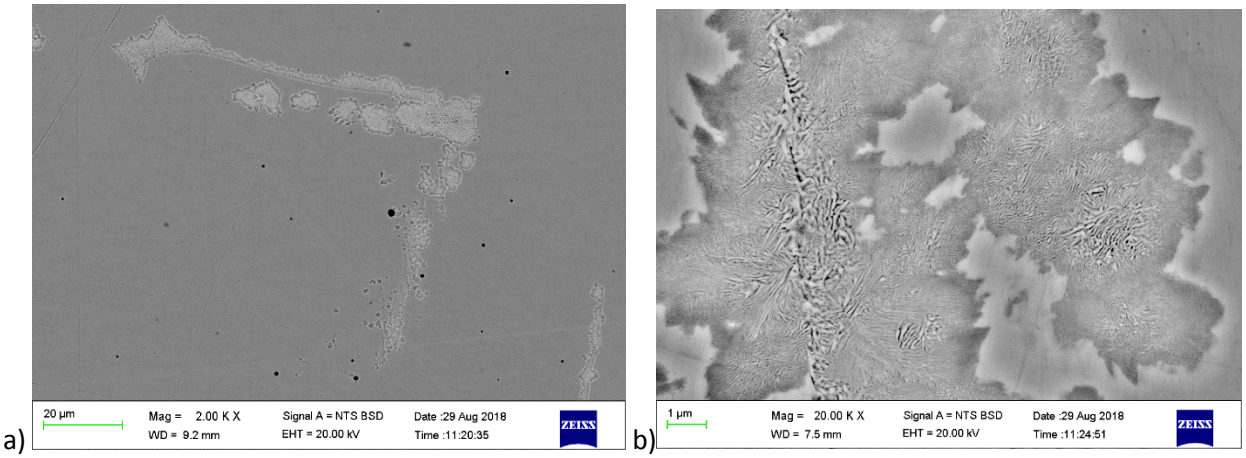


Figure 4.43. SEM-BSE images of Co_{20}:Fe_{50}:Pd_{30} (at.%), Alloy 3 annealed at 1000°C for 1000 h showing: a) an etched area, and b) two-phase area at higher magnification.

Table 4.15. EDX phase analyses for nominal Co_{20}:Fe_{50}:Pd_{30} (at.%), Alloy 3, annealed at 1000°C condition.

Phase description	Co	Fe	Pd	Phase
Overall	18.7 ± 0.1	48.5 ± 0.2	32.8 ± 0.1	-
Two-phase region	7.3 ± 0.7	39.5 ± 1.1	53.2 ± 1.8	(αFe) + A1 (γFe,αCo,Pd)
Surrounding area	18.9 ± 0.1	48.2 ± 0.2	32.9 ± 0.1	A1 (γFe,αCo,Pd)

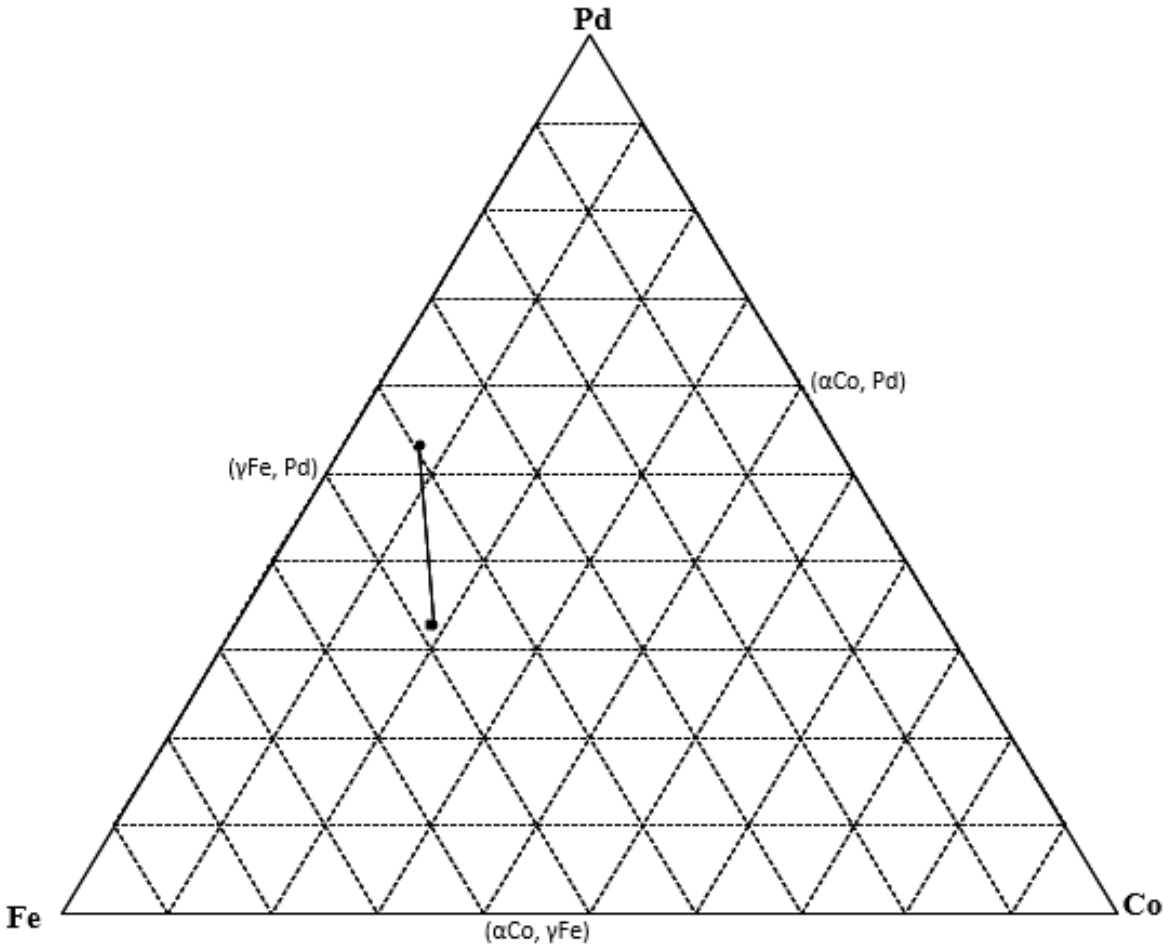


Figure 4.44. EDX analyses of nominal Co_{20}:Fe_{50}:Pd_{30} (at.%), Alloy 3 1000°C annealed condition. (■ Overall composition; ● phases)

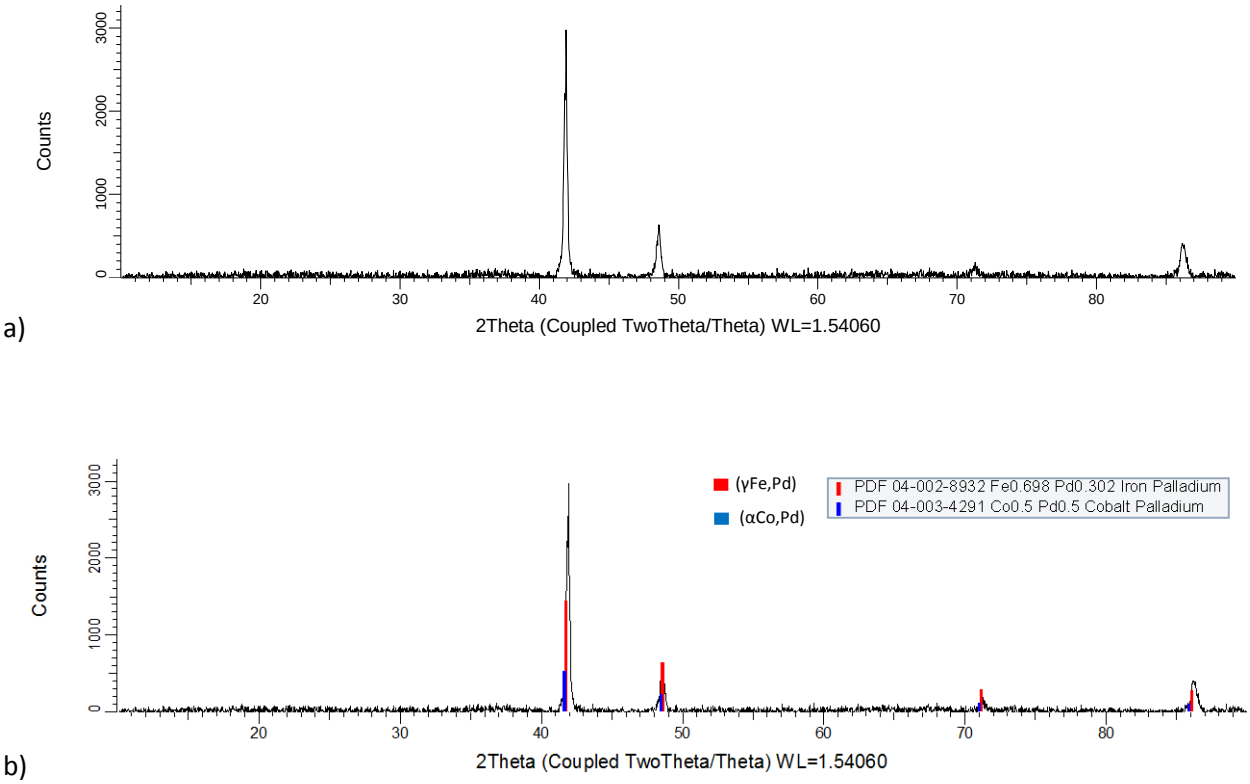


Figure 4.45. XRD patterns for nominal Co_{20}:Fe_{50}:Pd_{30} (at.%), Alloy 3 1000°C annealed condition: a) raw, and b) labelled.

4.2.4. Alloy 4: Nominal Co_{10}:Fe_{15}:Pd_{75} (at.%)

The microstructure of Alloy 4, Nominal Co_{10}:Fe_{15}:Pd_{75} (at.%) Figure 4.46, showed light and dark areas. The composition of the two areas were very similar (Table 4.16), and the different contrasts were due to the different orientations of the grains, Figure 4.47. There were small precipitates on the grain boundaries and within the grains. The XRD results shown in Figure 4.48 indicated that there was one phase present, A1 (γFe,αCo,Pd).

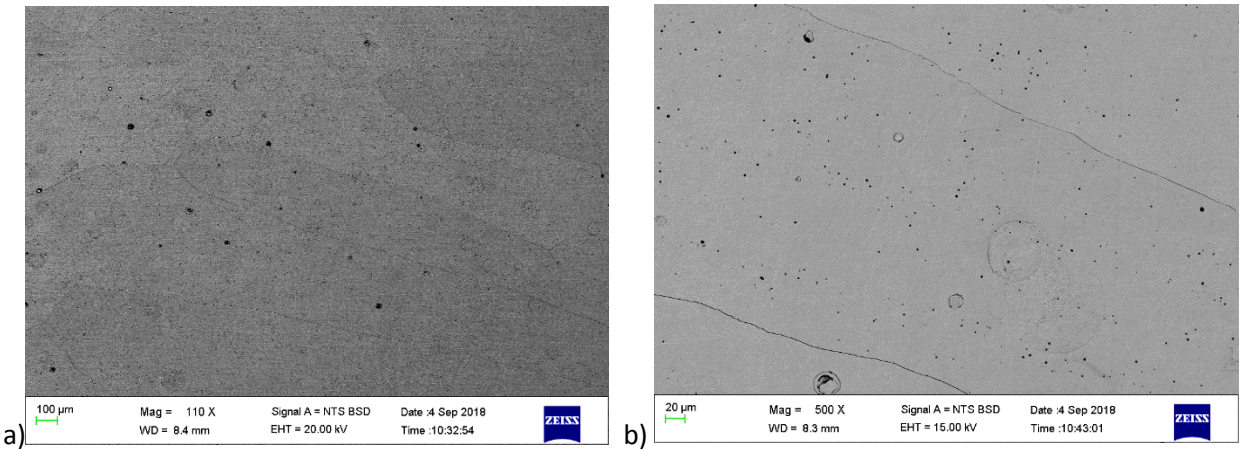


Figure 4.46. SEM-BSE images of Co_{10}:Fe_{15}:Pd_{75} (at.%), Alloy 4 annealed at 1000°C for 1000 h showing: a) grains of different contrast, and b) grain boundaries, ~$FePd_3$ precipitates and a region of different composition.

Table 4.16. EDX phase analyses for nominal Co_{10}:Fe_{15}:Pd_{75} (at.%), Alloy 4, annealed at 1000°C condition.

Phase description	Co	Fe	Pd	Phase
Overall	9.1 ± 0.0	14.0 ± 0.1	76.9 ± 0.1	-
Dark	8.9 ± 0.2	13.6 ± 0.2	77.5 ± 0.4	A1 (γFe,αCo,Pd)
Light	8.9 ± 0.2	14.0 ± 0.2	77.1 ± 0.2	A1 (γFe,αCo,Pd)

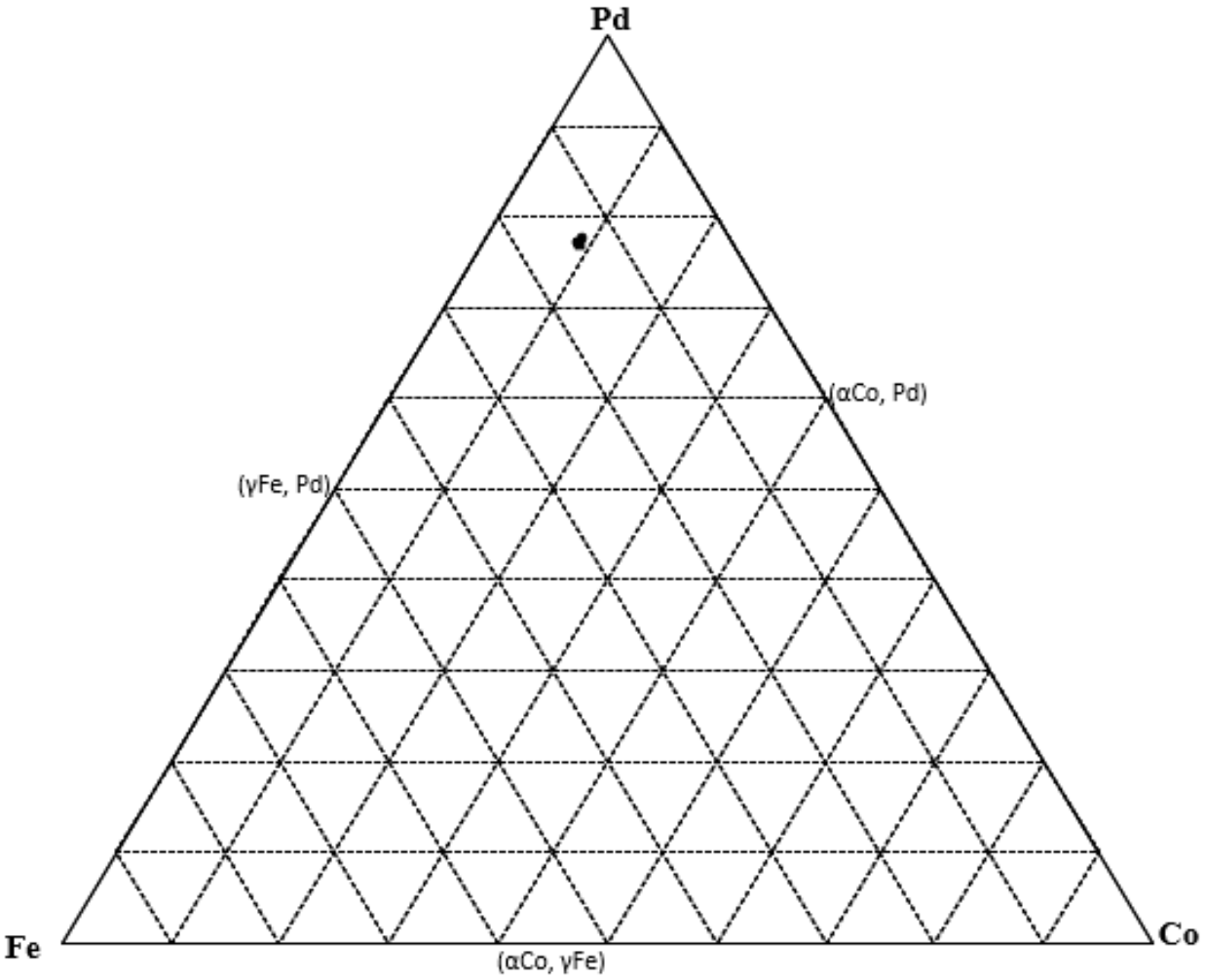
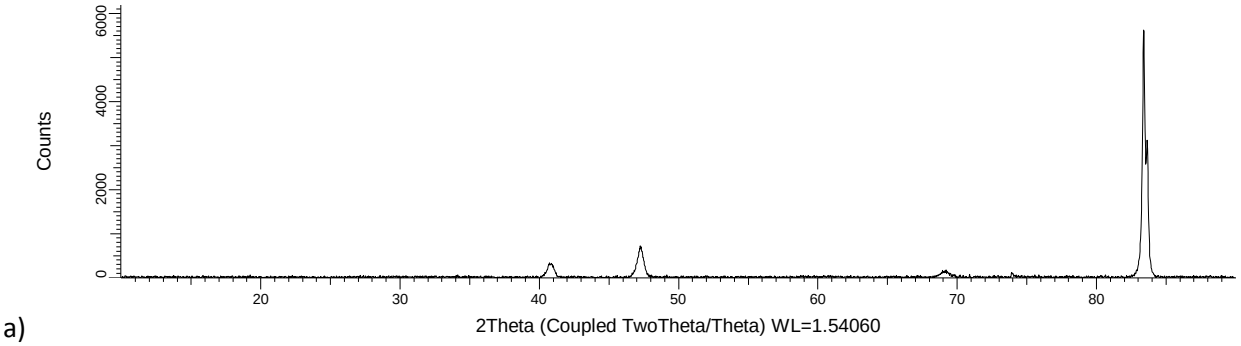
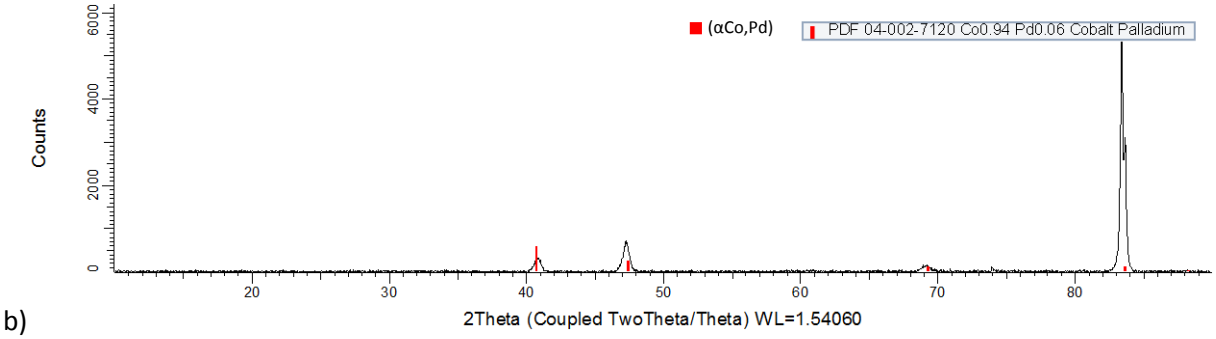


Figure 4.47. EDX analyses of nominal Co_{10}:Fe_{15}:Pd_{75} (at.%), Alloy 4 1000°C annealed condition. (■ Overall composition; ● phases)



a)



b)

Figure 4.48. XRD patterns for nominal Co_{10}:Fe_{15}:Pd_{75} (at.%), Alloy 4 1000°C annealed condition: a) raw, and b) labelled.

4.2.5. Alloy 5: Nominal Fe_{30}:Co_{30}:Pd_{40} (at.%)

Alloy 5, Nominal Co_{30}:Fe_{30}:Pd_{40} (at.%), Figure 4.49 had areas which etched differently, where the microstructure could be seen more clearly (Figure 4.49 b)), showing fine grains in a darker matrix. The latter was too fine to analyse individually. The grains and the bulk of the matrix had similar compositions, Table 4.17 and Figure 4.50. The XRD results, Figure 4.51, showed one phase, A1 (γFe,αCo,Pd).

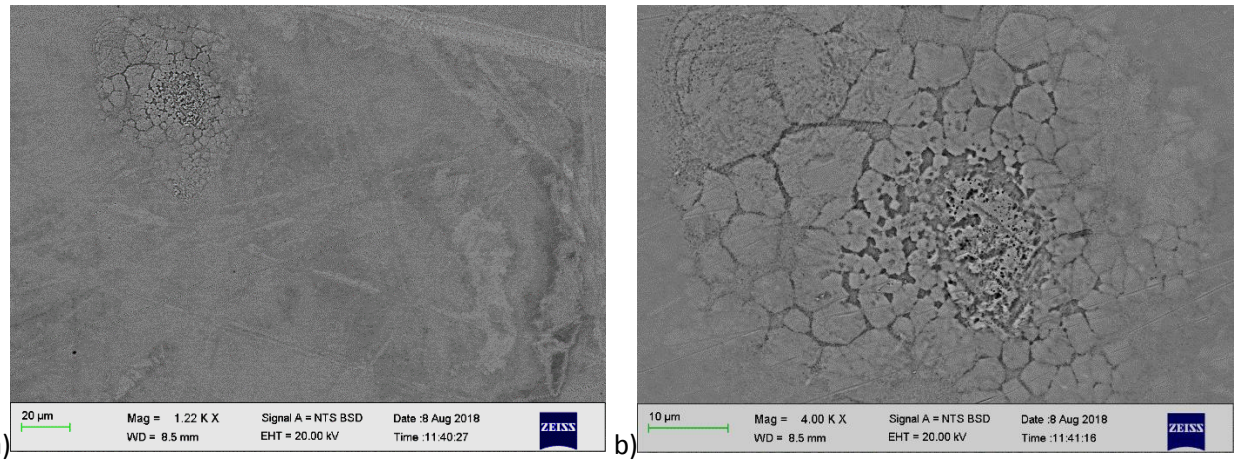


Figure 4.49. SEM-BSE images of Co_{30}:Fe_{30}:Pd_{40} (at.%), Alloy 5 annealed at 1000°C for 1000 h showing: a) light and dark areas, and b) a magnified patch that was etched.

Table 4.17. EDX phase analyses for nominal Co_{30}:Fe_{30}:Pd_{40} (at.%), Alloy 5, annealed at 1000°C condition.

Phase description	Co	Fe	Pd	Phase
Overall	28.2 ± 0.2	28.8 ± 0.1	43.0 ± 0.1	-
Fine grains	28.6 ± 0.2	28.5 ± 0.3	42.9 ± 0.2	A1 (γFe,αCo,Pd)
Surrounding area	28.7 ± 0.2	28.6 ± 0.2	42.7 ± 0.2	A1 (γFe,αCo,Pd)
Dark matrix	28.5 ± 1.9	27.6 ± 0.5	43.9 ± 1.6	A1 (γFe,αCo,Pd)

Data points may seem unclear in Figure 4.50 as there is a phase that has a very similar composition to the overall, hence the phase composition lies on the overall composition.

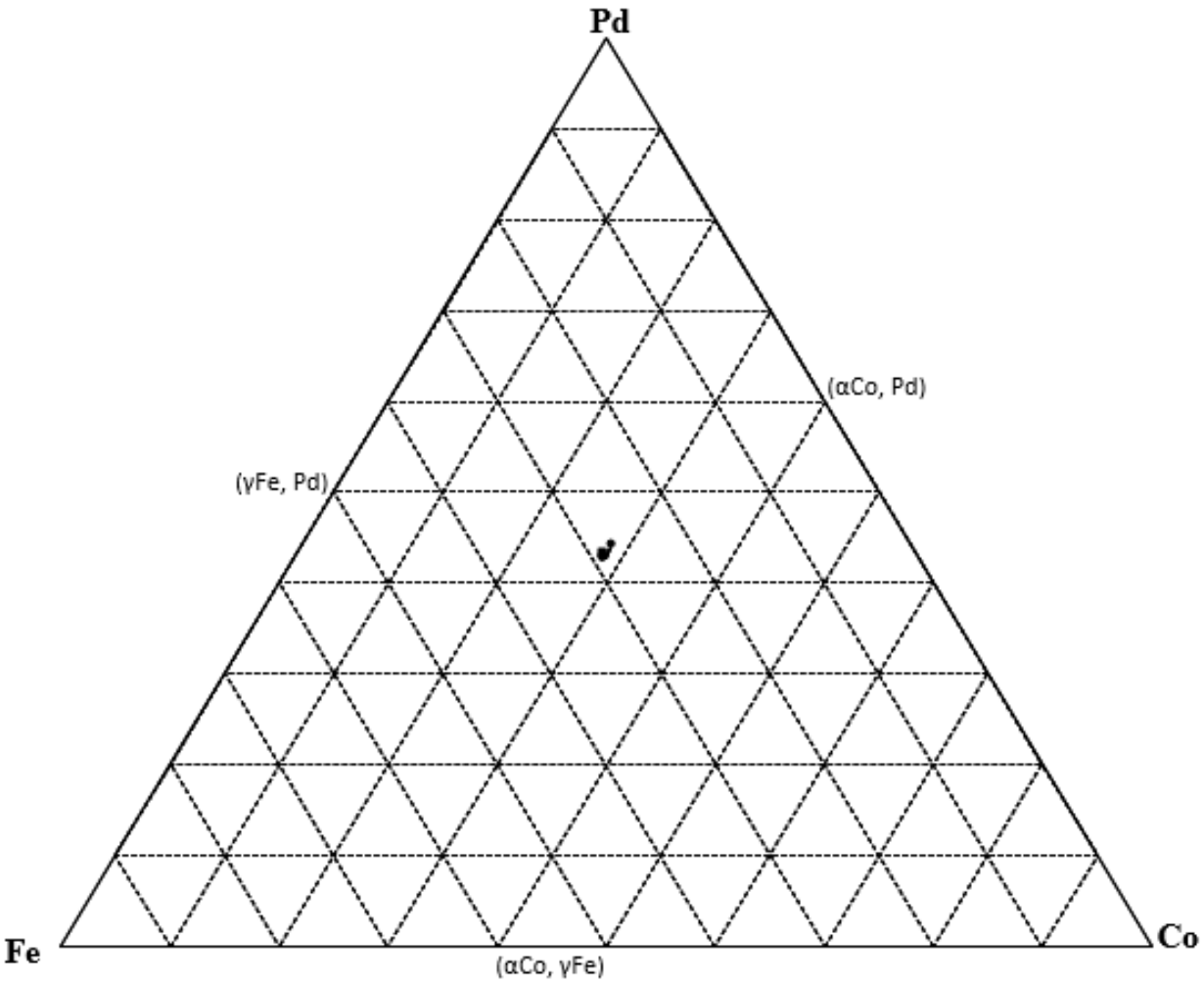


Figure 4.50. EDX analyses of nominal Co_{30}:Fe_{30}:Pd_{40} (at.%), Alloy 5 1000°C annealed condition. (■ Overall composition; ● phases)

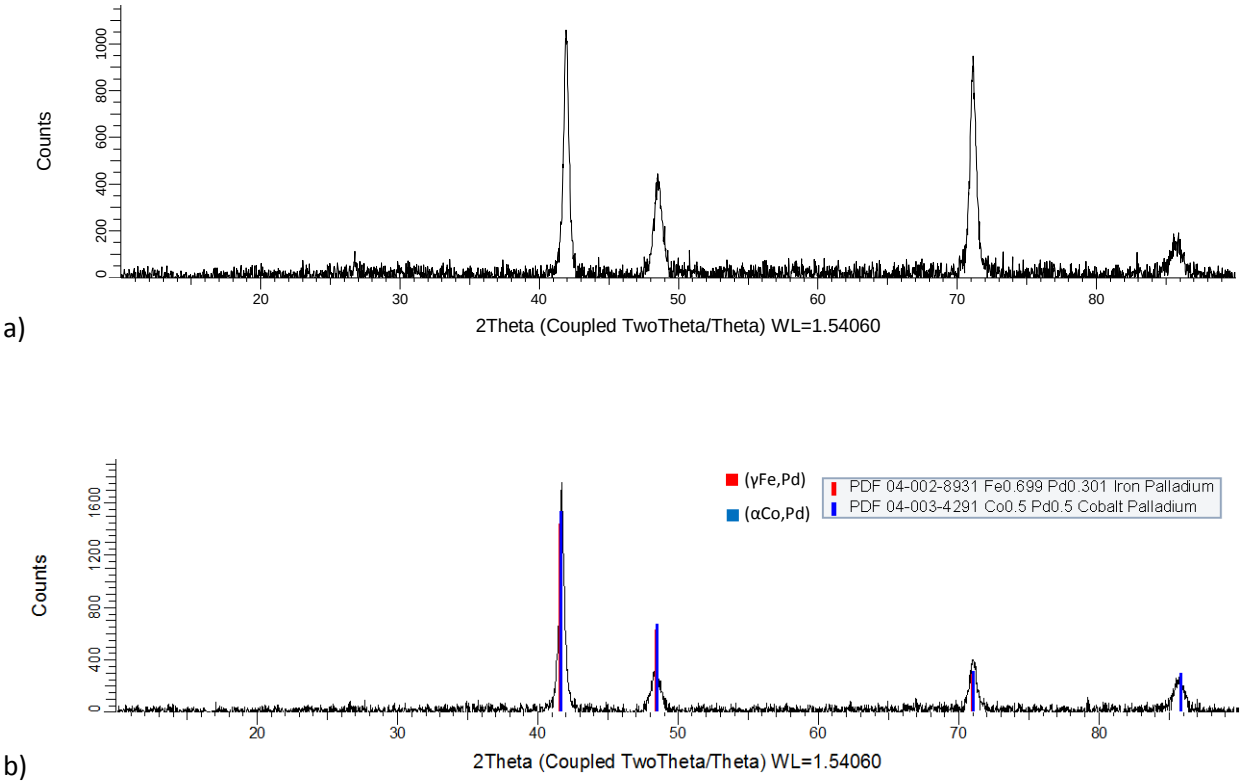


Figure 4.51. XRD patterns for nominal Co_{30}:Fe_{30}:Pd_{40} (at.%), Alloy 5 1000°C annealed condition: a) raw, and b) labelled.

4.2.6. Alloy 6: Nominal Co_{50}:Fe_{20}:Pd_{30} (at.%)

Figure 4.52b (Alloy 6, Nominal Co_{50}:Fe_{20}:Pd_{30} (at.%)) had a differently-etched area with grains and an irregular area which etched more clearly than the rest of the sample. The compositions were all very similar (Table 4.18 and Figure 4.53), although there were areas that etched more. Figure 4.54 shows one phase was present, A1 (γFe,αCo,Pd). The XRD pattern had very few peaks, with only one major peak, which was probably due to the preferred orientation not being annealed from as-cast sample, and was thus not of much use in phase identification. The first XRD scan was done for 10 minutes (Figure 4.54), and the XRD experiment was run for a longer period to see if the pattern quality would improve. The second test was done for 20 minutes, but there was no improvement.

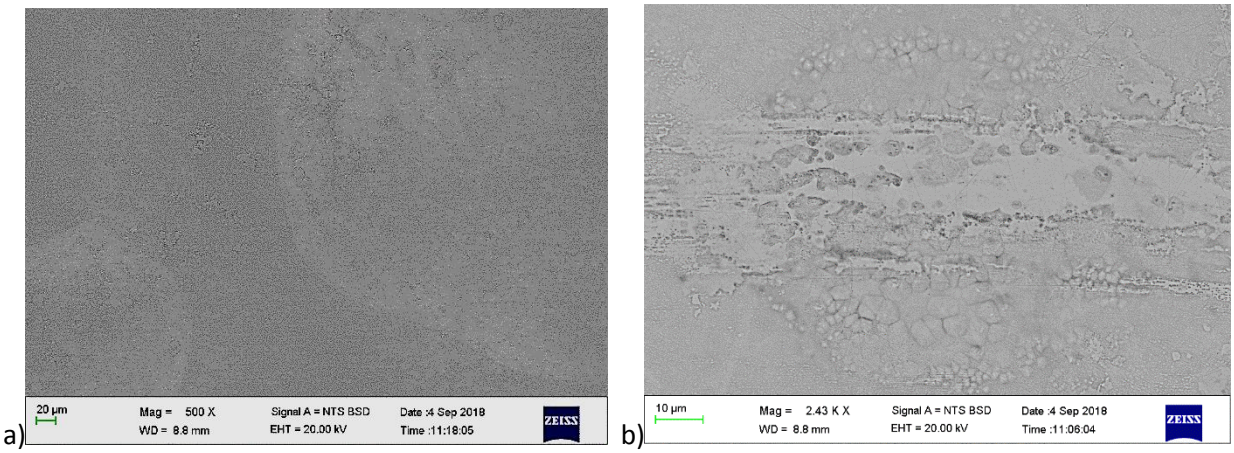


Figure 4.52. SEM-BSE images of Co_{50}:Fe_{20}:Pd_{30} (at.%), Alloy 6 annealed at 1000°C for 1000 h showing: a) at low magnification the overall area, and b) a better etched area.

Table 4.18. EDX phase analyses for nominal Co_{50}:Fe_{20}:Pd_{30} (at.%), Alloy 6, annealed at 1000°C condition.

Phase description	Co	Fe	Pd	Phase
Overall	48.4 ± 0.1	18.1 ± 0.1	33.5 ± 0.1	-
Irregular light area	47.8 ± 0.5	19.1 ± 0.1	33.1 ± 0.5	A1 (γFe,αCo,Pd)
Surrounding area	47.9 ± 0.8	19.2 ± 0.1	32.9 ± 0.8	A1 (γFe,αCo,Pd)

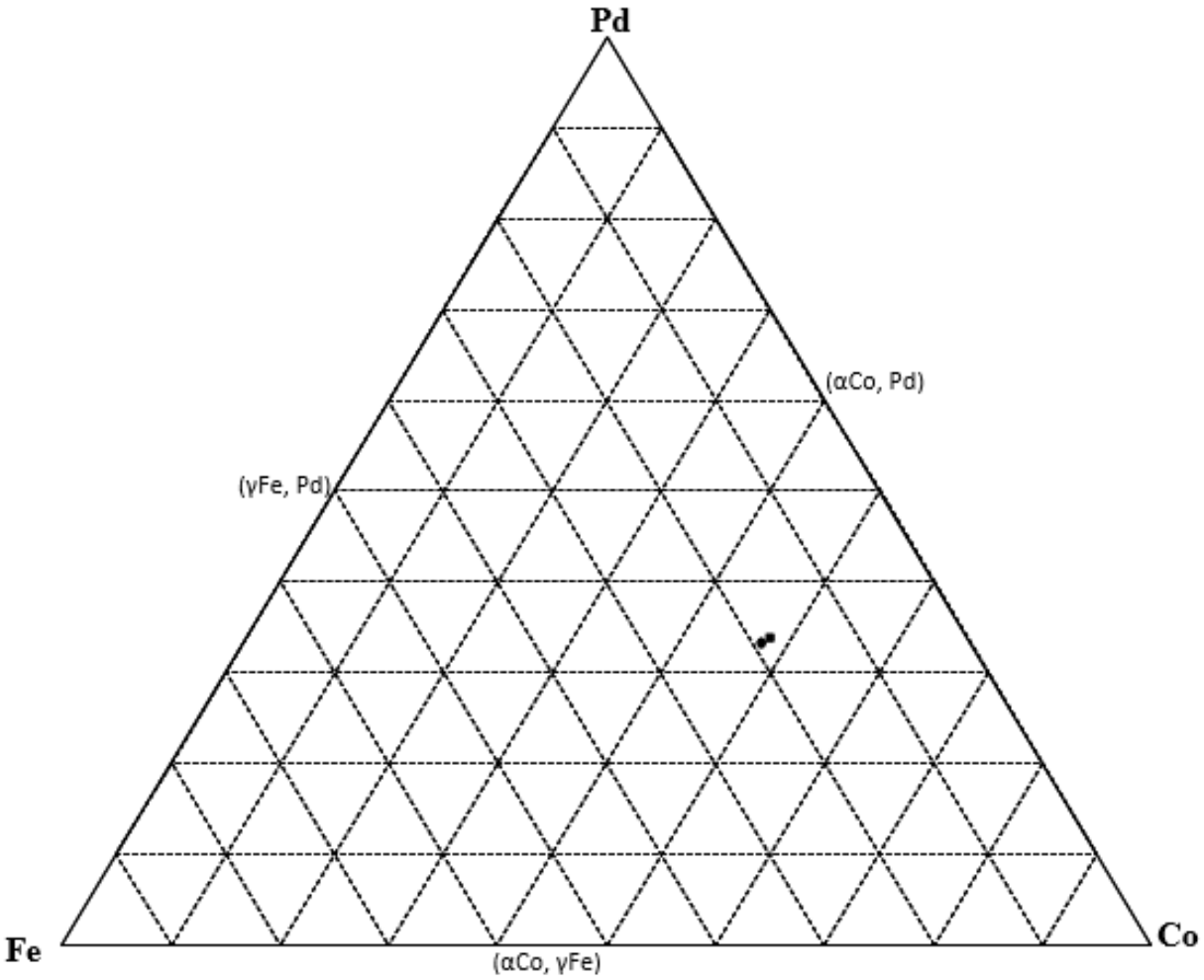


Figure 4.53. EDX analyses of nominal Co_{50}:Fe_{20}:Pd_{30} (at.%), Alloy 6 1000°C annealed condition. (■ Overall composition; ● phases)

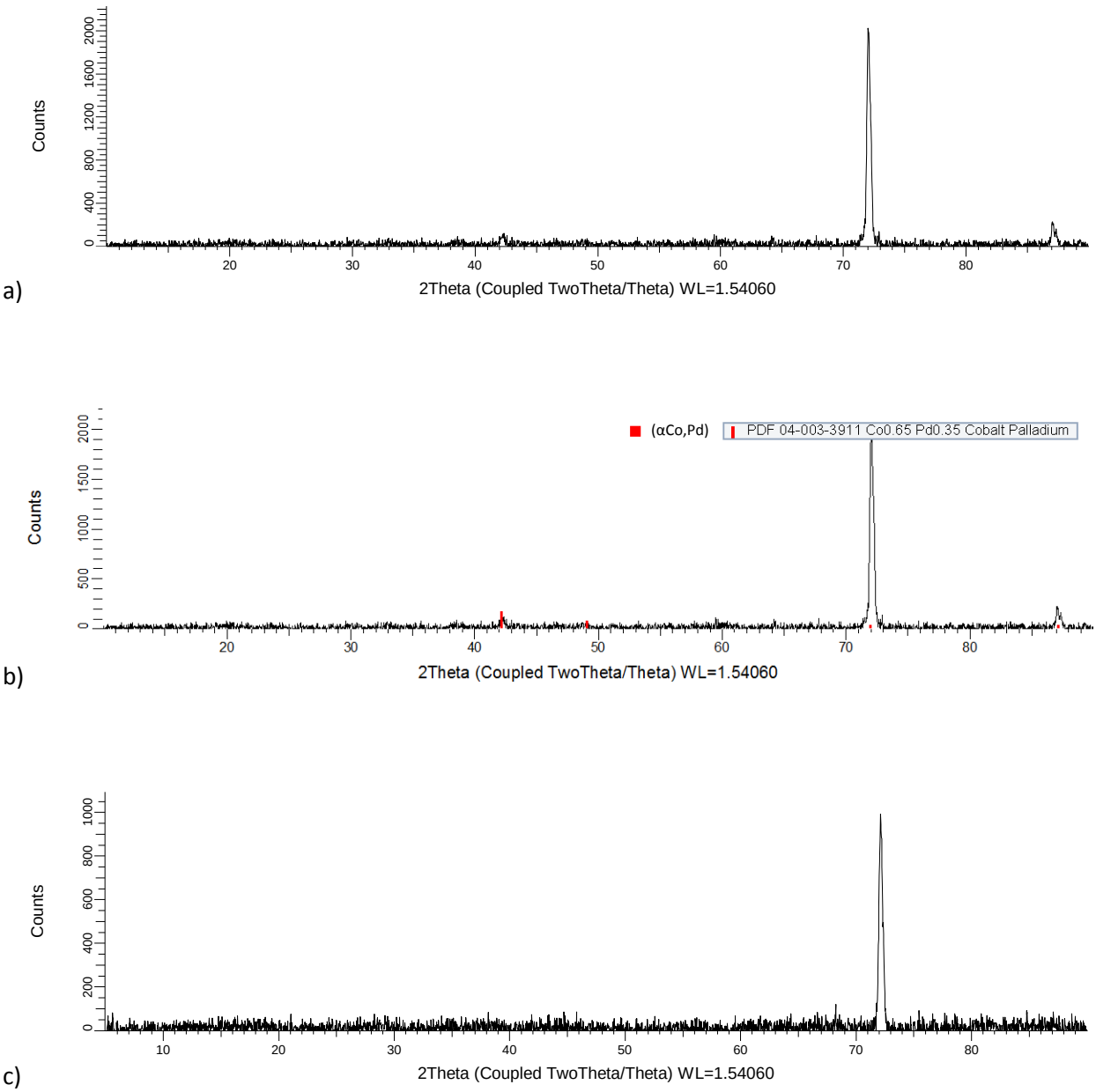


Figure 4.54. XRD patterns for nominal Co_{50}:Fe_{20}:Pd_{30} (at.%), Alloy 6 1000°C annealed condition: a) raw 10 minutes scan, b) labelled, and c) raw 20 minutes scan.

4.2.7. Alloy 7: Nominal Co_{10}:Fe_{30}:Pd_{60} (at.%)

Alloy 7, Nominal Co_{10}:Fe_{30}:Pd_{60} (at.%), Figure 4.55, shows a region that etched differently, and was apparently two-phase. Table 4.19 shows that the composition of the region and surrounding area did not differ much; this can also be observed in Figure 4.56. The XRD pattern showed that there was one phase present, A1 (γFe,αCo,Pd), Figure 4.57.

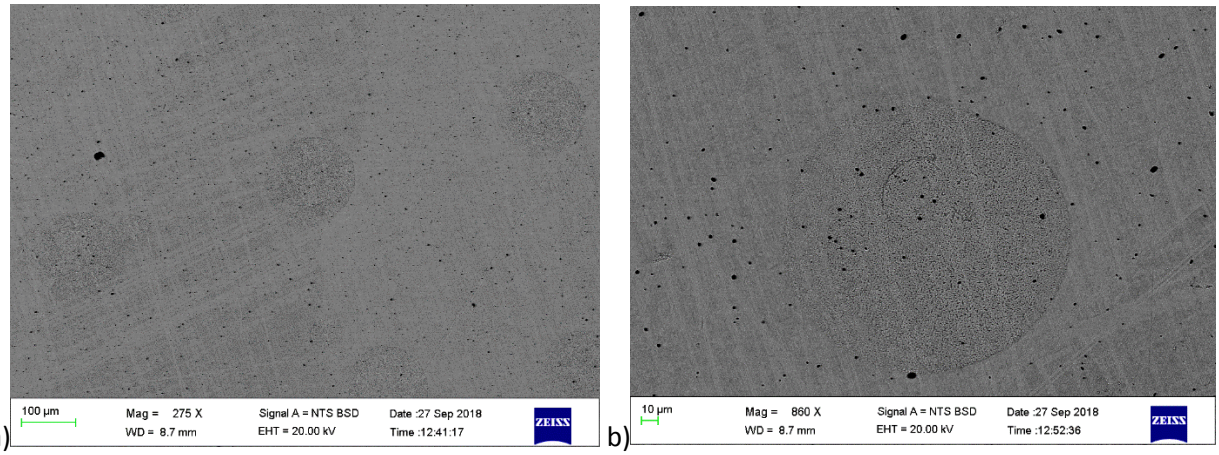


Figure 4.55. SEM-BSE images of Co_{10}:Fe_{30}:Pd_{60} (at.%), Alloy 7 annealed at 1000°C for 1000 h showing: a) etched-out patches, and b) patch at higher magnification.

Table 4.19. EDX phase analyses for nominal Co_{10}:Fe_{30}:Pd_{60} (at.%), Alloy 7, annealed at 1000°C condition.

Phase description	Co	Fe	Pd	Phase
Overall	9.0 ± 0.1	28.4 ± 0.2	62.6 ± 0.2	-
Circular region	8.9 ± 0.1	28.6 ± 0.1	62.5 ± 0.2	A1 (γFe,αCo,Pd)
Surrounding area	9.0 ± 0.1	28.3 ± 0.1	62.7 ± 0.1	A1 (γFe,αCo,Pd)

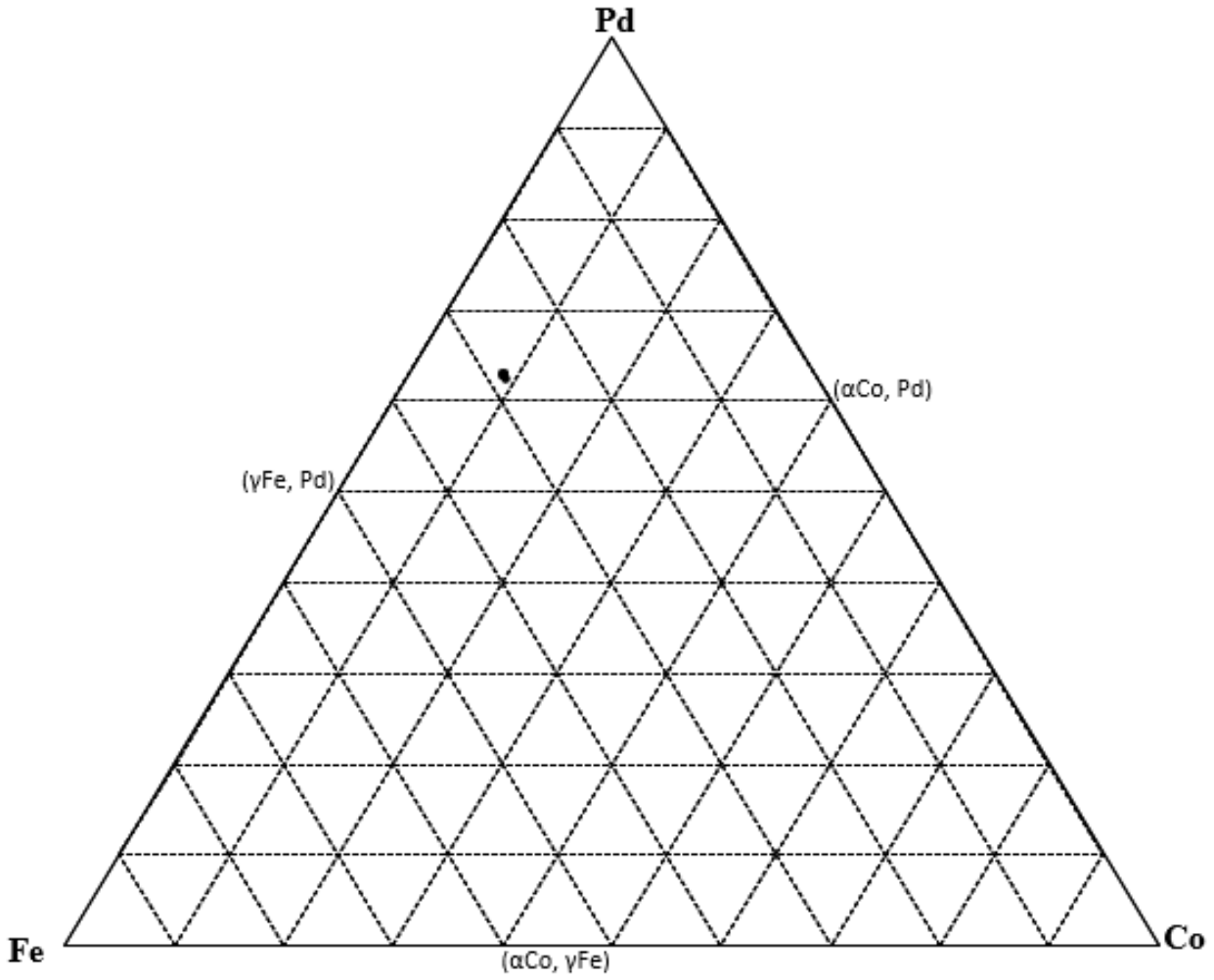


Figure 4.56. EDX analyses of nominal $Co_{10}:Fe_{30}:Pd_{60}$ (at.%), Alloy 7 1000°C annealed condition. (■ Overall composition; ● phases)

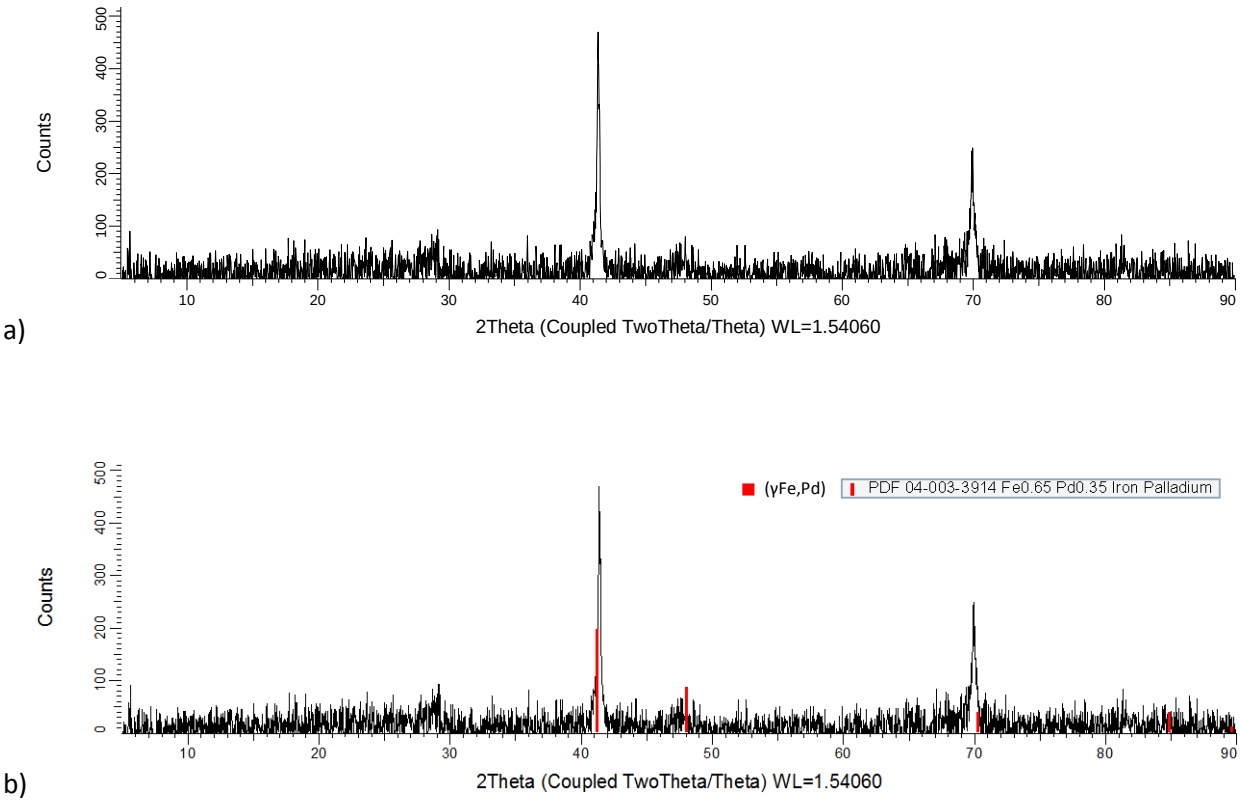


Figure 4.57. XRD patterns for nominal Co_{10}:Fe_{30}:Pd_{60} (at.%), Alloy 7 1000°C annealed condition: a) raw, and b) labelled.

4.2.8. Alloy 8: Nominal Co_{25}:Fe_{20}:Pd_{55} (at.%)

The microstructure of Alloy 8, Nominal Co_{25}:Fe_{20}:Pd_{55} (at.%), had a solid solution and a differently etched region with finer grains, Figure 4.58. The compositions of the grains and surrounding matrix were not very different, as shown in Table 4.20 and Figure 4.59. The XRD pattern (Figure 4.60) shows that A1 (γFe,αCo,Pd) was the only phase present, although the peaks were shifted, especially at higher angles.

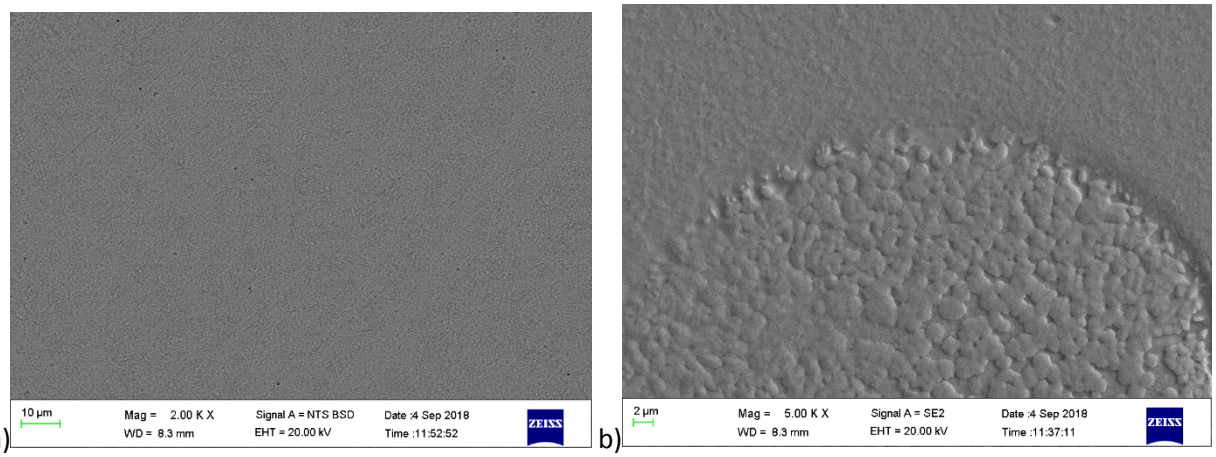


Figure 4. 58. SEM images of Co_{25}:Fe_{20}:Pd_{55} (at.%), Alloy 8 annealed at 1000°C for 1000 h showing: a) BSE image at low magnification and b) SE image of a region at higher magnification.

Table 4.20. EDX phase analyses for nominal Co_{10}:Fe_{25}:Pd_{55} (at.%), Alloy 8, annealed at 1000°C condition.

Phase description	Co	Fe	Pd	Phase
Overall	22.8 ± 0.1	18.9 ± 0.1	58.3 ± 0.1	-
Circular region	22.8 ± 0.2	18.9 ± 0.2	58.3 ± 0.1	A1 (γFe,αCo,Pd)
Bulk area	22.9 ± 0.1	18.8 ± 0.1	58.3 ± 0.1	A1 (γFe,αCo,Pd)

The overall and phase compositions on Figure 4.59 were very similar, therefore the data points lie on top of each other.

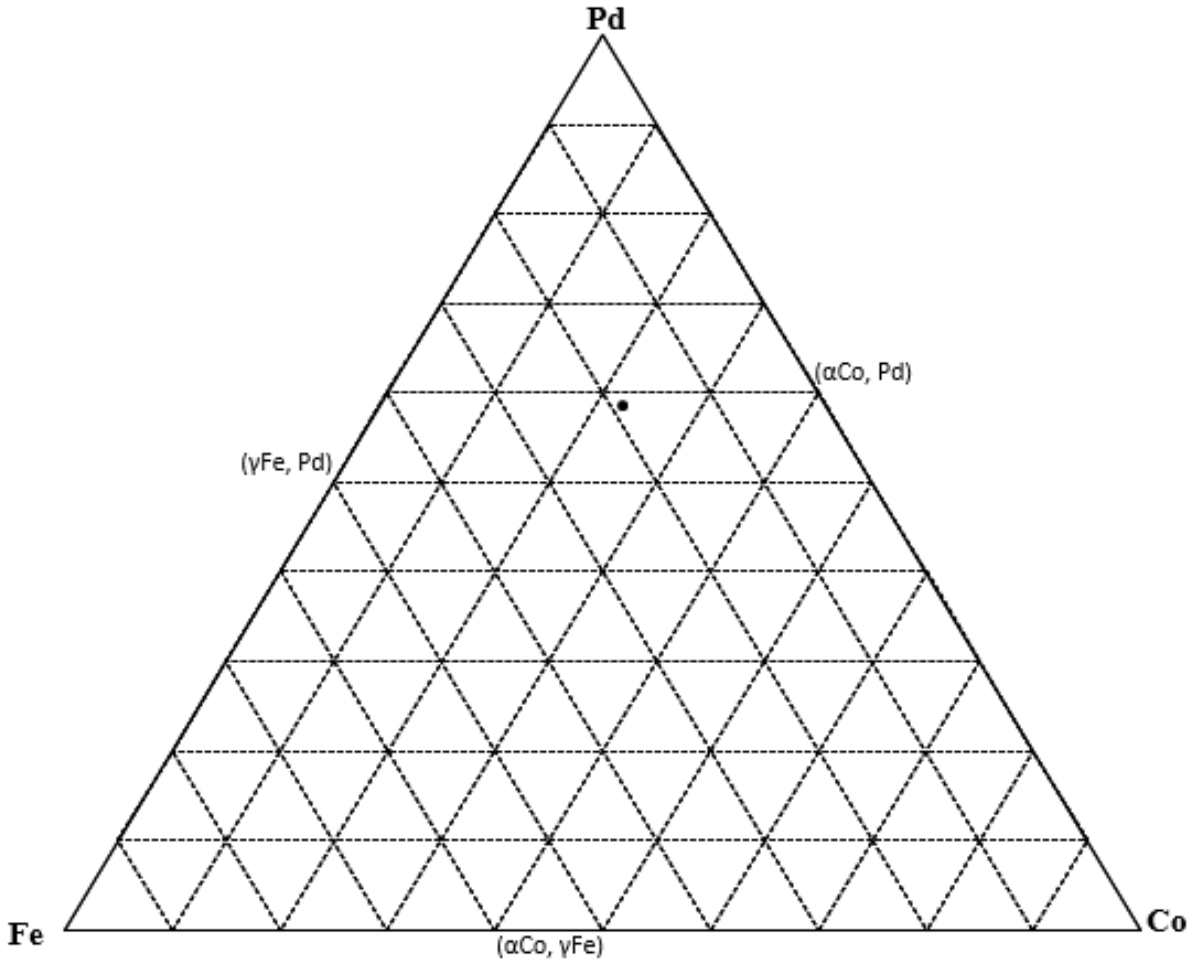


Figure 4.59. EDX analyses of nominal Co_{25}:Fe_{20}:Pd_{55} (at.%), Alloy 8 1000°C annealed condition. (■ Overall composition; ● phases)

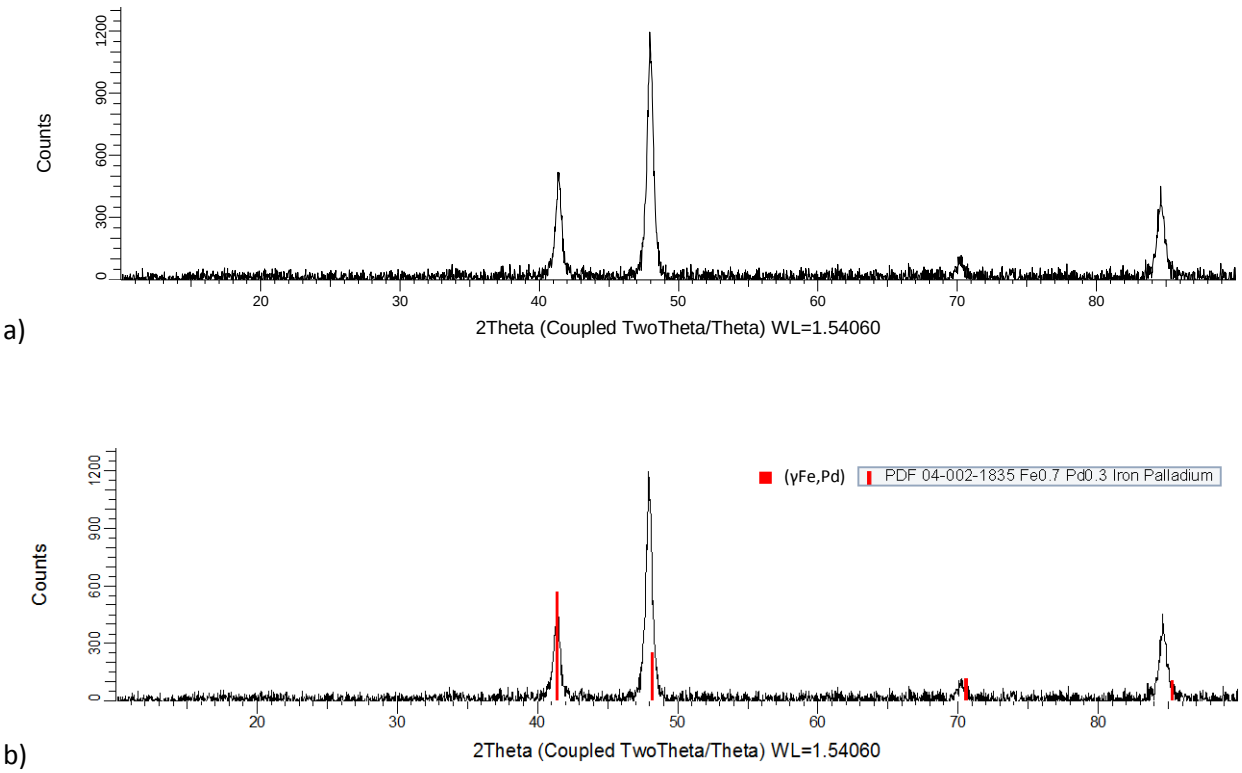


Figure 4.60. XRD patterns for nominal Co_{25}:Fe_{20}:Pd_{55} (at.%), Alloy 8 1000°C annealed condition: a) raw, and b) labelled.

4.2.9. Alloy 9: Nominal Co_{10}:Fe_{50}:Pd_{40} (at.%)

Figure 4.61 shows that Alloy 9, Nominal Co_{10}:Fe_{50}:Pd_{40} (at.%), had regions which etched differently, with lighter contrast particles. The compositions of the different areas were similar (Table 4.21 and Figure 4.62). The XRD pattern (Figure 4.63) shows that the one phase present was A1 (γFe,αCo,Pd), and there was one peak which was very large, probably due to preferred orientation, which was not reduced on annealing.

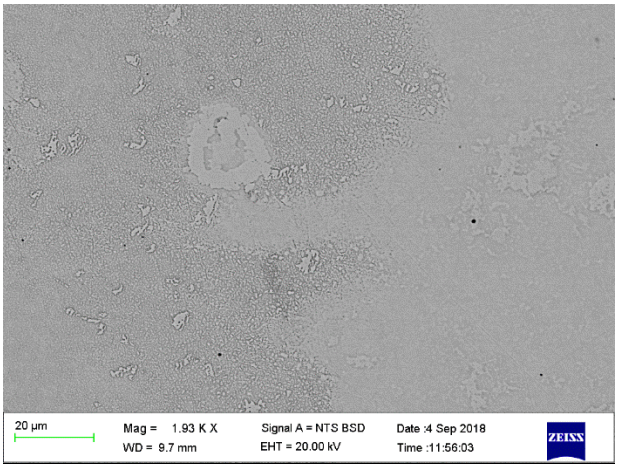


Figure 4.61. SEM-BSE image of Co_{10}:Fe_{50}:Pd_{40} (at.%), Alloy 9 annealed at 1000°C for 1000 h showing differently etched lighter grey particles.

Table 4.21. EDX phase analyses for nominal Co_{10}:Fe_{30}:Pd_{40} (at.%), Alloy 9, annealed at 1000°C condition.

Phase description	Co	Fe	Pd	Phase
Overall	9.0 ± 0.1	48.1 ± 0.1	42.9 ± 0.1	-
Bulk area	9.0 ± 0.1	48.0 ± 0.2	43.0 ± 0.2	A1 (γFe,αCo,Pd)
Light grey particles	8.9 ± 0.1	47.9 ± 0.3	43.2 ± 0.2	A1 (γFe,αCo,Pd)

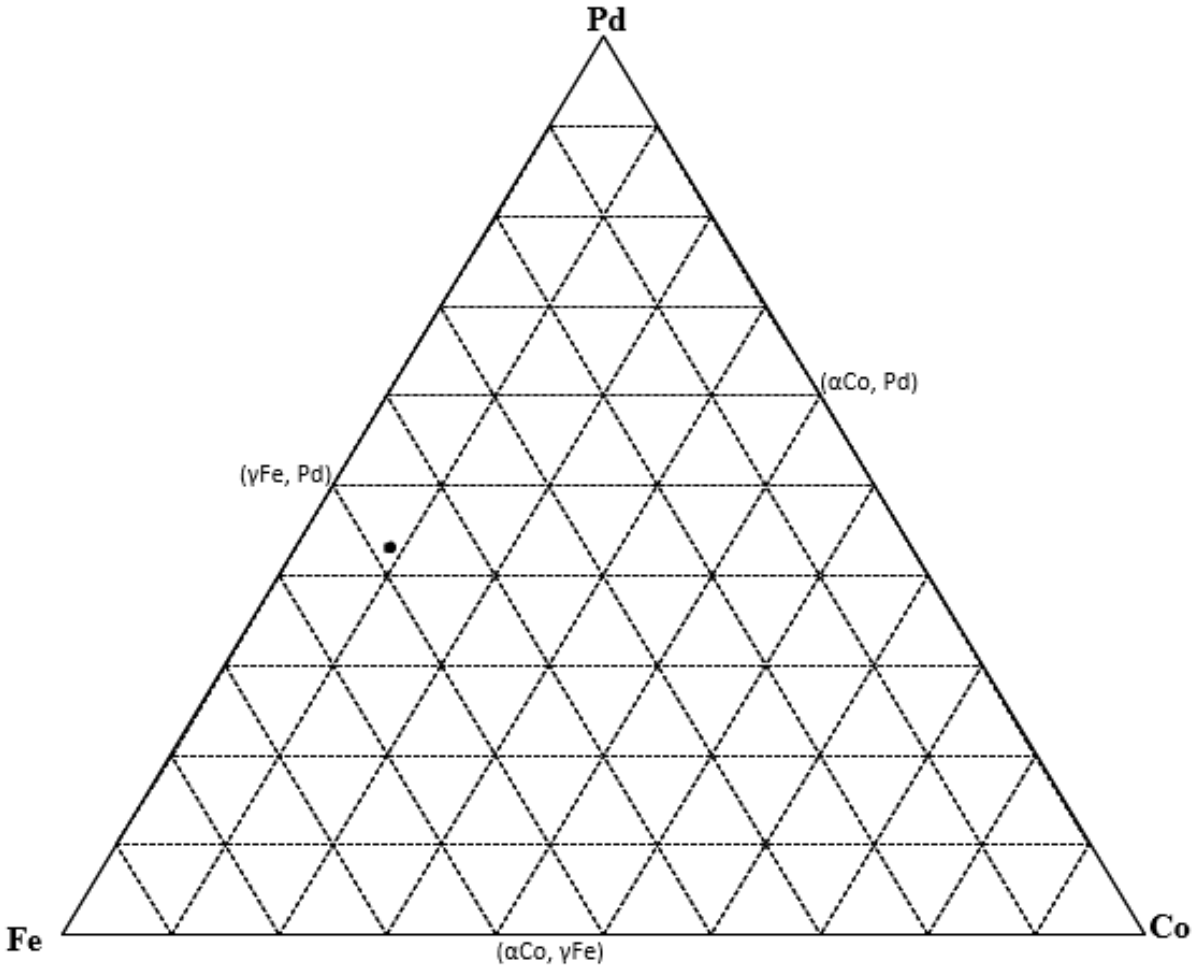


Figure 4.62. EDX analyses of nominal Co_{10}:Fe_{50}:Pd_{40} (at.%), Alloy 9 1000°C annealed condition. (■ Overall composition; ● phases)

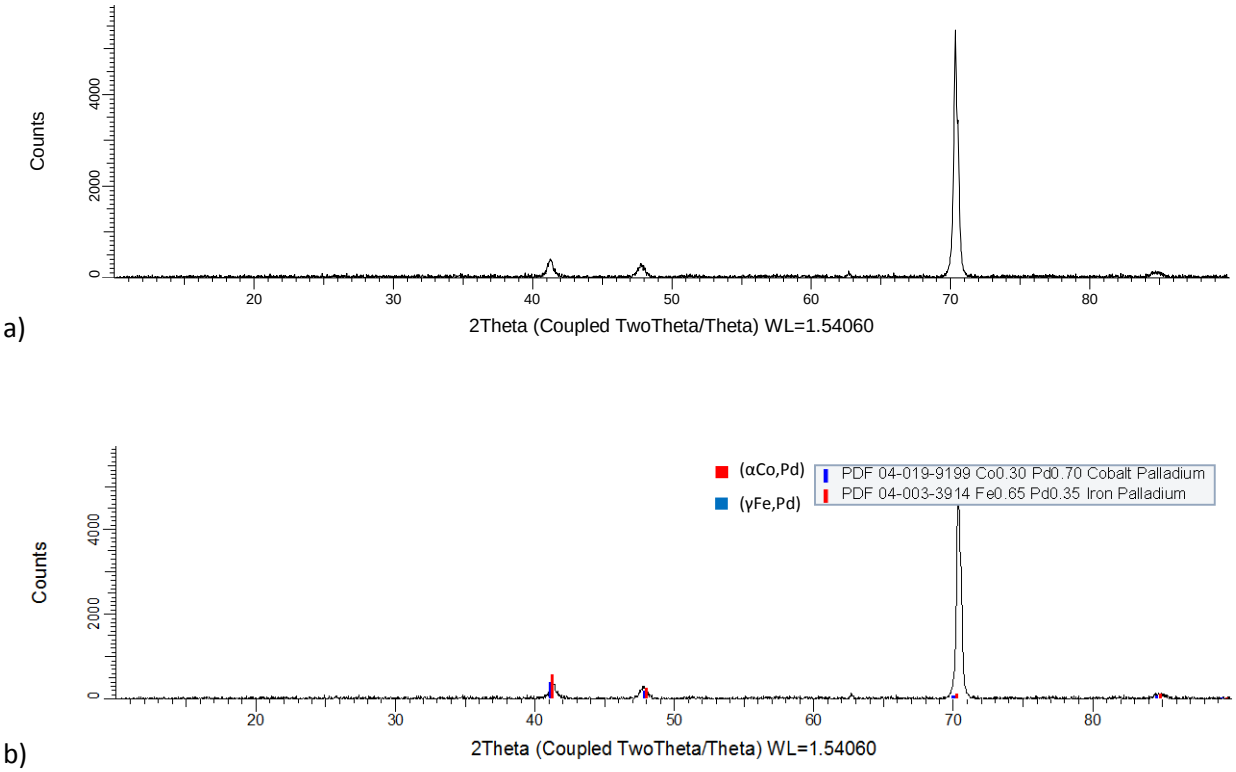


Figure 4.63. XRD patterns for nominal Co_{10}:Fe_{50}:Pd_{40} (at.%), Alloy 9 1000°C annealed condition: a) raw, and b) labelled.

4.2.10. Alloy 10: Nominal Co_{40}:Fe_{30}:Pd_{30} (at.%)

Figure 4.64 shows that Alloy 10, Nominal Co_{40}:Fe_{30}:Pd_{30} (at.%), had grains of different contrast. The compositions of these areas were almost the same, Table 4.22 and Figure 4.65. The XRD pattern in Figure 4.66 shows one phase present, A1 (γFe,αCo,Pd) and the height of the largest peak was probably due to preferred orientation which had not been removed on annealing. On the XRD pattern, there was one peak at ~67° (2 Theta) which could not be identified, but which could have been a shifted A1 peak.

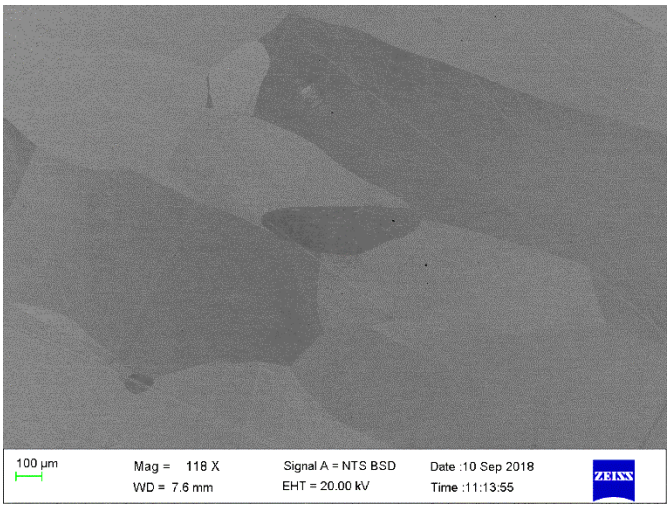


Figure 4.64. SEM-BSE image of Co_{40}:Fe_{30}:Pd_{30} (at.%), Alloy 10 annealed at 1000°C for 1000 h showing contrasting grains.

Table 4.22. EDX phase analyses for nominal Co_{40}:Fe_{30}:Pd_{30} (at.%), Alloy 10, annealed at 1000°C annealed condition.

Phase description	Co	Fe	Pd	Phase
Overall	37.7 ± 0.3	29.0 ± 0.2	33.3 ± 0.2	-
Dark	37.8 ± 0.3	28.9 ± 0.1	33.3 ± 0.2	A1 (γFe,αCo,Pd)
Light	37.7 ± 0.1	28.9 ± 0.2	33.4 ± 0.2	A1 (γFe,αCo,Pd)

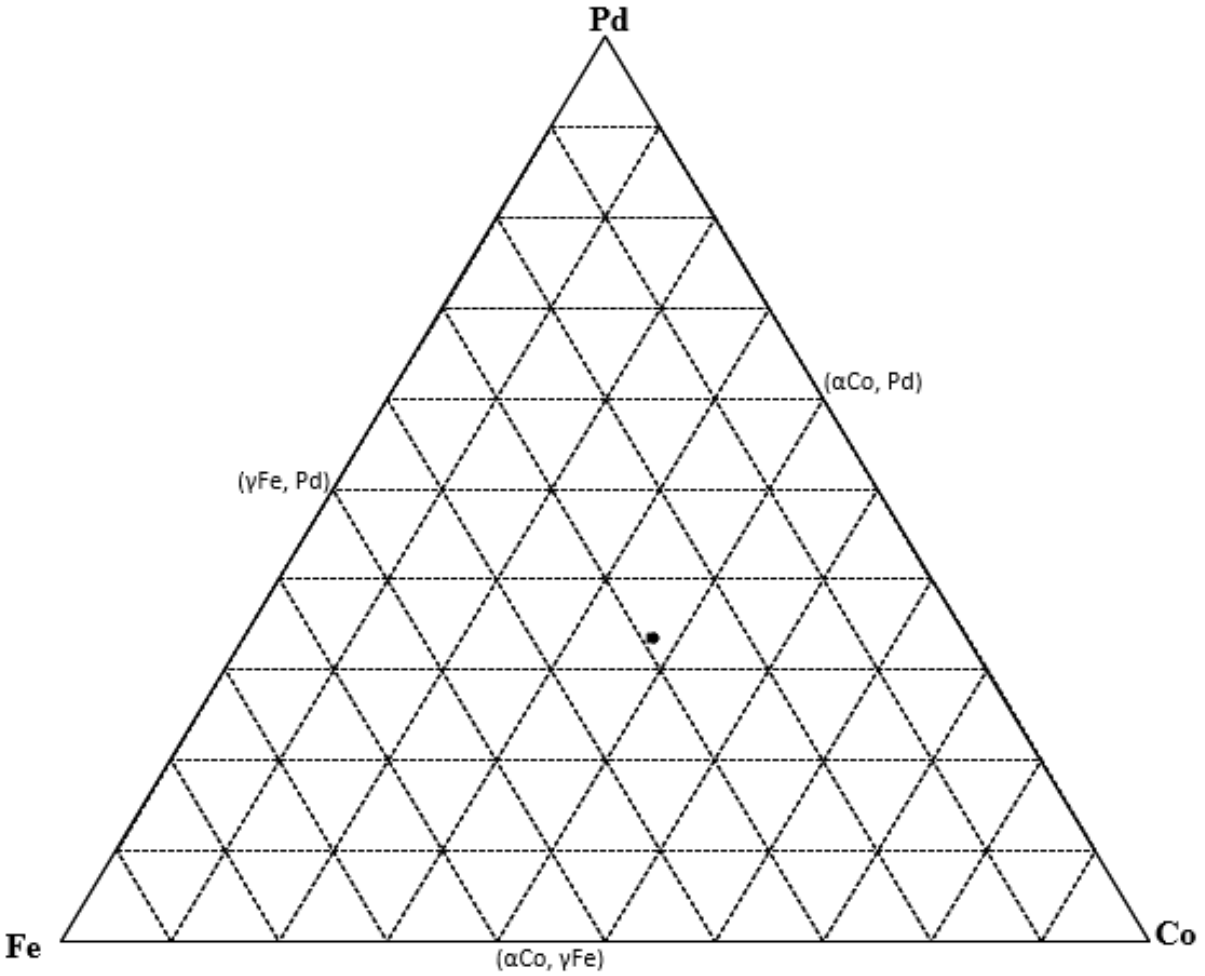


Figure 4.65. EDX analyses of nominal $Co_{40}:Fe_{30}:Pd_{30}$ (at.%), Alloy 10 1000°C annealed condition. (■ Overall composition; ● phases)

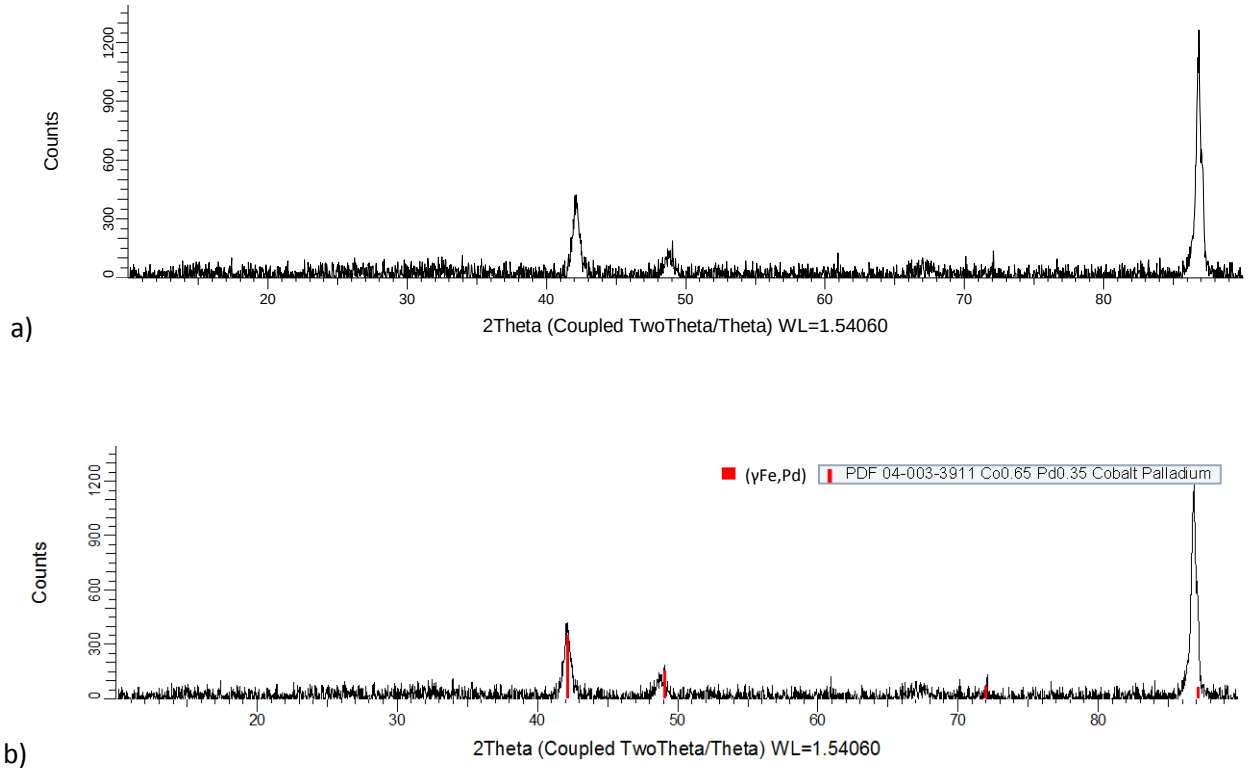


Figure 4.66. XRD patterns for nominal Co_{40}:Fe_{30}:Pd_{30} (at.%), Alloy 10 1000°C annealed condition: a) raw, and b) labelled.

4.2.11. Alloy 11: Nominal Co_{20}:Fe_{60}:Pd_{20} (at.%)

For Alloy 11, Nominal Co_{20}:Fe_{60}:Pd_{20} (at.%), light and dark regions are shown in Figure 4.67, which appeared to grow in a Widmanstätten manner within apparent grains and were quite coarse. Figure 4.67 b) shows fine precipitates formed in the bulk of the sample. The EDX analyses showed that the compositions were similar, Table 4.23 and Figure 4.68. The XRD pattern (Figure 4.69) had one phase present: A1 (γFe,αCo,Pd), although there were two peaks at ~63° and ~80° (2 Theta) which could not be identified with the phases: (αFe), ~$FePd_3$ or α', using the database [2018Dif], however they actually do match up with the α' in Appendix 1, with a high shift.

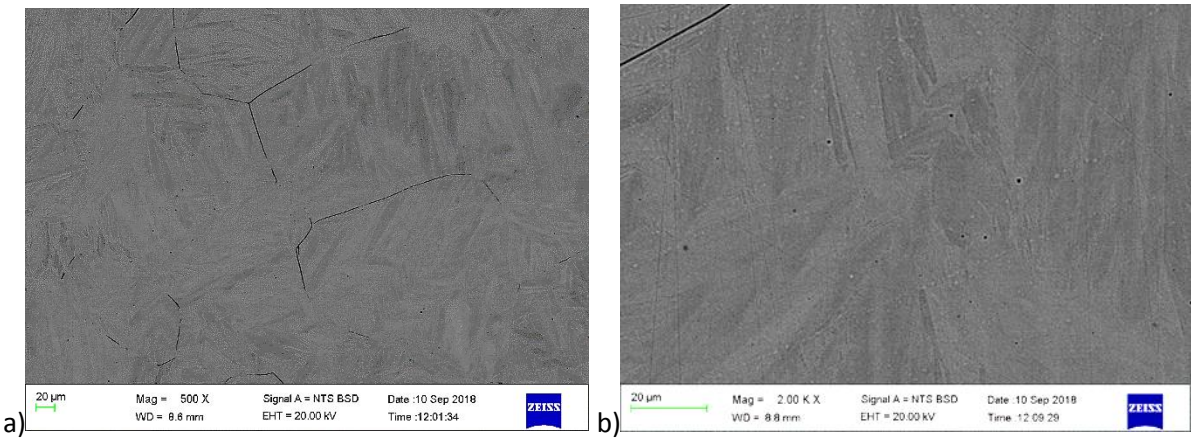


Figure 4.67. SEM-BSE images of Co_{20}:Fe_{60}:Pd_{20} (at.%), Alloy 11 annealed at 1000°C for 1000 h showing: a) contrasting regions with grain boundaries) and b) fine precipitates.

Table 4.23. EDX phase analyses for nominal Co_{20}:Fe_{60}:Pd_{20} (at.%), Alloy 11, annealed at 1000°C condition.

Phase description	Co	Fe	Pd	Phase
Overall	19.2 ± 0.1	58.7 ± 0.1	22.1 ± 0.1	-
Dark	19.1 ± 0.1	58.8 ± 0.2	22.1 ± 0.1	A1 (γFe,αCo,Pd)
Light	19.1 ± 0.1	58.9 ± 0.1	22.0 ± 0.1	A1 (γFe,αCo,Pd)

Figure 4.68 had similar compositions for the overall and phases, therefore the composition points lie on top of each other.

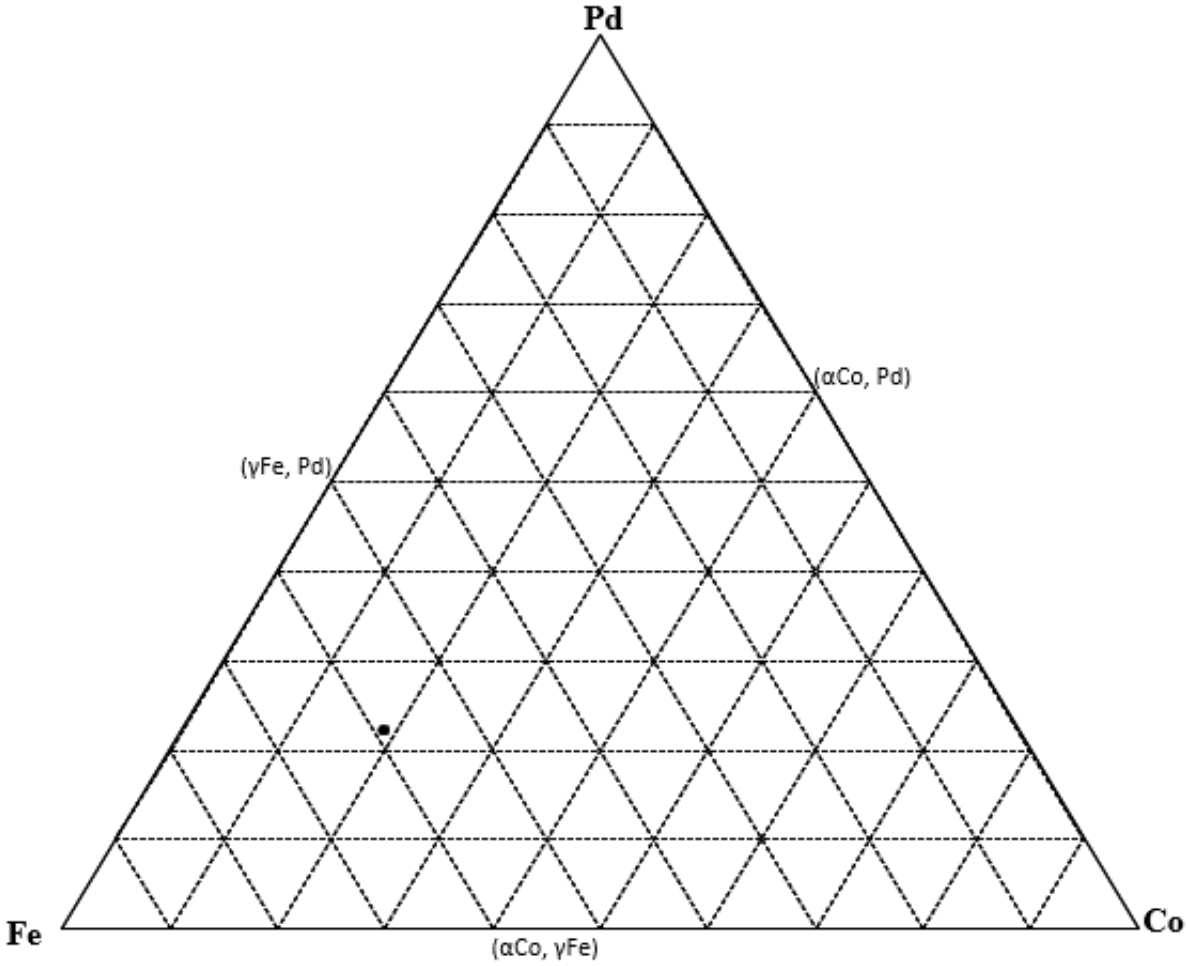


Figure 4.68. EDX analyses of nominal Co_{20}:Fe_{60}:Pd_{20} (at.%), Alloy 11 1000°C annealed condition. (■ Overall composition; ● phases)

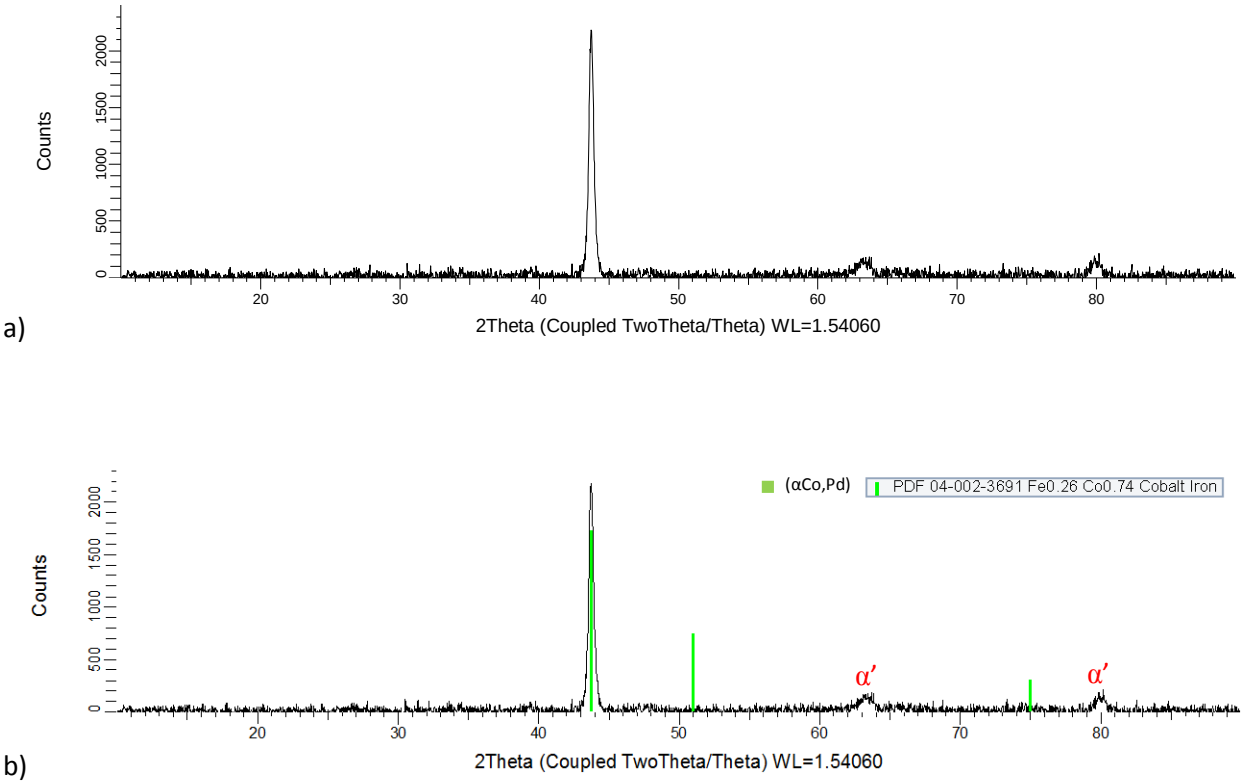


Figure 4.69. XRD patterns for nominal Co_{20}:Fe_{60}:Pd_{20} (at.%), Alloy 11 1000°C annealed condition: a) raw, and b) labelled.

4.2.12. Alloy 12: Nominal Co_{60}:Fe_{20}:Pd_{20} (at.%)

Alloy 12, Nominal Co_{60}:Fe_{20}:Pd_{20} (at.%), was one solid solution, Figure 4.70. Table 4.24 and Figure 4.71 showed there was no difference in composition in the slightly contrasting regions. The XRD pattern (Figure 4.72) was very poor, with much noise and low signal, and had been run for 10 minutes, and 20 minutes with no difference in the pattern, although the phase identified was A1 (γFe,αCo,Pd).

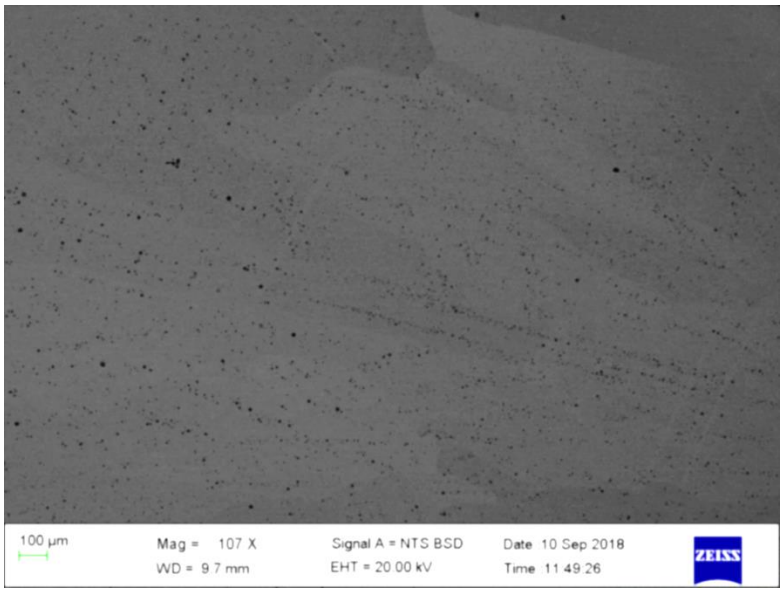


Figure 4.70. SEM-BSE image of Co_{60}:Fe_{20}:Pd_{20} (at.%), Alloy 12 annealed at 1000°C for 1000 h showing light and dark grains.

Table 4.24. EDX phase analyses for nominal Co_{60}:Fe_{20}:Pd_{20} (at.%), Alloy 12, annealed at 1000°C condition.

Phase description	Co	Fe	Pd	Phase
Overall	58.2 ± 0.1	19.0 ± 0.1	22.8 ± 0.1	-
Dark grains	57.6 ± 1.0	18.9 ± 0.3	23.5 ± 1.3	A1 (γFe,αCo,Pd)
Light grains	58.2 ± 0.3	18.9 ± 0.1	22.9 ± 0.3	A1 (γFe,αCo,Pd)

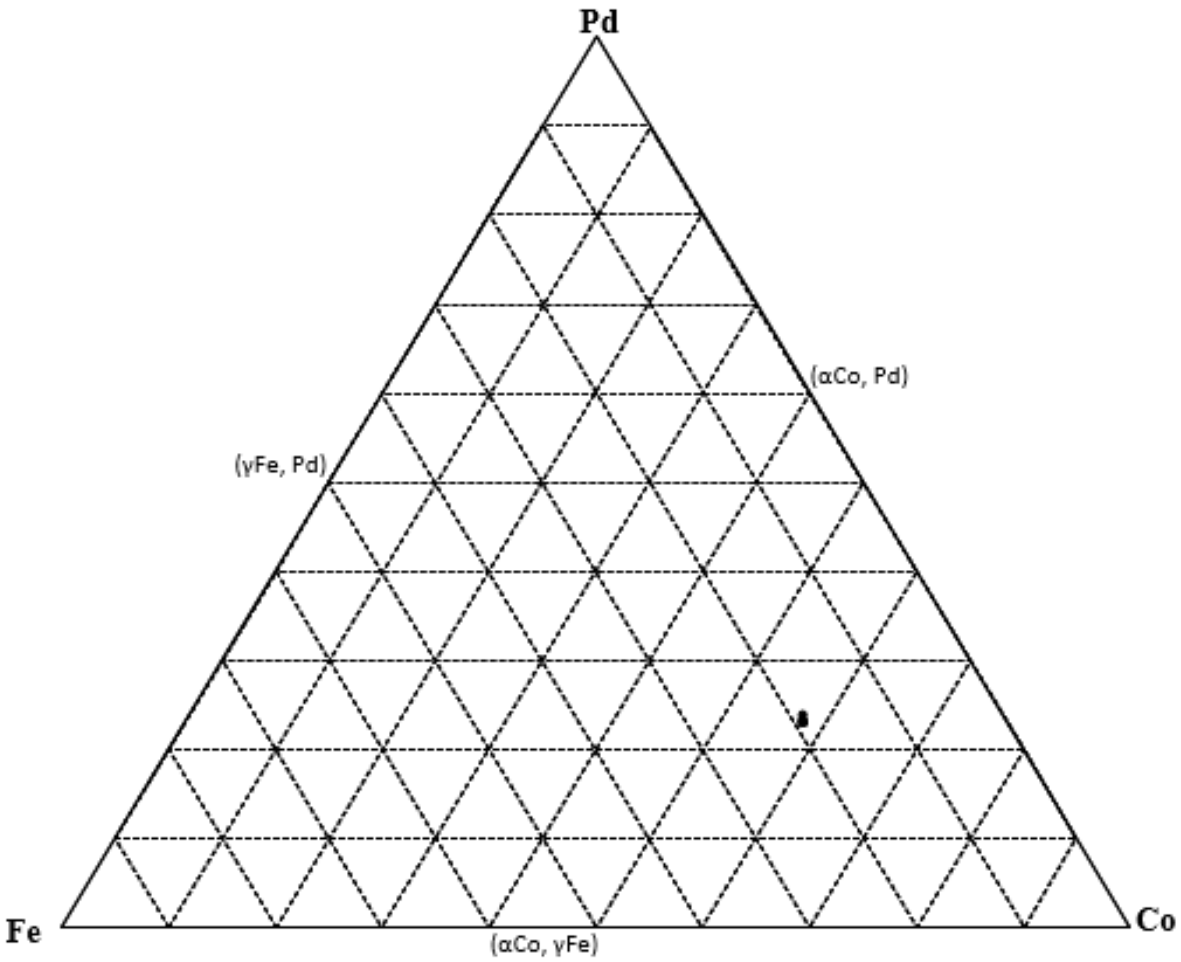


Figure 4.71. EDX analyses of nominal Co_{60}:Fe_{20}:Pd_{20} (at.%), Alloy 12 1000°C annealed condition. (■ Overall composition; ● phases)

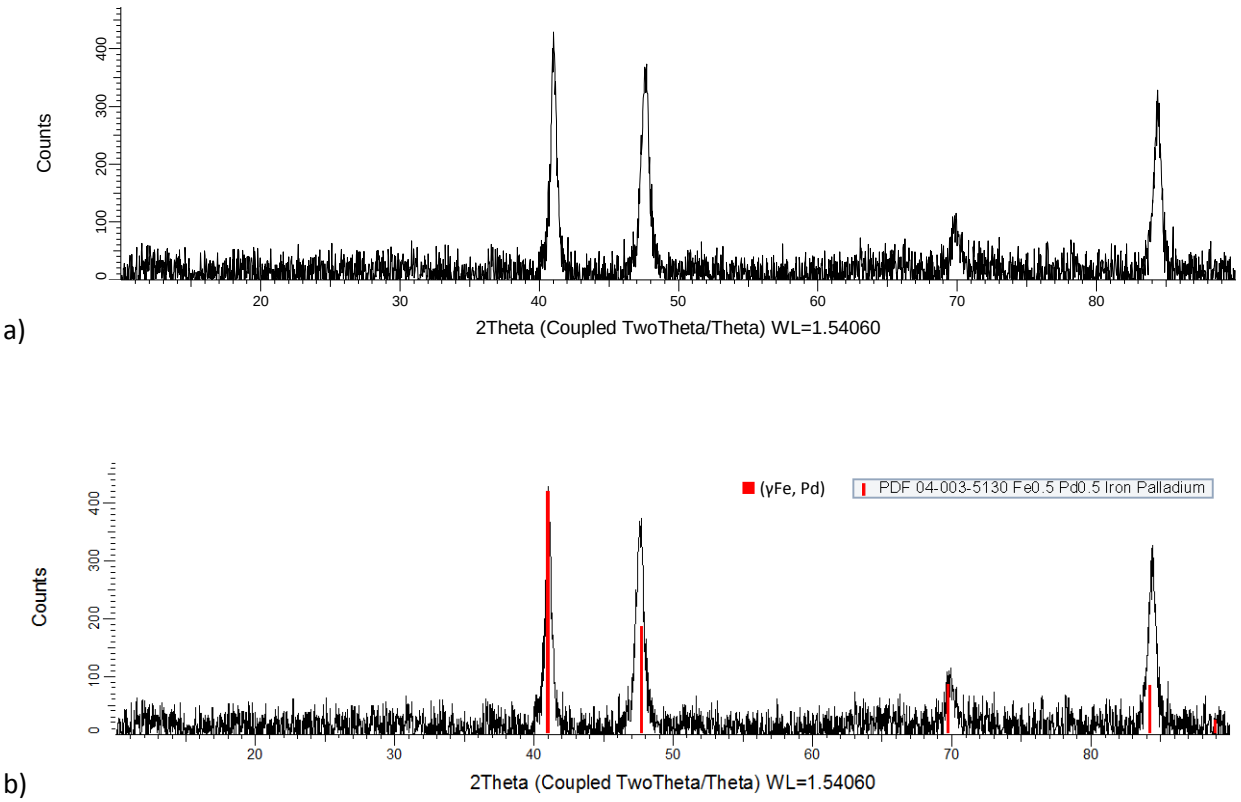


Figure 4.72. XRD patterns for nominal Co_{60}:Fe_{20}:Pd_{20} (at.%), Alloy 12 1000°C annealed condition: a) raw, and b) labelled.

4.3. Samples annealed at 650°C

4.3.1. Alloy 1: Nominal Co_{30}:Fe_{60}:Pd_{10} (at.%)

Figure 4.73 a) shows that Alloy 1, Nominal Co_{30}:Fe_{60}:Pd_{10} (at.%), formed apparent dendrites. At higher magnification (Figure 4.73 b)), the contrasting light and dark regions were discerned to have decomposed into different proportions of two fine phases. The regions analysed were very different, Table 4.25 and Figure 4.74. It was deduced from the XRD results in Figure 4.75 that the phases present were α' and A1 (γFe,αCo,Pd).

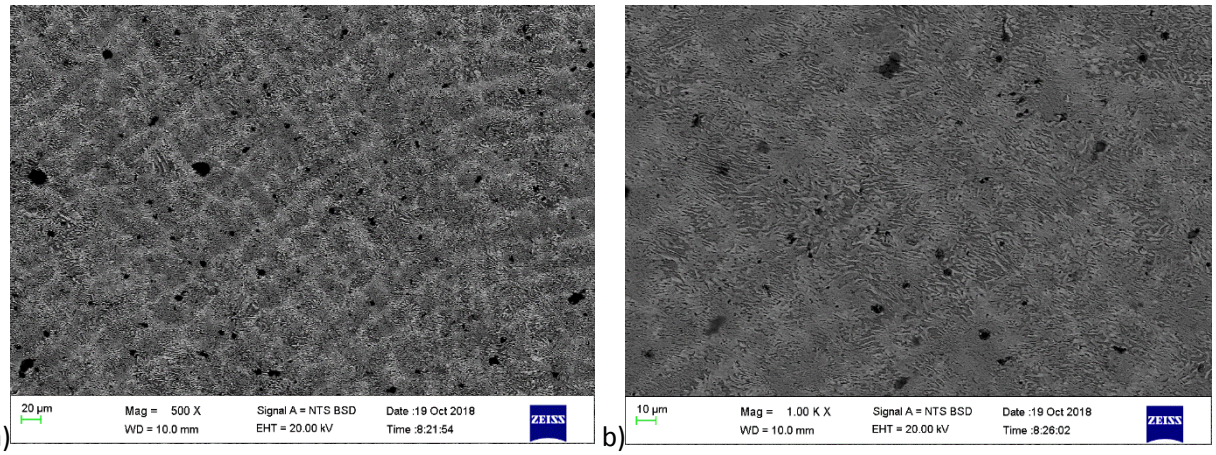


Figure 4.73. SEM-BSE images of Co_{30}:Fe_{60}:Pd_{10} (at.%), Alloy 1 annealed at 650°C for 1000 h showing: a) apparent dendrites, and b) higher magnification light and dark fine phases.

Table 4.25. EDX phase analyses for nominal Co_{30}:Fe_{60}:Pd_{10} (at.%), Alloy 1, annealed at 650°C condition.

Phase description	Co	Fe	Pd	Phase
Overall	25.8 ± 0.1	56.9 ± 0.1	17.3 ± 0.1	-
Dark	33.5 ± 2.0	62.4 ± 1.4	4.1 ± 3.4	Mainly α' with A1 (γFe,αCo,Pd)
Light	13.2 ± 4.0	49.2 ± 2.9	37.6 ± 6.9	Mainly A1 (γFe,αCo,Pd) with α'

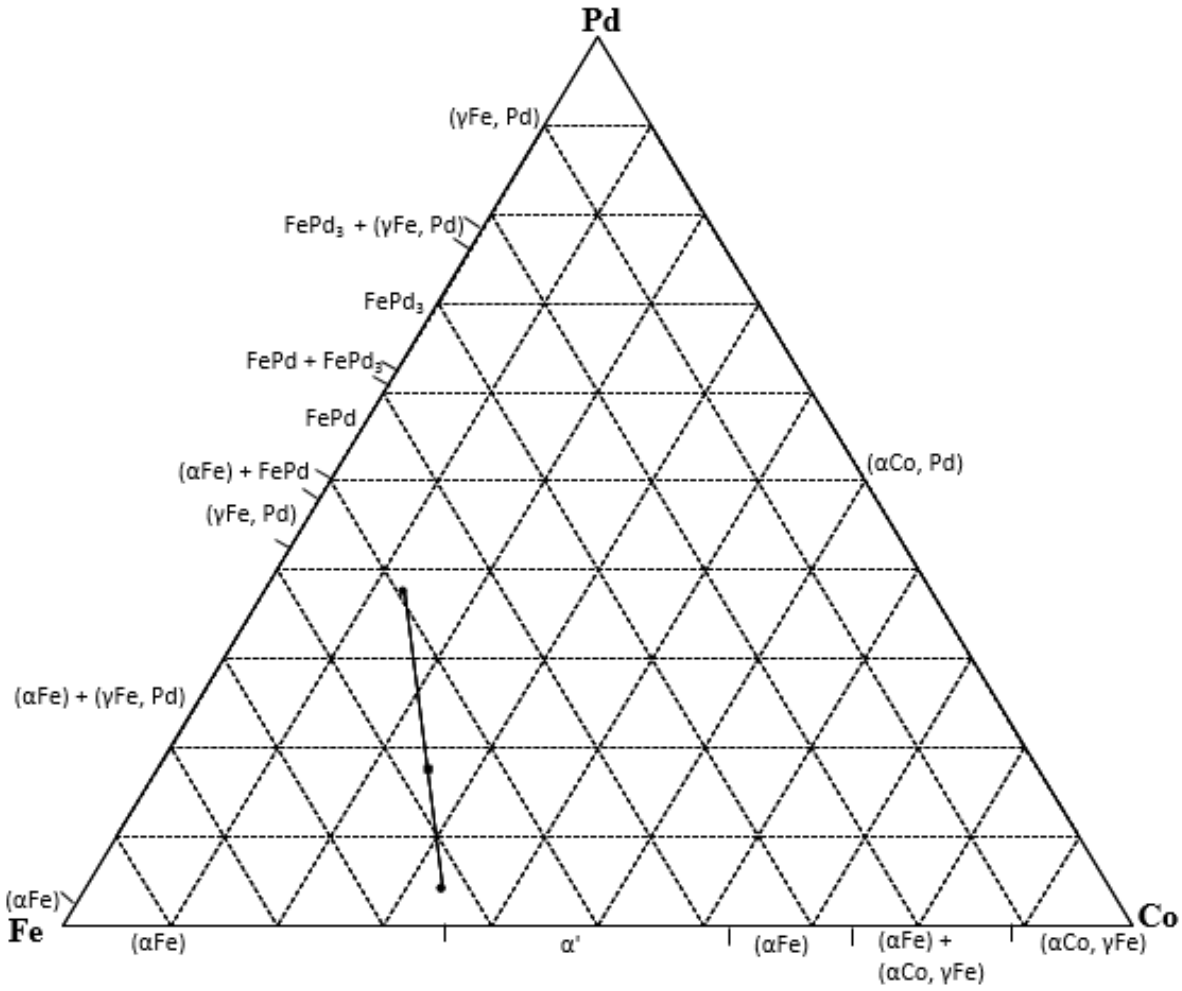


Figure 4.74. EDX analyses of nominal $Co_{30}:Fe_{60}:Pd_{10}$ (at.%), Alloy 1 650°C annealed condition. (■ Overall composition; ● phases)

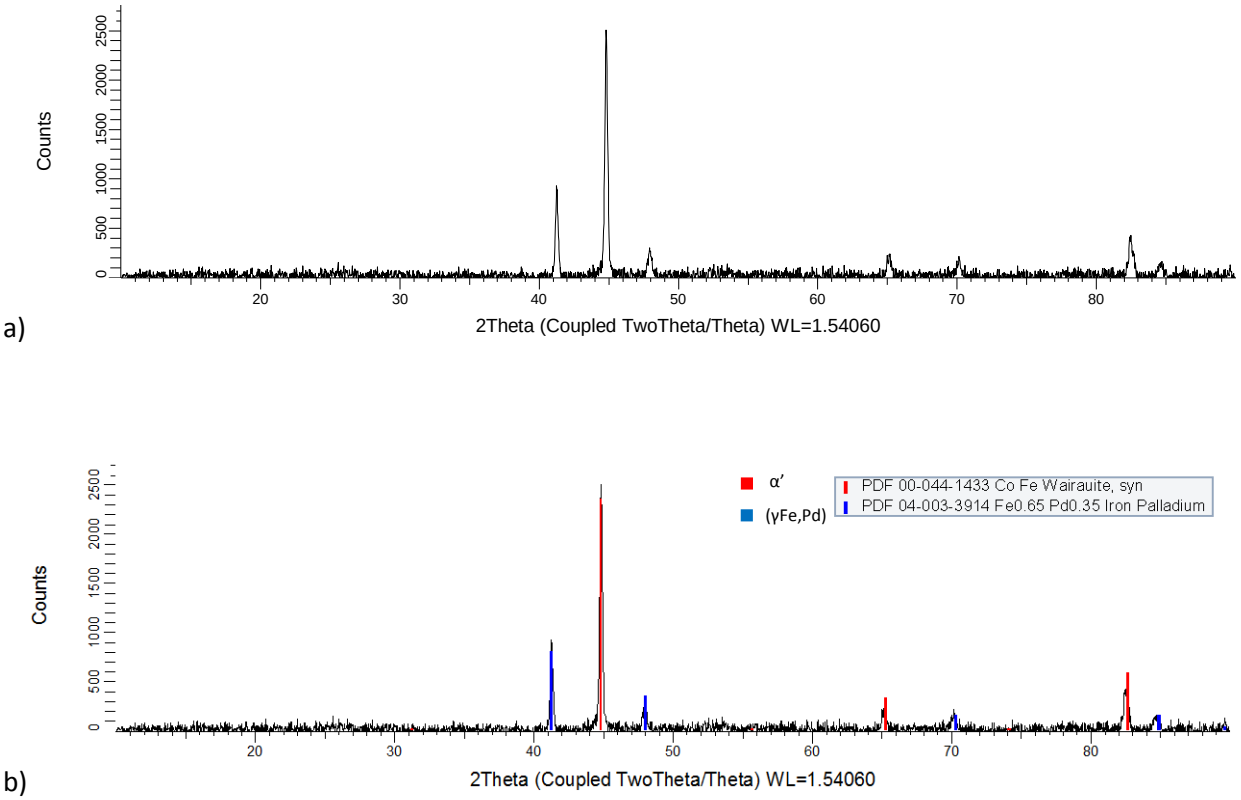


Figure 4.75. XRD patterns for nominal Co_{30}:Fe_{60}:Pd_{10} (at.%), Alloy 1 650°C annealed condition: a) raw, and b) labelled.

4.3.2. Alloy 2: Nominal Co_6:Fe_{44}:Pd_{50} (at.%)

For Alloy 2, Nominal Co_6:Fe_{44}:Pd_{50} (at.%), light and dark grains with grain boundaries were visible in Figure 4.76. The different contrasting areas had very similar EDX results, Table 4.26 and Figure 4.77. The phase found from the XRD pattern (Figure 4.78) was A1 (γFe,αCo,Pd).

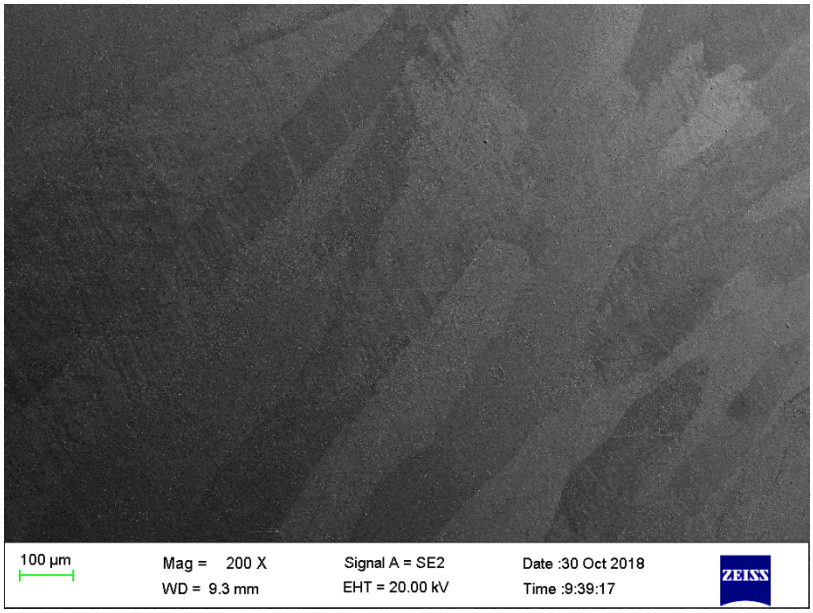


Figure 4.76. SEM-SE image of Co_6:Fe_{44}:Pd_{50} (at.%), Alloy 2 annealed at 650°C for 1000 h showing light and dark grains.

Table 4.26. EDX phase analyses for nominal Co_6: Fe_{44}:Pd_{50} (at.%), Alloy 2, annealed at 650°C condition.

Phase description	Co	Fe	Pd	Phase
Overall	5.9 ± 0.1	41.0 ± 0.1	53.1 ± 0.1	-
Dark	6.0 ± 0.4	41.0 ± 0.3	53.0 ± 0.2	A1 (γFe,αCo,Pd)
Light	5.9 ± 0.2	41.2 ± 0.1	52.9 ± 0.2	A1 (γFe,αCo,Pd)

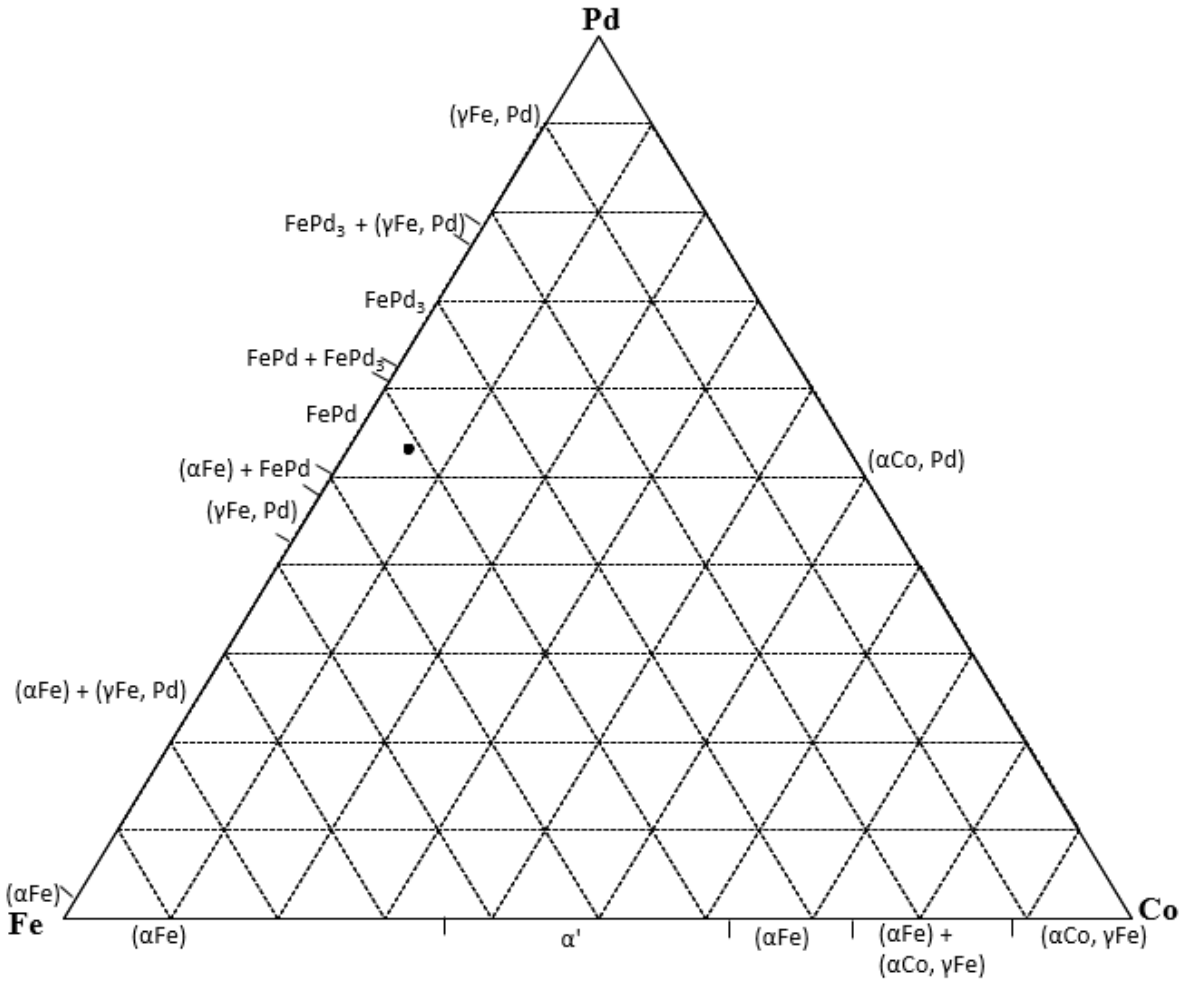
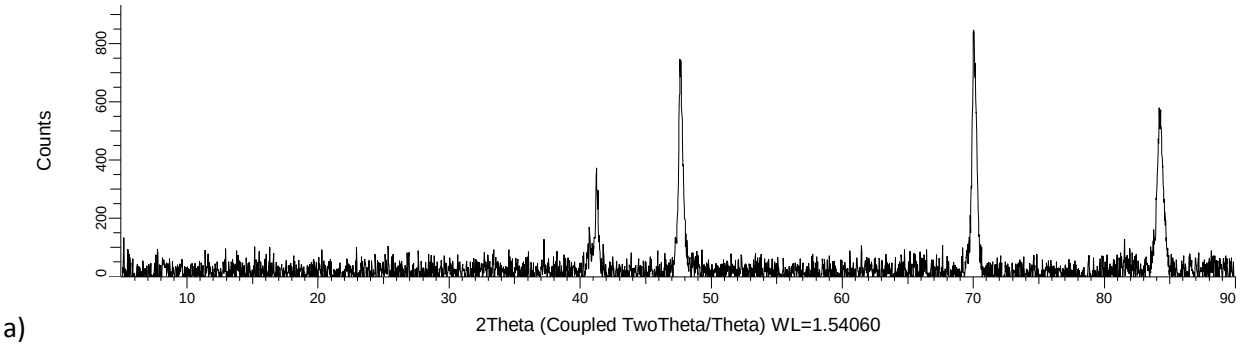
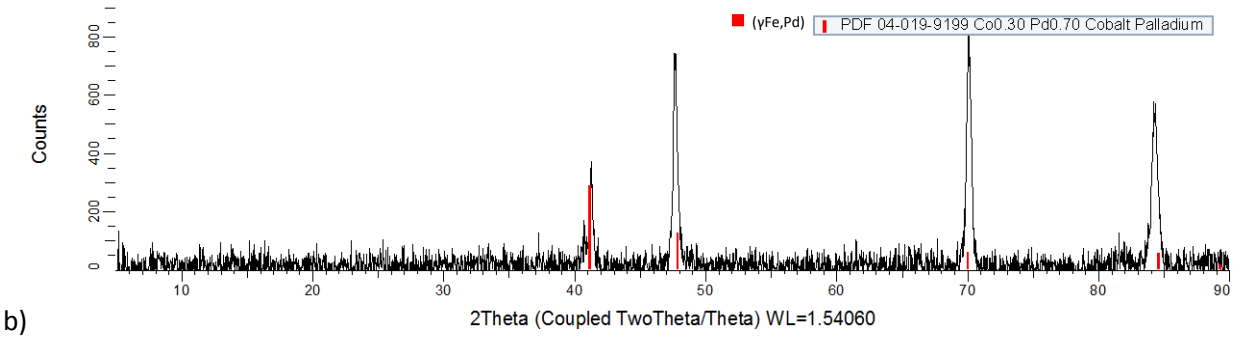


Figure 4.77. EDX analyses of nominal Co_6:Fe_{44}:Pd_{50} (at.%), Alloy 2 650°C annealed condition. (■ Overall composition; ● phases)



a)



b)

Figure 4.78. XRD patterns for nominal Co_6:Fe_{44}:Pd_{50} (at.%), Alloy 2 650°C annealed condition: a) raw, and b) labelled.

4.3.3. Alloy 3: Nominal Co_{20}:Fe_{50}:Pd_{30} (at.%)

Figure 4.79 (Alloy 3, Nominal Co_{20}:Fe_{50}:Pd_{30} (at.%)) shows an etched area and the dark spaces which were where one of the phases was etched out. The plot of the EDX results (Figure 4.80 and Table 4.27) shows that the overall of the alloy does not lie on the tie-line of the two phases analysed; the reason for this could be that one of the analyses was incorrect. It is not surprising that the analyses could be incorrect, as the phases were very fine, making the analyses difficult to obtain accurately, and also one phase was etched out. The XRD pattern, Figure 4.81, matched two phases, (αFe) and A1 (γFe,αCo,Pd).

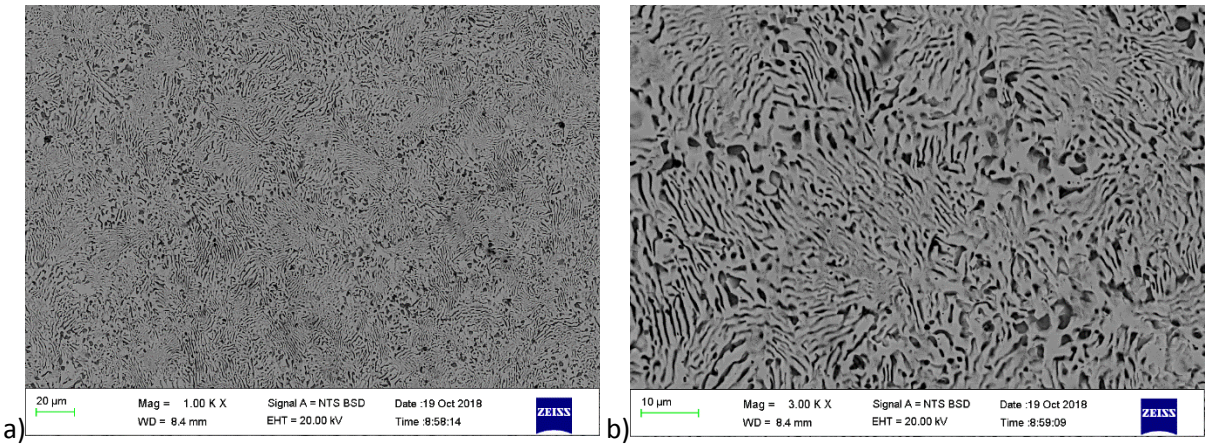


Figure 4.79. SEM-BSE images of Co_{20}:Fe_{50}:Pd_{30} (at.%), Alloy 3 annealed at 650°C for 1000 h showing: a) the overall etched area, and b) higher magnification.

Table 4.27. EDX phase analyses for nominal Co_{20}:Fe_{50}:Pd_{30} (at.%), Alloy 3, annealed at 650°C condition.

Phase description	Co	Fe	Pd	Phase
Overall	14.1 ± 0.1	46.3 ± 0.1	39.6 ± 0.1	-
Dark	7.6 ± 1.4	86.0 ± 0.1	6.4 ± 1.5	(αFe)
Light	9.5 ± 1.5	44.0 ± 0.7	46.5 ± 2.2	A1 (γFe,αCo,Pd)

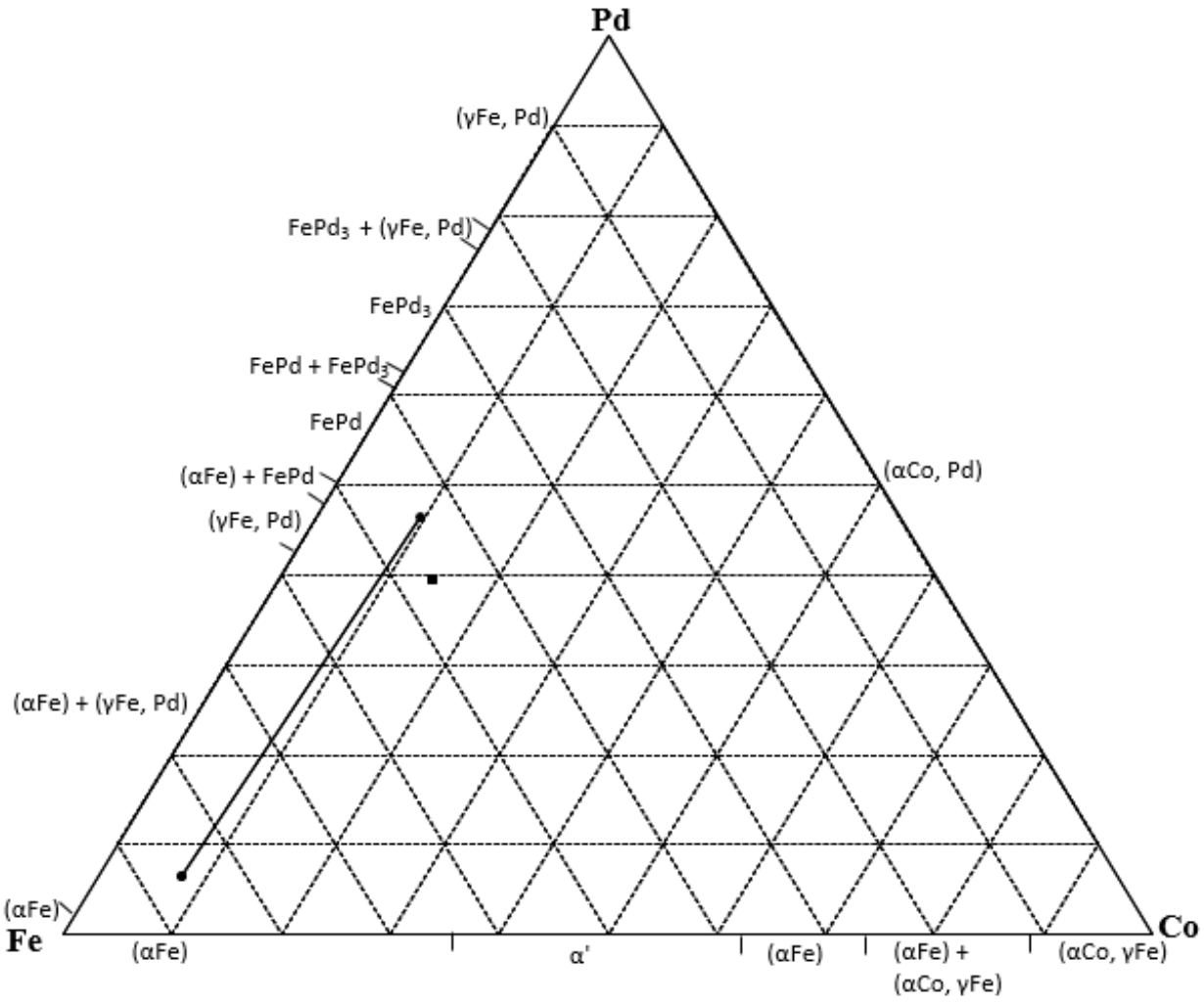


Figure 4.80. EDX analyses of nominal Co_{20}:Fe_{50}:Pd_{30} (at.%), Alloy 3 650°C annealed condition. (■ Overall composition; ● phases).

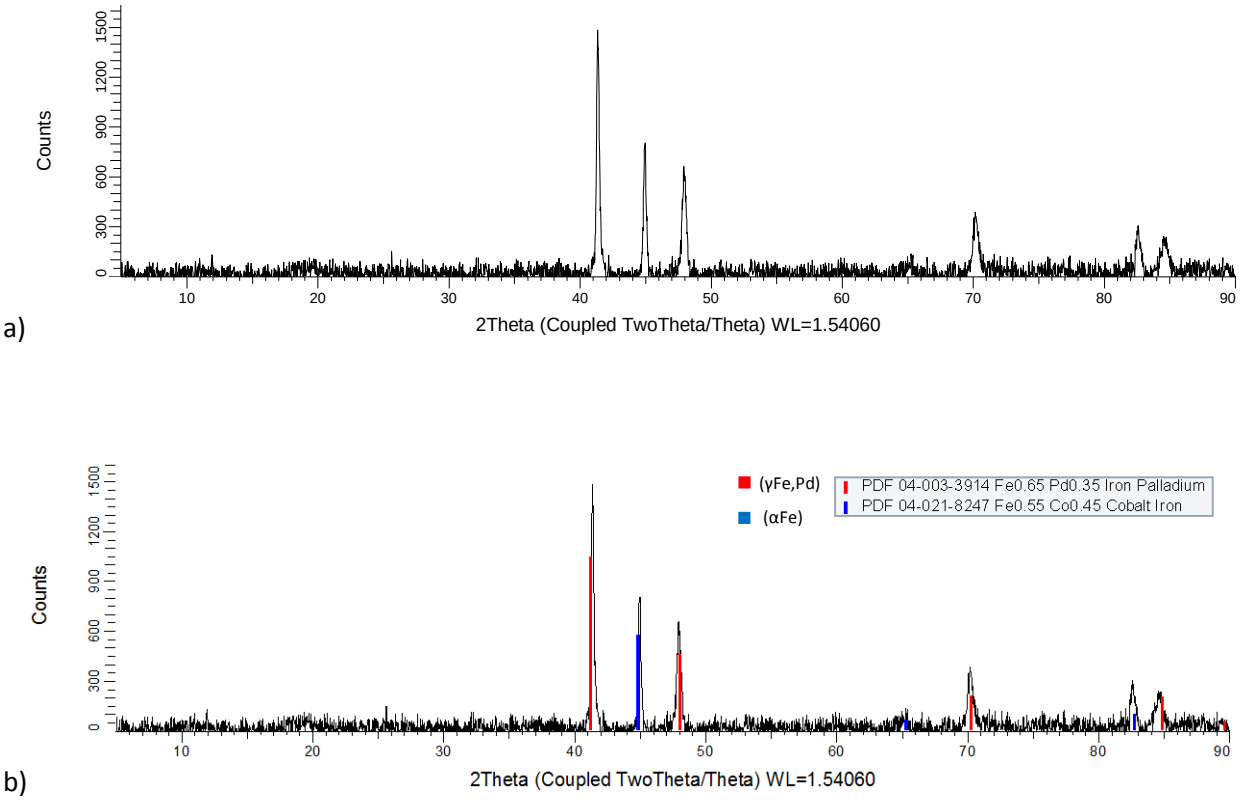


Figure 4.81. XRD patterns for nominal Co_{20}:Fe_{50}:Pd_{30} (at.%), Alloy 3 650°C annealed condition: a) raw, and b) labelled.

4.3.4. Alloy 4: Nominal Co_{10}:Fe_{15}:Pd_{75} (at.%)

The microstructure of Alloy 4, Nominal Co_{10}:Fe_{15}:Pd_{75} (at.%), Figure 4.82, shows light and dark areas, which were due to coring, given the lack of a distinct interface and the very similar compositions of the areas in Table 4.28 and Figure 4.83. Grain boundaries were also visible for very few grains. The XRD pattern, Figure 4.84, shows that there was only one phase present and that was A1 (γFe,αCo,Pd), although there were very few peaks in the pattern, and the high intensity peak at ~69° (2 Theta) was probably due to preferred orientation. In Figure 4.84, there was an identified peak at ~62° (2 Theta). The ~$FePd_3$ phase was also fitted to the XRD pattern, and it matched one peak only, which was not the unidentified peak.

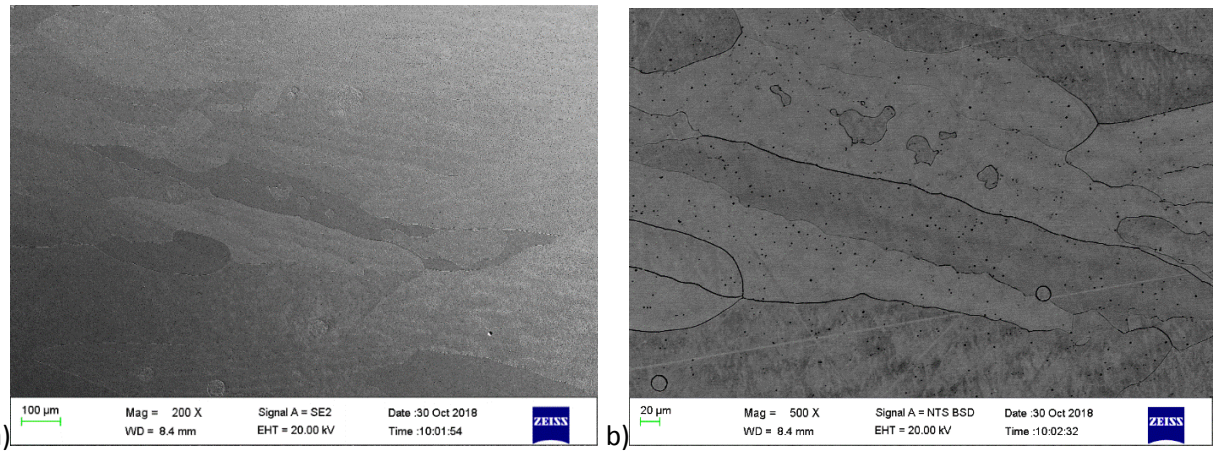


Figure 4.82. SEM-SE and SEM-BSE images of Co_{10}:Fe_{15}:Pd_{75} (at.%), Alloy 4 annealed at 650°C for 1000 h: a) showing contrasting areas, and b) showing contrasting areas and grain boundaries.

Table 4.28. EDX phase analyses for nominal Co_{10}:Fe_{15}:Pd_{75} (at.%), Alloy 4, annealed at 650°C condition.

Phase description	Co	Fe	Pd	Phase
Overall	9.1 ± 0.1	13.8 ± 0.1	77.1 ± 0.1	-
Dark	8.9 ± 0.2	13.8 ± 0.1	77.3 ± 0.2	A1 (γFe,αCo,Pd)
Light	9.1 ± 0.1	13.9 ± 0.1	77.0 ± 0.1	A1 (γFe,αCo,Pd)

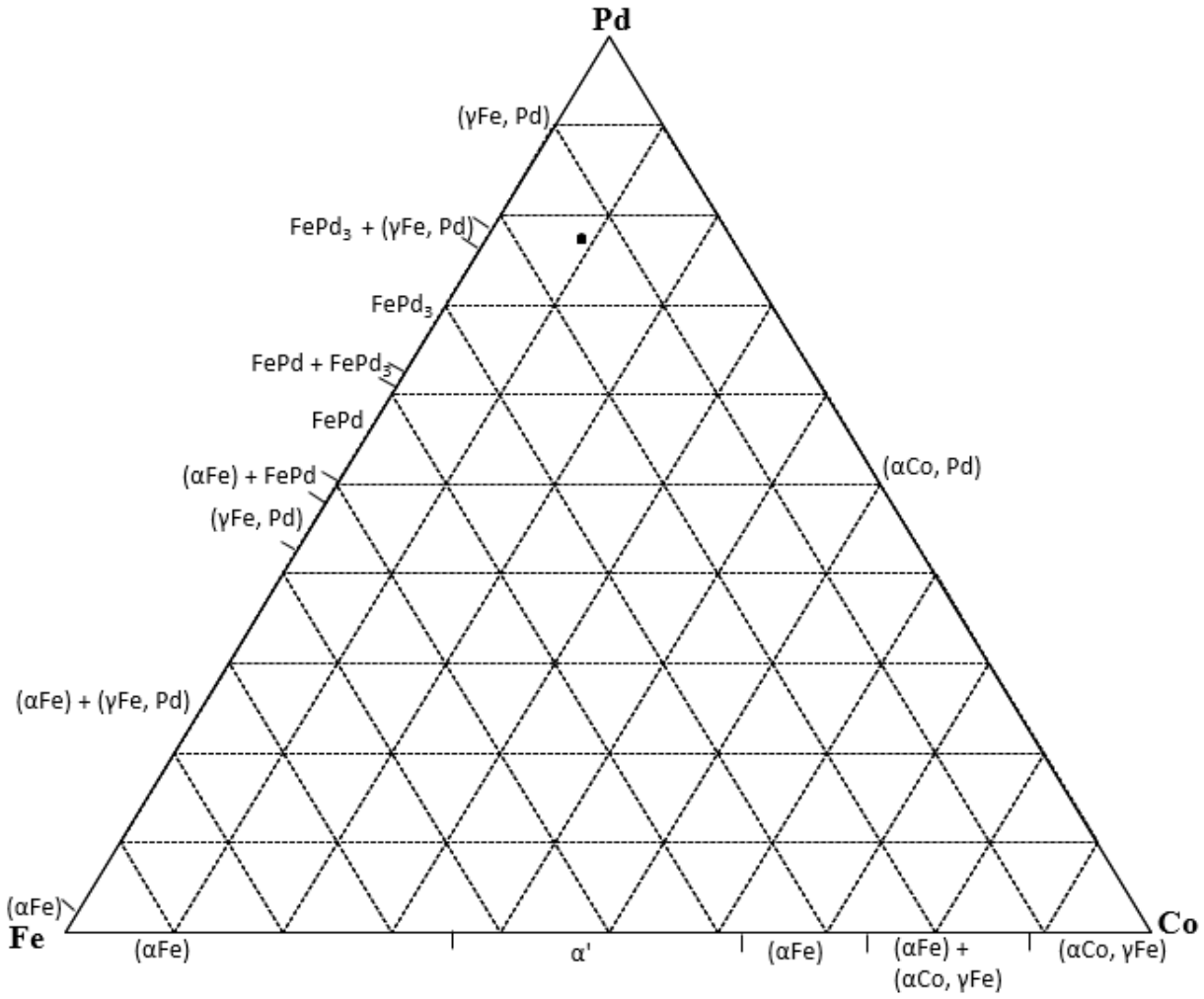


Figure 4.83. EDX analyses of nominal Co_{10}:Fe_{15}:Pd_{75} (at.%), Alloy 4 650°C annealed condition. (■ Overall composition; ● phases).

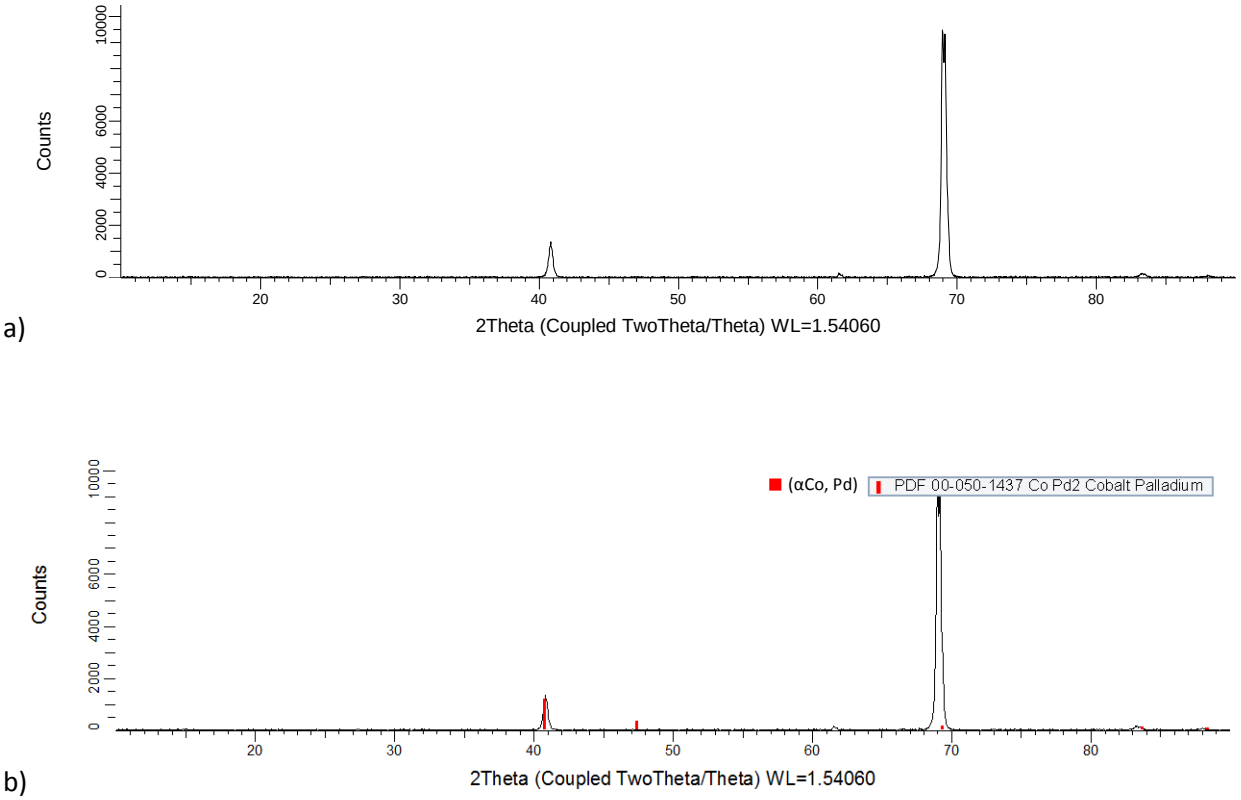


Figure 4.84. XRD patterns for nominal $Co_{10}:Fe_{15}:Pd_{75}$ (at.%), Alloy 4 650°C annealed condition: a) raw, and b) labelled.

4.3.5. Alloy 5: Nominal Co_{30}:Fe_{30}:Pd_{40} (at.%)

Alloy 5, Nominal Co_{30}:Fe_{30}:Pd_{40} (at.%), showed distinctive lamellae which were etched out, creating a distinctive microstructure; the lamellae were not all in the same direction and there were also black patches, Figure 4.85. The black regions had a very different composition from the overall composition of the sample and were rich in Fe, shown in Figure 4.86 and Table 4.29. From XRD (Figure 4.87), the phases present were (αFe) and A1 (γFe,αCo,Pd). The ~FePd and ~$FePd_3$ phases were also attempted as fits the XRD pattern, but they did not match the experimental peaks. There was also a very small peak at ~37° (2 Theta) on Figure 4.87, which could not be matched to any phases.

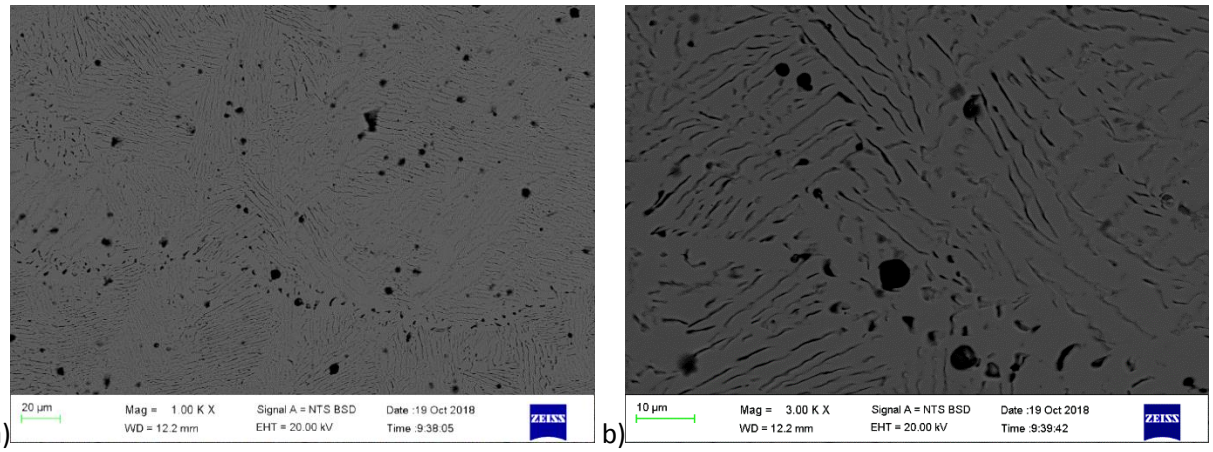


Figure 4.85. SEM-BSE images of Co_{30}:Fe_{30}:Pd_{40} (at.%), Alloy 5 annealed at 650°C for 1000 h showing: a) representative area of the alloy, and b) magnified image.

Table 4.29. EDX phase analyses for nominal Co_{30}:Fe_{30}:Pd_{40} (at.%), Alloy 5, annealed at 650°C condition.

Phase description	Co	Fe	Pd	Phase
Overall	23.9 ± 0.1	28.6 ± 0.1	47.5 ± 0.1	-
Fine two-phase	23.9 ± 0.3	28.2 ± 0.2	47.9 ± 0.3	(αFe) + A1 (γFe,αCo,Pd)

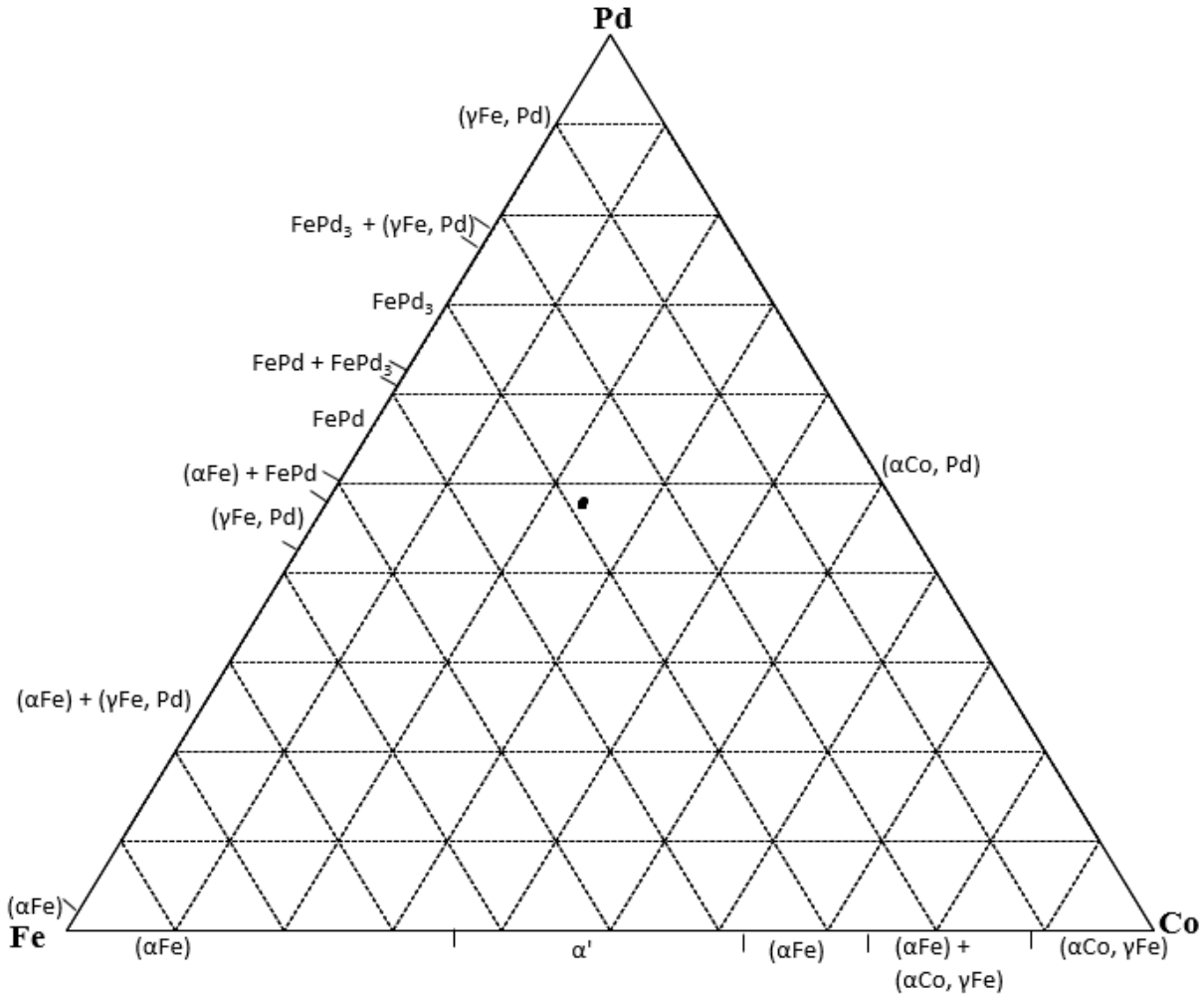


Figure 4.86. EDX analyses of nominal Co_{30}:Fe_{30}:Pd_{40} (at.%), Alloy 5 650°C annealed condition. (■ Overall composition; ● phases).

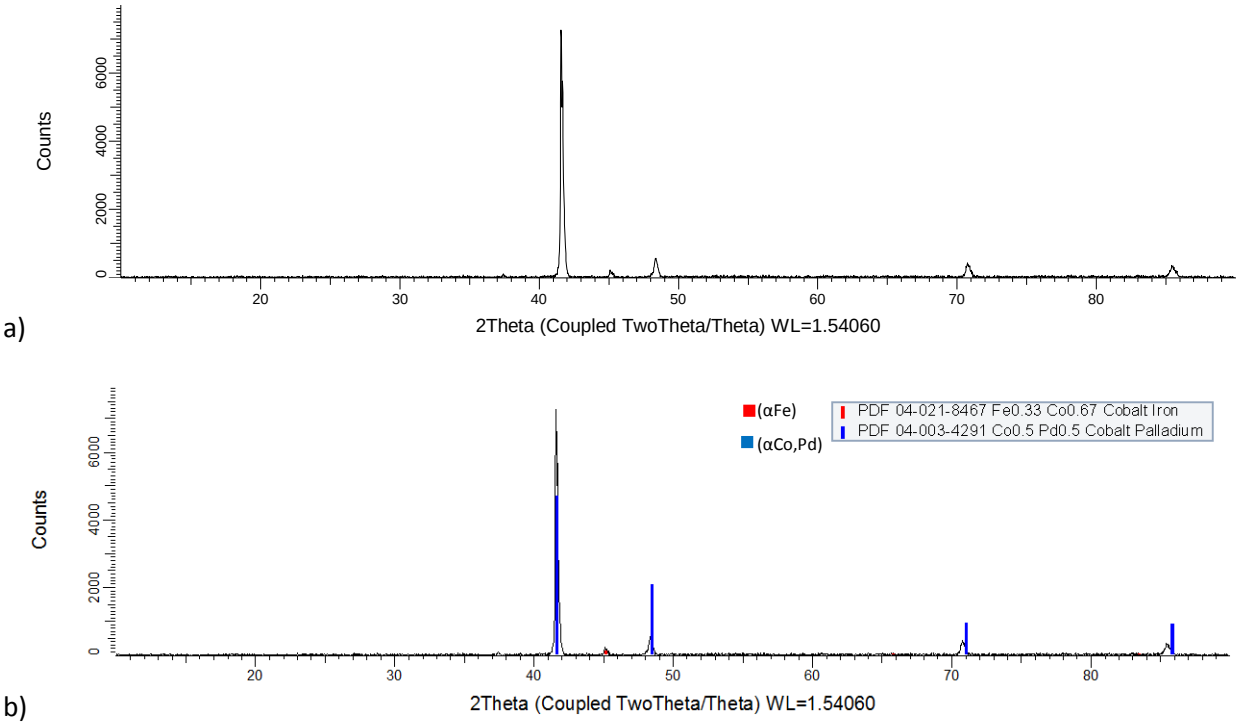


Figure 4.87. XRD patterns for nominal Co_{30}:Fe_{30}:Pd_{40} (at.%), Alloy 5 650°C annealed condition: a) raw, and b) labelled.

4.3.6. Alloy 6: Nominal Co_{50}:Fe_{20}:Pd_{30} (at.%)

For Alloy 6, Nominal Co_{50}:Fe_{20}:Pd_{30} (at.%), the microstructure was very fine (Figure 4.88), hence analyses could not be done on the individual phases. The EDX results on the lighter and darker regions were not similar, shown in Table 4.30 and Figure 4.89. The XRD pattern in Figure 4.90 showed one phase present, A1 (γFe,αCo,Pd), but with different spacings, suggesting two A1 phases with different compositions. The α' pattern was also fitted to the XRD pattern, and there was no match of the experimental peaks.

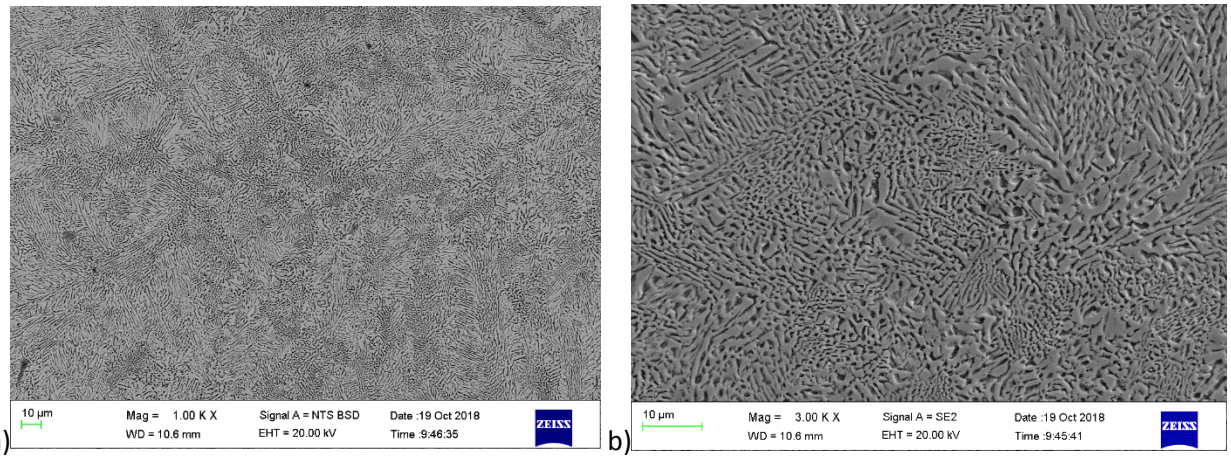


Figure 4.88. SEM images of Co_{50}:Fe_{20}:Pd_{30} (at.%), Alloy 6 annealed at 650°C for 1000 h showing: a) BSE overall of the alloy and b) SE microstructure at higher magnification.

Table 4.30. EDX phase analyses for nominal Co_{50}:Fe_{20}:Pd_{30} (at.%), Alloy 6, annealed at 650°C condition.

Phase description	Co	Fe	Pd	Phase
Overall	35.8 ± 0.1	21.6 ± 0.1	42.6 ± 0.1	-
Light	30.5 ± 0.5	22.3 ± 0.3	47.2 ± 0.5	A1 (γFe,αCo,Pd)
Dark	57.5 ± 1.3	16.8 ± 0.2	25.7 ± 1.5	A1 (γFe,αCo,Pd)

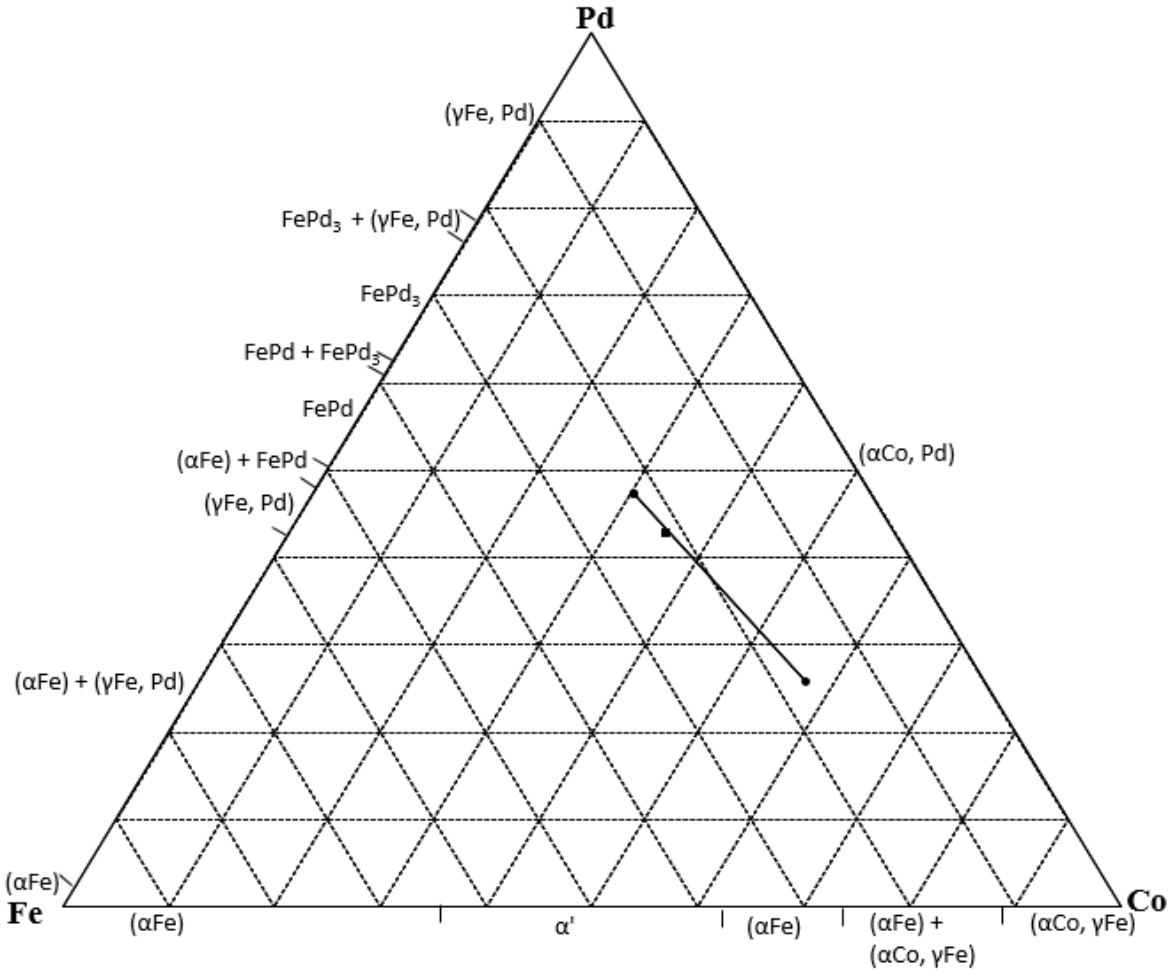


Figure 4.89. EDX analyses of nominal Co_{50}:Fe_{20}:Pd_{30} (at.%), Alloy 6 650°C annealed condition. (■ Overall composition; ● phases)

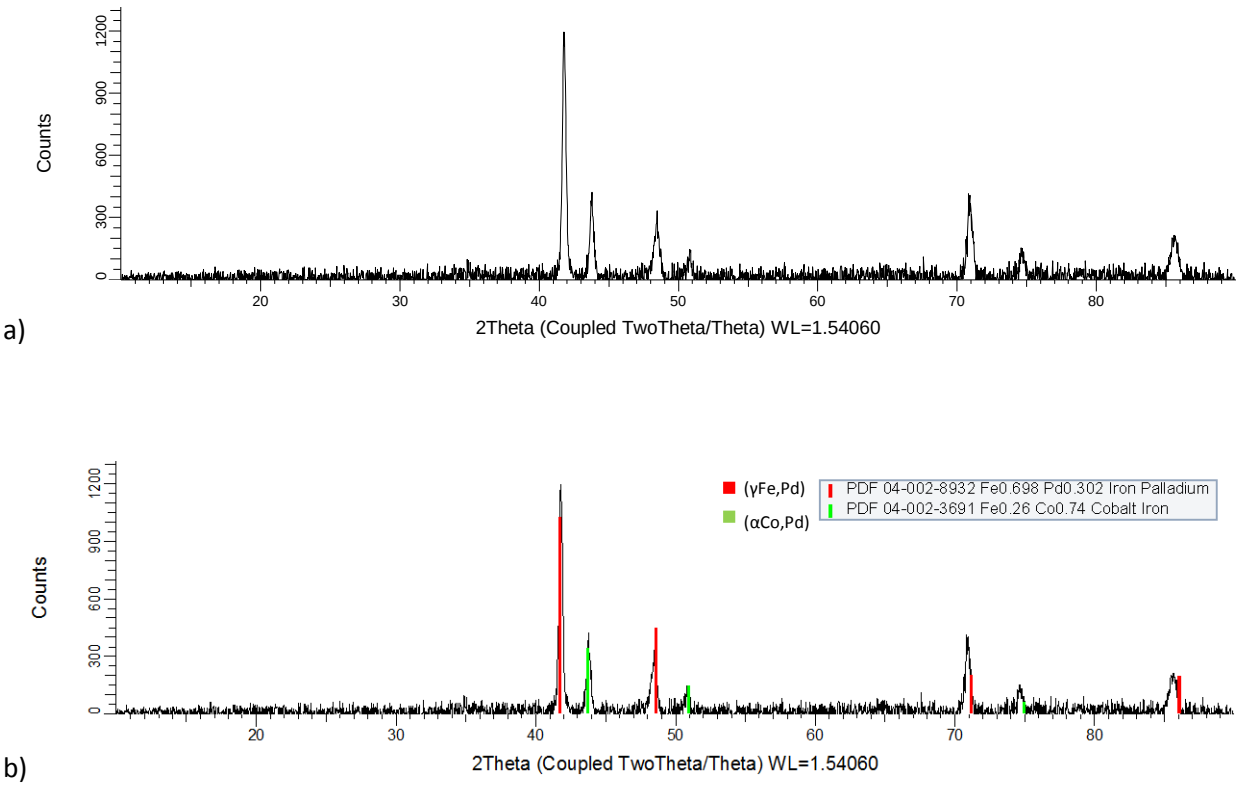


Figure 4.90. XRD patterns for nominal Co_{50}:Fe_{20}:Pd_{30} (at.%), Alloy 6 650°C annealed condition: a) raw, and b) labelled.

4.3.7. Alloy 7: Nominal Co_{10}:Fe_{30}:Pd_{60} (at.%)

For Alloy 7, Nominal Co_{10}:Fe_{30}:Pd_{60} (at.%), Figure 4.91, shows grain boundaries around light and dark regions; this was due to different grain orientations. The different regions had similar compositions of the phases (Table 4.31 and Figure 4.92). The XRD pattern in Figure 4.93 identified two phases: ~$FePd_3$ and A1 (γFe,αCo,Pd), and there was one peak at ~26° (2 Theta) that could not be identified. At higher magnification, there was no discernable microstructure and the entire sample had scratches, which might have masked the microstructure. This sample was very difficult to prepare, and even after several attempts the scratches could not be removed, probably due to the high Pd content, which made it softer.

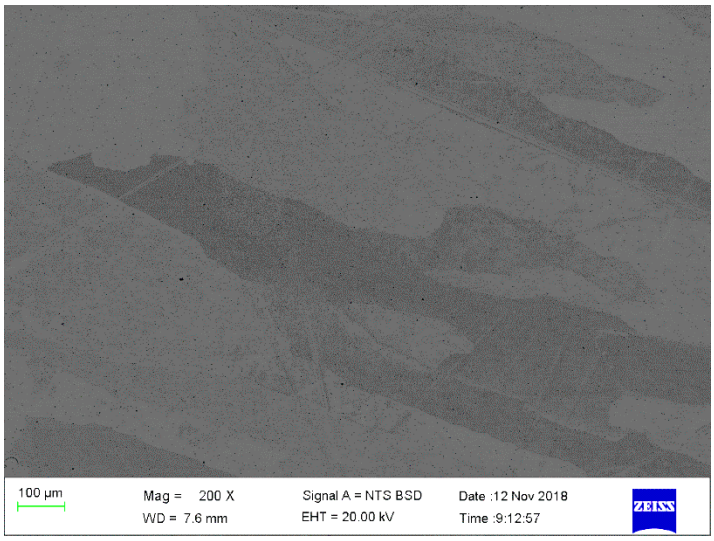


Figure 4.91. SEM-BSE image of Co_{10}:Fe_{30}:Pd_{60} (at.%), Alloy 7 annealed at 650°C for 1000 h showing different grains.

Table 4.31. EDX phase analyses for nominal Co_{10}:Fe_{30}:Pd_{60} (at.%), Alloy 7, annealed at 650°C condition.

Phase description	Co	Fe	Pd	Phase
Overall	9.0 ± 0.1	28.6 ± 0.1	62.4 ± 0.1	-
Dark	9.1 ± 0.2	28.4 ± 0.4	62.5 ± 0.3	A1 (γFe,αCo,Pd)
Light	9.0 ± 0.1	28.7± 0.3	62.3 ± 0.3	A1 (γFe,αCo,Pd)

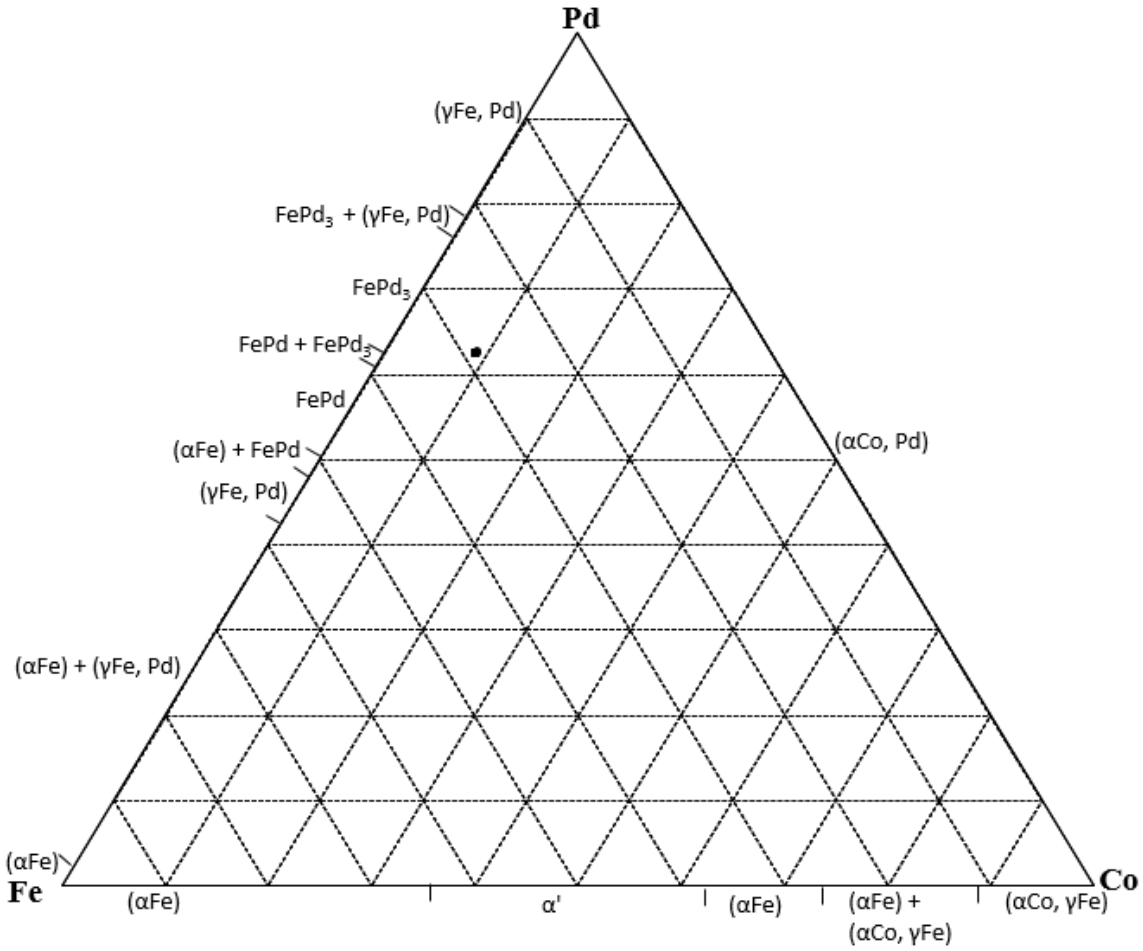


Figure 4.92. EDX analyses of nominal $Co_{10}:Fe_{30}:Pd_{60}$ (at.%), Alloy 7 650°C annealed condition. (■ Overall composition; ● phases)

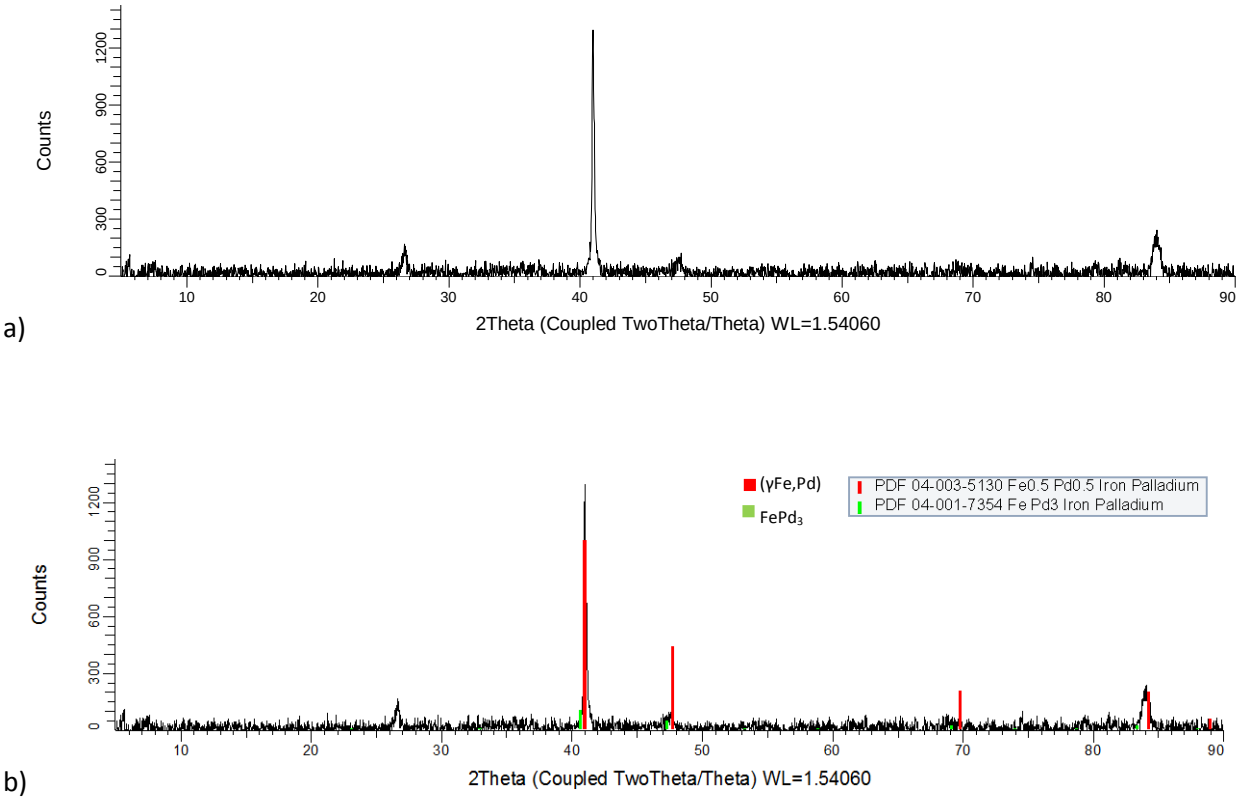


Figure 4.93. XRD patterns for nominal Co_{10}:Fe_{30}:Pd_{60} (at.%), Alloy 7 650°C annealed condition: a) raw, and b) labelled.

4.3.8. Alloy 8: Nominal Co_{25}:Fe_{20}:Pd_{55} (at.%)

Alloy 8, Nominal: Co_{25}:$Fe_{20}Pd_{55}$ (at.%), was a cored solid solution with the dendrites being lighter in contrast, as shown in Figure 4.94. The contrast was due to coring as the compositions of the areas were very similar (Figure 4.95 and Table 4.32), with no distinct interface. The solid solution was A1 (γFe,αCo,Pd), as shown in the XRD pattern in Figure 4.96, there was also (αFe), but it only matched one small peak which did not make it a reliable result, especially considering the relatively low Fe content.

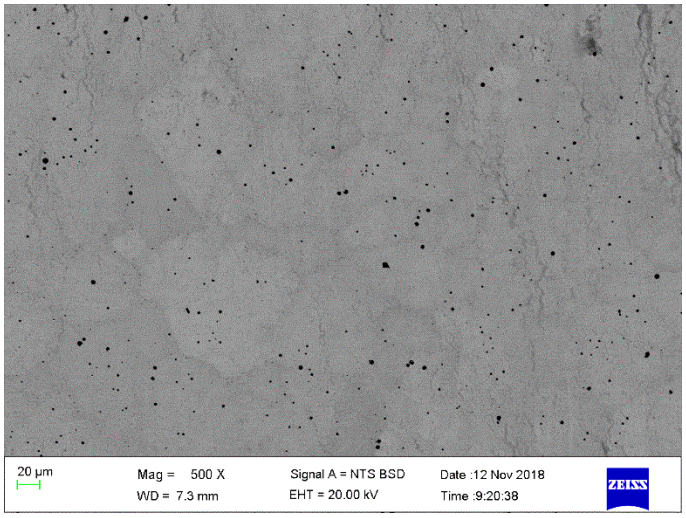


Figure 4.94. SEM-BSE image of Co_{25}:Fe_{20}:Pd_{55} (at.%), Alloy 8 annealed at 650°C for 1000 h showing coring.

Table 4.32. EDX phase analyses for nominal Co_{10}:Fe_{25}:Pd_{55} (at.%), Alloy 8, annealed at 650°C condition.

Phase description	Co	Fe	Pd	Phase
Overall	23.1 ± 0.1	19.2 ± 0.1	57.7 ± 0.1	-
Light	21.3 ± 0.2	19.4 ± 0.2	59.3 ± 0.1	A1 (γFe,αCo,Pd)
Dark	22.5 ± 0.2	19.1 ± 0.1	58.4 ± 0.2	A1 (γFe,αCo,Pd)

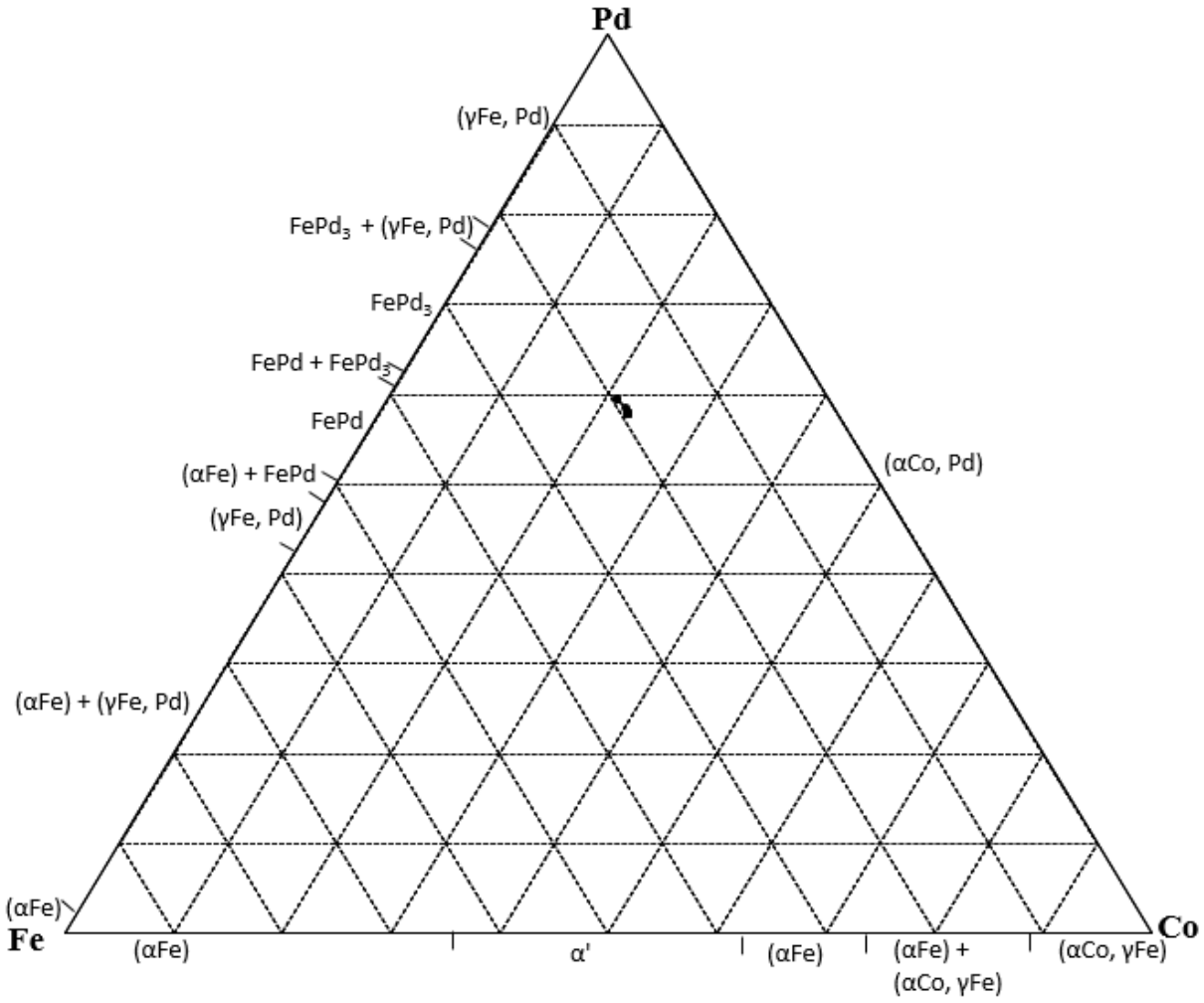


Figure 4.95. EDX analyses of nominal Co_{25}:Fe_{20}:Pd_{55} (at.%), Alloy 8 650°C annealed condition. (■ Overall composition; ● phases)

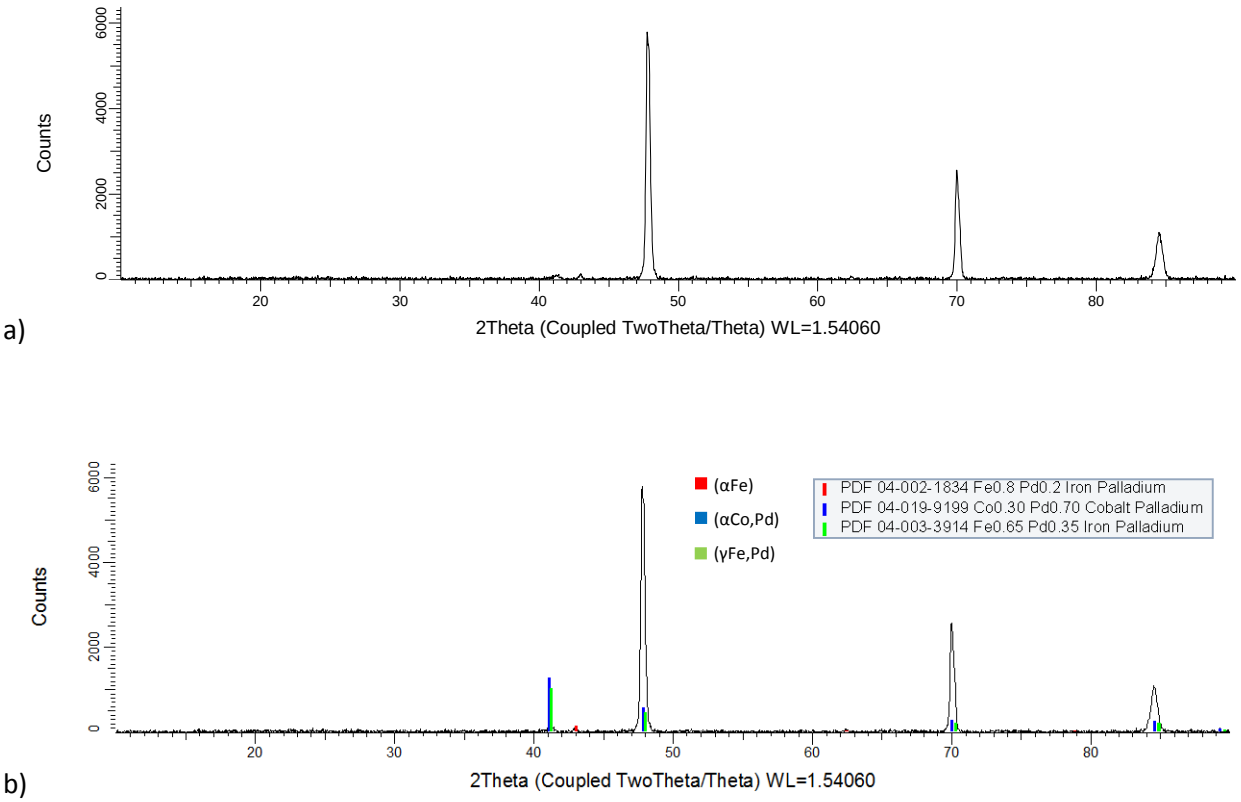


Figure 4.96. XRD patterns for nominal Co_{25}:Fe_{20}:Pd_{55} (at.%), Alloy 8 650°C annealed condition: a) raw, and b) labelled.

4.3.9. Alloy 9: Nominal Co_{10}:Fe_{50}:Pd_{40} (at.%)

The microstructure of Alloy 9, Nominal Co_{10}:Fe_{50}:Pd_{40} (at.%), Figure 4.97 a), shows a fine two-phase microstructure. Figure 4.97 b) shows at higher magnification that a coarse two-phase probably formed first and the area around it was etched more to reveal a fine "eutectoid-like" microstructure. Figure 4.98 and Table 4.33 shows how similar the compositions of the different areas were. From XRD (Figure 4.99), the phases were (αFe) and A1 (γFe,αCo,Pd). When the larger apparent single-phase areas were analysed, there were large errors for the light phase, but considering its contrast and the highest possible Pd content (with the large errors), the light phase was surmised to be A1 (γFe,αCo,Pd), and the dark phase was (αFe).

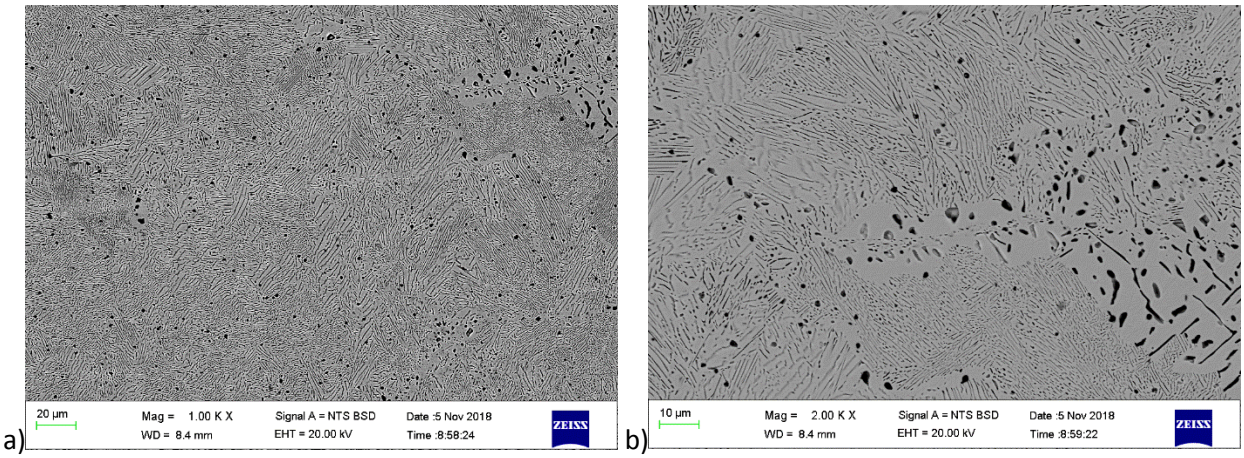


Figure 4.97. SEM-BSE images of Co_{10}:Fe_{50}:Pd_{40} (at.%), Alloy 9 annealed at 650°C for 1000 h showing: a) fine microstructure and b) fine and coarse two-phase regions.

Table 4.33. EDX phase analyses for nominal Co_{10}:Fe_{30}:Pd_{40} (at.%), Alloy 9, annealed at 650°C condition.

Phase description	Co	Fe	Pd	Phase
Overall	5.6 ± 0.1	45.8 ± 0.1	48.6 ± 0.1	-
Coarse two-phase	5.5 ± 0.1	45.6 ± 0.1	48.9 ± 0.2	(αFe) + A1 (γFe,αCo,Pd)
Fine two-phase	5.6 ± 0.2	46.0 ± 0.2	48.4 ± 0.3	(αFe) + A1 (γFe,αCo,Pd)
Dark spots	5.5 ± 0.2	45.3 ± 0.1	49.2 ± 0.3	Mainly (αFe) with A1 (γFe,αCo,Pd)
Large light	5.8 ± 0.6	48.0 ± 4.3	46.2 ± 4.9	Mainly A1 (γFe,αCo,Pd) with (αFe)

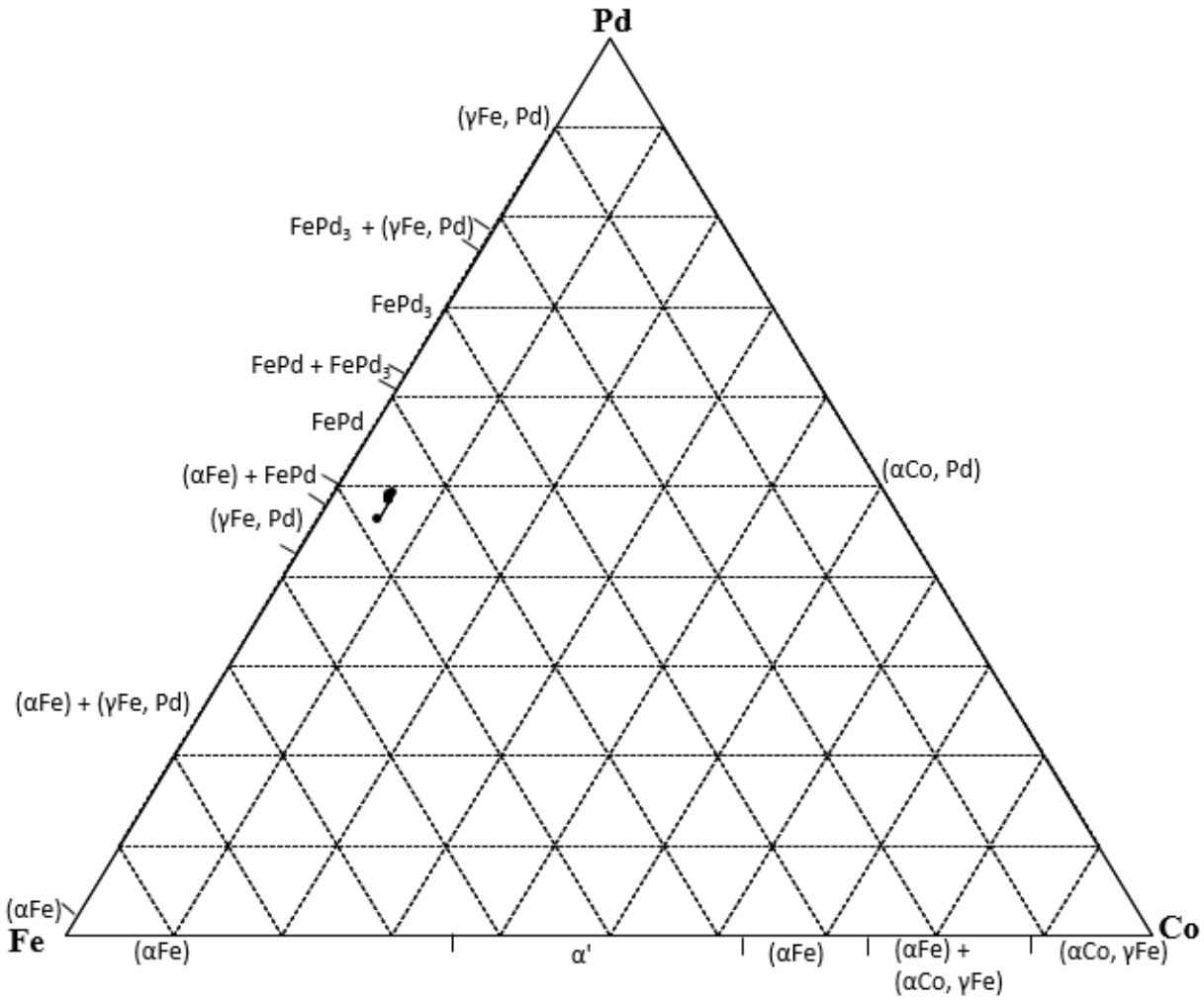


Figure 4.98. EDX analyses of nominal Co_{10}:Fe_{50}:Pd_{40} (at.%), Alloy 9 650°C annealed condition. (■ Overall composition; ● phases)

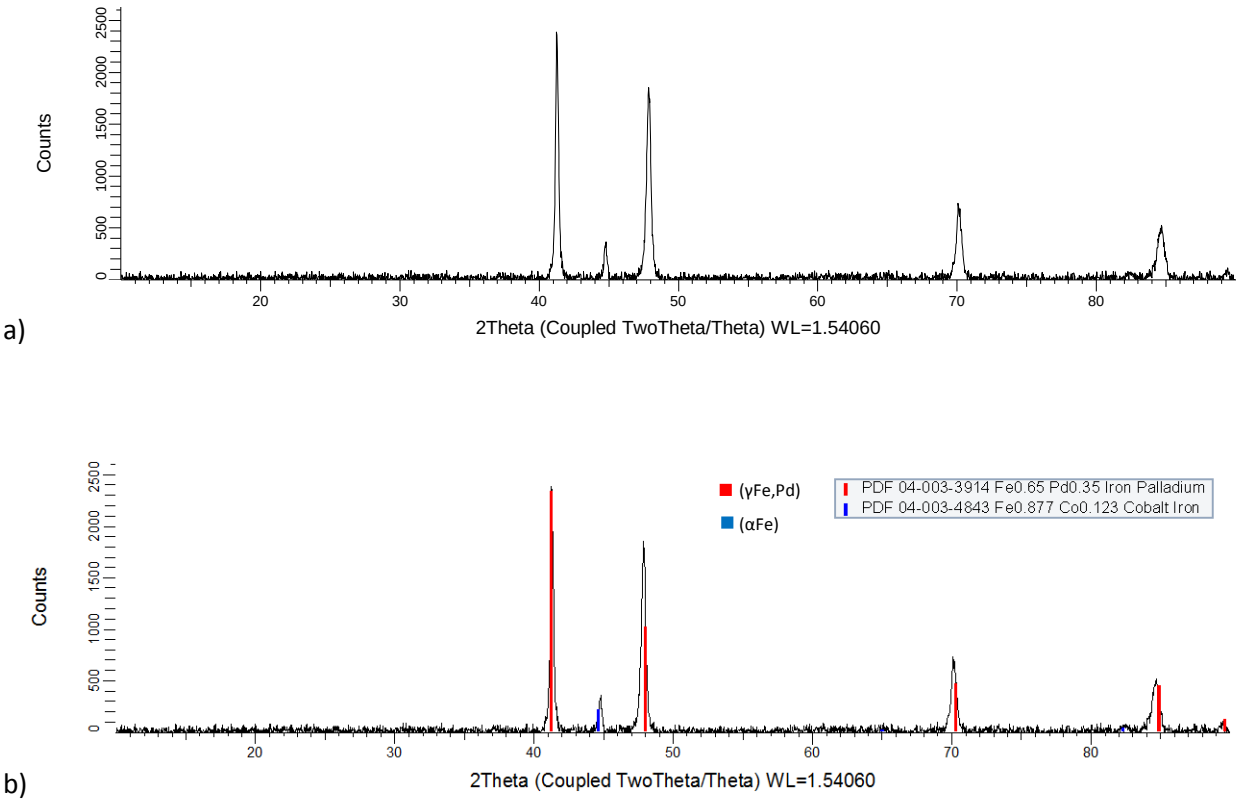


Figure 4.99. XRD patterns for nominal Co_{10}:Fe_{50}:Pd_{40} (at.%), Alloy 9 650°C annealed condition: a) raw, and b) labelled.

4.3.10. Alloy 10: Nominal Co_{40}:Fe_{30}:Pd_{30} (at.%)

Figure 4.100 (Alloy 10, Nominal Co_{40}:Fe_{30}:Pd_{30} (at.%)) shows two phases, the coarse light and dark phases were observed first, and the fine two-phase regions were only revealed after further etching. Figure 4.101 shows the compositions of the different phases. The XRD pattern (Figure 4.102) shows that two phases were present, A1 (γFe,αCo,Pd) and (αFe). The light phase was A1 (γFe,αCo,Pd) (Table 4.34), the dark phase was surmised to be (αFe), and the fine phase mixture was (αFe) + A1 (γFe,αCo,Pd).

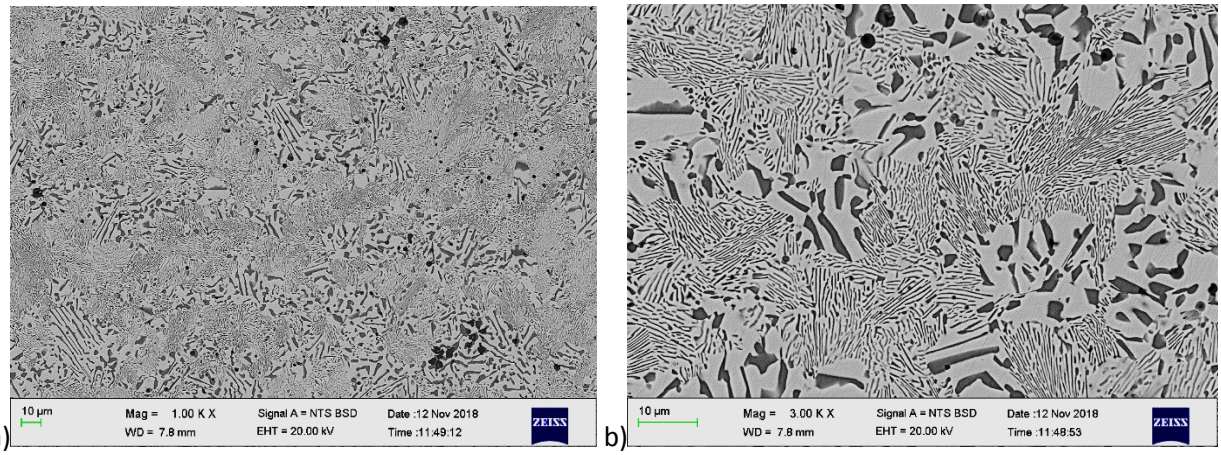


Figure 4.100. SEM-BSE images of Co_{40}:Fe_{30}:Pd_{30} (at.%), Alloy 10 annealed at 650°C for 1000 h showing: a) an overall, and b) formation of fine phase, light and dark phases.

Table 4.34. EDX phase analyses for nominal Co_{40}:Fe_{30}:Pd_{30} (at.%), Alloy 10, annealed at 650°C condition.

Phase description	Co	Fe	Pd	Phase
Overall	34.3 ± 0.1	28.9 ± 0.1	36.8 ± 0.1	-
Dark	65.3 ± 1.1	30.2 ± 0.1	4.5 ± 1.2	(αFe)
Light	25.4 ± 1.9	28.1 ± 0.1	46.5 ± 1.9	A1 (γFe,αCo,Pd)
Fine phase mixture	33.4 ± 0.8	28.5 ± 0.1	38.1 ± 0.8	(αFe) + A1 (γFe,αCo,Pd)

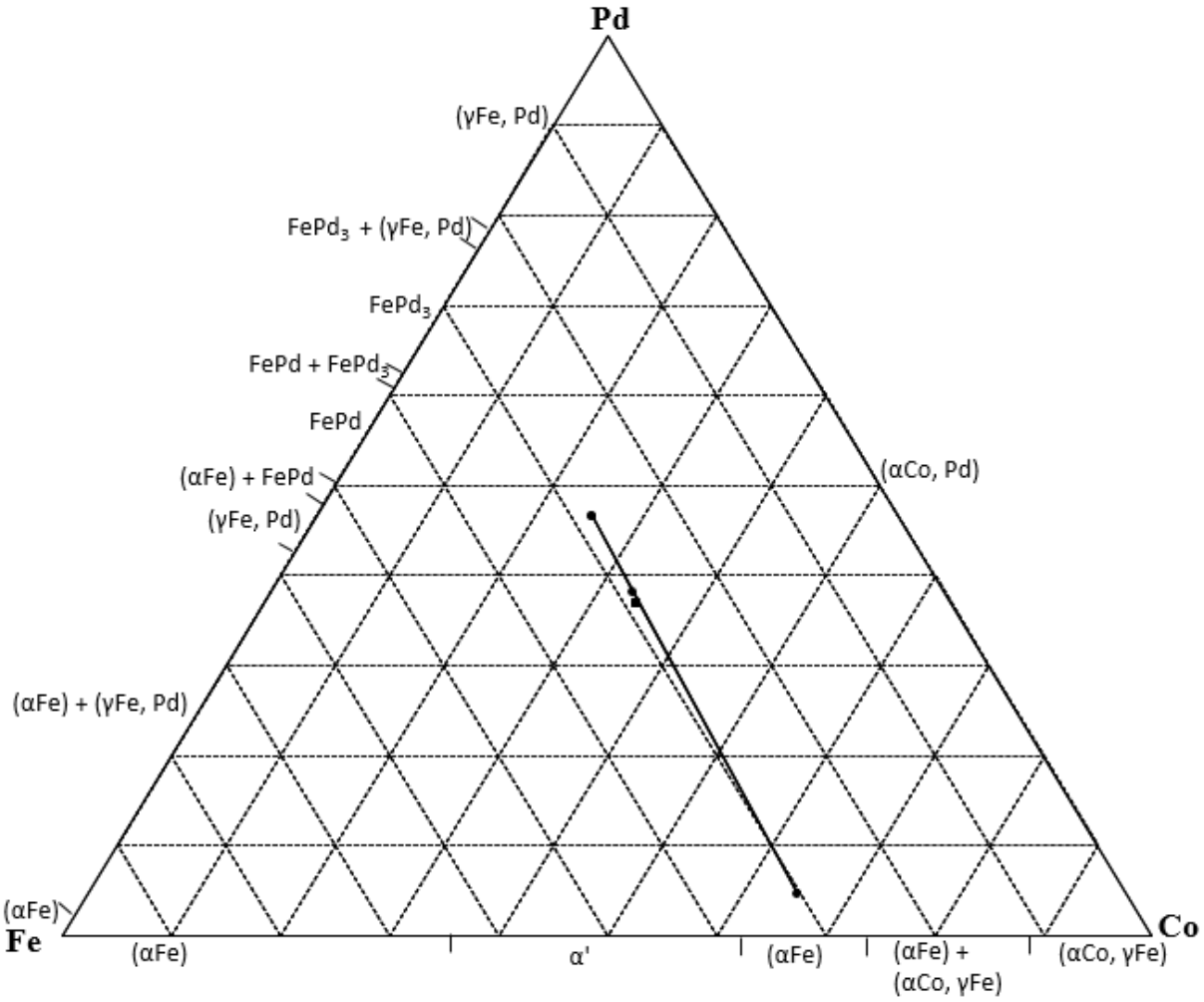


Figure 4.101. EDX analyses of nominal Co_{40}:Fe_{30}:Pd_{30} (at.%), Alloy 10 650°C annealed condition. (■ Overall composition; ● phases)

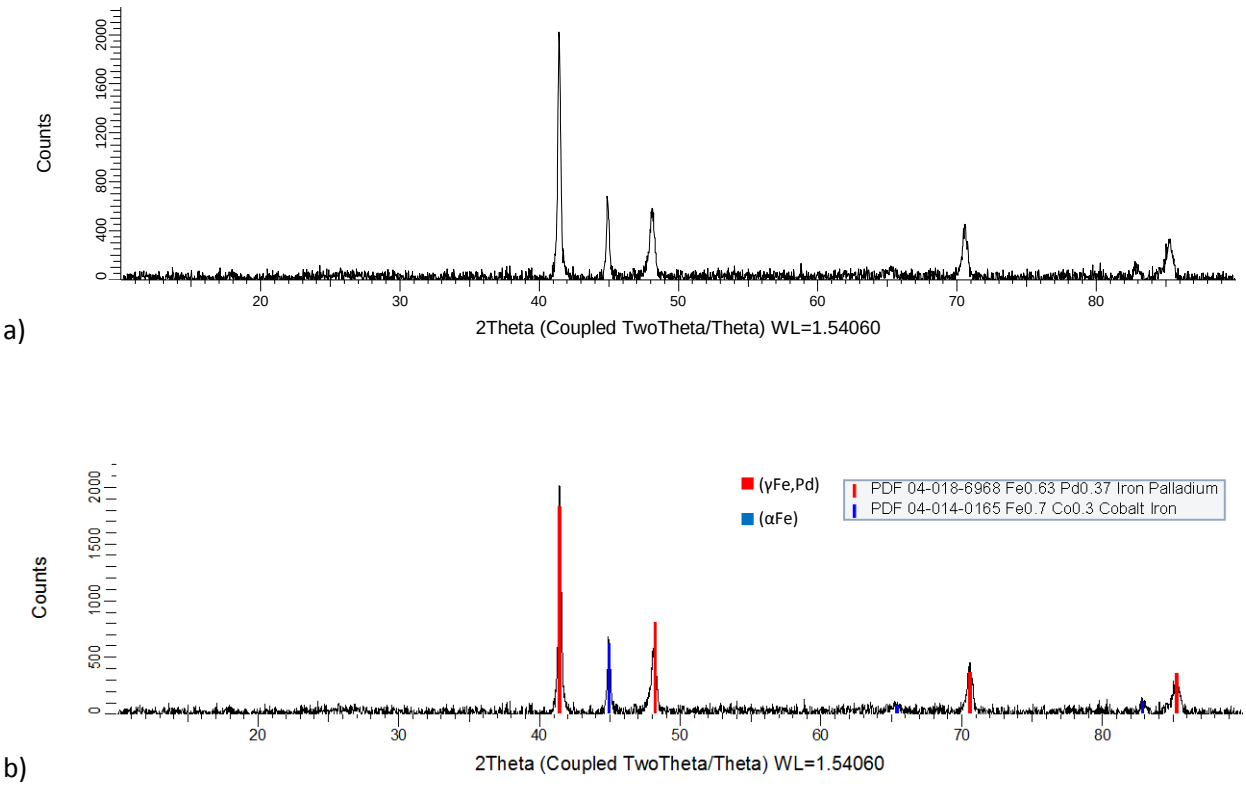


Figure 4.102. XRD patterns for nominal Co_{40}:Fe_{30}:Pd_{30} (at.%), Alloy 10 650°C annealed condition: a) raw, and b) labelled.

4.3.11. Alloy 11: Nominal Co_{20}:Fe_{60}:Pd_{20} (at.%)

Figure 4.103 a) shows that Alloy 11, Nominal Co_{20}:Fe_{60}:Pd_{20} (at.%), formed dark and light regions, but at higher magnification these were fine two-phase regions. The apparent dendrites comprised finer two-phase regions, and were probably due to the coring on solidification. The difference between the dendritic and interdendritic regions was due to the difference in proportions of the two phases. The compositions of the two areas were very different, Figure 4.104 and Table 4.35. The XRD pattern (Figure 4.105) identified two phases, (αFe) and A1 (γFe,αCo,Pd).

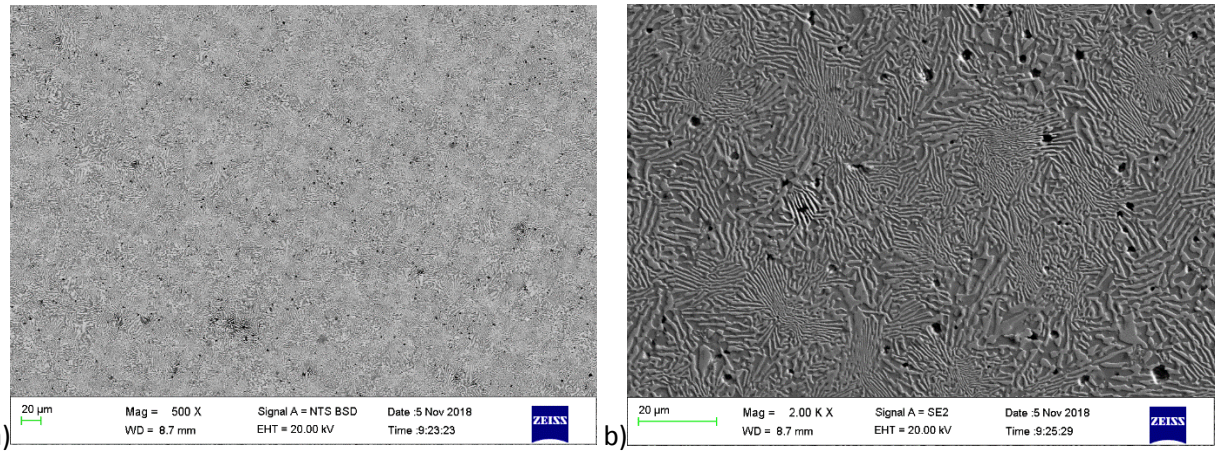


Figure 4.103. SEM images of Co_{20}:Fe_{60}:Pd_{20} (at.%), Alloy 11 annealed at 650°C for 1000 h showing: a) BSE apparent dendrites and b) SE higher magnification fine phase.

Table 4.35. EDX phase analyses for nominal Co_{20}:Fe_{60}:Pd_{20} (at.%), Alloy 11, annealed at 650°C condition.

Phase description	Co	Fe	Pd	Phase
Overall	18.4 ± 0.1	57.7 ± 0.1	23.9 ± 0.1	-
Dark	28.8 ± 0.4	66.7 ± 0.7	4.5 ± 1.1	(αFe)
Light	15.6 ± 1.9	55.5 ± 1.5	28.9 ± 3.4	A1 (γFe,αCo,Pd)

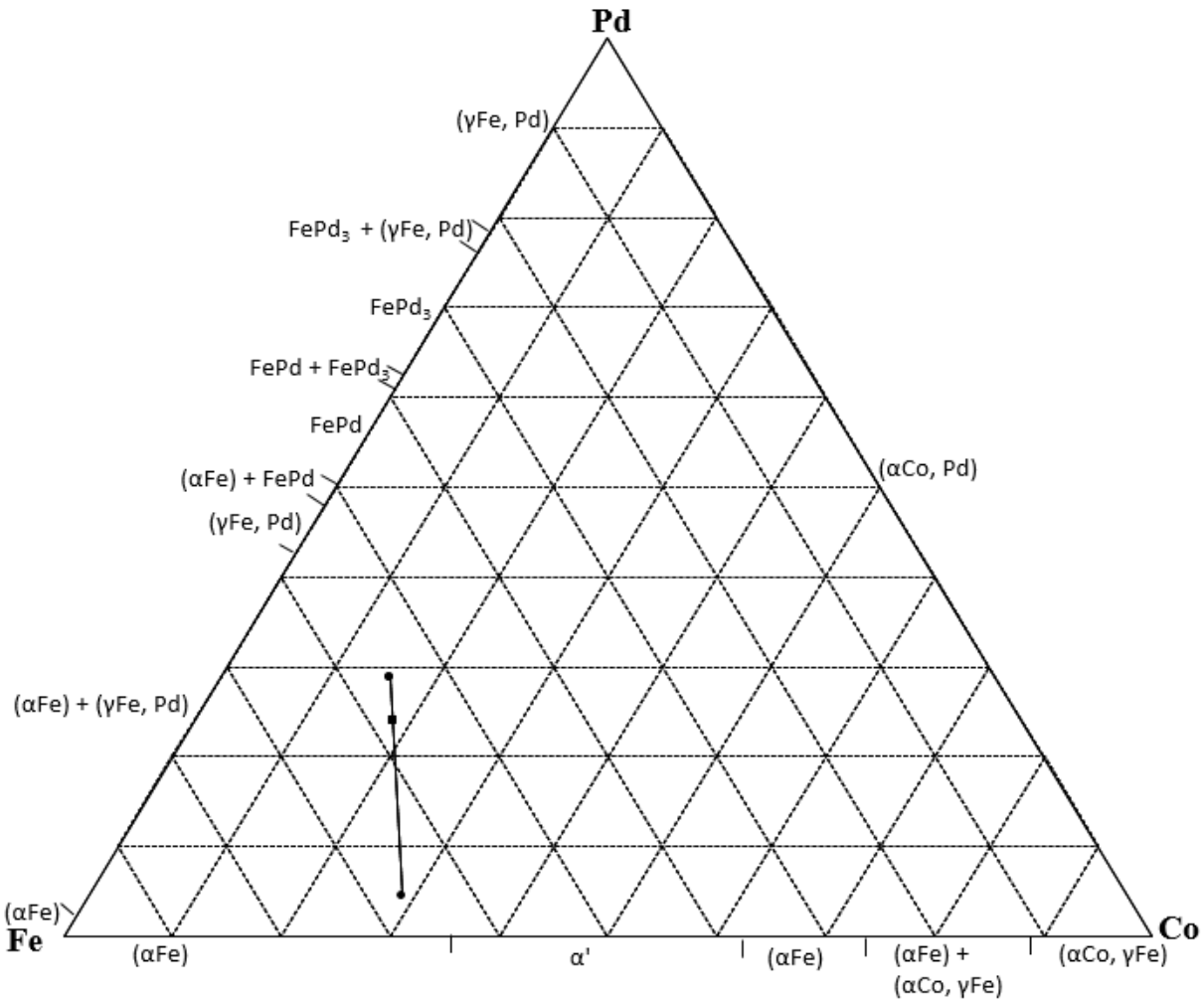


Figure 4.104. EDX analyses of nominal Co_{20}:Fe_{60}:Pd_{20} (at.%), Alloy 11 650°C annealed condition. (■ Overall composition; ● phases)

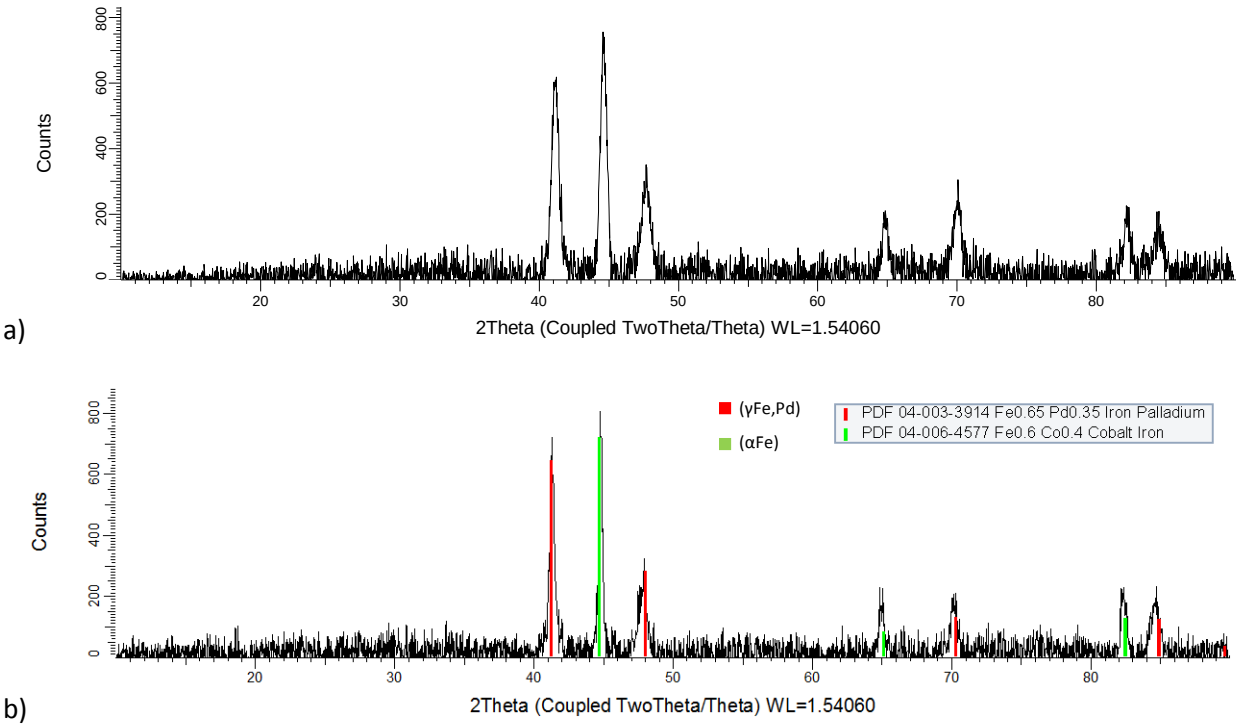


Figure 4.105. XRD patterns for nominal Co_{20}:Fe_{60}:Pd_{20} (at.%), Alloy 11 650°C annealed condition: a) raw, and b) labelled.

4.3.12. Alloy 12: Nominal Co_{60}:Fe_{20}:Pd_{20} (at.%)

For Alloy 12, Nominal Co_{60}:Fe_{20}:Pd_{20} (at.%), the microstructure showed apparent dendrites, and at higher magnification (Figure 4.106 b), a fine two-phase microstructure was visible. The dendritic and interdendritic areas had different amounts of the fine second phase. Although the phases are the same (Table 4.36 and Figure 107) the compositions of the dark and light regions were not similar. The phase found by XRD, Figure 4.108 was A1 (γFe,αCo,Pd), but with two different d-spacings, suggesting two different A1 phase compositions.

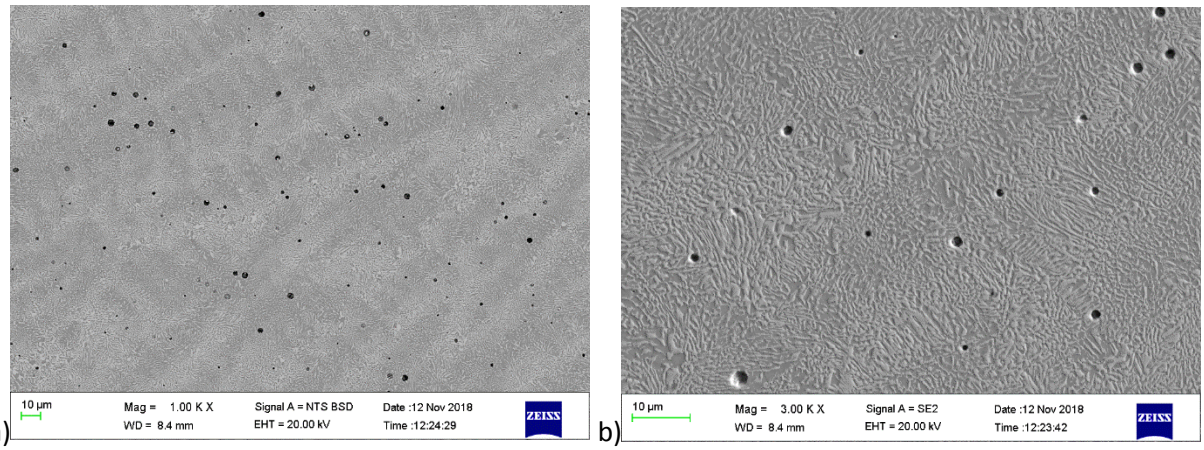


Figure 4.106. SEM-BSE images of Co_{60}:Fe_{20}:Pd_{20} (at.%), Alloy 12 annealed at 650°C for 1000 h showing: a) dendrites, and b) higher magnification decomposition of dendrites.

Table 4.36. EDX phase analyses for nominal Co_{60}:Fe_{20}:Pd_{20} (at.%), Alloy 12, annealed at 650°C condition.

Phase description	Co	Fe	Pd	Phase
Overall	57.7 ± 0.1	19.1 ± 0.1	23.2 ± 0.1	-
Dark	70.5 ± 2.8	16.4 ± 0.8	13.1 ± 2.0	A1 (γFe,αCo,Pd)
Light	35.4 ± 3.8	23.5 ± 1.1	41.1 ± 2.7	A1 (γFe,αCo,Pd)

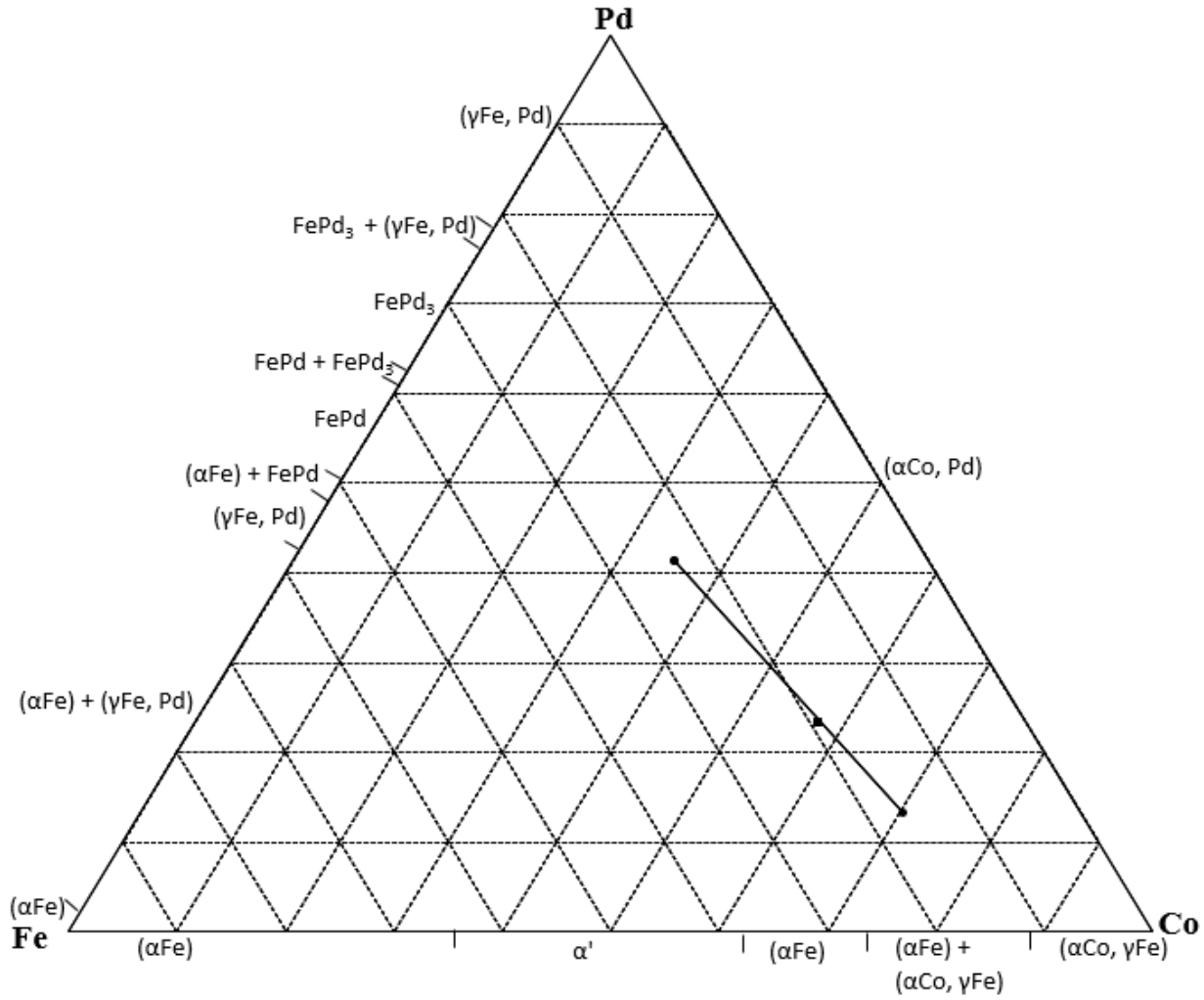


Figure 4.107. EDX analyses of nominal Co_{60}:Fe_{20}:Pd_{20} (at.%), Alloy 12 650°C annealed condition. (■ Overall composition; ● phases)

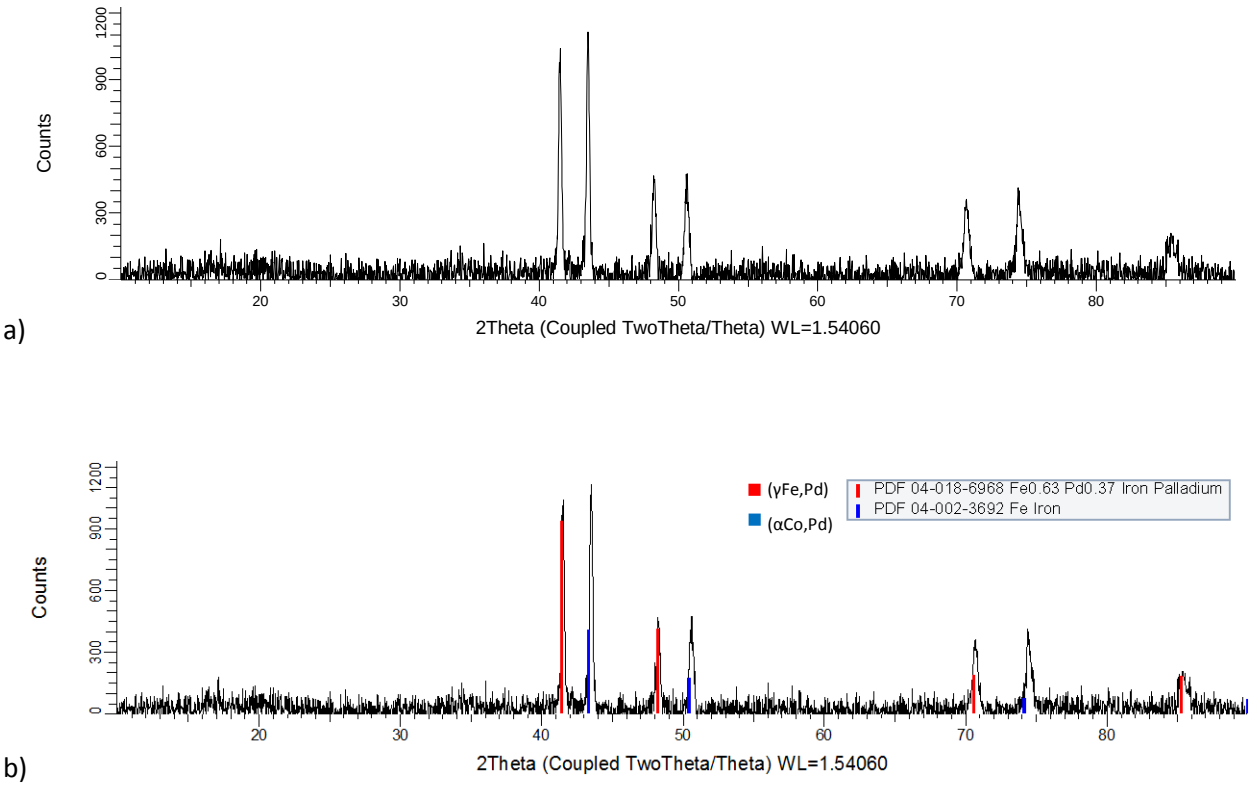


Figure 4.108. XRD patterns for nominal $Co_{60}:Fe_{20}:Pd_{20}$ (at.%), Alloy 12 650°C annealed condition: a) raw, and b) labelled.

Chapter 5: - Microhardness results

Table 5.1 shows all the hardness results for the alloys. The hardness of the alloys increased with increased Fe and decreased with increased Pd.

Table 5.1. Vickers microhardness values and errors for all alloys.

Nominal composition (at.%)	**As-cast Hardness (HV)**	**1000°C Annealed Hardness (HV)**	**650°C Annealed Hardness (HV)**
Alloy1: Co_{30}:Fe_{60}:Pd_{10}	241 ± 9	382 ± 3	285 ± 3
Alloy 2: Co_{6}:Fe_{44}:Pd_{50}	164 ± 7	216 ± 3	186 ± 5
Alloy 3: Co_{20}:Fe_{50}:Pd_{30}	238 ± 6	252 ± 7	252 ± 5
Alloy 4: Co_{10}:Fe_{15}:Pd_{75}	118 ± 6	119 ± 4	119 ± 5
Alloy 5: F Co_{30}:e_{30}:Pd_{40}	182 ± 6	213 ± 3	194 ± 6
Alloy 6: Co_{50}:Fe_{20}:Pd_{30}	189 ± 6	205 ± 6	200 ± 6
Alloy7: Co_{10}:Fe_{30}:Pd_{60}	171 ± 7	183 ± 7	172 ± 6
Alloy 8: Co_{25}:Fe_{20}:Pd_{55}	172 ± 1	176 ± 1	172 ± 7
Alloy 9: Co_{10}:Fe_{50}:Pd_{40}	189 ± 2	191 ± 6	173 ± 8
Alloy 10: Co_{40}:Fe_{30}:Pd_{30}	216 ± 9	220 ± 8	190 ± 2
Alloy 11: Co_{20}:Fe_{60}:Pd_{20}	526 ± 10	530 ± 7	529 ± 2
Alloy 12: Co_{60}:Fe_{20}:Pd_{20}	190 ± 4	201 ± 3	197 ± 4

Figures 5.1-5.3 shows the data from Table 5.1 plotted onto the ternary diagrams with the overall value for each alloy. All three figures follow the same trend.

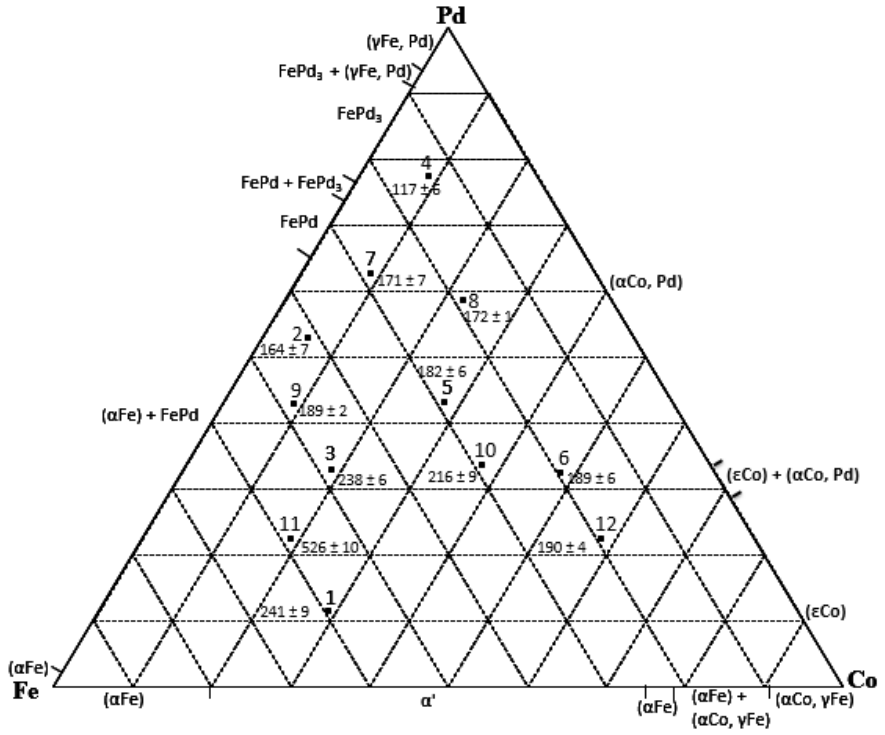


Figure 5.1. Ternary plot with microhardness values and errors for as-cast alloys. (■ Overall composition)

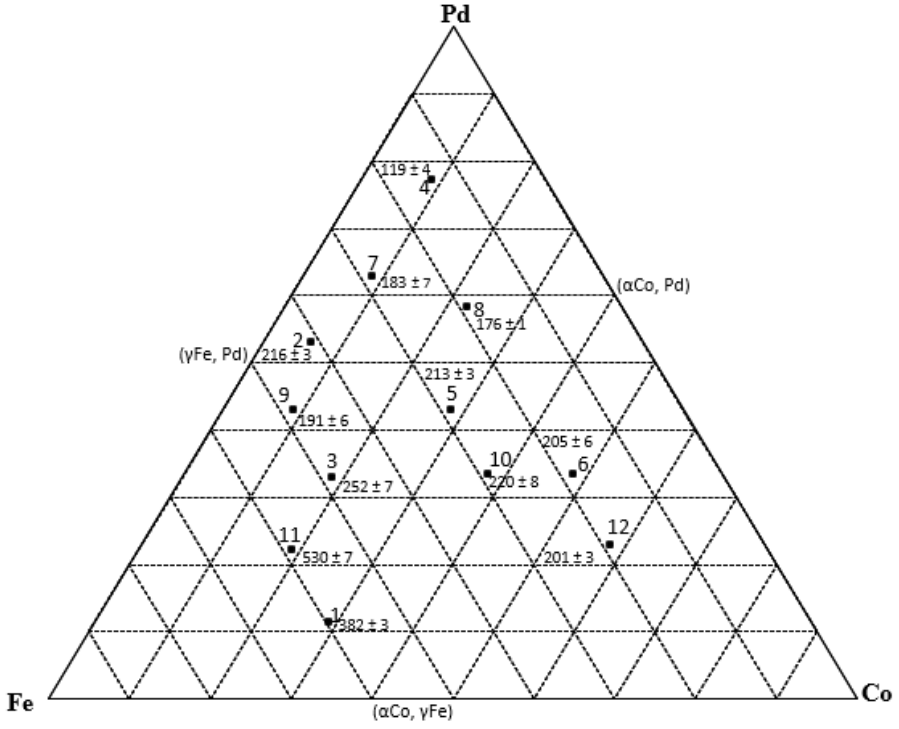


Figure 5.2. Ternary plot with microhardness values and errors for alloys annealed at 1000°C. (■ Overall composition)

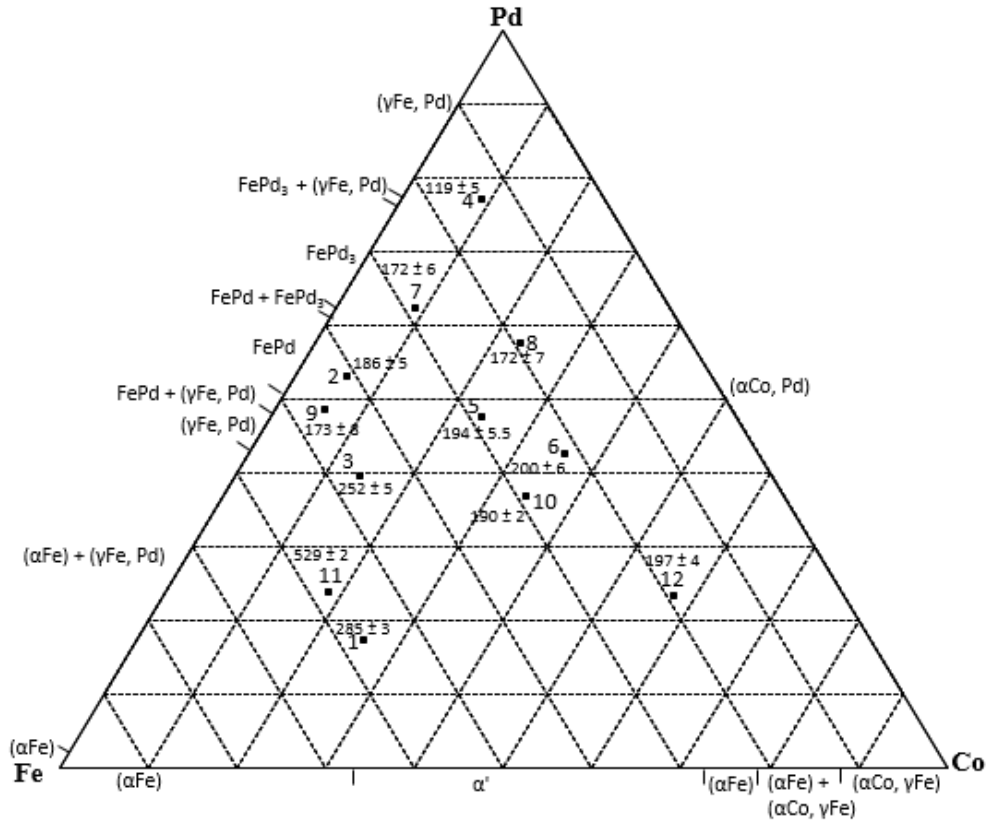


Figure 5.3.Ternary plot with hardness values and errors for alloys annealed at 650°C. (■ Overall composition)

Chapter 6: Discussion

6.1. Interpretation of the data

The system was very difficult to interpret for three major reasons: the difficulty in identifying XRD peaks, the difficulty in making the samples homogenous, and the fineness of some of the microstructures after annealing. The latter meant that accurate EDX measurements could not be obtained, because the volume of interaction was larger than the size of the phase, so signals were always collected from two phases. It would be expected that the samples might be difficult to make homogenous, because the melting points are quite high (1495°C for Co [1990Mas], 1538°C for Fe [1990Mas], and 1555°C for Pd [1990Mas]), and the samples were only homogenised for 1000 hours. Often ampules used for longer times than this at high temperatures collapse, and the samples become contaminated [1986Cor]. Since the samples were made by arc melting, preferred orientation could be expected on solidification, and this was indicated in the XRD patterns, because one particular peak was consistently higher than expected. The preferred orientation was not always removed on annealing, showing that homogeneity was probably not attained.

For XRD, one difficulty was that the A1 (γFe,αCo,Pd) fcc phase extended over almost the entire composition range, and so was difficult to match with existing XRD peaks [2018Dif]. This meant that often peaks from two different binary systems were matched, even though it was one phase, for example as-cast Alloy 5 (Figure 4.15), as-cast Alloy 8 (Figure 4.24), Alloy 2 after annealing at 1000°C (Figure 4.42), Alloy 3 after annealing at 1000°C (Figure 4.45), Alloy 5 after annealing at 1000°C (Figure 4.51), Alloy 9 after annealing at 1000°C (Figure 4.63), and Alloy 8 after annealing at 650°C (Figure 4.96). Conversely, after annealing at 650°C, Alloys 6 (Figure 4.90) and 12 (Figure 4.107) showed two distinct sets of A1 (γFe, αCo, Pd) peaks, showing that there was a miscibility gap.

A second reason for the difficulty in interpreting the XRD patterns of the system was that some of the peaks overlapped between the different phases, due to the similar distances between the different atoms in the planes. This meant that care had to be taken to use several peaks to identify the phases. Examples of this are as-cast Alloy 4 (Figure 4.12), as-cast Alloy 7 (Figure 4.21), as-cast Alloy 8 (Figure 4.24) and Alloy 7 annealed at 650°C (Figure 4.93).

A third reason for the difficulty in interpreting the XRD patterns was that the peaks were sometimes small, and this meant that there were few peaks to use in identification. The preferred orientation exacerbated this problem. The samples were probably smaller than they should have been, because of a shortage of expensive palladium, and these small samples would have led to poor patterns. One particular bad example of a very low signal to noise ratio was as-cast Alloy 11 (Figure 4.33), even though it was in the polished condition.

Using XRD to distinguish between the ordered phases was also problematic, because a lot of the peaks had very low intensity, especially $FePd_3$ (Appendix A, [2018Dif]) and α' (Appendix A, [2018Dif]). This made the ordered phases very difficult to distinguish, because the important peaks were often lost in the background.

6.2. As-cast alloys

The first difficulty in this work was that the alloys had very different responses to etching, and could not all be etched using the same method. Alloy 1 used the least aggressive etching technique of electro-etching in a solution of H_2O + HCl, with steel wire as a cathode. Alloys 2, 3, 4, 5, 6, 9, 10, 11 and 12 were immersion etched in a solution of H_2O + HCl + HNO_3, using steel wire as the cathode. Alloys 7 and 8 were electro-etched in a solution of H_2O + HCl, with graphite as a cathode. Many different etching techniques were used due to the different compositions of the alloys, and the alloys with more Pd used the more aggressive etching technique.

Due to the samples containing Pd, a high acceleration voltage (20 kV) had to be used on the SEM in order to excite the Pd X-rays for EDX analysis. Using a high kV causes the electron beam to spread out further [1981Gol], making the collection area for accurate EDX analysis larger (typically $\geq$2 microns), hence the samples with fine microstructures could not be accurately analysed in the SEM.

Given the very wide A1 (γFe,αCo,Pd) liquidus of the system and the few solid phases [1958Kup, 1959Kup, 1961Gri, 1961Kup, 1992Rag], it was not surprising that the alloys were cored, because they mainly solidified to the same phase, A1 (γFe,αCo,Pd). In some of the samples, there was so little difference

between the compositions of the cored phases that they were within the experimental errors. None of the microstructures found were similar to those of the previous workers [1958Kup, 1959Kup, 1961Gri, 1961Kup], although the decomposition of Alloy 1 would be expected from the ~25°C isothermal section of Raghavan [1992Rag], because that alloy composition lies in a two-phase region. However, the phases found here were A1 (γFe,αCo,Pd) and (αFe), whereas Raghavan [1992Rag] deduced that the phases should be A1 (γFe,αCo,Pd) and α'. Thus, Alloy 1 suggests a wider A1 (γFe,αCo,Pd) + (αFe) phase field than Raghavan [1992Rag] (Figure 2.9). Since the original papers [1958Kup, 1959Kup, 1961Gri, 1961Kup] were inconsistent, most of the comparisons were with Raghavan [1992Rag].

Alloys 2 and 3 were both A1 (γFe,αCo,Pd) solid solutions, suggesting that the A1 (γFe,αCo, Pd) region extends further than that suggested by Raghavan's isothermal section at ~25°C [1992Rag] (Figure 2.9), and the same was shown for Alloy 6 which also had a A1 (γFe,αCo,Pd) match. Due to the results for Alloy 3 suggesting the structure was not quite cubic, this would possibly show one of the ordered phases was present which is tetragonal, ~FePd. Alloy 4 shows that the A1 (γFe,αCo,Pd) phase was narrower than Raghavan [1992Rag] indicated near this composition. Conversely, Alloy 5, being a single-phase solid solution of A1 (γFe,αCo,Pd), showed that this phase had a greater extent at this alloy composition than in Raghavan's isothermal section [1992Rag].

Alloy 7 was one of only two alloys that agreed with Raghavan's isothermal section [1992Rag] (Figure 2.9), although the ~$FePd_3$ phase only precipitated out in certain areas of the sample, and not in the entire sample, the precipitation could have been due to inhomogeneous solidification of the alloys during manufacturing. Similar to Alloy 4, Alloy 8 did not agree with Raghavan's isothermal section [1992Rag], suggesting that the A1 (γFe,αCo,Pd) phase was narrower than Raghavan [1992Rag] indicated. Alloy 9 did not agree with Raghavan's isothermal section [1992Rag], suggesting that the three-phase field did not lie in that region for the particular composition of the alloy.

Alloys 10 and 11 did not agree with Raghavan's isothermal section [1992Rag] (Figure 2.9), indicating that the α' + A1 (γFe,αCo,Pd) phase region was much narrower than Raghavan suggested. Alloy 12 was the only other alloy that agreed with Raghavan's isothermal section [1992Rag]; the region is α + A1 (γFe,αCo,Pd).

There was better agreement of the as-cast samples (Figure 6.1) with the 25°C isothermal section of Raghavan [1992Rag] (Figure 2.9) than with that of Kuprina and Grigorev [1958Kup] (Figure 2.7). Strictly, the as-cast samples of this work should not have been compared to the ~25°C isothermal sections of Kuprina and Grigorev [1958Kup] and Raghavan [1992Rag], but there was no other information available for comparison. It should be remembered that Raghavan [1992Rag] stated that his 25°C section was highly speculative, given the problems in the source papers [1958Kup, 1959Kup, 1961Gri, 1961Kup].

The coring and dendrites in Alloys 1, 4, 6, 10, 11 and 12 were used to assess the validity of the two liquidus surfaces (Figure 2.10 a)) [1958Kup], (Figure 2.10 b)) [1992Rag] since the dendrites would form first, and the interdendritic area would form next, so the direction from the former to the latter should give the slope of the liquidus surface. The deduced liquidus slope agreed with both of the liquidus surfaces [1958Kup, 1992Rag], so it was not possible to choose a better one; this can be seen in Figure 6.1.

The XRD patterns showed very few peaks, making identification of the phases difficult. However, most of the samples just showed the fcc solid solution, A1 (γFe,αCo,Pd), so this was expected. The different directions of the shifts of the fcc peaks in Alloy 3 suggests that there might be some ordering to form a tetragonal structure. This would be consistent with the ~FePd phase [2018Lau]. However, the sample was quite far from the Fe-Pd binary, which might be too far to experience this type of ordering, although Buschow [1983Bus] reported it for both Fe-Pd and Co-Pd binary alloys. There were some unidentified peaks in some of the samples, and these are shown in Table 6.1; none of the peaks were the same.

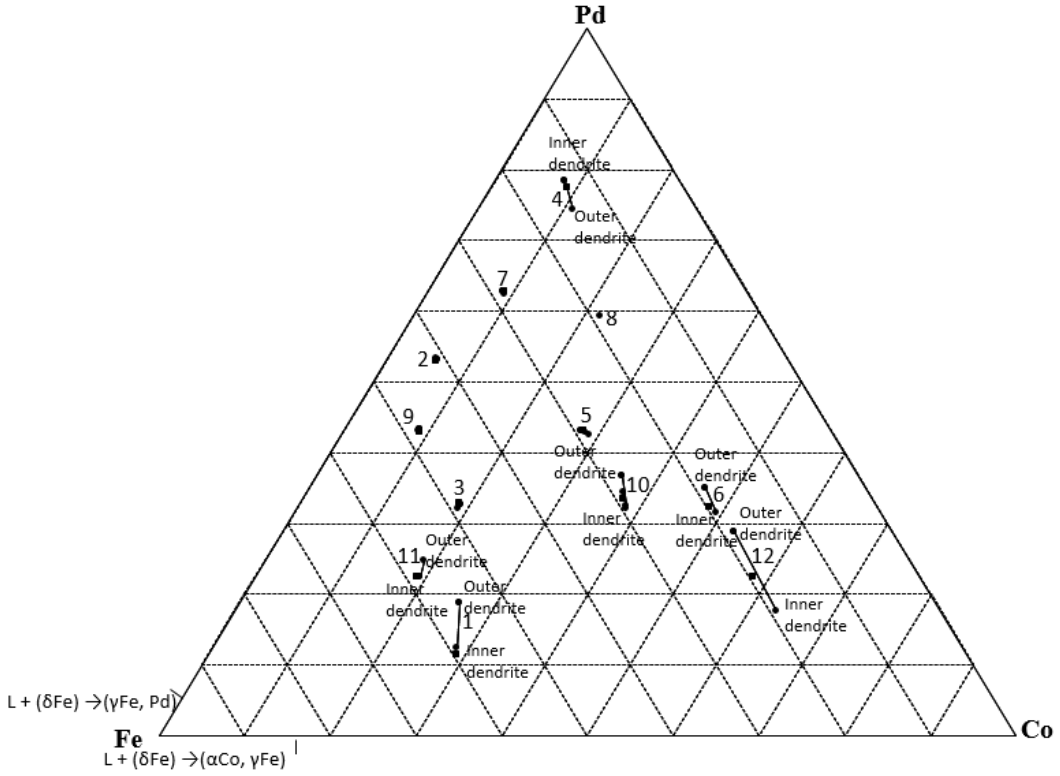


Figure 6.1 Solidification projection for the as-cast Co-Fe-Pd system. (■ Overall composition; ● phases)

Table 6.1. Unidentified peaks for the as-cast alloys.

Alloy number and nominal composition (at.%)	Peak position (2 Theta)	Intensity ($I\backslash I^{100}$)
9: Co_{10}:Fe_{50}:Pd_{40}	~75°	3
10: Co_{40}:Fe_{30}:Pd_{30}	~38°	3
11: Co_{20}:Fe_{60}:Pd_{20}	~80°	67
12: Co_{60}:Fe_{20}:Pd_{20}	~73°	10

6.3. Alloys annealed at 1000°C

The alloys were not totally homogeneous because there were areas, sometimes circular, of different compositions, shown in Alloys 2, 5, 6, 7, 8 and 9. The circular regions suggested that these inhomogeneities arose in the liquid phase, which means that there could be a tendency for immiscibility in the liquid phase. Also, because the A1 (γFe,αCo,Pd) solid solution extended across nearly the whole

system, it could be matched at different compositions with patterns from alloys of different compositions from the different binaries. Alloys 4 and 10 showed limited contrast between the regions, and this was expected as the sample was made up of only A1 (γFe,αCo,Pd), therefore not much would have shown in the microstructure. Alloy 11 was one of the unusual samples that appeared to exhibit a Widmanstätten microstructure; this can be a characteristic of steels or alloys that have high Fe contents and low carbon content [2004Phe], but can actually occur in many instances where a fairly major second phase grows in from the grain boundaries in the solid state, e.g. brass [1972Cha].

Apart from Alloys 1, 3 and 11 which had two phases (αFe) + A1 (γFe,αCo,Pd), all the other alloys comprised only A1 (γFe,αCo,Pd). These alloys showed that (αFe) is stable to higher temperatures within the ternary than in the Co-Fe binary (Figures 6.2 and 6.3). Alloy 3 also had a local inhomogeneity. The alloys were annealed at this temperature for another project [2017Man], even though this temperature was not ideal for a phase diagram investigation because it was above all the reactions of the component binary phase diagrams. Alloy 1 had a lamellar microstructure, due to discontinuous precipitation of the two phases which have reduced solubility at lower temperatures, which promotes precipitation of the other phase. It was expected that annealing the samples would coarsen the grains and allow for more accurate analyses, but this did not occur in these alloys, and was probably due to the high melting points of the system. The only alloy that showed a difference in composition was Alloy 3, although the error on one of the analyses was quite high, which meant it picked up the signal of the surrounding phases, or that the sample was inhomogeneous.

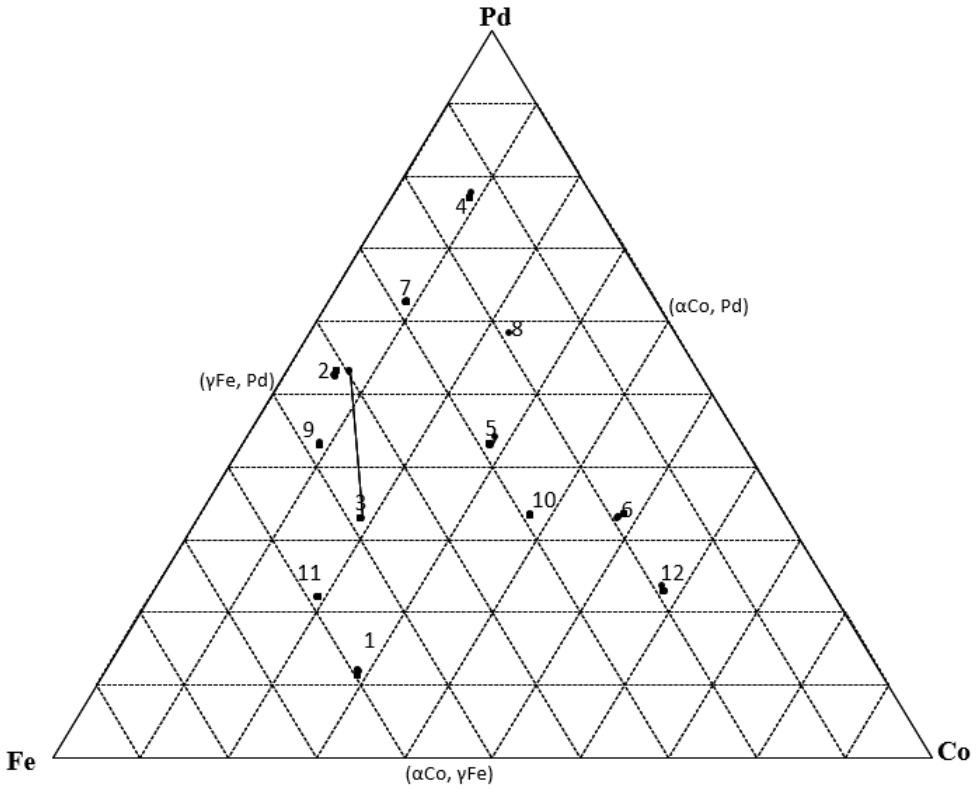


Figure 6.2. Results of the alloys annealed at 1000°C for the Co-Fe-Pd system (at.%). (■ Overall composition; ● phases)

The annealed samples were very sensitive and prone to scratching during sample preparation, indicating that they were quite soft, and for most of these samples Aqua Regia worked the best for etching. The other method used for Alloys 2 and 3 was electro-etching in a solution of H_2O + HCl, and for Alloys 8 and 11 immersion etching in a solution of H_2O + HCl + HNO_3.

It was determined that the ~FePd and ~$FePd_3$ regions in the Fe-Pd binary diagram did not extend further into the ternary system, although it was difficult to discern the superlattice peaks of ~FePd because they were so small in the reference pattern [2018Dif] (the patterns are given in Appendix A). These small peaks might show that the degree of ordering was very slight, and to find them, synchrotron XRD would be necessary.

Figure 6.3 shows the isothermal section at 1000°C, however the position of the (αFe) and

(αFe) + A1 (γFe,αCo,Pd) regions are very speculative, although there was XRD evidence for (αFe) in Alloys 1 (Figure 4.39) and 11 (Figure 4.69), and microstructural evidence in Alloy 3 (Figure 4.43). The maximum for (αFe) in the Co-Fe binary was taken into account when choosing the regions. Although it would appear anomalous that a bcc phase should appear within a fcc region where all the components are fcc at that temperature (1000°C), there is a bcc phase just below it (~980°C). Although the pattern was poor for the as-cast sample, a definite (αFe) was identified and the sample showed a two-phase structure, even though a phase was partially etched out. To clarify this more alloys should be studied in this region.

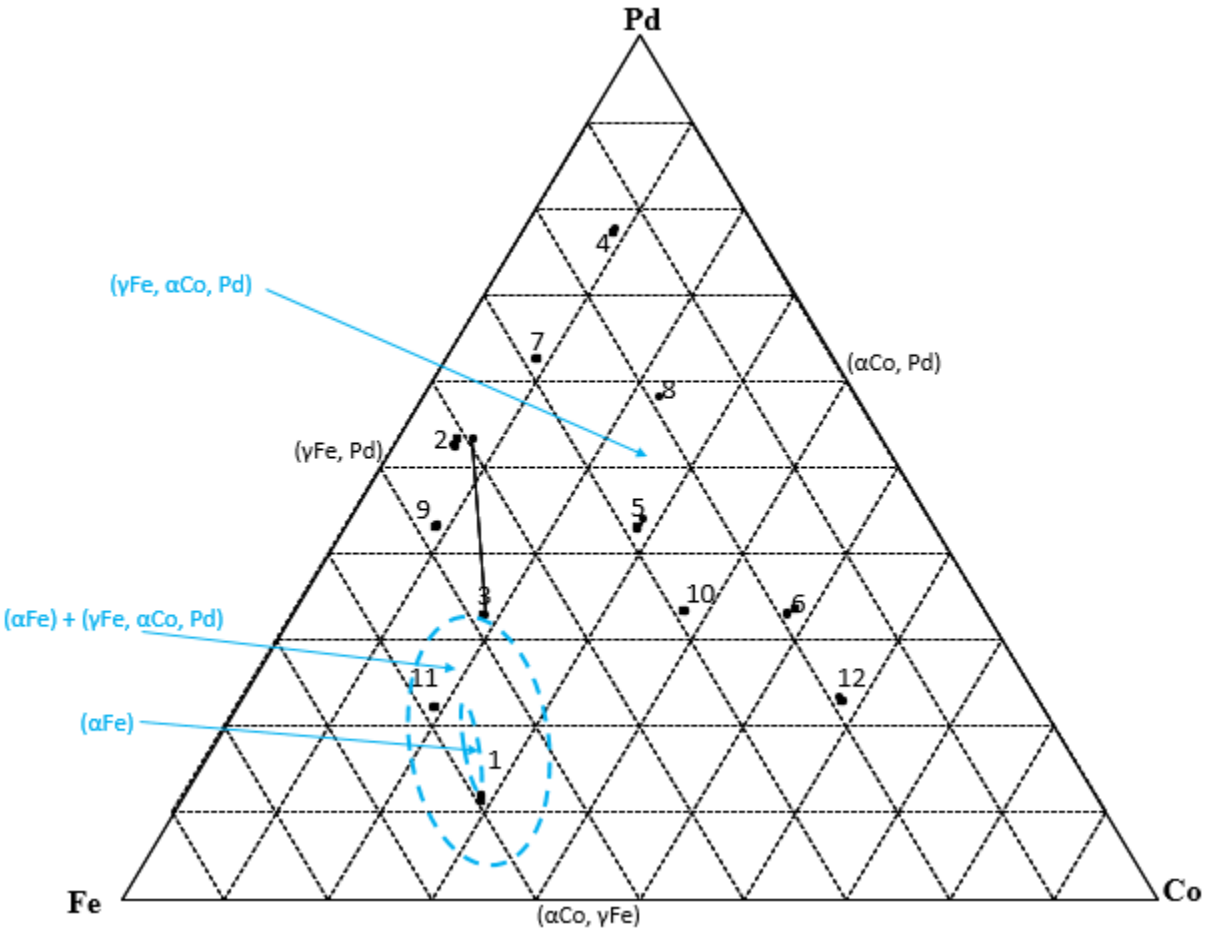


Figure 6.3. Isothermal section at 1000°C for the Co-Fe-Pd system (at.%). (■ Overall composition; ● phases)

6.4. Alloys annealed at 650°C

Given that the alloys annealed at 1000°C did not show many differences (being mainly A1 (γFe,αCo,Pd)), the samples had to be annealed at a lower temperature, which had to be below the phases

transformations in the component binaries. The results from all of the samples annealed at 650°C are shown in Figure 6.4.

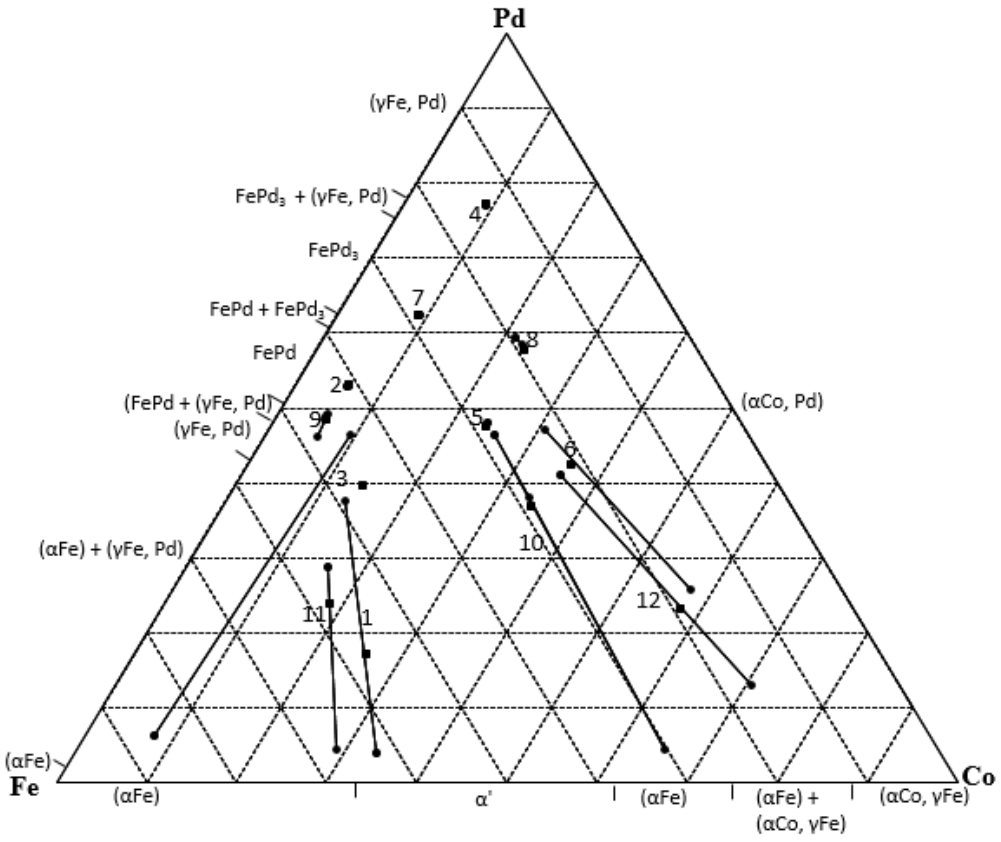


Figure 6.4. Results for the alloys annealed at 650°C for the Co-Fe-Pd system (at.%). (■ Overall composition; ● phases)

The EDX results were plotted on to the ternary diagram and the binary phase limits at 650°C were used as boundaries to determine where the different phase regions would lie, the interpretation is shown in Figure 6.5. The ~FePd and ~$FePd_3$ regions were drawn near the Fe-Pd binary, because Alloys 2 and 7 were A1 (γFe,αCo,Pd), so it was deduced those phases would not extend beyond Alloys 2 and 7. Also, ~FePd and ~$FePd_3$ were difficult to find and distinguish from the random A1 (γFe,αCo,Pd) solid solution, due to their ordered peaks being so small [2018Dif]. There had to be a three-phase region, so it was inferred at that point (indicated by dashed triangle along Fe-Pd binary).

The (αFe) + A1 (γFe,αCo,Pd) region was determined by the composition of Alloys 3, 5 and 10, which had to join up to the Co-Fe binary. The A1 (γFe,αCo,Pd) miscibility gap indicated by the dashed line was placed there as it would not have fitted in with the (αFe) + A1 (γFe,αCo,Pd) region and Alloys 6 and 12 contained only A1 (γFe,αCo,Pd) with two different compositions. The miscibility gap was not near the circular regions found in some microstructures (Alloy 2, Figure 4.40; Alloy 7, Figure 4.55 and Alloy 8, Figure 4.58). No coring should have existed after annealing, so a miscibility gap was inferred. However, this miscibility gap was near the (αFe) + A1 (γFe,αCo,Pd) two-phase region, so could be an artefact. On annealing at 650°C, Alloy 6 had a very different overall composition from the other two conditions; there was a loss of Co. There were losses for the other elements, but they were minor compared to Co. Alloys 1, 2 and 3 had losses of Fe and Co, and losses for the other alloys were negligible. The (αFe) region was matched up using Alloys 3, 10 and 11 and the Co-Fe binary; similarly, the α' region was determined. There was no two-phase boundary between the (αFe) and α', due to the order of transformation being first-order [2009Por]. Although Matsuda et al. [2016Mat] reported α' in their Co_{50}:Fe_{40}:Pd_{10} alloy, this was not reflected in the 650°C isothermal section, because their sample was processed at a different temperature.

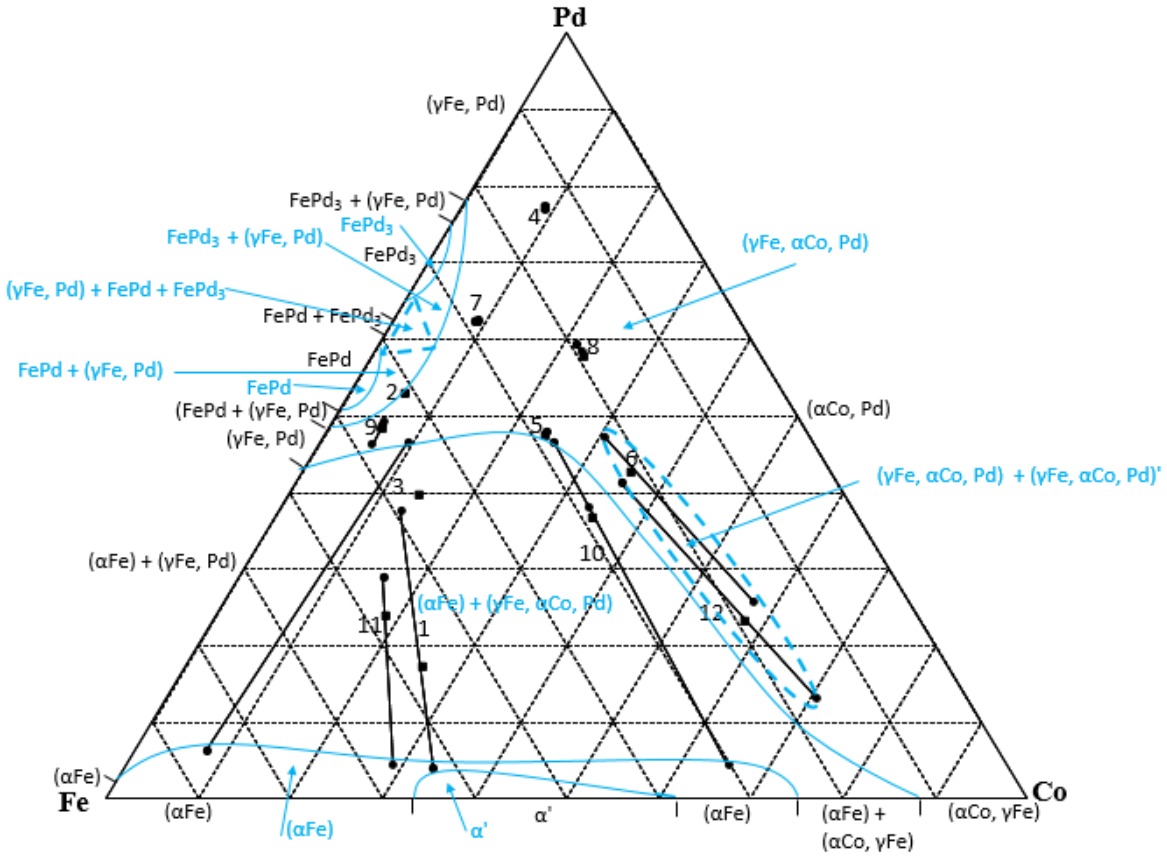


Figure 6.5. Isothermal section at 650°C annealed for the Co-Fe-Pd system (at.%). (■ Overall composition; ● phases)

The XRD patterns for the annealed samples were poor and the peaks were very similar for most of the phases present, one example would be α and α' (patterns of peaks used to match the phases shown in Appendix A). The intensity of the ordered peaks for α' were less than 1% of the maximum peak, and the data possibly came from a phase that showed very little ordering, therefore it was unlikely that they would have been picked up during XRD. The FePd and $FePd_3$ phases are ordered $L1_0$ and $L1_2$ structures and FePd had reasonable peaks in the reference pattern [2012Kuv, 2018Lou, 2018Dif], whereas $FePd_3$ had very small peaks [2018Dif] (Appendix A), which made it very difficult to distinguish from A1 (γFe,αCo,Pd), in Alloy 7.

As with the as-cast samples, the analysis of fine phases was very difficult, due to the fineness of the sample microstructures. When analyzing one phase, the phases around it were also picked up, making the analysis errors very high; examples of this can be seen in Alloys 1 and 11. Alloys 1 and 11 had the same microstructure, showing that α and α' were present in both samples, although it was not picked up by XRD. Alloys 2 and 4 had similar microstructures, and they both comprised A1 (γFe,αCo,Pd), although the XRD pattern for Alloy 2 had very few peaks, because it was fcc, A1 (γFe,αCo,Pd), which does not have many peaks, and so the interpretation of the pattern was inconclusive.

For Alloy 3, the overall was outside of the two phases analysed, which indicated that a phase was etched out and could not be analysed properly by EDX. Also, because of the very fine microstructure, it was not surprising that a phase was not detected. It was surmised that the (αFe) phase was etched out of the surface of Alloy 5, hence only one phase was picked up by EDX, although the microstructure appears to be two-phase.

Alloy 8 was one of three alloys that still showed coring, even after annealing. The only difference from the other cored alloys, Alloys 2 and 4, was that there were lighter dendrites which were visible. Alloys 9 and 10 showed very similar microstructures. The dark areas which were surmised to be (αFe) on Alloy 9 were etched away on the surface, hence the high errors for some areas of this alloy. Since this system was particularly difficult to analyse, in order to better understand it, a similar system could be studied, such as Co-Fe-Pt [2017Chi, 2018Cor, 2019Cor].

6.5. Microhardness results

From Figures 6.6-6.8, it can be seen that the hardness of the material increased with increased Fe and decreased with increased Pd contents, as well as decreasing with higher Co contents for alloys which were fcc, A1 (γFe,αCo,Pd). This was expected, since Fe is expected to increase the hardness of the material due to its higher hardness. The errors were small for some of the samples, showing that the samples were fairly homogeneous.

Figures 6.6-6.8 followed the same trends as each other. The alloys that were unusual were Alloys 11 and 3, which had significantly higher hardness values, although the errors were also quite high, so there could have been an inhomogeneity, or these alloys could have had some ordered structures. The XRD results as-cast sample of Alloy 3 suggested that there was ordering to a more tetragonal structure, because the peak shifts from the reference were in different directions. To explain the highest hardness shown by Alloy 11, it was the only sample to show what appeared to have a Widmanstätten microstructure after being annealed at 1000°C, and it also had the highest proportion of the lamellar phases, which would be strengthening. The as-cast alloy had a phase which was etched out on the surface, and the XRD pattern was so poor it was difficult to discern the phases, although the A1 (γFe,αCo,Pd) and a peak from (αFe) was present. Thus, the high hardnesses of samples of this composition were due to the presence of these two phases.

In Figures 6.7 and 6.8, Alloys 3 and 11 are in the (αFe) + A1 (γFe,αCo,Pd) phase region, which is likely to be the reason for the high hardness. Alloys 6 and 12 were in the region of miscibility for A1 (γFe,αCo,Pd), and had higher hardnesses than the trend. Alloy 9 had a lower hardness than Alloy 2. The higher hardness for Alloy 2 could have been due to ordering, because the composition is near that of the FePd ordered phase, and the hardness disagrees with the trend of increasing hardness with increasing Fe contact.

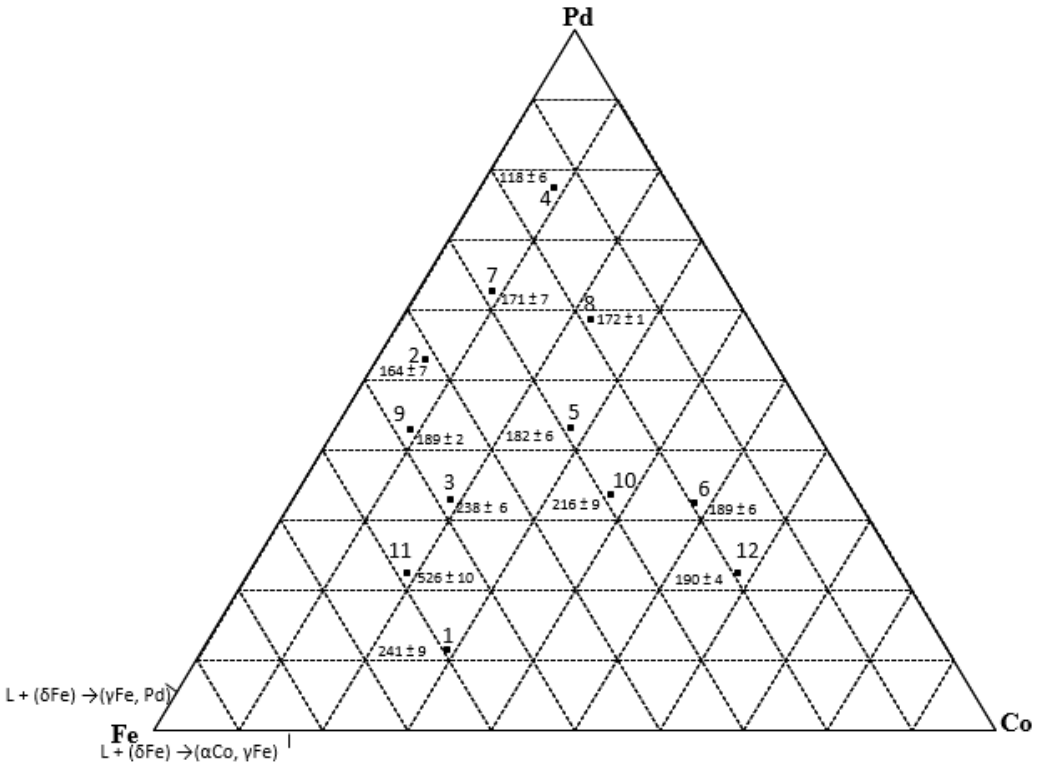


Figure 6.6. Solidification projection with hardnesses for as-cast Co-Fe-Pd alloys. (■ Overall composition)

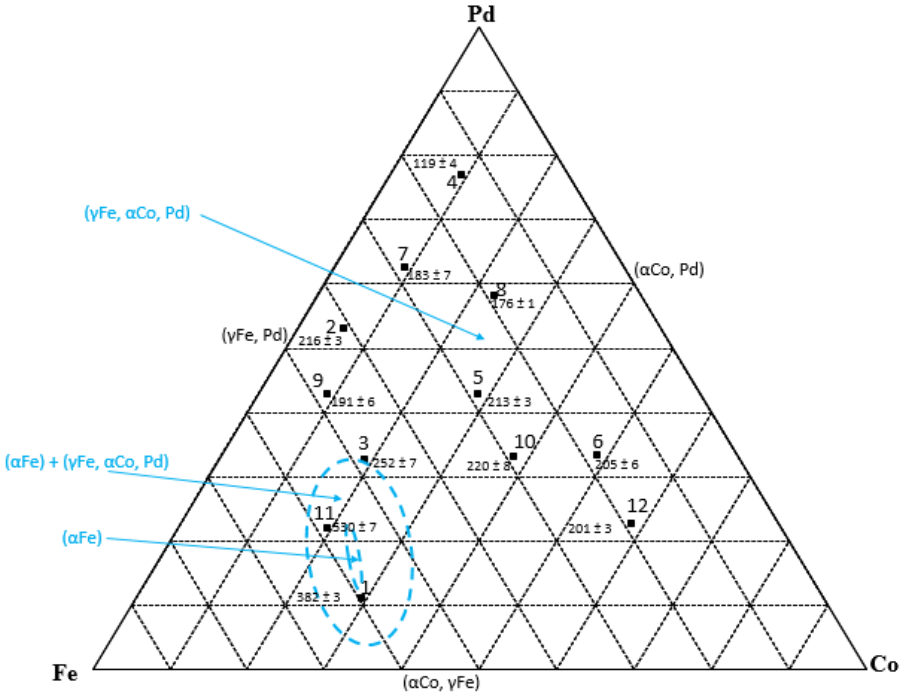


Figure 6.7. Isothermal section at 1000°C for the Co-Fe-Pd system with hardnesses. (■ Overall composition)

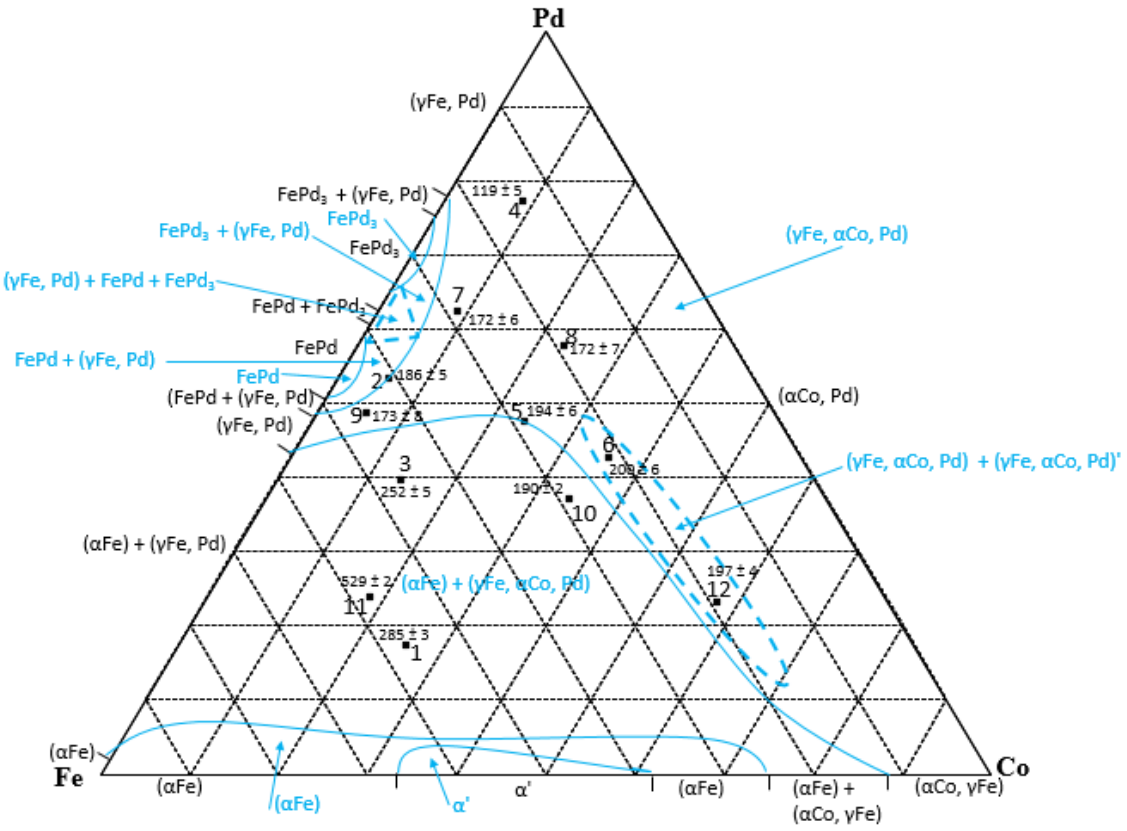


Figure 6.8. Isothermal section at 650°C for the Co-Fe-Pd system with hardnesses. (■ Overall composition)

Figure 6.9 shows that the hardnesses for the as-cast alloys had the lowest values, whereas the alloys annealed at 1000°C had the highest hardnesses, and the alloys annealed at 650°C had values between these. Alloys 4 and 11 had very similar values for all the conditions, and Alloy 4 had the same A1 (γFe,αCo,Pd) phase for all the conditions. Alloys 1 and 2 showed the greatest difference in values, which was due to the different microstructures of the different conditions.

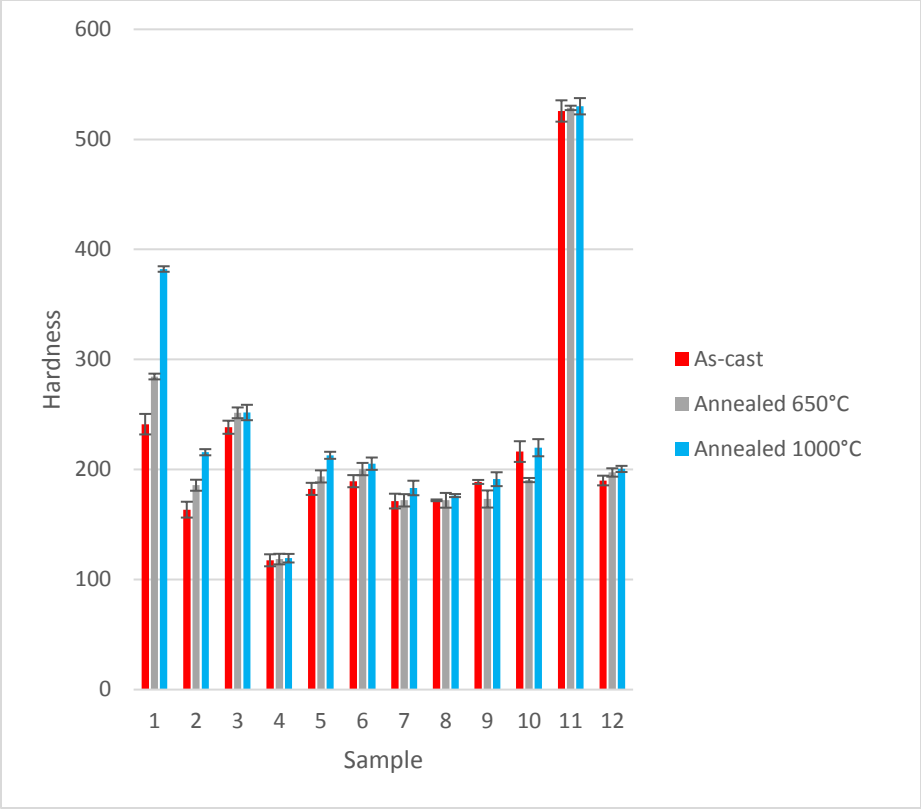


Figure 6.9. Comparison of hardnesses for all of the alloys in the different conditions.

Chapter 7: Conclusions

Twelve samples were made by melting pure elemental powders in a button arc furnace. The buttons were cut and half was used for the as-cast and the other for the annealing. They were annealed at 1000°C and 650°C for 1000 hours, and studied using XRD. After XRD, they were etched and studied using SEM in SE and BSE modes, and EDX was used to analyse the phases present and the overall compositions.

7.1. As-cast alloys

Given the very wide A1 (γFe,αCo,Pd) liquidus surface of the system and the few solid phases, it was not surprising that the alloys were cored. Using metallography, the slope of the liquidus agreed with previous workers. None of the microstructures in the as-cast state found to date were similar to those of the previous workers.

The Co_{30}:Fe_{60}:Pd_{10} (at.%) alloy suggested a wider A1 (γFe,αCo,Pd) + (αFe) phase field than Raghavan [1992Rag]. The alloys were fcc solid solutions, suggesting that the A1 (γFe,αCo,Pd) region extends further than that by Raghavan. The Co_{10}:Fe_{15}:Pd_{75} and Co_{25}:Fe_{20}:Pd_{55} (at.%) alloys showed that the A1 (γFe,αCo,Pd) phase was narrower than Raghavan's isothermal [1992Rag] section at 25°C. Conversely, the Co_{30}:Fe_{30}:Pd_{40} (at.%) alloy, a solid solution of A1 (γFe,αCo,Pd), showed that this phase had a greater extent at this composition than in Raghavan's 25°C isothermal section [1992Rag]. The results of this study for the Co_{10}:Fe_{50}:Pd_{40} (at.%) alloy did not agree with Raghavan's three-phase field region, and the α' + A1 (γFe,αCo,Pd) two-phase region was much narrower in the current study. The Co_{10}:Fe_{30}:Pd_{60} and Co_{60}:Fe_{20}:Pd_{20} (at.%) samples agreed with Raghavan's [1992Rag] regions of $FePd_3$ + A1 (γFe,αCo,Pd) and (αFe) + A1 (γFe,αCo,Pd). There was better agreement of the as-cast samples with the ~25°C isothermal section of Raghavan [1992Rag] than with that of Kuprina and Grigorev [1961Kup], even considering that it was not strictly correct to use the ~25°C isothermal section for the as-cast samples.

7.2. Alloys annealed at 1000°C

Not all of the alloys annealed at 1000°C were totally homogeneous. The isothermal section was drawn and the system consisted of mainly A1 (γFe,αCo,Pd). Only three alloys had two phases,

(αFe) + A1 (γFe,αCo,Pd), and all the other alloys comprised only A1 (γFe,αCo,Pd). The two-phase regions show that (αFe) is more stable in the ternary than the Co-Fe binary. The ~FePd and ~$FePd_3$ regions in the Fe-Pd binary diagram did not appear to extend very far into the ternary system.

7.3 Alloys annealed at 650°C

It was difficult to identify the ordered phases, because the reported ordered peaks were small, and the XRD patterns were not good, even when run for longer times. As with the as-cast samples, the analysis of fine phases was very difficult, hence errors were very high in Co_{30}:Fe_{60}:Pd_{10} and Co_{20}:Fe_{60}:Pd_{20} (at.%), and α and α' were present in both, although not detected by XRD.

There was a miscibility gap in the A1 (γFe,αCo,Pd) phase which had a range of Co_{31}:Fe_{22}:Pd_{47} – Co_{71}:Fe_{16}:Pd_{13} (at.%), which had not been reported before. Some alloys showed coring, even after annealing.

7.4. Microhardness

The hardness of the alloys increased with increased Fe and decreased Pd, and those with higher Co contents also had lower hardnesses. The samples were homogeneous, giving small errors in the hardness measurements. The Co_{20}:Fe_{50}:Pd_{30} and Co_{20}:Fe_{60}:Pd_{20} (at.%) alloys had significantly higher hardness values; Co_{20}:Fe_{60}:Pd_{20} (at.%) had the highest hardness, with an apparent Widmanstätten microstructure after being annealed at 1000°C. The local higher hardness for the Co_6:Fe_{44}:Pd_{50} (at.%) alloy could have been due to some FePd ordering, since the alloy composition was close to that phase, and the hardness did not follow the trend of increasing with increasing Fe content. The hardness trend for the different conditions was: annealed at 1000°C > annealed at 650°C > as-cast.

Chapter 8: Recommendations for Future work

- Undertake XRD measurements at different temperatures to ascertain the temperature of ordering or phase transformation, for Alloys 1, 2, 7, 9 and 11.
- Study a similar system such as Co-Fe-Pt to help better understand the system.
- Use synchrotron techniques to undertake XRD for samples which could show ordering, so that better signals are obtained, and the small peaks of alloys with ordering might be discerned.
- Study more alloys around the region of the A1 (γFe,αCo,Pd) miscibility gap found at 650°C.
- Study more alloys around the speculated (αFe) and (αFe) + A1 (γFe,αCo,Pd) regions for 1000°C.
- Undertake and compare area analyses of the circular regions of the as-cast samples with the alloy overall analyses to ascertain if there is a miscibility gap in the liquid phase.

References

[1951Boz] Bozorth, R.M., "Ferromagnetism, D.Van Nostrand Co. Inc., Toronto, Canada, (1951)

[1958Kup] Kuprina, V.V., Grigorev, A.T., "Investigation of Alloys of Fe-Co-Pd System. I. Fusibility Diagram of the Fe-Co-Pd System" (in Russian), Zh. Neorg. Khim., 3 (12), 2736-2739, (1958).

[1959Kup] Kuprina, V.V., Grigorev, A.T., "Solid-State Transformations in Alloys of Iron with Cobalt and Palladium" (in Russian), Zh. Neorg. Khim., 4(7), 1606-1610 (1959), English translation: J. Inorg. Chem., 4(7), 724-727, (1959).

[1961Boz] Bozorth, R.M., Wolff, P.A., Davis, D.D., Compton, V.B. and Wernick, J.H., "Ferromagnetism in Dilute Solutions of Cobalt in Palladium", Phys. Rev., 122, 1157-1160, (1961).

[1961Gri] Grigorey, A.T. and Kuprina, V.V., "Order-Disorder Transformations in Alloys of Iron with Cobalt and Palladium" (in Russian), Zh. Neorg. Khim., 6 (8), 1891-1898 (1961), English translation: J. Inorg. Chem., 6(8), 966-970, (1961).

[1961Kup] Kuprina, V.V. and Grigorev, A.T., "Polymorphic Transformation in Alloys of Iron with Cobalt and Palladium" (in Russian), Izv. Vyss. Uchebn. Zaved., Khim., Khim. Tekhnol., 4 (1), 7-10, (1961).

[1962Kne] Kneller, E., "Ferromagnetism", Springer, Berlin, Germany, (1962).

[1963Got] Gottlieb, M.A. and Pfeiffer, R., "The Feynman lecture on physics", New millennium edition, California Institute of Technology, (1963).

[1964Kus] Kussman, A., Muller, K. and Angew, Z., Phys., 17, 509, (1964), as quoted by [2007Yab].

[1971Vat] Vatolin, N.A., Timofeev, A.I, Esin, O.A, and Dubinin, E.L., Russ. J. Phys. Chem., 45, 1146-1149, (1971).

[1972Cul] Cullity, B.D., "Introduction to magnetic materials, Addison-Wesley, Massachusetts, USA, (1972).

[1972Cha] Chadwick, G.A., "Metallography of Phase Transformations", Butterworth, London, (1972).

[1973Iva] Ivanov, O.A., Solina, A.V., Demshila,V.A, and Magat, L.M., Merallogr, 35, 92, (1973), as quoted by [2007Yab].

[1973Yos] Yoshida, H., Kimura, H.M., Yamura, S., Shima, T. and Inoue, A., Merallogr, 35, 92, (1973), as quoted by [2007Yab].

[1980Bar] Barrett, C.S. and Massalski, T.B., "Structure of Metals", Int. Ser. Mat. Sci.Tec., 35, 270-279, (1980).

[1981Gol] Goldstein, G.I., Newberry, D.E., Echlin, P., Joy, D.C., Fiori, C. and Lifshin, E.,

"Scanning Electron Microscopy and X-Ray Microanalysis" (New York: Plenum Press), 56-59, (1981).

[1981Osh] Oshima, R., Scripta Metall., 15, 829-833, (1981), as quoted by [2003Tsu].

[1982Kub] Kubaschewski, O., "Iron-Binary phase diagrams", 27-31 88-90, (1982).

[1982Osh] Oshima, R. and Sugiyama, M., J. Phys. (Paris), 43, 383-388, (1982), as quoted by [2003Tsu].

[1983Bus] Buschow, K.H.J., Van Engen, P.G. and Jongebreur, R., "Magneto-optical properties of metallic ferromagnetic materials", J. Magm. Mag. Mat, 38(1), 1-22, (1983).

[1984Nis] Nishizawa, T. and Ishida, K., "The Co-Fe (cobalt-iron) system", Bull. Alloy Phase

Diagr., 5(3), 250–259, (1984).

[1986Cor] Cornish, L.A., "Computer calculation of phase diagrams including the molybdenum-based intermetallics in uranium dioxide fuel pins", Ph.D Metallurgy and Materials, Birmingham University, UK

[1986Pet] Pettifor, D.A., "Pettifor order", J. Phys., C(19), 281-313, (1986).

[1988Ray] Raynor, G.V. and Rivlin, V.G., "Phase equilibria in iron ternary alloys", The Institute of Metals, 28, (1988).

[1990ASM] ASM Handbook, “Alloy Phase Diagrams”, Volume 3, 118, (1990).

[1990Mas] Massalski, T.B., “Binary Alloy Phase Diagrams”, 2nd edition. *ASM international* , (1990).

[1991Ish] Ishida, K. and Nishizawa, T., “The Co-Pd (Cobalt-Palladium) System”, J. Phase Equilibria, 12(1), 83-87, (1991).

[1992Rag] Raghavan, V., “The Co-Fe-Pd (Cobalt-Iron-Palladium) System” (in English), Phase Diagrams of Ternary Iron Alloys, Indian Institute of Metals, Calcutta, 6A, 623-627, (1992).

[1995Nis] Nishizawa, T. “Effect of Magnetic Transition on Phase Equilibria in Iron Alloys”, J. Phase Equilibria, 16(5), 379-389, (1995).

[1996Kim17] Kim, T.H., Cadeville, M.C., Dinia, A., Pierron-Bohnes, V., Rakoto, H., “Magnetic Properties and Magnetic Phase Diagram of the Frustrated $Co_{1-x}Fe_xPt_3$ Compounds” (in English), Phys. Rev. B: Condens. Matter, 54 (5), 3408-3419, (1996).

[1996Win] Wing, G. “A lexicon of metallographic etchants”, MSc Thesis, University of the Witwatersrand, South Africa, (1996).

[1998Fur] Furuya, Y., Hagwood, W., Kimura, H., Watanabe, T., Mater. Trans., JIM, 39, 1201-1201, (1998), as quoted by [2003Tsu].

[1998Jam] James, R.D., Wuttig, M., Philos. Mag., 77A, 1273-1299, (1998), as quoted by [2003Tsu].

[1998Wha] Whang, S.H., Feng, Q. and Gao, Y.Q., Acta. Mater, 46, 6485, (1998), as quoted by [2010Chb]

[1999Gho] Ghosh, G., Kantner, C. and Olson, G.B., “Thermodynamic modelling of the Pd-X (X= Ag, Co, Fe, Ni) systems”, J. Phys. Equi, 20(3), 295-308, (1999).

[1999Tod] Todorovic, M., Schultz, S., Wong, J. and Scherer, A. “Writing and reading of single magnetic domain per bit perpendicular patterned media”, Appl. Phys. Lett., 74, 2516–2518, (1999).

[1999Wel] Weller, D. and Moser, A., IEEE trans. Magn., 35, 4423, (1999) as quoted by [2010Chb].

[2001Koe] Koeda, J., Nakamura, Y., Fukuda, T., Kakeshita, T., Takeuchi, T., Kishio, K. Trans. Mater. Res. Soc. Japan, 26, 215-217, (2001), as quoted by [2003Tsu].

[2002Kat] Kato,H., Liang, Y., Taya, M. Scripta Mater., 46 471-475, (2002), as quoted by [2003Tsu].

[2002Ohn] Ohnuma, I., Enoki, H., Ikeda, O., Kainuma, R., Ohtani, H., Sundman, B. and Ishida, K., "Phase equilibria in the Fe-Co binary system", Acta Materiala, 50, 379-393, (2002).

[2003Nos] Nose´, Y., Kushida, A., Ikeda, T., Nakajima, H., Tanaka, K., Numakura, H., "Re-examination of Phase Diagram of Fe-Pt System", Materials Transactions, 44 (12), 2723-2731, (2003).

[2003Tak] Takanashi, Y.K., Ohnuma, M., and Hono, K., J. Appl. Phys., 93, 7580, (2003), as quoted by [2007Yab].

[2003Tsu] Tsuchiya, K., Nojiri, T., Ohtsuka, H., Umemoto, M., "Effect of Co and Ni on Martensitic Transformation and Magnetic Properties in Fe-Pd Ferromagnetic Shape Memory Alloys", Mater. Trans., 44(12), 2499-2502, (2003).

[2004Des] Deshpande, A.R., Xu, H. and Wiezorck, J.M.K., Acta. Mater, 52, 2903, (2004), as quoted by [2010Chb].

[2004Phe] Phelan, D. and Dippenaar, R., "Widmanstätten Ferrite Plate Formation in Low-Carbon Steels", Met. Mat. Trans., 35A, 3701, (2004).

[2005Gig] Gignoux, D., Schleiker, M. and Lacheisserie, E.T., "Magnetism fundamentals", (2005).

[2005Gop] Gopalan, R., Kundig, A.A., Ohnuma, M., Kishimolo, S. and Hono, K., Scripta Mater, 52, 761, (2005), as quoted by [2007Yab].

[2005Ter] Terris, B.D. and Thomson, T. "Nano fabricated and self-assembled magnetic structures as data storage media", J. Phys., D38, 199–222, (2005).

[2005Vok] Vokoun, D., Wang, Y.W., Goryczka, T., Hu, C.T., "Magnetostrictive and Shape Memory Properties of Fe-Pd Alloys with Co and Pt Additions", Smart Mater. Struct., 14(5), S261, (2005).

[2006Iss] Issro, C., Abes, M., Puschl, W., Sepiol, B., Pfeiler, W., Rogl, P., Schmerber, G., Soffo, W.A, Kozubski, R. and Pierron-Bohnes, V., Met. Mat. Trans., 37A, 3415, (2006), as quoted by [2010Chb].

[2006Man] Mangin, S., Ravelosona, D., Katine, J.A., Carey, M.J., Terris, B.D. and Fullerton, E.E. "Current-induced magnetization reversal in nano-pillars with perpendicular anisotropy", Nat. Mater. 5, 210–215, (2006).

[2006Nag] Naganuma, R., Sato, K. and Hirotsu, Y., J. Appl. Phys., 99, 08N706, (2006), as quoted by [2007Yab].

[2007Van] Vander Voort, G.F., "Metallography Principles and Practice", *ASM international*, (2007).

[2007Yab] Yabe, H., O'Handley, R.C. and Kuji, T., "Magnetic properties of metastable Fe-Pd alloys by mechanical alloying", J. Magntc. Mag. Met., 310, 2500-2502, (2007).

[2008Oka] Okamoto, H., "Co-Fe (Cobalt-Iron)", J. Phase Equilibria and Diffusion, 29, 383-384, (2008).

[2008San] Sanchez-Alarcos, V., Recarte, V., Perez-Landazabal, J.I., Gomez-Polo, C., Chernenko, V.A., Gonzalez, M.A., "Reversible and Irreversible Martensitic Transformations in Fe-Pd and Fe-Pd-Co Alloys", Eur. Phys. J. Spec. Topics, 158(1), 107-112, (2008).

[2009Pot] Porter, D.A., Easterling, K.E., and Sherif, M.Y., "Phase transformations in metals and alloys" , CRC Press, (2009)

[2010Chb] Chbihi, A., Sauvage, X., Genevois, C., Blavette, O., Gunderov, D. and Popov, A.G. "Optimization of the magnetic properties of FePd alloys by severe plastic deformation", 12(8), 708-713, (2010).

[2010Rip] Rippard, W.H., Deac, A.M., Pufall, M.R., Shaw, J.M., Keller, M.W., Russek, S.E., Bauerand, G.E.W. and Serpico, C. "Spin-transfer dynamics in spin valves with out-of-plane magnetized CoNi free layers", Phys. Rev. B 81, (2010).

[2010San] Sánchez-Alarcos, V., Pérez-Landazábal, J.I., Recarte, V. "Effect of Co and Mn Doping on the Martensitic Transformations and Magnetic Properties of Fe-Pd Ferromagnetic Shape Memory Alloys", Mater. Sci. Forum, 635, 103-110, (2010).

[2011Gil] Gilles, R., Hofmann, M., Johnson, F., Gao, Ya., Mukherji, D., Hugenschmidt, C., Pikart, P., "Analysis of Antiphase Domain Growth in Ternary FeCo Alloys After Different Cooling Rates and Annealing Treatments Using Neutron Diffraction and Positron Annihilation", J. Alloys Compd., 509(2), 195-199, (2011).

[2012Kau] Kauffmann-Weiss, S., Hamann, S., Gruner, M.E., Buschbeck, J., Ludwig, A., Schultz, L. and Fähler, S., "Understanding the Magnetic Shape Memory System Fe-Pd-X by Thin Film Experiments and First Principle Calculations", Adv. Eng. Mater., 14 (8), 724-749, (2012).

[2012Kva] Kvashnin, Y.D., Khmelievskyi, S., Kurdnovsky, J., Yaresko, A.N., Genovese, L, and Bruno, P., "Noncollinear magnetic ordering in compressed $FePd_3$ ordered alloy: A first principal study", Phys. Rev. B, (2012)

[2012Veg] Vega, V., García, J., Rosa, W.O., Vivas, L.G., Prida, V.M.., Hernando, B. and Vázquez, M., "Magnetic Properties of (Fe, Co)-Pd Nanowire Arrays", J. Nanosci. Nanotechnol., 12 (9), 7501-7504, (2012).

[2013Din] Ding, J. and Adeyeye, A.O. "Binary ferromagnetic nano-structures: fabrication, static and dynamic properties", Adv. Funct. Mater. 23, 1684–1691, (2013).

[2015Zha] Zhang, D., Shaw, J.M., Smith, D.J. and McCartney, M.R., "Domain structure and perpendicular magnetic anisotropy in CoFe/Pd multilayers using off-axis electron holography" (in English), J. Magn. Magn. Mater. 388, 16-21, (2015).

[2016Mat] Matsuda, M., Sago, R., Akamine, K., Tsurekawa, S., Takashima, K. and Nishida, M., "Enhancement of ductility in Fe-Co based alloys by substitution of Pd" (in English), J. Alloys Compd., 682, 124-131, (2016).

[2017Chi] Chipise, L., Cornish, L.A., Jain, P. and Mwabora, J., "Co-Pd Binary Phase Diagram Evaluation", in MSI Eureka, Effenberg, G. (Ed.), MSI, Materials Science International, Stuttgart (2017), Document ID: 20.32756.1.8.

[2017Man1] Mantyi, H.C., "Development of nanocystalline Fe-Co-Pd magnetic alloy", PhD proposal submitted to the University of the Witwatersrand, (2017).

[2017Man2] Mantyi, H.C., Cornish, L.A., Mwamba, I.A. and Strydom, A.M., "Magnets- The vitamins of a modern economy. A review", AMI Precious Metals 2017, The Precious Metals Development Network (PMDN) Conference, Polokwane, South Africa, 17th-19th October 2017.

[2018Cor] Cornish, L.A., Dyal Ukabhai, K. and Fabuyide, A., "Co-Fe-Pd ternary phase diagram evaluation", Ternary Evaluations, MSI Eureka, MSI, Materials Science International, Stuttgart, 2018, available at: http://www.msi-eureka.com/full-html/10.41430.1.0/Co-Fe-Pd_Ternary. (On-line only)

[2018Dif] Diffrac.Eva suite software package, 2018 International Centre for Diffraction Data.

[2018Lau] Laughlin, D.E., "Atomic ordering in alloys", Carnegie Mellon University, slide show available at: www.slideplayer.com\slide\4486725, (2018).

[2018Pei] Pei, Z., Eisenbach, M. and Stocks, G.M., "Error controlling of the combined cluster-expansion and Wang-Landau Monte-Carlo method and its application to FeCo", Computer physics Communications, (2018).

[2019Cor] Cornish, L.A. and Fabuyide, A., "Co-Fe-Pt Ternary Phase Diagram Evaluation", to be submitted ton MSI Eureka, Effenberg, G. (Ed.), MSI, Materials Science International, Stuttgart, (2019).

[2019Nat] "Magnetism", available at: www.nationalgeographic.org, accessed on 28/01/2019.

Appendix A: Peaks used to match phases on XRD patterns

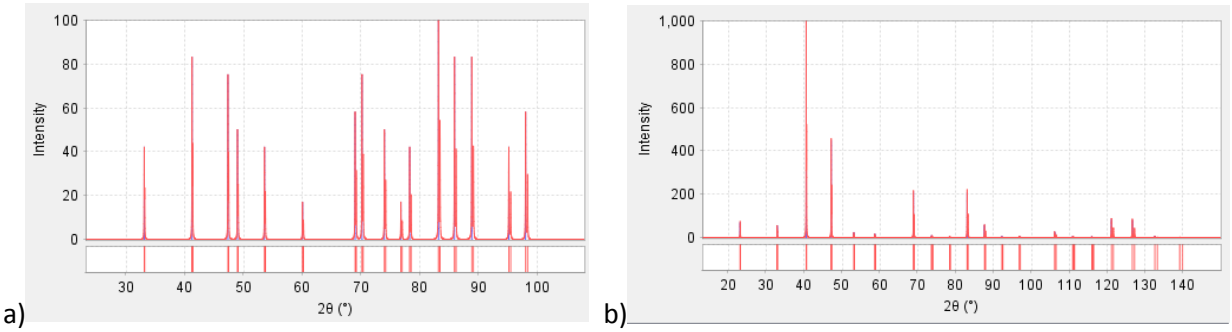


Figure 1. XRD peaks used to identify a) FePd and b) $FePd_3$ [2018Dif].

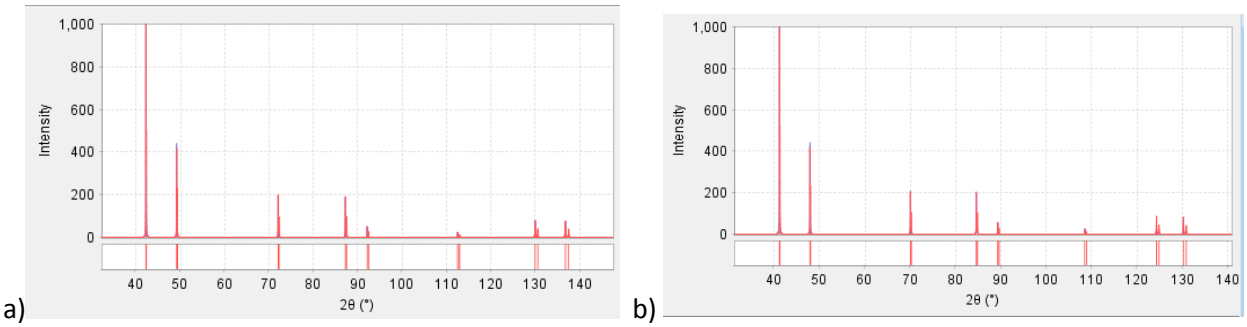


Figure 2. XRD peaks used to identify a) (γFe, Pd) and b) (αCo, Pd) [2018Dif].

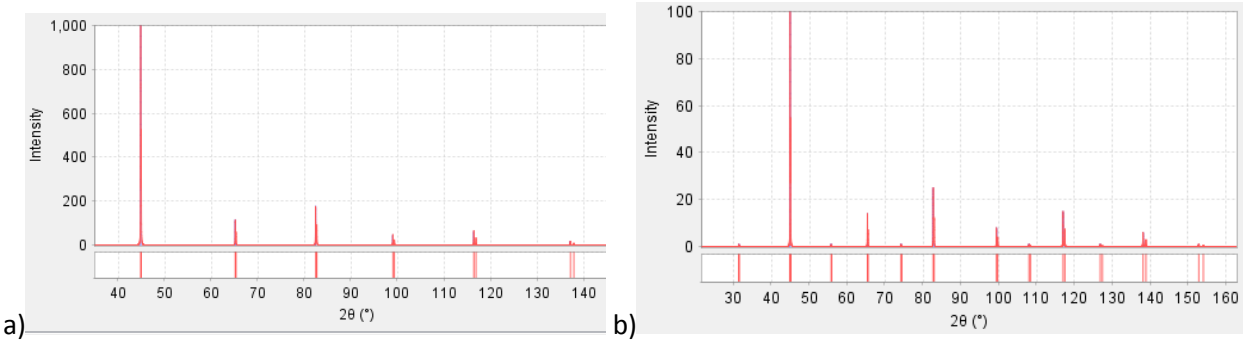


Figure 3. XRD peaks used to identify a) (αFe) and b) α' [2018Dif].

Appendix B: Work published

- K. Dyal Ukabhai and L.A. Cornish, Study of as-cast Co-Fe-Pd samples, AMI Precious Metals 2017, The Precious Metals Development Network (PMDN) Conference, (Book of) Abstracts of papers presented at the conference, pp. 63-64, Polokwane, South Africa, 17th-19th October 2017.

- K. Dyal Ukabhai and L.A. Cornish, Initial study of as-cast Co-Fe-Pd samples, Proceedings of Microscopy Society of Southern Africa (MSSA), Vol. 47, p. 27, Bela-Bela, South Africa, 4th- 7th December 2017.

- L.A. Cornish, K. Dyal Ukabhai and A. Fabuyide, Co-Fe-Pd Ternary Phase Diagram Evaluation, Ternary Evaluations, MSI Eureka, MSI, Materials Science International, Stuttgart, 2018, available at: http://www.msi-eureka.com/full-html/10.41430.1.0/Co-Fe-Pd_Ternary. (Online only)

- K. Dyal Ukabhai, I.A. Mwamba and L.A. Cornish, Phase analyses of the Co-Fe-Pd ternary alloys, CoSAAMI-2018, IOP Conf. Series: Materials Science and Engineering, 430, 012023, Vanderbijlpark, South Africa, 23rd-26th October 2018.


ami
advanced metals initiative
science & technology
SAIMM
SYMPOSIUM SERIES S94
AMI Precious Metals 2017
THE PRECIOUS METALS DEVELOPMENT NETWORK (PMDN)
17–19 October 2017
Protea Hotel Ranch Resort, Polokwane, South Africa
MINTEK
necsa
We're in your world
CSIR
Abstracts of papers presented at the conference

Study of as-cast Co-Fe-Pd samples

K. Dyal Ukabhai and L.A. Cornish
School of Chemical and Metallurgical Engineering, University of the Witwatersrand, Johannesburg, and DST-NRF Centre of Excellence in Strong Materials, hosted by University of the Witwatersrand, Johannesburg

There is potential for using Fe-Co-Pd rare-earth-doped alloys for magnets, because FeCo is a soft magnetic material with a high saturation magnetism and a high Curie temperature, due to the cobalt. Palladium nano-particles have localised paramagnetism, and have the potential to become magnetic and so would be a useful addition. Pd has already been shown to improve the magneto-crystalline anisotropy of FeCo. Thus, the system offers possible alternatives for the heavy and expensive rare-earth magnets. The phase diagram of Fe-Co-Pd was derived by Russian workers (Kuprina and Grigorev, 1958, 1959, 1961; Grigorev and Kuprina, 1961) and reviewed by Ragavhan (1992), who stated that it was very speculative. However, the original work was inconsistent, and so the system needs to be studied again so that the phase diagram can be used as a guide to which alloys to develop. In order to study the phase diagram, samples of different compositions were synthesised. The compositions of the samples focused on areas where good magnetic properties have been reported or are expected, and the extension of the $FePd_3$ phase. The samples were made in a button arc furnace in an argon atmosphere on a water-cooled copper hearth. They were sectioned, mounted, ground, polished and etched, and analysed by scanning electron microscopy with energy dispersive X-ray spectroscopy to ascertain the microstructures and to determine the overall and phase compositions. Further analysis is to be conducted using XRD. Once enough data has been collected, the solidification projection of the different phases will be constructed.

REFERENCES

Grigorev, A.T. and Kuprina, V.V. (1961). Order-disorder transformation in alloys of iron with cobalt and palladium. *Russian Journal of Inorganic Chemistry*, 6 (8), 966–970.

Kuprina, V.V. and Grigorev, A.T. (1958). Investigation of alloys of Fe-Co-Pd system. I. Fusibility diagram of the Fe-Co-Pd system. *Zhurnal Neorganicheskoi Khimii*, 3 (12) 2736-2739 (in Russian).

Kuprina, V.V. and Grigorev, A.T. (1959). Solid-state transformations in alloys of iron with cobalt and palladium. *Russian Journal of Inorganic Chemistry*, 4 (7), 724–727.

Kuprina, V.V. and Grigorev, A.T. (1961). $\alpha > \gamma$ Polymorphic transformation in alloys of iron with cobalt and palladium. *Izvestiya Vysshikh Uchebnykh Zavedenii, Khimiya i Khimicheskaya Tekhnologiya*, 4 (1) 7-10 (in Russian).

Raghavan, V. (1992). The Co-Fe-Pd (cobalt-iron-palladium) system. *Phase Diagrams of Ternary Iron Alloys*. Indian Institute of Metals, Calcutta, 6A, 623–627.

Notes

INITIAL STUDY OF AS-CAST Co-Fe-Pd SAMPLES

K. Dyal Ukabhai and L.A. Cornish

School of Chemical and Metallurgical Engineering, University of the Witwatersrand, Johannesburg, and DST-NRF Centre of Excellence in Strong Materials, hosted by University of the Witwatersrand, Johannesburg

There is potential for Fe-Co-Pd rare earth-doped alloys for magnets, because FeCo is a soft magnetic material with a high saturation magnetism and a high Curie temperature, due to the cobalt.[1] Palladium nano-particles have localized paramagnetism, with the potential to become magnetic, and could be a useful addition, as Pd has already been shown to improve the magneto-crystalline anisotropy of FeCo.[1] Thus, the system offers possible alternatives for the heavy and expensive rare-earth magnets.

The phase diagram of Fe-Co-Pd was derived by Russian workers[2, 3] and reviewed by Ragavhan[4], who stated that his interpretation of the system was very speculative. However, the original work[2, 3] was inconsistent, and thus the system needs to be studied again so that the phase diagram can be used as a guide to develop alloys from, so that the required phases can be targeted.

In order to study the phase diagram, samples of different compositions were made. The sample composition were areas where good magnetic properties have been reported.[1] The samples were made in a button arc furnace, then sectioned, mounted, ground, polished and etched in either dilute hydrochloric acid and nitric acid, or electrically in dilute and hydrochloric acid with a graphite cathode, between 3 V and 10 V. They were analysed in a Zeiss SEM with energy dispersive X-ray spectroscopy to identify the microstructures and to determine the overall and phase compositions. XRD was conducted using the Bruker D2.

The dendrites (Fig. 1) were due to coring, given the closeness of the analyses. At higher magnification (Fig. 2) the decomposition of the dendrites into two fine phases was seen, although these two phases were too fine to analyse individually. It was surmised that the fine phases were α´ martensite within the parent γ (Pd); this was confirmed by XRD. Fig. 3 shows a microstructure where dark needles formed first, and then reacted peritectically to give the surrounding lighter phase. Next, a darker region formed. The phase compositions were very similar, which is surprising because the phases should have been sufficiently coarse to analyse accurately. The regions in Fig. 3 were confirmed by XRD to be FePd (dark), α´ (medium) and γ (Pd) (light). Future work will include annealing the samples and more compositions.

References:
1. Kovacs, A., Sato, K. and Hirotsu, Y. (2007) J. App. Phys. 101, 03310.
2. Grigorev, A.T. and Kuprina, V.V. (1961). Zh. Neorg. Khim. J. Inorg. Chem. 6(8), 966.
3. Kuprina, V.V. and Grigorev, A.T. (1961) Izv. Vyss. Uchebn. Zaved., Khim., Khim. Tekhnol. 4(1), 7.
4. Raghavan, V. (1992) Phase Diagrams of Ternary Iron Alloys 6A, 623.

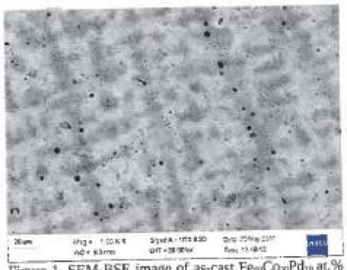


Figure 1. SEM-BSE image of as-cast $Fe_{60}Co_{30}Pd_{10}$ at.% showing darker contrast dendrites.

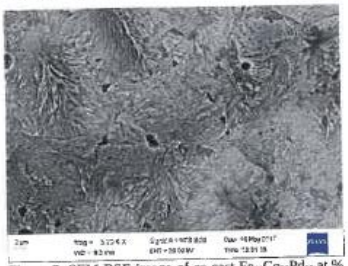


Figure 2. SEM-BSE image of as-cast $Fe_{60}Co_{30}Pd_{10}$ at.% showing decomposition of the dendrites.

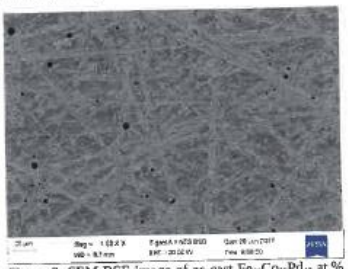


Figure 3. SEM-BSE image of as-cast $Fe_{30}Co_{30}Pd_{40}$ at.% showing needles (dark), peritectically-formed phase (light), with dark matrix.

Corresponding author: 669011@students.wits.ac.za

Phase analyses of the Co-Fe-Pd ternary alloys

K Dyal Ukabhai[1, 2,*], I A Mwamba[2, 3] and L A Cornish[1, 2]

[1] School of Chemical and Metallurgical Engineering, University of the Witwatersrand, Johannesburg, South Africa
[2] DST-NRF Centre of Excellence in Strong Materials, hosted by University of the Witwatersrand, Johannesburg, South Africa
[3] Advanced Materials Division, Mintek, Randburg, South Africa

*Kiyaasha.dyalukabhai@students.wits.ac.za

Abstract. Samples of different compositions of Co-Fe-Pd were made in a button arc furnace, under an argon atmosphere on a water-cooled copper hearth. They were sectioned and a half was kept in the as-cast state. The samples were analysed in a scanning electron microscope with energy dispersive X-ray spectroscopy, and in an X-ray diffractometer to derive the microstructures and to determine the overall and phase compositions. Coring occurred in many samples, which was expected due to the wide composition range of the main solid solution in the system. The microstructures were not similar to any of the work of sixty years ago when the Co-Fe-Pd phase diagram was studied. Some of the phases were too fine to be analysed with EDS in the as-cast samples.

1. Introduction

Magnetic materials are essential in many industries, and there is a need to replace expensive rare earth metals with cheaper and more readily available metals. Historically, patents held by American and Japanese companies have been a barrier to entry into the magnet market. However, China's establishment of research institutes in the 1950s and 1960s, and the expiry of the American and Japanese patents in the 1980s has enabled China to enter and dominate the magnet market. Currently, China has a monopoly on the magnet value chain, producing 90% of the world's permanent magnets, and China also has most of the world's rare earth resources.

There is potential to use Co-Fe-Pd rare earth-doped alloys for magnets, because FeCo is a soft magnetic material with high saturation magnetism and a high Curie temperature, due to the cobalt [1]. Palladium nano-particles have localized paramagnetism, with the potential to become magnetic, and so Pd can improve the magneto-crystalline anisotropy of FeCo. Thus, the Co-Fe-Pd system offers possible alternatives to the heavy and expensive rare-earth magnets, which are in current use.

The Fe-Co-Pd alloy has potential applications in biotechnology, electronics and green technologies. Magnetic thin films and nanostructures, which are magnetized perpendicular to their surfaces, are essential to many developing technologies, including spintronics devices [2] and patterned media [3, 4]. This maintained the thermal stability even as the device dimensions became increasingly nanoscale. Multilayers or superlattice structures consisting of alternating ferromagnetic and non-magnetic layers are highly suitable for these applications, due to their tunable perpendicular magnetic anisotropy (PMA) and saturation magnetization [5, 6].

Content from this work may be used under the terms of the Creative Commons Attribution 3.0 licence. Any further distribution of this work must maintain attribution to the author(s) and the title of the work, journal citation and DOI.
Published under licence by IOP Publishing Ltd

By combining the soft magnetic properties of iron and the hard magnetic properties of cobalt and palladium, an optimal magnetic material could be developed. Fe-Co alloys have a B2 structure which makes them extremely brittle at room temperature [1]. The workability of these alloys can be improved by adding nickel or palladium, and palladium especially leads to a higher tensile strength and elongation at room temperature [1].

Apart from the mechanical properties [1] of the Fe-Co-Pd alloys and research on the magnetic shape memory properties [7, 8, 9], little work has been done on the ternary phase diagram [10-13]. The published phase diagram work is from four papers by a group in Russia [10-13] and these papers are contradictory, even sometimes within the same paper. Ragavhan [14] attempted to assess the system, and was unable to satisfactorily interpret it due to the contradictory data, and admitted that his interpretation was very speculative. His isothermal section at 25 °C [14] is given in figure 1, and is much simpler than that of Grigorev and Kuprina [13].

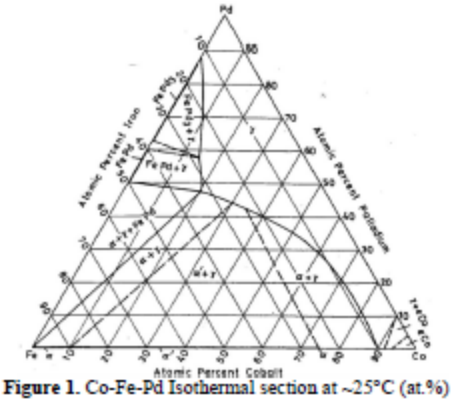


Figure 1. Co-Fe-Pd Isothermal section at ~25°C (at.%) [14].

Table 1. Nominal composition of samples.

Alloy	Fe (at.%)	Co (at.%)	Pd (at.%)
1	60	30	10
2	15	10	75
3	30	30	40

Since Co-Fe-Pd alloys are being studied to improve their magnetism [15], it is necessary to know the extent of the promising Co-Fe phases into the ternary system. There are problems with the phase diagram [14], and so this study was to identify the extents of those phases.

2. Experimental procedure

The composition of the samples shown in table 1 were determined by choosing three-phase regions from the 25°C isothermal section of Raghavan [14], as well as compositions of interest for magnetic properties [15]. The alloys were prepared from 99.99% pure elemental powders of Fe, Co and Pd. The powders were weighed, mixed and cold compacted (to hold the components together prior to melting) and then melted in a button arc-furnace (BAF), according to standard preparation method PMD-SOP-O37. An argon atmosphere and a water-cooled copper hearth were used, together with a titanium oxygen-getter, which was melted before making each sample. The samples were cut using a Struers automatic cutting machine with an Accutom cutting wheel, mounted in a mounting press, ground and polished. Grinding and polishing were done using a Saphire 520 automatic machine. One half of each sample was studied in the as-cast condition. Once the samples were polished, they were removed from the polyfast resin and X-ray diffraction (XRD) was conducted using a Bruker D2 Phaser and the Diffrac Plus EVA program with the 2018 database to analyse the data.

Due to the wide range of compositions of the samples (from 10-75 at.% Pd), different etching techniques were tried, and the best results for each sample was used. The first etch tried was using a

steel wire cathode and a solution of 90ml water and 10ml hydrochloric acid [16]. The second etch was immersion in a solution of distilled water (50 ml), hydrochloric acid (SG 1.19, 100 ml) and nitric acid (SG 1.4, 10ml) [16]. Once the samples were etched, they were analyzed on a Sigma Zeiss scanning electron microscope (SEM) using backscattered (BSE) and secondary electron (SE) modes. Once the microstructures were visible, EDX analyses were done to determine the composition of the different phases and the overall compositions of each sample.

3. Results

For Alloy 1 (Fe_{60}:Co_{30}:Pd_{10} (at.%)), the low Pd content allowed a less aggressive etchant to be used: electric etching with a steel wire cathode in a solution of water and hydrochloric acid. The dendrites in figure 2a were due to coring from the fast cooling from arc-melting, given the lack of a definite interface between the dendritic and interdendritic regions, and they also had similar compositions, table 1. There was also a finer, darker phase visible, which was too small (<2 μm) to analyse accurately [17], without collecting X-rays from the surrounding phase. The XRD results (figure 3) showed that the major phase was γ (fcc), and the minor phase was α (bcc).

Alloy 2 (Fe15:Co10:Pd75 (at.%)) needed the most aggressive etchant method, 2, because of its high Pd content. The microstructure in figure 2b shows dendrites, and two-phase interdendritic regions, where the second phase was darker. Once again, the smallest phases were too fine to analyse accurately [17], resulting in similar compositions of the dendritic and interdendritic areas, table 2. The XRD pattern (figure 4) indicated FePd3 and FePd.

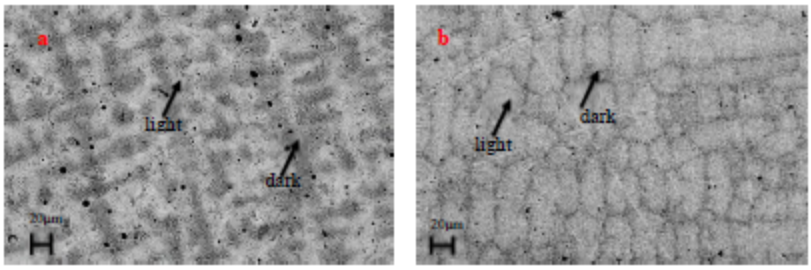


Figure 2. SEM-BSE images of as-cast a) Alloy1 Fe_{60}:Co_{30}:Pd_{10} (at.%) showing dendrites (darker) and b) Alloy 2 Fe_{15}:Co_{10}:Pd_{75} (at.%) showing gamma dendrites (lighter) and two phase interdendritic area (dark).

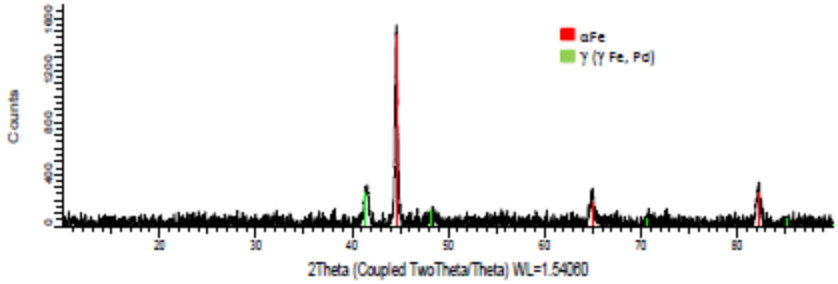


Figure 3. XRD pattern for Alloy 1 Fe_{60}:Co_{30}:Pd_{10} (at.%), as-cast condition.

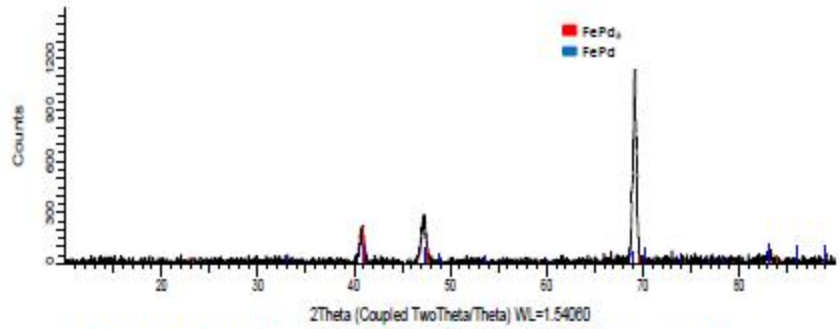


Figure 4. XRD pattern for nominal Alloy 2 Fe_{15}:Co_{10}:Pd_{75} (at.%), as-cast condition.

Figure 5 of Alloy 3 (Fe30:Co30:Pd40 (at.%)) shows a single phase, with pores filled with debris from grinding. The XRD pattern in figure 6 shows one major phase which matched two different compositions of γ, with wide peaks, indicating a cored phase.

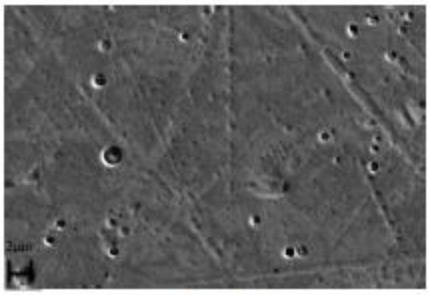


Figure 5. SEM-BSE image of as-cast Alloy 3 Fe_{30}:Co_{30}:Pd_{40} (at.%) showing a single phase with pores.

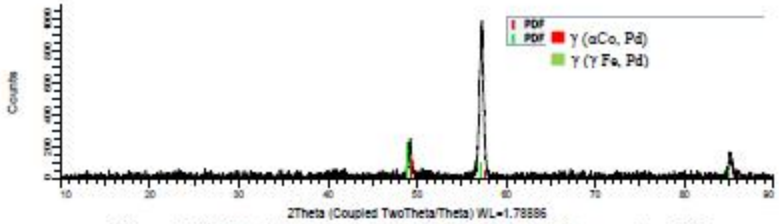


Figure 6. XRD pattern for nominal Fe_{30}:Co_{30}:Pd_{40} (at.%), as-cast condition.

Table 2. SEM-EDS analyses of the sample overalls and the phases of different contrasts.

Alloy	Overall	Dark: γ	Light: γ	Light: FePd	Dark: $FePd_3$
	Fe 59.6	59.1±0.1	54.8±1.2		
1	Co 29.1	28.5±0.3	25.1±1.3	--	--
	Pd 11.3	12.4±0.3	20.1±2.5		
	Fe 13.6			13.4±0.4	14.5±0.1
2	Co 9.0	--	--	8.2±0.4	11.1±1.3
	Pd 77.4			78.4±0.5	74.4±1.2
	Fe 28.2	28.7±0.1	29.2±0.1		
3	Co 28.3	28.3±0.1	27.7±0.1	--	--
	Pd 43.5	43.0±0.1	43.1±0.1		

4. Discussion

Due to the samples containing Pd, a high acceleration voltage (20kV) had to be used on the SEM in order to excite the Pd X-rays for EDS. Using a high kV causes the electron beam to spread out further [17], making the area for accurate EDS analysis larger (typically ≥2 microns), hence the samples with fine microstructures could not be accurately analysed in the SEM.

Given the very wide γ liquidus of the system and the few solid phases [10-14], it is not surprising that the alloys were cored. None of the microstructures found to date was similar to those of the previous workers [10-14], although the decomposition of Alloy 1 would be expected from the ~25°C isothermal section of Raghavan [14] because the alloy composition lies in a two-phase region. However, the phases found here were γ and α, whereas Raghavan [14] showed that the phases should be γ and α′ (Figure 1). Thus, Alloy 1 suggests a wider γ + α phase field than Raghavan [14]. Alloy 2 shows that the γ phase was more narrow than Raghavan [14] indicated (Figure 1). Conversely, Alloy 3, is a single-phase solid solution of γ, showed that this phase had a greater extent at this alloy composition than in Raghavan's isothermal section [14], Figure 1.

There was a better agreement of the as-cast samples with the 25°C isothermal section of Raghavan [14] than with that of Kuprina and Grigorev [11]. Strictly, the as-cast samples of this work should not have been compared to the ~25°C isothermal sections of Kuprina and Grigorev [11] and Rhagavan [14], but there was no other information available for comparison.

The coring in Alloy 1 was used to assess the validity of the two liquidus surfaces [11, 14] since the dendrites would form first, and the interdendritic area would form next, and the direction from the former to the latter should follow the slope of the liquidus surface. The deduced liquidus slope agreed with both of the liquidus surfaces [11, 14], so it was not possible to choose a better one. The XRD patterns showed very few peaks, making identification of the phases difficult.

5. Conclusions

Three alloys of different compositions were manufactured by arc melting and studied in the as-cast condition. Alloy 1 comprised γ and α, suggesting a wider γ + α phase field than Raghavan [14]. Alloy 2 showed that the γ phase was more narrow than Raghavan [14], whereas Alloy 3, a single-phase solid solution of γ, showed a greater extent than Raghavan's isothermal section [14]. The results were in better agreement with Raghavan's [14] isothermal section at ~25°C The compositions of the cored microstructures of Alloy 1 agreed with both published liquidus surfaces.

References

[1] Matsuda M, Sago R, Akamine K, Tsurekawa S, Takashima K and Nishida M 2016 Enhancement of Ductility in Fe-Co Based Alloys by Substitution of Pd (in English) *J. Alloys*

Compd. **682** 124-131
[2] Ravelosona M S, Katine D, Carey J A, Terris M J and Fullerton E E 2006 Current-induced magnetization reversal in nano-pillars with perpendicular anisotropy *Nat. Mater.* **5** 210–215
[3] Todorovic M, Schultz S, Wong J and Scherer A 1999 Writing and reading of single magnetic domain per bit perpendicular patterned media *Appl. Phys. Lett.* **74** 2516–2518
[4] Ding J and Adeyeye A O 2013 Binary ferromagnetic nano-structures: fabrication, static and dynamic properties *Adv. Funct. Mater.* **23** 1684–1691
[5] Terris B D and Thomson T 2005 Nano fabricated and self-assembled magnetic structures as data storage media *J.Phys.* D **38** 199–222
[6] Rippard W H, Deac A M, Pufall M R, Shaw J M, Keller M W, Russek S E, Bauerand G E and Serpico C 2010 Spin-transfer dynamics in spin valves with out-of-plane magnetized CoNi free layers *Phys. Rev.* B **81**
[7] Koeda J, Nakamura Y, Fukuda T, Kakeshita T, Takeuchi T and Kishio K 2001 *Trans. Mater. Res. Soc.* (Japan) **26** 215-217 as quoted by [18]
[8] Oshima R 1981 *Scripta Metall.* **15**, 829-833 as quoted by [18]
[9] Kauffmann-Weiss S, Hamann S, Gruner M E, Buschbeck J, Ludwig A, Schultz L and Fähler S 2012 Understanding the Magnetic Shape Memory System Fe-Pd-X by Thin Film Experiments and First Principle Calculations *Adv. Eng. Mater.* **14** (8) 724-749
[10] Grigorey A T and Kuprina V V 1961 Order-Disorder Transformatiom in Alloys of Iron with Cobalt and Palladium (in Russian) *Zh. Neorg. Khim.* **6** (8) 1891-1898, English translation: *J. Inorg. Chem.* **6**(8) 966-970
[11] Kuprina V V and Grigorev A T 1958 Investigation of Alloys of Fe-Co-Pd System. I. Fusibility Diagram of the Fe-Co-Pd System (in Russian) *Zh. Neorg. Khim.* **3** (12) 2736-2739
[12] Kuprina, V V and Grigorev AT 1959 Solid-State Transformations in Alloys of Iron with Cobalt and Palladium (in Russian) *Zh. Neorg. Khim.* **4** (7) 1606-1610 English translation: *J. Inorg. Chem.* **4** (7) 724-727
[13] Kuprina V V and Grigorev A T 1961 Polymorphic Transformation in Alloys of Iron with Cobalt and Palladium (in Russian) (Izv. Vyss. Uchebn. Zaved. Khim., Khim. Tekhnol) **4** (1) 7-10
[14] Raghavan V 1992 The Co-Fe-Pd (Cobalt-Iron-Palladium) System (in English) Phase Diagrams of Ternary Iron Alloys (Indian Institut of Metals, Calcutta) **6** A, 623-627 .
[15] Manyti H 2017 Personal communication
[16] Wing G 1996 A lexicon of metallographic etchants, MSc Thesis (University of the Witwatersrand South Africa)
[17] Goldstein G I, Newberry D E, Echlin P, Joy D C, Fiori C and Lifshin E 1981 *Scanning Electron Microscopy and X-Ray Microanalysis* (New York: Plenum Press) 56-59
[18] Tsuchiya K, Nojiri T, Ohtsuka H and Umemoto M 2003 Effect of Co and Ni on Martensitic Transformation and Magnetic Properties in Fe-Pd Ferromagnetic Shape Memory Alloys *Mater. Trans.* **44** (12) 2499-2502